Measurement of ^{146}Sm Half-Life
and
Ionization Produced by 254 eV_{nr} Nuclear Recoils in Germanium

by

Alexander R. Kavner

A dissertation submitted in partial fulfillment
of the requirements for the degree of
Doctor of Philosophy
(Applied Physics)
in the University of Michigan
2024

Doctoral Committee:

Professor Igor Jovanovic, Chair
Dr. Geon-Bo Kim, LLNL
Professor Cagliyan Kurdak
Professor Bjoern Penning
Professor David Wehe

Alexander R. Kavner
akavner@umich.edu
ORCID iD: 0009-0009-8655-3426

DEDICATION

To Josh, Kyle, Lon, and my mom. Thank you for your unending support.

ACKNOWLEDGEMENTS

I want to thank my advisor, Professor Igor Jovanovic, both for his tremendous guidance and support and also for accepting me into his research group under less than typical circumstances (as I left UChicago and during the height of the Covid-19 pandemic!). I would like to thank Professor Jovanovic for supporting me in conducting my own independent research into low-energy nuclear recoils in germanium. I would like to thank Professor Cagliyan Kurdak the director of the Applied Physics Program who accepted me to the University and waived many course requirements.

At Lawrence Livermore National Laboratory, I would like to thank Dr. Geon-Bo Kim for hosting me and allowing me to work in his group at the lab. He provided hands-on experience with cryogenic systems for which I am grateful. I would like to thank Dr. Stephan Friedrich for similarly hosting me at the lab. And I would like to thank Professor Stephen Boyd for teaching me about superconducting circuits and electronics, particularly while he spent his sabbatical at the lab. There are numerous scientists who contributed to the successful ^{146}Sm half-life measurement. I would like to thank all of them for their work and contributions. Of specific note, I would like to thank Dr. Kelly Kmak and Dr. Quinn Shollenberger. Both of them contributed much of their own time and energy towards this project for which I am incredibly grateful.

There are many fellow graduate students whom I could not do this without. At LLNL, I was helped in many ways by Dr. Nathan Hines, Connor Bray, and Spencer Fretwell. They assisted in everything from opening and closing the fridge, to discussions on digital signal processing, and many more. At the University of Michigan, I would like to thank Dr. Kris Ogren, Colton Graham, Oskar Searfus, and Andrew Wilhelm, who put up with and assisted in my schemes and shenanigans.

There are numerous funding sources I would like to thank for their support. The DOE NNSA Laboratory Residency Graduate Fellowship funded me for the majority of my PhD and paid for me to spend extended periods at Lawrence Livermore National Laboratory. I am incredibly grateful for the fellowship, the committee that selected me, and Kris Moran for her work as the fellowship coordinator. I was additionally funded by the Department of Energy National Nuclear Security Administration, Consortium for Monitoring, Verification and Technology (DE-NE000863). The ^{146}Sm half-life measurement was funded by the Laboratory-Directed Research and Development program of Lawrence Livermore National Laboratory (20-LW-024). This work was performed under the auspices of the U.S. Department of Energy by Lawrence Livermore National Laboratory

under Contract DE-AC52-07NA27344. The work on low-energy nuclear recoils in germanium was supported by the U.S. Department of Energy, Office of Nuclear Energy under DOE Idaho Operations Office Contract DE-AC07- 051D14517 as part of a Nuclear Science User Facilities experiment. The low-energy nuclear recoil experiment was further supported by the University of Michigan Rackham Graduate Fellowship which helped fund material expenditures.

TABLE OF CONTENTS

LIST OF FIGURES

FIGURE

LIST OF TABLES

TABLE

LIST OF ACRONYMS

DOE Department of Energy

NNSA National Nuclear Safety Administration

CRM Certified Reference Material

LLNL Lawrence Livermore National Laboratory

LANL Los Alamos National Laboratory

ORNL Oak Ridge National Laboratory

MMC Magnetic Microcalorimeter

TES Transition Edge Sensor

STJ Superconducting Tunnel Junction

SQUID Superconducting Quantum Interference Device

TIMS Thermal Ionization Mass Spectrometry

HPGe High Purity Germanium (detector)

FWHM Full Width at Half Maximum

CPS Counts Per Second

FFT Fast Fourier Transform

ROI Region of Interest

PPM Parts Per Million

FPGA Field Programmable Gate Array

ABSTRACT

Cryogenic-quantum radiation detectors have long been heralded for their unique capabilities, though have been utilized in only a few use cases given their high complexity and operational cost. Historically, cryogenic calorimeters and bolometers have been used for the study of the cosmic microwave background, dark matter searches, and neutrino experiments. In such experiments, magnetic microcalorimeters and/or transition edge sensors measure the micro-heat imparted by electromagnetic radiation and fundamental particle interactions.

Recently, groups have developed detectors and techniques for nuclear sciences and applications such as high-resolution X-ray and gamma-ray spectroscopy. This dissertation discusses the development of absolute decay counting for long-lived isotopes based upon decay energy spectroscopy whereby radioactive samples are embedded within a cryogenic detector enabling measurement of the entire decay energy. These techniques were developed for the measurement of the ^{146}Sm half-life, an important value for nuclear astrophysics and cosmo-chemistry with tension between prior measurements.

A ^{146}Sm source was produced at the TRIUMF Laboratory and then processed and purified at Lawrence Livermore National Laboratory, yielding a pure sample. The source was embedded within a 4π thermal absorber coupled to a magnetic microcalorimeter achieving nearly 100% counting efficiency. Experimental uncertainties were studied and modeled, including the thermal coupling of the source to the absorber, pulse pile-up, trigger, and event selection efficiencies. The absolute activity of the pure ^{146}Sm source was measured to better than 1% uncertainty.

The precise sample mass was determined by mass spectrometry measurements performed by radio-chemists at Lawrence Livermore National Laboratory. From these measurements, the half-life was found to be 86 million years, a value between the two previous measurements. A second decay counting experiment was performed which verified this half-life value.

A second experimental campaign was performed to measure the ionization produced by 254 eV_{nr} nuclear recoils in high-purity germanium. This work was conducted to better characterize the material response of germanium for use as a dark matter or neutrino detector.

The ionization produced by low-energy nuclear recoils is the primary signature of dark matter. Despite the urgency of dark matter detection and the recent measurements of coherent elastic neutrino-nucleus scattering, detector response is still not well characterized across a variety of

materials in the keV_{nr} and sub-keV_{nr} regime. We have re-performed a measurement of the ionization produced by monoenergetic 254 eV_{nr} nuclear recoils in Ge with improved digital electronics and event tagging scheme. Our results indicate an ionization yield of 66 ± 5 eV_{ee} corresponding to a quenching factor of 25 ± 2 %, greater than 14% predicted by the Lindhard Model. This quenching enhancement would greatly improve the sensitivity of high-purity Ge detectors for both dark matter detection and measurement of neutrinos via coherent scattering.

CHAPTER 1

Introduction

1.1 Topical Overview

The primary contributions of my doctoral research discussed within this thesis is on the development of techniques to perform precision nuclear measurements utilizing cryogenic magnetic microcalorimeters. This has included the development of digital signal processing algorithms, simulations of detector pile-up and efficiency, studies of embedding samples within detectors, and substantial data analysis.

The primary aim was to perform a half-life measurement of ^{146}Sm using microcalorimetry with secondary goals of performing measurements relevant to nuclear safeguards and nuclear forensics which are more broadly relevant to the mission of Lawrence Livermore National Laboratory and the National Nuclear Security Administration within the Department of Energy. Towards these goals, a large number of measurements were performed with a variety of radiation sources including: ^{146}Sm, ^{147}Sm, and various actinides.

This first chapter will provide a brief introduction to cryogenic microcalorimetry and describe the physics problems aimed at being solved through decay energy spectroscopy (DES) measurements. The scope of the remaining chapters is as follows:

Chapter 2: operational principles of Magnetic Microcalorimeters.
Chapter 3: digital signal processing and application of digital filtering to microcalorimeters.
Chapter 4: simulations of pile-up and detector efficiency.
Chapter 5: early DES measurements performed on ^{147}Sm and ^{241}Am.
Chapter 6: half-life measurement of ^{146}Sm.
Chapter 7: various actinide measurements.
Chapter 8: low energy nuclear recoils in germanium.

The final content chapter, discusses a separate topic, the ionization produced by low-energy

nuclear recoils in germanium. This work is separate from the work on microcalorimetry but is similarly motivated as a high-precision nuclear physics measurement.

1.2 Cryogenic Microcalorimetry

1.2.1 Magnetic Microcalorimeters

Metallic Magnetic Microcalorimeters (MMCs) are highly sensitive thermal detectors with excellent energy resolution [1, 2]. Detectors are generally comprised of three primary components: a gold-foil radiation absorber, a paramagnetic sensor (typically an Ag or Au alloy with ~500 ppm of enriched ^{166}Er [3]) positioned above a niobium superconducting coil, and a direct current superconducting quantum interference device (DC-SQUID) that measures current induced by change in magnetization of the paramagnetic sensor [3].

At millikelvin temperatures, the paramagnetic spin system exhibits strong temperature dependence. Spin flips induce a change in current within the superconducting coil which is amplified and measured. The energy required to flip a spin is of order micro-electron volts. In comparison, the energy required to produce an electron-hole pair signal carrier in germanium is 3 electron volts; this value is temperature-dependent and can change but not by orders of magnitude. Thus the energy required to flip one erbium spin is five to six orders of magnitude smaller than the energy required to produce an electron-hole pair in germanium. Stated differently, a given amount of energy produces 5–6 orders of magnitude more information carriers. Because of this, microcalorimeters can be employed as ultrahigh-precision radiation detectors which can far surpass traditional technologies in terms of resolving power, defined as the full-width-half-maximum (FWHM) of a peak expressed in energy units. The theoretical best resolution attainable with a microcalorimeter is limited by its heat capacity. The working principles of MMCs are discussed in greater detail in Chapter 2.

1.2.2 Radiation Detection

Traditional calorimetry, within the context of nuclear physics, entails the measurement of the steady-state heat produced by a radioactive object as it decays. Typically large masses of radioactive material are used from which the activity can be of order curies or greater. Microcalorimetry instead measures the micro-heat produced by individual radiation interactions within the aforementioned radiation absorber. Energetic phonons are produced by radiation deposition. These phonons thermalize via interaction with the conduction electrons of the gold raising the system temperature. The conduction electrons then interact with the spin system inducing the previously discussed spin flips [1].

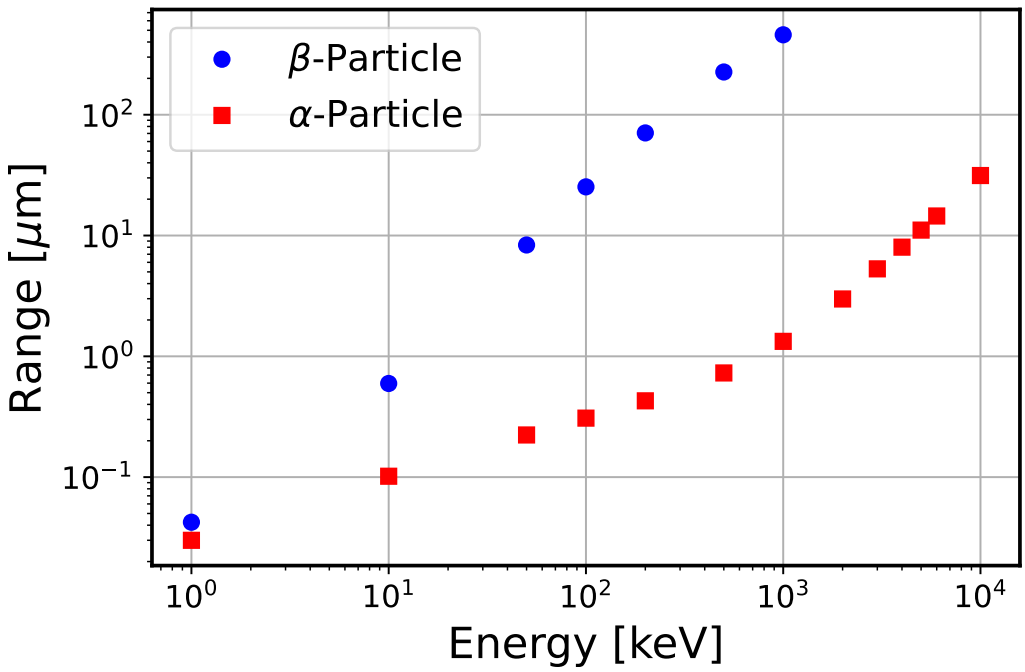

Figure 1.1: The range of keV to MeV energy alpha (*red*) and beta particles (*blue*) in gold. Data taken from NIST ASTAR and ESTAR databases [4].

For example, a 5-MeV alpha decay increases the temperature of a few milligrams of gold by a few hundredths of a millikelvin, which corresponds to ~1 Φ_0 of magnetic flux for the sensors utilized in this research. Here, Φ_0 is the fundamental magnetic flux quantum equal to $2.067833848 \cdot 10^{-15}$Wb.

Gold is an ideal material for use as a thermal absorber. In addition to its thermal properties of high conductivity and low heat capacity at cryogenic temperatures, its density is high at 19.3 g/cm^3 and it is a high Z material with atomic number 79. This makes gold an ideal choice for stopping charged particles such as alpha or beta radiation. The range of a 5 MeV alpha particle or a 200 keV beta particle is approximately 10 μm. Such foils are readily commercially available and can be made into radiation absorbers with low heat capacities.

1.2.3 Decay Energy Spectroscopy

The decay energy spectroscopy (DES) technique entails embedding radionuclide(s) within a thermal absorber. If an alpha-decay species, such as ^{146}Sm, is embedded within a gold foil (the absorber), the entire decay energy can be measured with ~100% efficiency, including energy deposited from the alpha particle, nuclear recoil, soft X rays, Auger electrons, and conversion electrons. The gold foil is only insensitive to higher energy photons and only partially sensitive to beta particles, neither of which are emitted by ^{146}Sm.

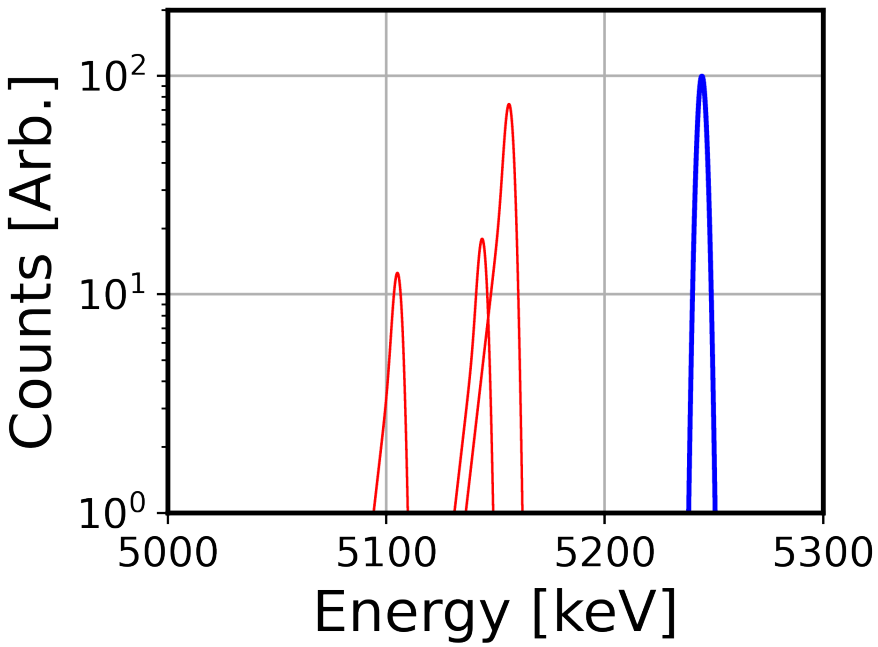

Figure 1.2: Hypothetical alpha spectra (*red*) and decay energy spectra (*blue*) of ^{239}Pu. The $\sim$ 100 keV difference between the highest energy alpha peak and the decay energy peak is due to the inclusion of the ^{235}U nuclear recoil in the decay energy spectroscopy measurement. Slight low energy tailing is shown in the alpha spectroscopy case to represent modest source self attenuation.

The DES technique allows isotopes to be identified via their unique decay energies. Because the source is embedded within the active volume of the detector, no energy is lost to the outside environment or detector dead layer(s). The effect is a great simplification of the reconstructed energy spectrum for alpha decaying isotopes. For example, the decay of ^{239}Pu has three primary alpha branches [5]. If decays are measured via alpha spectroscopy, three alpha peaks are observed at 5105.5 keV, 5144.3 keV, and 5156.6 keV with relative intensities of 11.94%, 17.11%, and 70.77% respectively. The remaining 0.18% of decays go to different alpha branches. In the decay energy spectroscopy case, all decays are measured in a single peak at the decay energy of 5244.5 keV. The difference between alpha and decay energy spectroscopy for ^{239}Pu is depicted in Figure 1.2. The impact of the resultant spectral simplification is magnified for mixed isotope samples and enables nuclear metrology [6].

1.3 ^{146}Sm Motivation

1.3.1 Long-Lived Half-Life Problem

Large uncertainties exist within the nuclear data for long-lived radioisotopes [7, 8, 9]; of the 54 known isotopes with half-lives between 30 and 10^8 years, 23 have poorly measured half-lives with uncertainties greater than 5% [10]. These uncertainties originate from the difficulty of producing pure isotopic samples as well as challenges in the determination of the source absolute activity. Tightening of these uncertainties contributes to diverse areas of nuclear science including nuclear astrophysics, radioisotope dating, nuclear forensics, power generation, and nuclear medicine [7, 8, 11, 12, 13, 14, 15, 16, 17]. The half-lives of short-lived radionuclides are conventionally determined via observation of the relative decrease in the decay rate. If the experimental apparatus is not changed during the measurement, systematic effects such as detection efficiency and quantity of source material cancel out [18, 19].

For radionuclide species with long half-lives, the decay in the activity rate cannot be measured in a feasible amount of time, and the half-life is instead determined via the measurement of the absolute activity of a precisely quantified source. In such experiments, understanding detection efficiency is crucial for accurate results [10].

The activities of alpha-decay species are typically measured with a surface barrier or similar charged particle detectors. These detectors exhibit relatively low efficiencies ($\lesssim$20%) as well as large uncertainties in the geometric efficiency [20, 18, 19]. Even if deposited on the detector surface, uncertainties due to source self-attenuation are difficult to quantify and can cause tailing, among other spectral distortion features [18].

The efficiency can be improved by dissolving the source in a liquid scintillator. However, this introduces a different set of challenges, as the heavy charged particles exhibit strong quenching of light output in scintillators. The liquid scintillation counting method pushes the alpha peak to lower energies, into the region where beta decays and the Compton continuum from gamma rays create a high background [21, 22]. Light output quenching in liquid scintillators can be exacerbated by the presence of nitrates, chlorides, and other contaminants introduced via the dissolution of the source [22]. Additionally, the generally poor energy resolution of ~0.5–1.0 MeV further complicates alpha decay counting.

1.3.2 The Sm-Nd Chronometer & ^{146}Sm

^{146}Sm is a noteworthy isotope for its relevance to the Sm-Nd nuclear chronometer, an important dating technique [23]. The two most recent measurement of the ^{146}Sm half-life yielded 103 ± 5 Ma [20] and 68 ± 7 Ma [24]. While both of those measurements report uncertainty in the range

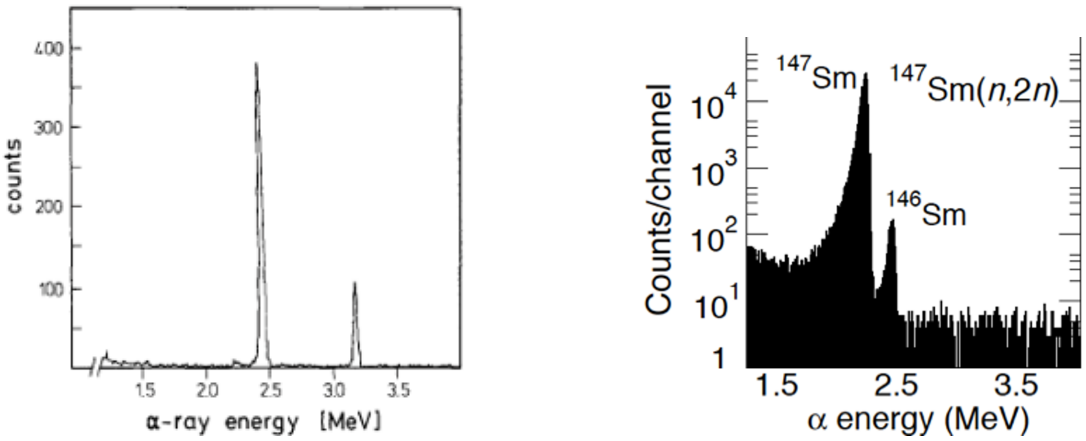

Figure 1.3: *Left*: Experimental ^{146}Sm alpha spectrum taken from Figure 1 of [20]. The prominent peak at ~2.4 MeV is from ^{146}Sm while the smaller higher energy peak at ~3.2 MeV is from a ^{148}Gd calibration source. *Right*: Experimental alpha spectrum containing both ^{146}Sm and ^{147}Sm alpha peaks. The systematic uncertainty from prominent line overlap can be easily seen and is exacerbated by the several order of magnitude difference in count rates between the two alpha sources. The spectrum is taken from Figure 1 of [24].

of 5–10%, they differ by 50%.

Samarium-neodymium chronometers are important and common tools for establishing a timeline of early solar-system events including the formation of the first solids, formation of the Earth's Moon, solidification of the Martian surface, and similar events [23, 25, 26, 27]. The methodology utilizes the long-lived decay of ^{147}Sm into ^{143}Nd, the extinction of ^{146}Sm into ^{142}Nd, and the natural abundance of stable ^{144}Nd. Sample ages are determined by taking the ratios of these isotopes [28].

Lack of accuracy for the ^{146}Sm half-life complicates the uses of the ^{146}Sm-^{142}Nd chronometer and the Sm-Nd dating system [23]. Both of these are important tools for establishing a timeline of early solar-system events including the formation of the first solids, lunar formation, and solidification of the Martian surface [23, 25, 26, 27].

1.3.3 Discussion of Past Measurements

The accuracy of the Sm-Nd technique as an independent chronometer depends on accurate half-life measurements of ^{147}Sm and ^{146}Sm. While the half-life of ^{147}Sm has been measured with ~1% uncertainty [29], experimental tension exists between various measurements of the ^{146}Sm half-life. Measured values range from 68 Ma to 103 Ma [20, 24]. Figure 1.4 summarizes the results of past experimental measurements of the ^{146}Sm half-life. The large discrepancy between the past two experiments motivates a new measurement of the ^{146}Sm half-life with novel techniques.

Both the Meissner and Kinoshita experiments utilized surface barrier charged particle de-

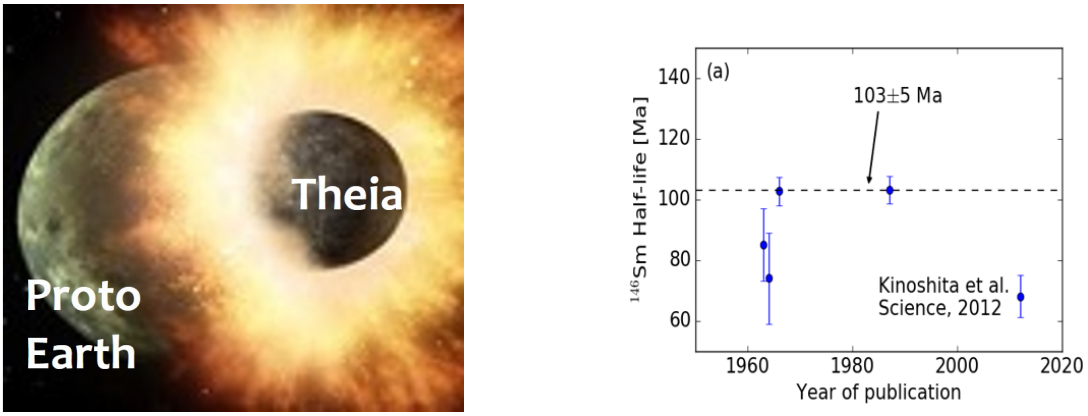

Figure 1.4: *Left*: Artist rendering of proto-planet Theia impacting proto-Earth the ejecta from which formed the moon. Image taken from [30]. *Right*: Various past measurements of the ^{146}Sm half-life with Kinoshita's result labeled and the previously accepted Meissner result with a dotted line.

tectors [20, 24]. These detectors exhibit relatively low efficiencies of $\lesssim$20% as well as large uncertainties of geometric efficiency [20, 18, 19]. Even if deposited on the detector surface, uncertainties due to source self-attenuation are difficult to quantify [18]. Such source self-attenuation can alter counting results by "moving" events out of the full energy deposition peak resulting in an underestimation of the true source activity.

The Meissner *et al.* measurement (1987) was statistically limited with only 833 counts over a 15.4-day period, hindered by 18.7 % geometric efficiency [20]. Notably, the 4.36% relative uncertainty in Meissner's result only includes statistical and geometric uncertainties of 3.46% and 2.67%, respectively. Commonly observed source self-attenuation and alpha-tailing are not discussed and can potentially systematically bias the measurement to lower activities [20, 18].

Kinoshita *et al.* (2012) addressed the aforementioned systematic uncertainties through a relative experiment of both ^{146}Sm and ^{147}Sm [24]. The half-life was calculated via the ratio of activities, the ratio of masses, and the better-known half-life of ^{147}Sm ($10.7 \cdot 10^{11}$ years) [24, 29]. However, Kinoshita *et al.* does not discuss spectral analysis or the calculation of activity. Alpha-tailing causes overlap of the ^{146}Sm and ^{147}Sm peaks along with the orders of magnitude more ^{147}Sm can potentially affect their result. It should be noted this work was retracted in 2023.

1.3.4 MMCs for ^{146}Sm Half-Life Measurement

Resolution of the contentious ^{146}Sm half-life as well as, more broadly, improving the nuclear data of other long-lived isotopes motivates new measurements that employ novel techniques. To address the aforementioned challenges presented by current counting techniques, a ^{146}Sm source was produced and encapsulated within a 4π thermal absorber and then coupled to a cryogenic

microcalorimeter. The heat produced in each decay is measured as a resultant temperature change to the system. The full source encapsulation allows for absolute decay counting, for each decay to be counted with a ~100% efficiency.

Absolute decay counting utilizing microcalorimeters greatly reduces the systematic uncertainties of these measurements. Total source enclosure within the 4π absorber also ensures no loss to self-absorption and the detector dead layer. Alpha escape can be assessed via both absorber preparation as well as through pulse-shape discrimination. Utilization of the trapezoidal filter and extensive study of spectral distortion due to pile-up allow precise quantification of the remaining uncertainties to $\lesssim 1\%$.

The half-life of ^{146}Sm, can be determined via the half-life equation:

$$T_{1/2} = \ln 2 \, \frac{N}{A}, \tag{1.1}$$

where A is the activity assessed via absolute decay counting and N is the number of ^{146}Sm atoms within the counted sample. The number of atoms within the sample is assessed via Thermal Ionization Mass Spectrometry (TIMS) which was performed by radiochemists at Lawrence Livermore National Laboratory.

1.3.5 Nuclear Recoils in Germanium

Measurement of nuclear recoils is an important signature of nuclear reactions. Fast neutrons produced by fission, fusion, spallation, or other sources, interact via elastic scattering off nuclei. Measurement of neutrons via scattering is frequently preferred over capture reactions as spectral information is more accessible.

Similarly, the primary signatures of theorized dark matter and neutrinos interacting via Coherent Elastic Neutrino-Nucleus Scattering (CEνNS) are low-energy nuclear recoils. The recoil energy from dark matter and neutrinos on heavier nuclei is significantly smaller than that from fast neutrons scattering on lighter nuclei; typically, it imparts a few keV$_{\text{nr}}$ or sub-keV$_{\text{nr}}$ to the recoiling nucleus. In this low-energy regime, the detector response of many materials is poorly understood [31].

High Purity Germanium (HPGe) detectors, traditionally utilized for X-ray and gamma-ray spectroscopy, have expanded in popularity for both dark matter searches and neutrino experiments [32, 33, 34, 35, 36, 37, 38, 39]. To better characterize the response of germanium to nuclear recoils, an experiment was performed at the Ohio State University Nuclear Reactor Laboratory to measure the ionization produced by 254 eV$_{\text{nr}}$ recoiling ^{73}Ge nuclei. This measurement utilized the emission of high-energy gamma rays from neutron capture to produce nuclear recoils. The experiment found an enhanced ionization over what is predicted by Lindhard theory, which can dramatically affect the prospects of current and upcoming dark matter and CEνNS experiments.

CHAPTER 2

MMC Working Principles

2.1 Cryogenic Detectors

2.1.1 Cryogenic Calorimeters

Calorimeters measure the energy released by an interaction via the change in temperature of a well-characterized system. The change in temperature is equal to the energy deposited divided by the heat capacity of the system:

$$\triangle T = E/C. \tag{2.1}$$

Calorimeters have previously been employed in non-radiation detection contexts to measure the heat produced by exothermic chemical reactions; in 1935 F. Simon proposed the use of calorimeters for radiation and nuclear physics measurements [40]. By minimizing the heat capacity, the sensitivity of a microcalorimeter is increased. The heat capacity of many materials can be significantly reduced at millikelvin temperatures allowing detectors to be sensitive to the micro-heat produced by radiation interactions. Calorimeters for radiation detection application would not emerge until the 1980's due to the difficulty in achieving the required low temperatures and sensitivities [41, 42, 43].

A calorimeter detector in a simplified model is comprised of three thermal bodies: the radiation absorber, temperature sensor, and heat bath. A simplified detector heat schematic is shown in Figure 2.1. Each body is characterized by a heat capacity and temperature, the heat capacity of the thermal bath is taken to be infinite. Figure 2.1 depicts a purely metallic detector on the left and a crystal detector on the right. For the sake of a simple model, the conversion of acoustic phonons within the crystal to heat can be taken as some efficiency factor ϵ.

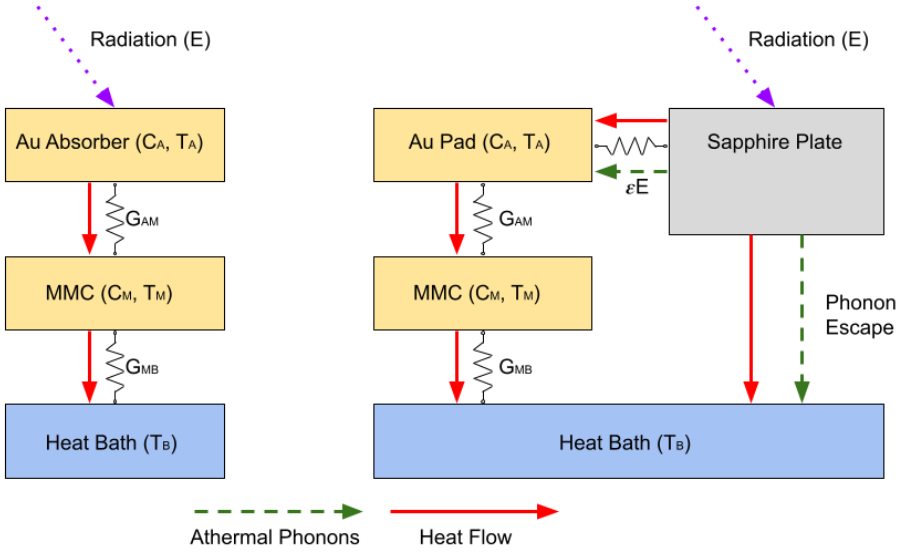

Figure 2.1: Thermal heat capacity ("C") and conductivity ("G") of detector components for metallic (left) and crystal (right) detectors. Labeling is consistent with that used in Equation (2.2). This figure is analogous to Figure 16 of Ref. [1].

2.1.2 Thermal Model

The thermal bodies described in Figure 2.1 can be transcribed into a system of differential equations:

$$\begin{aligned} C_A \frac{dT_A}{dt} &= P_A(t)\delta_{(t-t_0)} - G_{AM}(T_A - T_M) - G_{AB}(T_A - T_B) \\ C_M \frac{dT_M}{dt} &= G_{AM}(T_A - T_M) - G_{MB}(T_M - T_B). \\ T_B &= const.(< 0.05\ K). \end{aligned} \tag{2.2}$$

The system of equations describes some power, P_A deposited within the thermal absorber at time t_0. The temperature of the absorber, denoted with subscript A, and the sensor, denoted with subscript m, vary with time. The terms C_A and C_M are the heat capacities of the absorber and sensor respectively while the G terms are the thermal conductivity between absorber, sensor, and base as denoted. The base temperature is taken to be constant given its massive heat capacity in comparison to the sensor or absorber. The general solution to Equation (2.2) is:

$$T_M = \frac{E}{C_{tot.}} \cdot \left(e^{-t/\tau_1} - e^{-t/\tau_2}\right) \cdot \Theta_{(t-t_0)}, \tag{2.3}$$

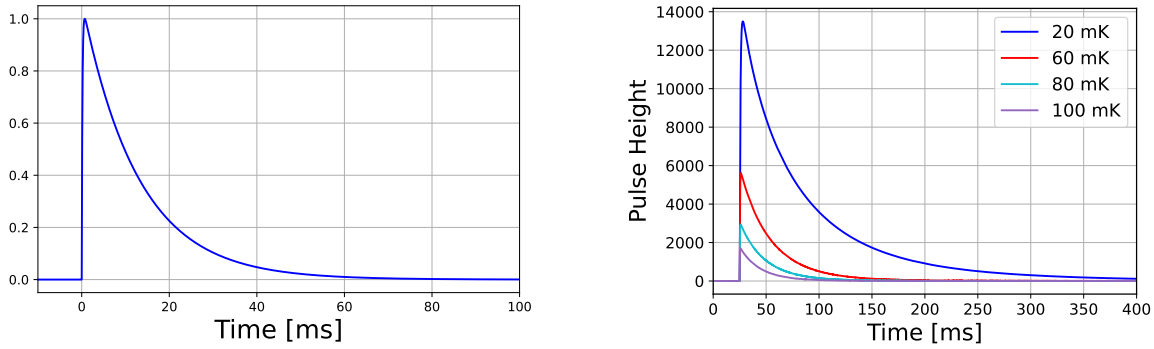

Figure 2.2: *Left*: Drawn solution to thermal model equation with values described in text. *Right*: Pulse shape and amplitude of averaged ^{241}Am waveforms at various temperatures.

with the time constants given by:

$$\begin{aligned} \tau_{1,2} &= \frac{1}{2Z}\big(-X \pm \sqrt{X^2 - 4Y}\big) \\ X &= C_a G_{am} + C_m G_{am} + C_a G_{mb} \\ Y &= C_a C_m G_{am} G_{ab} \\ Z &= C_a C_m. \end{aligned} \tag{2.4}$$

The solution, Equations (2.3) and (2.4) describes a "pulse" shape with an exponential rise and decay. The primary measurements conducted in this thesis are of alpha decay species with decay energies of order ~2–6 MeV. Therefore relatively large MMC sensors and absorbers are utilized compared to other experiments. From references [44, 45, 46, 47], a sensor heat capacity of 1 nJ/K is adopted as a reasonable assumption. A ten times larger value of 10 nJ/K is used for the absorber. The thermal conductivity is set by the number of wire bonds between various components. We estimate about 1 nW/K for thermal conductivity per wire bond and make a reasonable guess of 10 bonds between the absorber and temperature sensor and 2 bonds between the sensor and the heat bath. The heat bath is taken to be 50 mK. With these values the pulse shown on the left of Figure 2.2 which describes a pulse with a rise time of 0.5 ms and decay time of 15 ms, very close to the shape of the 60 mK pulse (red) on the right of Figure 2.2.

The resolution of cryogenic detectors is fundamentally limited by thermodynamic fluctuation noise. The thermal energy within a system can be described as $E = C_{tot}T$ while the thermal phonon energy is given by $\epsilon = k_B T$. The number of thermal phonons is then $N = E/\epsilon$ and the variation is then $\triangle N = \sqrt{N} = \sqrt{E/\epsilon}$. The variation in energy is then $\triangle E = \triangle N\epsilon = \sqrt{E/\epsilon}\epsilon$. Therefore, the statistical thermal fluctuation in noise is given by:

$$\triangle E = \sqrt{E\epsilon} = \sqrt{C_{tot.} k_B T^2}. \tag{2.5}$$

In the ideal case, this noise limit will be that of the detector but this can be difficult to achieve in practice.

2.1.3 Temperature Sensors

The microcalorimeter detection scheme relies on the ability to precisely measure the system temperature or changes in temperature with sufficient resolving power. The three most commonly utilized technologies are semiconductor thermistors (Si and neutron transmission doped Ge), Transition Edge Sensors (TESs), and metallic magnetic calorimeters (MMCs). The latter is commonly also referred to as a magnetic microcalorimeter.

Semiconductor thermistors are the most simple of the three temperature sensors. Ion-implanted silicon and neutron-transmuted doped germanium are widely used in a variety of experiments [47] and are exponentially sensitive to changes in temperature [48]. The second advantage is their compatibility with non-cryogenic amplifiers and electronics and therefore do not require superconducting electronics which are discussed below. Their primary disadvantage is their poorer resolution in comparison to TESs and MMCs and their slower response times [49, 48]. The latter in particular makes them unsuitable for high-count rate experiments like those discussed in this thesis.

Transition edge sensors function by measuring the change in resistance of a superconducting material as it transitions from superconducting to normal. Their sensitivity comes from the dependence of resistance on this phase and the steepness of the dR/dT slope [50]. Challenges arise when working with the TES as the working point is typically greater than the cryostat temperature. The cryostat temperature is minimized to reduce heat capacity; however, keeping the TES at this lower temperature would reduce its sensitivity. The TES is warmed above this temperature and kept near its transition temperature by an electro-thermal feedback scheme [50]. The second challenge with the TES is the non-linearity of the resistance-temperature curve. This makes TES detectors less advantageous for certain applications that require high dynamic ranges such as neutrino-less double-beta decay experiments but do not pose challenges for other experiments such as direct dark matter searches [47, 50, 1].

Magnetic microcalorimeters are the third temperature sensor and will be discussed in greater detail in the following section. The detector-sensing element is a paramagnetic material within a magnetic field. The average spin state within the paramagnet depends on the field and the temperature. While the technology is less mature than TES sensors, a major advantage is the well-characterized linearity of MMCs which allows them to be employed for experiments that require large dynamic ranges [1, 47, 49].

Both MMCs and TESs offer superior energy resolution and response times compared to semi-

conductor thermistor detectors but require complex superconducting quantum amplifiers to produce measurable signals as discussed in the following section. Both Los Alamos National Laboratory (LANL) and Lawrence Livermore National Laboratory (LLNL) have groups that utilize cryogenic sensors to perform decay energy spectroscopy measurements. The group at LANL utilizes TES detectors while the LLNL group utilizes MMCs. MMCs are discussed in further detail and are the sensor utilized for the ^{146}Sm half-life experiment and other experiments at LLNL.

2.2 Magnetic Microcalorimeters

2.2.1 Detection Principle

Thermal energy and temperature changes cannot be quantitatively measured. The only quantitatively measurable quantity is voltage; current can be measured as voltage through the use of a standardized resistor. The MMC device must therefore convert thermal energy into an electrical current signal which can then be measured. This transformation of signals is described by:

$$\delta E \rightarrow \delta T \rightarrow \delta M \rightarrow \delta \Phi \rightarrow \delta I. \tag{2.6}$$

Equation (2.6) can be written in text as:

$$\delta \text{ Energy} \rightarrow \delta \text{ Temperature} \rightarrow \delta \text{ Magnetization} \rightarrow \delta \text{ Flux} \rightarrow \delta \text{ Current}. \tag{2.7}$$

The MMC sensing element is a paramagnet that allows it to convert a change in temperature into a change in current. If we model the MMC as an ideal and dilute spin system placed in a magnetic field of strength B, the magnetization is described by:

$$M = M_0 \tanh\left(\alpha B/T\right), \tag{2.8}$$

where M_0 is the total magnetization, T is the temperature, and α is a spin coupling factor described in Refs. [1, 47]. The change in magnetization is then described by:

$$\delta M = \frac{\partial M}{\partial T}\delta T = \frac{\partial M}{\partial T}\frac{\delta E}{C_{tot.}} \tag{2.9}$$

The total system heat capacity, $C_{tot.}$ is the sum of the absorber heat capacity, the electronic heat capacity of the sensor, and the spin heat capacity of the sensor: $C_{tot.} = C_a + C_e + C_s$. Only the energy (heat) that couples to the spin system is detected. Therefore, the fraction of energy measured is $C_s/C_{tot.}$. The heat capacity of a non-interacting spin system is described by the

Schottky equation [1]:

$$C_s = Nk_B\left(\frac{\tilde{g}\mu_B B}{k_B T}\right)^2 \frac{e^{\tilde{g}\mu_B B/k_B T}}{\left(1+e^{\tilde{g}\mu_B B/k_B T}\right)^2}, \tag{2.10}$$

where N is the multiplicity of the spin system, k_B is the Boltzmann constant, μ_B is the Bohr magneton, and $\tilde{g}$ is the magnetic g-factor. The quantity $\triangle\epsilon = \tilde{g}\mu_B B$ is the Zeeman splitting energy. Equation (2.10) can then be rewritten as:

$$C_s = Nk_B\left(\frac{\triangle\epsilon}{k_B T}\right)^2 \frac{e^{\triangle\epsilon/k_B T}}{\left(1+e^{\triangle\epsilon/k_B T}\right)^2}. \tag{2.11}$$

Detector sensitivity is maximized in the small field limit where $\triangle\epsilon \ll k_B T$ and the spin heat capacity equals the absorber and electronic heat capacities [1, 47]. The constraint to minimize total heat capacity but maximize the relative contribution of the spin system to the heat capacity can complicate sensor design and development.

2.2.2 Paramagnetic Material

Gold doped with erbium is most commonly chosen as the paramagnetic material [1, 47]. The Er^{3+} ion substitutes for gold at regular FCC-lattice sites giving three of its electrons to the conduction band [1]. The ion has the atomic electron configuration:

$$[\mathbf{Kr}]4d^{10}4f^{11}5s^2 5p^6. \tag{2.12}$$

Natural erbium comprises 6 isotopes, 162, 164, 166, 167, 168, 170. The 162 and 164 isotopes only comprise 0.14% and 1.60% respectively. ^{166}Er is the dominant isotope with 33.5% of natural abundance. The ^{167}Er isotope exhibits a strong nuclear spin which diminishes sensor sensitivities at temperatures below ~20 mK [1]. For this reason, erbium depleted of the ^{167}Er isotope is necessary, and in common practice enriched ($\gtrsim$98%) ^{166}Er is used for sensor material. MMC devices typically contain a few hundred ppm of ^{166}Er doped within the gold material depending on the application [1, 47]. For typical devices, at millikelvin temperatures, the Zeeman splitting energy is 1.5 µeV within a 1.5 mT magnetic field [47].

2.2.3 Meander Type Device

The magnetic field is provided by a meander-shaped coil through which the current is running. The Au:Er paramagnetic material is sputtered on top of this pickup coil. A diagram of a two-pixel device is shown in Figure 2.3. The two meander loops are labeled as inductor L. One of the loops is highlighted in orange indicating the paramagnetic Au:Er material. In this diagram, the other

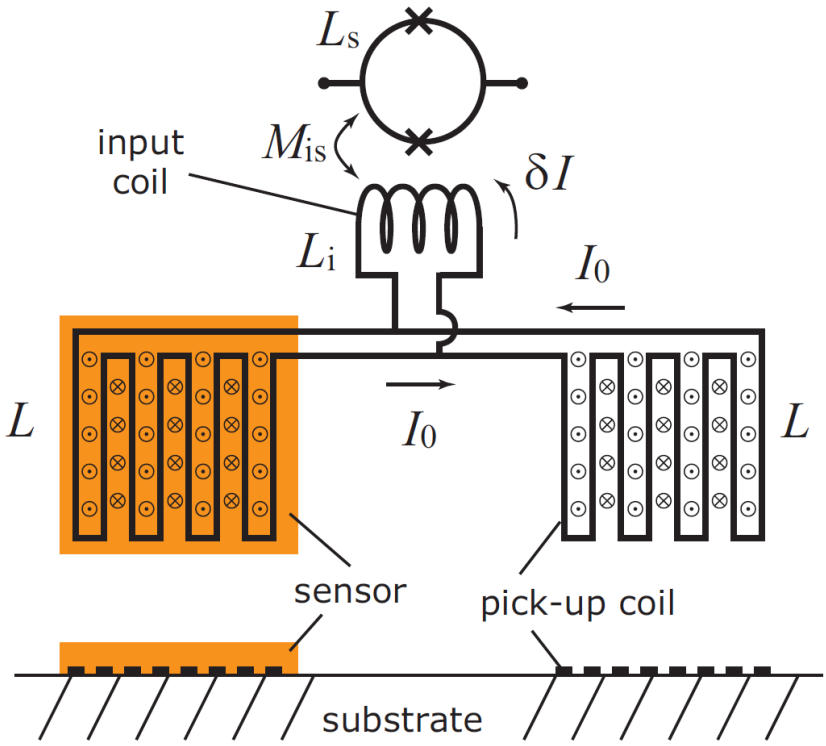

Figure 2.3: Diagram of typical MMC detector with two meander-shaped wire loops. The highlighted one represents the pixel embedded within the Au:Er paramagnet. The loop labeled *input coil* towards the top is the input coil of the DC SQUID. This diagram is representative of the detector shown in Figure 2.8. The diagram is taken from Figure 9 of [1].

coil is left blank. In common practice, both pixels are covered with paramagnetic material; one of which is connected to the absorber while the other is left unattached. This configuration allows the subtraction of global temperature fluxes. The coil is wired to the input coil of a DC superconducting quantum interference device (SQUID) which is used to amplify current signals.

A persistent current is trapped within the coil through the use of a heat switch. A short superconducting wire loop connected to a current supply is placed in parallel with the bias circuit. As both loops are superconducting the current will take the shortest path bypassing the meander loop. A small heater is used to break the superconductivity loop carrying the current allowing the current to flow into the meander loop which is now the only superconducting loop. Once the chip cools, the current is trapped within the coil.

When the system temperature changes, due to radiation depositing heat within the sensor, or otherwise, the magnetization of the Au:Er paramagnet changes as discussed in the preceding section. This change in magnetization produces a change in magnetic field which forces an opposing change

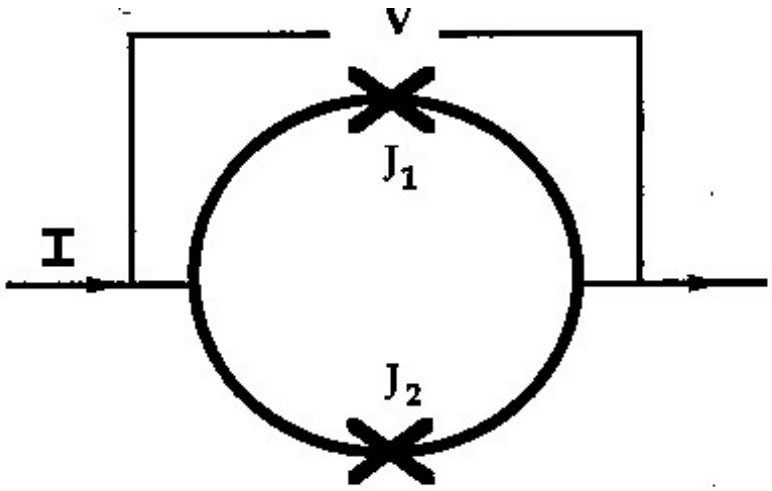

Figure 2.4: Simple diagram of a DC SQUID loop with two Josephson Junctions labeled *J1* and *J2*. The current and voltage across the loop, labeled I and V vary as a function of the magnetic flux through the loop.

in current to preserve constant magnetic flux through the coil loop. If we label the current going through each of the meander coils $I_{1,2}$ (coil 1 will refer to the coil embedded within the paramagnet and coil 2 the blank) and the current going to the input coil of the DC-SQUID as I_i. then by Kirchhoff's circuit law, we have:

$$\delta I_1 + \delta I_2 + \delta I_i = 0. \tag{2.13}$$

Magnetic flux is related to current by inductance:

$$\begin{aligned} \delta\Phi + L_m\delta I_1 - L_m\delta I_2 = 0 \\ L_m\delta I_2 - L_i\delta I_i = 0. \end{aligned} \tag{2.14}$$

The relationship between induced current in the input coil to the SQUID and change in magnetization is given by:

$$\delta I_i = \frac{C_{ms}\ \delta\Phi}{L_m + 2L_i}, \tag{2.15}$$

where C_{ms} is the input coupling between the MMC and the SQUID. Devices can be selected for optimal coupling based on the coupling constant and matching inductance.

2.2.4 DC SQUIDs

The current output of the MMC is amplified via two stages of DC SQUID. The basic SQUID is comprised of a superconducting wire loop broken at two points by a thin insulating barrier called

a Josephson Junction. The insulating barrier is thin enough such that Cooper pairs can tunnel through the junction meaning that for a small current below some critical value, there is no voltage drop across the barrier. The critical current is given by:

$$I_{crit.} = \frac{\pi}{2e}\frac{G_n \triangle T}{A}\tanh\left(\frac{\triangle T}{2k_B T}\right), \tag{2.16}$$

where A is the junction area, G_n is the tunneling conductance, and $\triangle T$ is the superconducting energy gap [51]. The voltage drop across the loop as a function of bias current through the circuit is shown in Figure 2.5. As current is increased, minimal voltage drop across the junctions occurs. However, once the critical current is reached, the Cooper pairs which can tunnel through the barrier are saturated and the gap behaves as a typical resistor. The critical current is labeled "Working Point" in Figure 2.5.

In the absence of any external conditions, the same current flows along each path through the Josephson Junctions. In the presence of an external magnetic field, the phase of the wave function through one path is altered compared to the other. For a phase ϕ, the current and voltage across the junctions are:

$$\begin{aligned} I &= I_{crit}\sin(\phi) \\ V &= \frac{h}{4\pi\, e}\frac{d\phi}{dt}. \end{aligned} \tag{2.17}$$

This is sometimes written in terms of, Φ_0, the magnetic flux quantum equal to $h/2e$, equal to $2.0678 \cdot 10^{-15}$ Wb.

The phase shift between the two paths is maximized when the magnetic flux equals $\Phi_0/2$ and is minimized for integer multiples of Φ_0. To measure the change in current from the MMC device, the MMC meander loop is connected to an inductance loop, the input coil, of the SQUID. Change in current into this coil produces a change in magnetic flux across the loop which alters the voltage drop across the Josephson junctions and a corresponding change in the current through the device.

2.2.5 SQUID Tuning and Locking

The SQUID device is tuned in a 3-dimensional phase space comprising: the bias current through the device, the bias voltage, and "test" magnetic flux. The voltage response across the device is measured as these parameters are tuned.

The test magnetic flux simulates signal input into the SQUID and is controlled by ramping current through an inductor. Using the Magnicon [52] electronics at LLNL, the current is modulated by a triangular waveform pattern. Bias current is then applied through the SQUID to maximize the

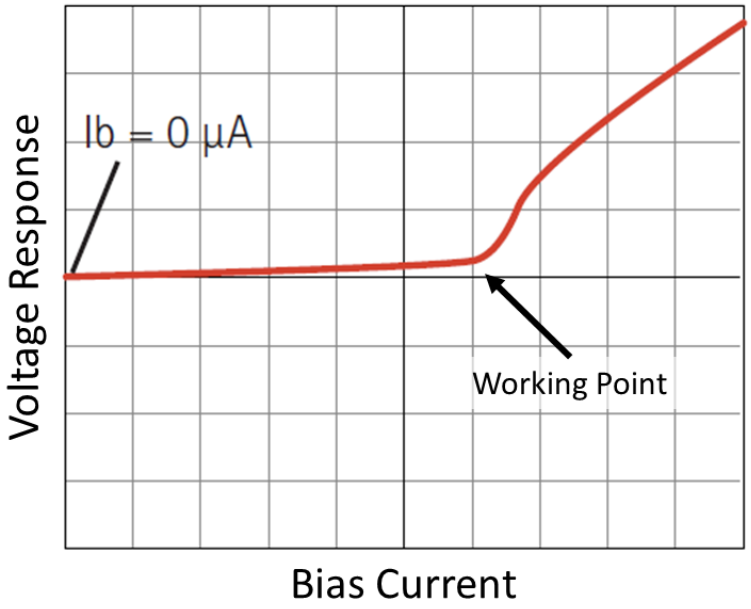

Figure 2.5: Voltage drop across the junctions of a DC SQUID as current through the loop is raised. Minimal drop occurs until the critical current labeled "Working Point" is reached. Figure is taken from the Magnicon reference manual [52].

response. The ideal working point for the bias is labeled in Figure 2.5, just before the critical current. This optimal bias maximizes the amplitude of the sinusoidal response function depicted in Figure 2.6.

Figure 2.6 depicts the sinusoidal response voltage response of Equation (2.17) as the test current is periodically modulated through the inductor. The presence of additional magnetic flux, for example from the MMC device, results in a phase shift depicted in the right panel of Figure 2.6.

Because this phase-shift response to a signal is nonlinear, the SQUID(s) are operated with a flux lock loop (FLL) whereby a feedback circuit is utilized to maintain constant magnetic flux through the SQUID (input SQUID in a multi-stage design). The locking point is determined by finding the point in the response curve where the voltage drop across the SQUID is minimized and is depicted with a black dot in Figure 2.6. Because there can be arbitrary voltage offsets, a canceling voltage is applied, labeled V_b in the left panel of Figure 2.6. When the SQUID is operated in FLL mode, the current is applied to a feedback inductor to maintain this zero voltage response from the SQUID. The required feedback current is what is measured as a linearization of the input signal. However, if a sufficiently large magnetic signal is input to the SQUID, the lock can be lost and the SQUID will re-lock onto the nearest crossing point which can be any integer number of phases away. In practice, when this occurs, it is associated with a change in the SQUID baseline and a re-settling period through the readout electronics.

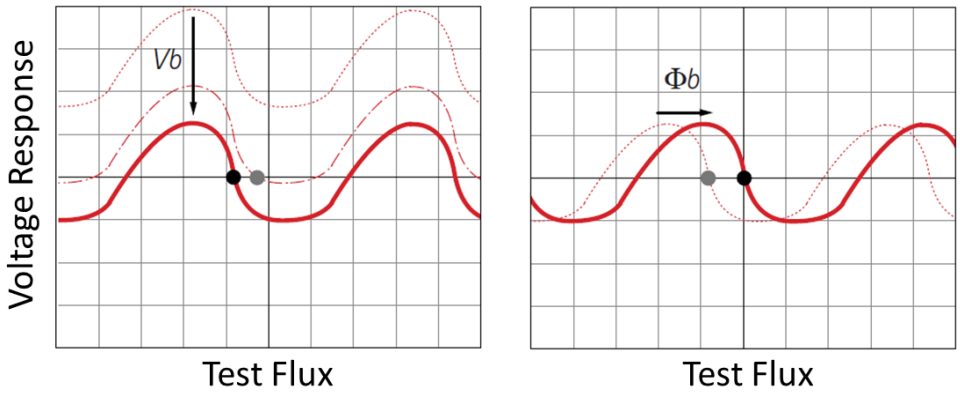

Figure 2.6: Both panels depict the sinusoidal voltage response as magnetic flux through the SQUID loop is modulated. The left panel depicts how the offset can be changed by altering the voltage of the bias circuit. The right panel depicts the effect of additional magnetic flux (signal) which modulates the phase of the response curve. The figure is taken from the Magnicon reference manual [52].

A schematic diagram of the system utilized at LLNL is shown in Figure 2.7. The MMC is wired to the input coil of the first stage SQUID; a change in current produces a change in the current through this SQUID which is wired to the input of a second SQUID, and the output of the second SQUID is integrated through a transimpedance amplifier at room temperature. The output signal is then passed through a feedback resistor to produce a current signal to feed through the feedback resistor canceling the original signal. The voltage required to cancel the original MMC signal is what is measured.

Wiring of a MMC to single-stage DC SQUID is shown in Figure 2.8. This detector is the one I constructed for various measurements performed at LLNL during my extended residency.

2.2.6 Cryogenic Cooling

Very low temperatures are required for detector operation. As previously discussed, minimization of the system heat capacity, which is reduced at low temperatures, is required for a sufficiently measurable increase in temperature resulting from the energy deposited by an alpha decay. Additionally, superconductivity is required both for the SQUID as well as the bias current within the MMC. Were these circuits non-superconducting, current flowing through a non-zero resistance wire would introduce heat and increase the system temperature. Superconductivity requires temperatures below a few Kelvin while minimization of heat capacity requires temperatures below ~100 mK.

Cooling a system to ~4 K can be achieved through a thermal connection to a liquid helium heat bath or through the use of a helium compressor. Cooling below this is typically achieved

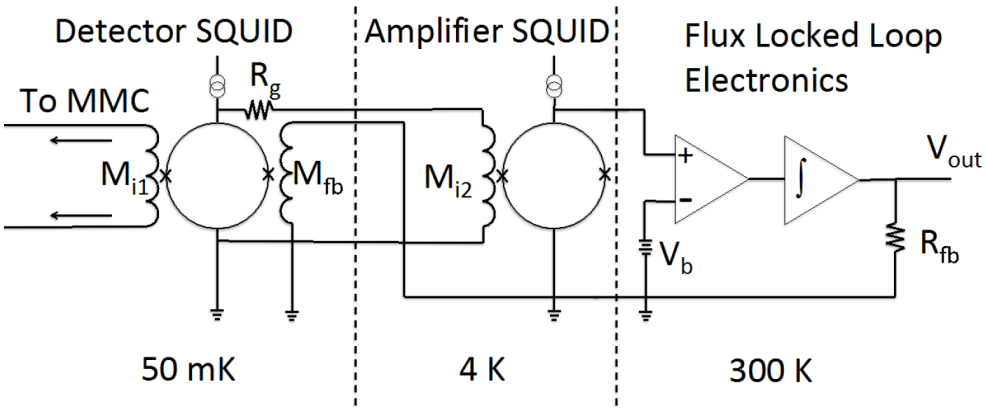

Figure 2.7: Diagram of SQUID amplification system at LLNL. The 4 k and 300 K electronics are fixed Magnicon systems [52] while the input SQUID is wired next to the MMC as shown in Figure 2.8. Diagram is taken from [49].

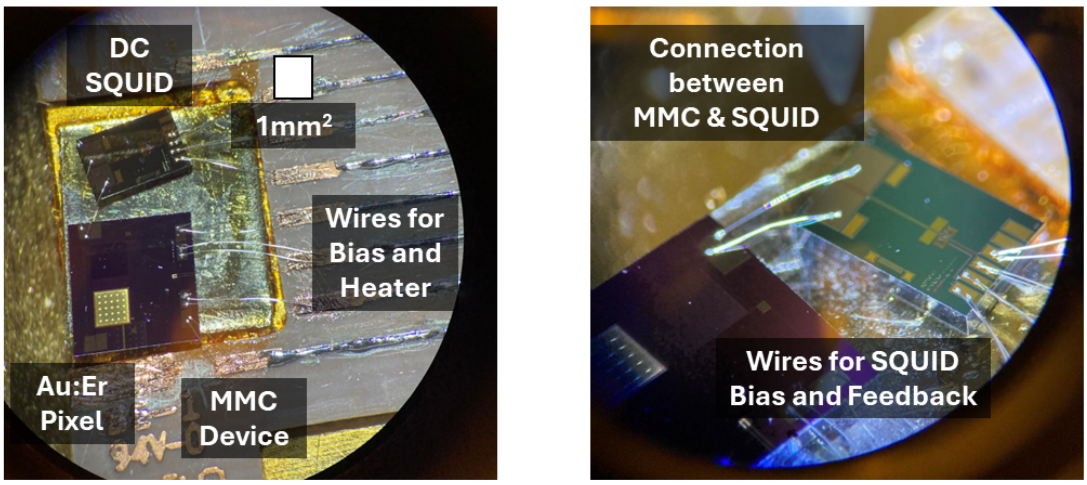

Figure 2.8: *Left*: Microscope image of detector assembled at LLNL. The MMC utilized is a device fabricated by the Korean Institute of Scientific Standards (KRISS) [45, 46] which can be seen with the Au:Er pixel with area 1 mm^2. The SQUID wired to the MMC is a Star Cryoelectronics SQ2250 V1. *Right*: Wire bonded connection between the MMC meander coil and input coil to the SQUID. The two wire bonds connecting the devices are seen in the center of the microscope objective while the four bonds on the right are connections to the SQUID bias and feedback circuits.

Figure 2.9: Megaman dilution refrigerator at LLNL closed (*left*) and open with three detector capsules hanging from the 7 mK stage (*right*).

through the use of a dilution refrigerator or an adiabatic demagnetization refrigerator (ADR). Both technologies are utilized at LLNL though my doctoral work primarily used the group's dilution refrigerator named "Megaman". The Dilution Refrigerator operates by cooling a mixture of ^{3}He and ^{4}He which obey Fermi-Dirac Statistics and Bose-Einstein Statistics respectively. Through the use of a gaseous compressor, the ^{4}He is condensed to form a super-fluid. ^{3}He is then diluted within the super-fluid. Because ^{4}He obeys Bose-Einstein Statistics, these atoms preferentially accumulate in the lowest allowed energy state while the ^{3}He atoms occupy higher energy levels. The system is cooled through evaporative cooling whereby turbo-molecular pumps pull a vacuum on the chamber holding the super-fluid. Because the ^{3}He atoms occupy higher energy levels, they disproportionately evaporate and take a higher fraction of the energy cooling the system. Heat is then exchanged with a thermal bath and the ^{3}He is re-diluted back into the super-fluid. The Bluefors system used at LLNL was able to achieve temperatures below 7 mK using this methodology.

CHAPTER 3

Digital Signal Processing

3.1 Introduction

3.1.1 Preface

This chapter describes various digital signal processing techniques commonly utilized in the area of radiation detection and measurement. It also describes the application of various filters to microcalorimeter signals. The quantification of filter performance has been a large focus of my research given the ^{146}Sm decay counting experiment has required a custom analysis. This work represents my understanding, adaptation, and implementation from the following primary sources: "Digital synthesis of pulse shapes in real time for high resolution radiation spectroscopy" and "Digital techniques for real-time pulse shaping in radiation measurements" by Jordanov and Knoll [53, 54]; "Radiation Detection and Measurement" by Knoll [55]; "The Scientist and Engineer's Guide to Digital Signal Processing" by Steven W. Smith [56]; and "Numerical Recipes in C" by W.H. Press, S.A. Teukolsky, W.T. Vetterling, and B.P. Flannery [57]. Various works by E. Gatti, including Ref. [58], and F.S. Goulding, including Ref. [59], are foundational in detector signal analysis.

3.1.2 Detector Signals

Pulse processing or digital signal processing (DSP) within the context of radiation detection and measurement refers to the broad practice of extracting physically meaningful information from the current or voltage output of a radiation detector. When radiation interacts with a detector, it deposits its energy either in the form of scintillation, ionization, or thermal heat. The detector processes this energy via internal electronics and outputs what is commonly referred to as a voltage "pulse". When viewed in the time domain, pulse shapes vary considerably from detector type to detector type but can broadly be characterized as an exponential rise and fall with either the magnitude of the deviation from the baseline (null-signal) or the integrated deviation of the baseline being proportional to the energy deposited within the detector.

Detector	Organic Scintillator	Inorganic Scintillator	Semiconductor	TES / MMC
Rise-Time	1 ns	10 ns	100 ns	100 µs
Fall-Time	100 ns	1 µs	100 µs	100 ms
Energy	Area	Area	Height	Both
Sampling	1 GHz	100 MHz	10 MHz	100's kHz

Table 3.1: Orders of magnitude of pulse shape characteristics of various commonly used radiation detectors [55]. The table is arranged from left to right in increasing detector response time. The sampling rate is a "ballpark" estimate and is not to be taken as an exact value. Similarly, the metrics proportional to the energy deposited depend on detector coupling, use of a preamplifier, and other factors.

Figure 3.1 depicts typical waveforms from the detector categories of Table 3.1. Note the time scale in each subplot varies many orders of magnitude from a width of 200 ns in the case of EJ-309 to 25 ms in the case of the MMC Microcal pulse. Each detector is representative of its class and is widely used in both nuclear physics and nuclear engineering. The pulses are saved waveforms from various experiments.

Digital signal processing is still relatively new, first emerging in the mid-1990s [55, 53, 54]. In comparison, Wilhelm Röntgen and Henri Becquerel discovered artificial and natural (ionizing) radiation with phosphorescent film in 1895 and 1896 respectively. In the century between the 1890s and 1990s analog electronics were developed and matured as a means of quantifying the signals induced by radiation on the simultaneously developing detector technologies.

The top of Figure 3.2, depicts the fully mature analog signal processing chain. From left to right, a small current pulse is produced by the detector, the charge is integrated, shaped, and amplified. The signal must be split into multiple paths for different analog logic calculations. The output of these calculations is saved by a computer. The bottom plot demonstrates the power of digital electronics. The preamplifier output is directly digitized and all the subsequent calculations are performed digitally. Both diagrams in Figure 3.2 come from the CAEN CoMPASS users' manual for their commercial digital signal processing systems.

3.1.3 Pulse Processing

Digital pulse processing begins with the Analog-to-digital conversion of detector signals. Real detector signals are continuous in time. In practice, pulses are digitized, where the voltage value is measured at some sampling frequency (also commonly referred to as the digitizing frequency or sampling rate). The choice of sampling rate is application-specific and depends on the timescale at which physical information is carried. The approximate orders of magnitude of sampling rates for

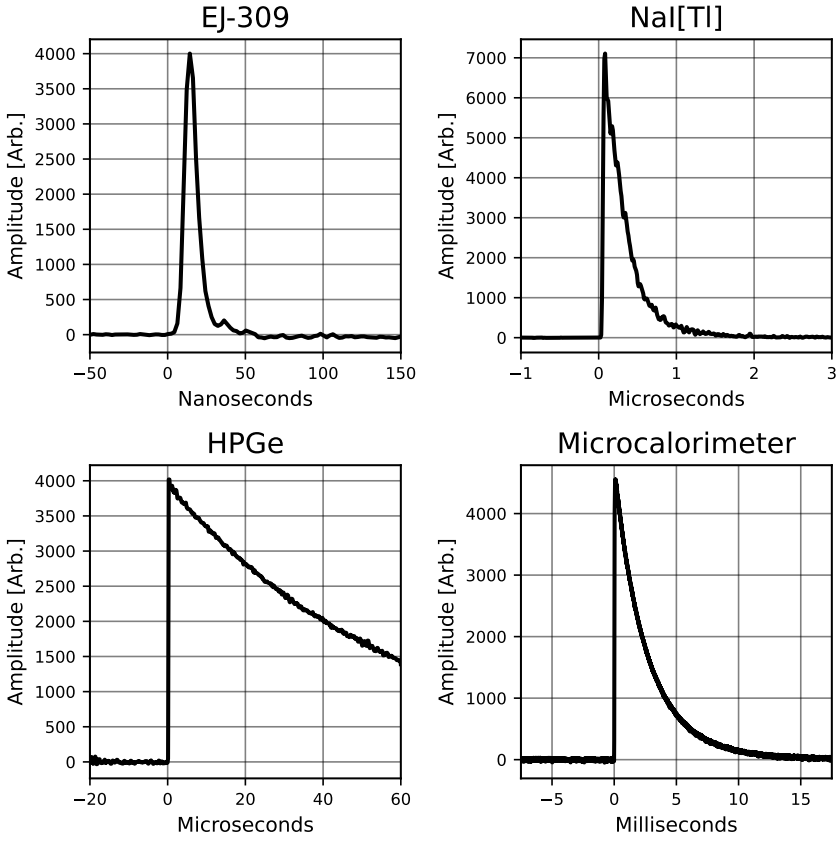

Figure 3.1: Digitized output pulses from commonly utilized radiation detectors as examples. Note the time-scale varies between the panels.

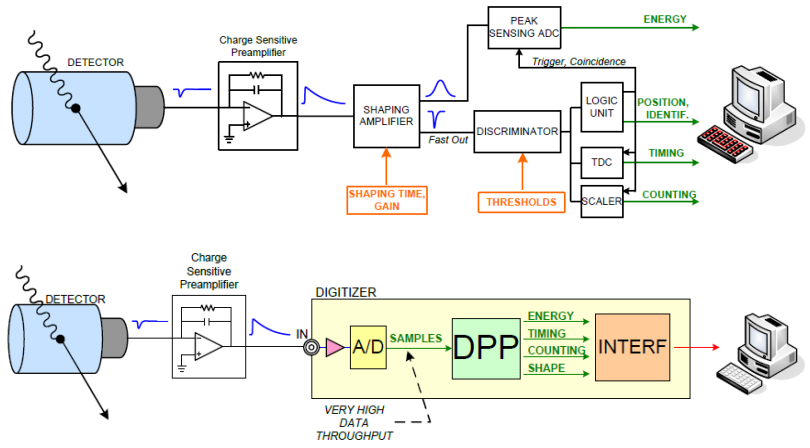

Figure 3.2: Images are taken from the user's manual for CoMPASS a program developed by CAEN for the processing of signals produced by radiation detectors. These can be found in Figure 4.1 and Figure 4.5 in [60].

various detector types are shown in the bottom row of Table 3.1.

The choice of sampling rate for an experiment is important as under-sampling can result in lost physical information while over-sampling can result in the addition of digitizer noise as well as practicality issues of large file sizes. Digitization of signals also affects the mathematics for the calculation of filters and other parameters. Analysis of digitized signals occurs in discrete time units; as a general common practice that will be utilized throughout this thesis, time will be assumed to be discrete for the calculation or derivation of any filter or analysis parameter.

3.1.4 Digital Filtering

Digital filtering is a class of mathematical linear transforms (functions) that maps a raw signal space, in our case the digitized detector output, to a filtered signal space. Typically, signals are transformed to the filtered space as physically relevant parameters can more readily be extracted than from the raw signal [53, 54].

The "raw" pre-filtered signal, mathematically, is the domain while the filtered signal is the range. The digital filter is a linear transform between the domain and the range. These calculations are performed in a discrete time set by the digitizer sampling rate:

$$\mathbf{X} \Rightarrow \mathbf{Y} \tag{3.1}$$

The calculation of a filtered signal, **Y** of Equation (3.1) is a linear sum of values (samples) from the raw signal **X**. There are two broad classes of digital filters, Finite Impulse Response (FIR) and Infinite Impulse Response (IIR). FIR filters are ones where the filtered signal is only calculated with a finite number of samples from the pre-filtered signal. IIR filters, as their name implies, include every preceding value of the pre-filtered signal. For great simplification, practical IIR filters, are ones that can be written as a finite sum of values from the pre-filtered domain and a finite sum of values from the filtered range.

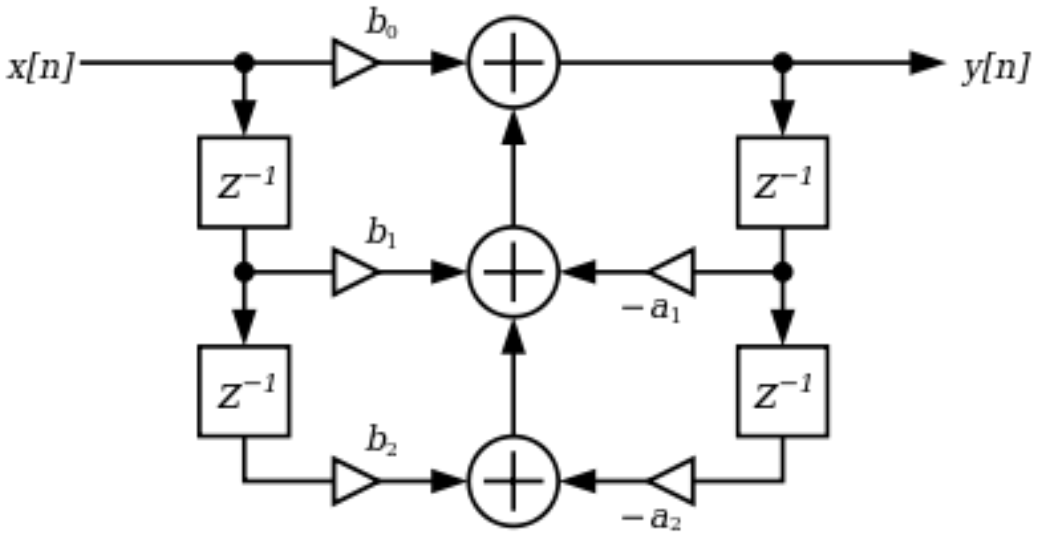

Figure 3.3: Visualization of the implementation of IIR and FIR digital filters using delay filter or Z-transform. The image is taken from Professor J.O. Smith's website on signal processing found at [61].

The architecture of these linear sums can be expressed using the Z-transform diagram depicted in Figure 3.3. The values x_n are the time-ordered elements of the domain (the pre-filtered signal) while the values y_n are the filtered values of the range. The Z^{-1} is a delay operator that acts as:

$$Z^{-1}(x_n) = x_{n-1}. \tag{3.2}$$

The Z-operator, also called the Z-transform or delay-operator, is the discrete-time adaptation of the Laplace-transform [56]. The arrows in Figure 3.3 are multiplication operators, the circles with addition signs are addition operators, and the terms b_n and a_n are the coefficients that define a specific filter. Reading Figure 3.3 as an equation yields:

$$y_n = (b_0 \cdot x_n) + (b_1 \cdot x_{n-1}) + (b_2 \cdot x_{n-2}) - (a_1 \cdot y_{n-1}) - (a_2 \cdot y_{n-2}). \tag{3.3}$$

Equation (3.3) can be expanded and generalized to be written as either Equation (3.4) or Equa-

tion (3.5). The variables i and j are the filters order. Depending on the source a_0 is included in the equation but conventionally is almost always set equal to 1.

$$a_0 \cdot y_n = \left(\sum_{i=0}^{N_b} b_i x_{n-i} \right) - \left(\sum_{j=1}^{N_a} a_j y_{n-j} \right) \tag{3.4}$$

$$\sum_{j=0}^{N_a} a_j y_{n-j} = \sum_{i=0}^{N_b} b_i x_{n-i} \tag{3.5}$$

Equations (3.4) and (3.5) define an arbitrary IIR digital filter. If all the a terms were set to zero with the exception of setting a_0 equal to 1, we simplify to Equation (3.6) which gives the generalized definition of an FIR filter:

$$y_n = \sum_{i=0}^{N} b_i x_{n-i}. \tag{3.6}$$

Though Equation (3.4) allows simple calculation of the n-th filtered point, digital filters are more commonly written in terms of their transfer functions $H_{(z)}$. In this definition, z is again the Z-operator. The transfer function notation of Equation (3.4) is:

$$H_{(z)} = \frac{\sum_{i=0} b_i z^{-i}}{1 + \sum_{j=1} a_j z^{-j}}. \tag{3.7}$$

The transfer equation notation is preferred because the filters between the Dirac delta function and any arbitrary shape can be calculated from the Z-transform. This will be demonstrated in Section 3.1.6.

3.1.5 Convolution

Any FIR filter can also be implemented via convolution:

$$\text{KER} = [b_0, b_1, ..., b_{N-1}, b_N]. \tag{3.8}$$

If we define the "kernel" function above, Equation (3.8), as an array of length N containing each coefficient b_i from Equation (3.6), the filtered signal can be calculated by the operation:

$$Y = \text{KER} * X. \tag{3.9}$$

Equation (3.6) is the evaluation of the convolution operator to calculate filtered signal element y_n. Convolution can be more generally defined by its identity operation:

$$f_{(x)} * \delta_{(x-t)} = f_{(t)}. \tag{3.10}$$

Many common filters can and are implemented as convolution. As shown in Section 3.2, simple mathematical operators including differentiation and integration are FIR filters that can be implemented via convolution. Convolution is more broadly defined as:

$$y_k = \sum_{i=0}^{n} x_{k-i} \cdot \mathbf{Ker}_i. \tag{3.11}$$

Various sources and references use different but equivalent versions of Equation (3.11). For example, the indexing might be changed, or the window could be defined symmetrically where instead of summing from 0 to n, the sum is performed from $-n/2$ to $n/2$. It is also important to note the orientation of the kernel with respect to the summation as this too changes between references.

One of the most common examples of digital filtering used in radiation detection and measurement, "trapezoidal shaping", can be implemented by convolution:

$$H_{(z)} = \frac{\sum_{i=0} b_i z^{-i}}{1 + \sum_{j=1} a_j z^{-j}}. \tag{3.12}$$

It should be noted that notation, exact coefficient definitions, etc. can and do vary across various references and literature. These changes are nearly always trivial, such as swapping a and b with regards to which are the domain and which are the range coefficients. Care should be taken to ensure one does not make errors as a result.

3.1.6 The Z-Transform

The Z-transform is the discrete time domain implementation of the Laplace transform [56]. The transform defines the digital filter, which as mentioned is a linear function, which maps the Dirac delta distribution to a given functional form [56]. More commonly in DSP references, the term "impulse response" is used. From the Z-transform table found in Reference [62] the transfer function for an exponential decay with time constant τ is given by:

$$H_{(z)} = \frac{z}{z - e^{-1/\tau}}. \tag{3.13}$$

Multiplication by z^{-1} yields:

$$H_{(z)} = \frac{1}{1 - e^{-1/\tau} z^{-1}}. \tag{3.14}$$

Reading Equation (3.14), the filter coefficients are: $a_0 = 1$, $a_1 = -e^{-1/\tau}$, and $b_0 = 1$. The iterative implementation of the filter is:

$$y_n = x_n + y_{n-1} \cdot \ e^{-1/\tau}. \tag{3.15}$$

It is evident that if $x_n = \delta_{(x-x_0)}$, the application of this filter will be an exponential decay from an initial value of 1 at x_0. The filter, like all digital filters, can be inverted by swapping the variables which is equivalent to swapping the a and b coefficients.

3.2 Simple Filter Examples

3.2.1 Differentiation & Integration

The first simple example covered is the transform between the Heaviside step function and the Dirac delta distribution (function) denoted as $\Theta_{(t)}$ and $\delta_{(t)}$ respectively. The Heaviside step function serves as a useful approximation to the output of a charge-sensitive preamplifier while the Dirac delta distribution serves as an approximation of the impulse response of an HPGe (or other fast) detector signal before integration by the preamplifier.

The Heaviside step function and the Dirac delta distribution are related by integration and differentiation. Differentiation in discrete time is simply the difference of two samples adjacent in time. The filtered signal is given by:

$$y_n = x_n - x_{n-1}, \tag{3.16}$$

where x is the raw or pre-filtered signal and y is the filtered signal. Within the context of arbitrary digital signal processing and by comparison to the transfer function defined in Equation (3.14), it can simply be seen that $a_0 = 1$, $b_0 = 1$, and $b_1 = -1$, and the transfer function written as:

$$H_{(z)} = \frac{1 - 1 \cdot z^{-1}}{1}. \tag{3.17}$$

Since a_0 is the only non-zero a-coefficient, this is an FIR filter and can be written as convolution with our kernel being:

$$Ker = [1, -1]. \tag{3.18}$$

Application of this filter via the iterative algorithm, the transfer function, or convolution will transform the Heaviside step function to the Dirac delta function (distribution). Integration can be approached similarly either as a finite width integral or a running integral of infinite width. In the

finite case of length l, the filtered output is the summation of the prior l elements, though this can be shifted in time:

$$y_n = \sum_{n-l}^{n} x_n + x_{n-1} + ... + x_{n-l}. \tag{3.19}$$

Similarly to differentiation, finite integration is an FIR filter and can be written either as a transfer function or as convolution. If written as a transfer function, $a_0 = 1$ and b_0, b_1, ... b_l all equal 1. If written as convolution, all elements of the kernel would also equal 1. An infinite running integral filter can be written more simply than an infinite sum using what is described as a summing element by Jordanov and Knoll [53, 54]:

$$y_n = x_n + y_{n-1}. \tag{3.20}$$

Here, the term y_{n-1} holds the summation of all previous values of x_{n-i} for all i's. The filter coefficients for writing the transfer function are $a_0 = 1$, $a_1 = -1$, and $b_0 = 1$.

In common digital signal processing material such as in References [56, 57], filters are applied to the infinite impulse response (Dirac delta distribution) as the underlying test signal, whereas in radiation detection and measurement, the step-function is the underlying distribution to which filters are typically applied. As shown in this section, the two underlying distributions are related by simple transforms, the derivative and running integral filters.

3.2.2 Moving Average

The moving average filter, sometimes referred to as the "boxcar" is a simple integration window of a given width with the output normalized to one divided by the width of said window. A filter averaging the previous n can be written as:

$$y_n = \frac{1}{L} \sum_{i=0}^{L} x_{n-i}. \tag{3.21}$$

The transfer function would be the same as that for a finite integral except with the normalization term. Thus in effect, the moving average and finite integral are the same filter. The moving average can be centered by a one-half phase shift which changes the calculation to:

$$y_n = \frac{1}{L} \sum_{i=-L/2}^{L/2} x_{n-i}. \tag{3.22}$$

Application of the moving average filter in this form is depicted in Figure 3.4 through the panels. The black points represent the underlying data while the green shaded box is the average window of width 200 time-units. The white square in the center of the window is the filter output evaluated

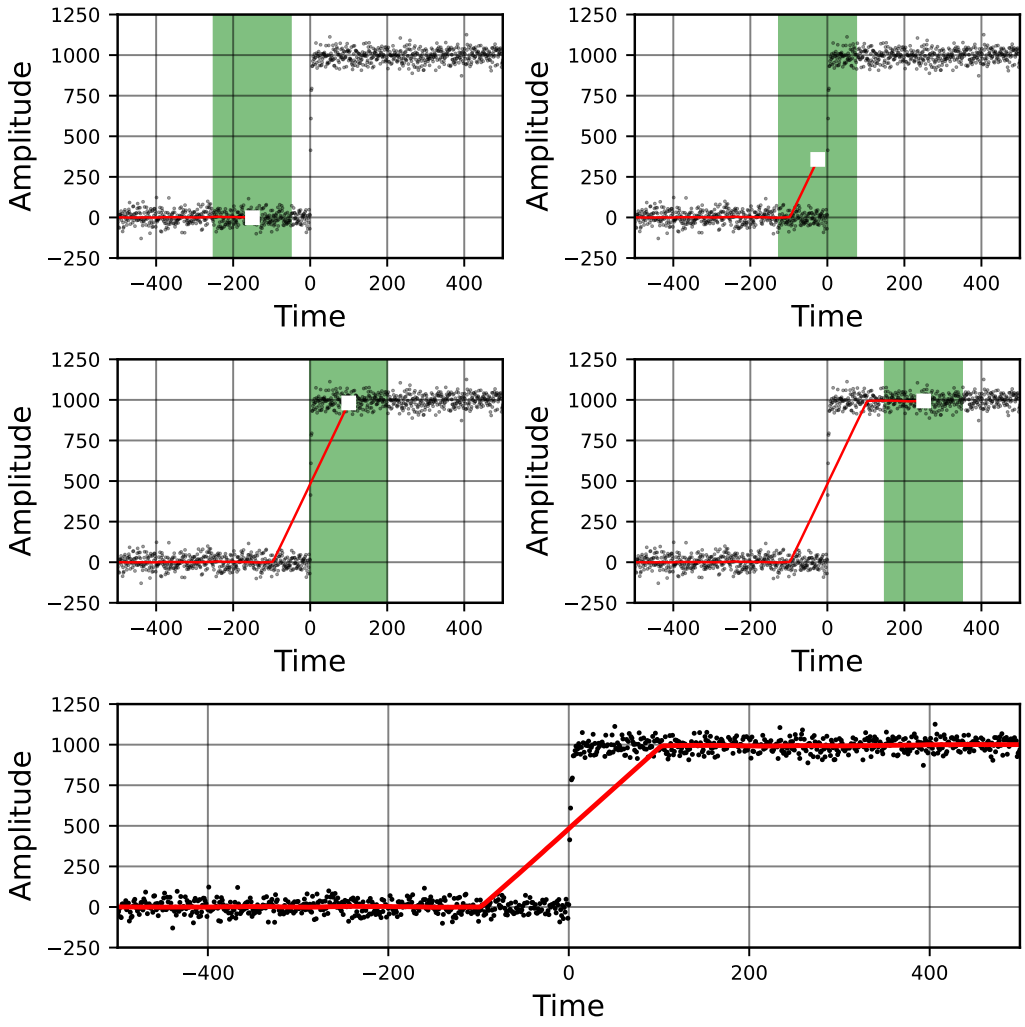

Figure 3.4: Application of a moving average filter over a step-function input with noise. The data points within the green shaded window (width of 200 samples) are averaged. The white square is the computed average value and the red line are previously calculated values. The averaging filter is moved over the entire pulse to produce the filtered signal in red shown in the bottom plot.

at that time while the red line is the previous filter output.

3.2.3 Savitzky-Golay Filter

The Savitzky-Golay Filter is a weighted moving average specifically designed to preserve the underlying polynomial shape of the data. The filter accomplishes this by calculating the best fit polynomial value at a given data point for a pre-selected filter width and polynomial order [63]. The filter is FIR and the coefficients can be readily retrieved from online databases or simple Python codes such as Ref. [64].

3.2.4 High-Pass, Low-Pass, & Band-Pass Filters

Physical high-pass and low-pass filters are constructed from electronic components the response from which can be calculated by using Kirchhoff's Law(s). Simple first-order high-pass and low-pass filters are constructed from resistors and capacitors and are commonly denoted as "RC" filters [65]. As ohms multiplied by farads gives seconds, "RC" numerically is the time constant of the filter [65]. In radiation detection and signal processing, the high-pass filter is referred to as a "CR" filter and the low-pass as a "RC" filter [55].

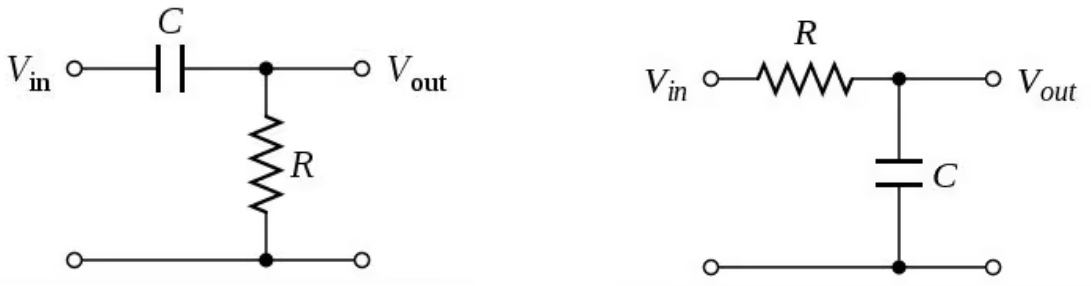

Figure 3.5: *left*: Simple RC high-pass filter *right*: Simple RC low-pass filter. Images are copied from [65].

With τ =RC, we can define parameters α and β as:

$$\alpha = \frac{\tau}{\tau + dt} \quad \beta = \frac{dt}{\tau + dt}, \tag{3.23}$$

where dt is the sampling time period. If RC is set in units of sampling period, $dt = 1$. The high-pass and low-pass filters can be defined by iterative equations:

$$y_n = \alpha \cdot y_{n-1} + \alpha \cdot (x_n - x_{n-1}), \tag{3.24}$$

$$y_n = (1 - \beta) \cdot y_{n-1} + \beta \cdot x_n. \tag{3.25}$$

Both filters are IIR designs, the coefficients for which are the following. High-pass: $a_0 = 1$, $a_1 = -\alpha$, $b_0 = \alpha$, and $b_1 = -\alpha$. Low-pass: $a_0 = 1$, $a_1 = \beta - 1$, and $b_0 = \beta$. A band-pass filter can be constructed from successive high and low-pass filters. These sets of filters are used commonly in analog and digital electronics. For example, the analog shaping amplifier in NIM electronics is a CR-RC^n which is a high-pass filter followed by n low-pass filters. Another example is that the output of a charge-integrating preamplifier is passed through a high-pass filter such that it doesn't sum to infinity.

3.3 The Optimal Filter

The optimal filter is the digital signal processing (DSP) technique of choice implemented by the majority of cryogenic microcalorimetry experiments [66, 67, 68, 69]. The filter is designed to yield the best resolution for any pulse shape and noise profile [56, 57, 69]. The filter is built from a pulse template and a template of the average noise. In effect, the optimal filter is a one-dimensional fitting algorithm that is calculated by convolution and summing, an inner product, in the frequency domain space. The free parameter is the pulse amplitude which minimizes the chi-squared between the pulse data and the template multiplied by said free parameter. I commonly refer to the template multiplied by the filter calculated amplitude as the "fit" and the difference between the data and the fit as the "residual".

To achieve the best resolution, the optimal filter must be applied to the entire pulse shape until it returns to baseline. In cases of pile-up, the filter will return a bad result. This is not a problem as typically, microcalorimeters are applied to purely spectroscopy measurements where the absolute count rate is not measured and pile-up events are cut from the analysis [6]. In moderate high count rate cases, a full pulse template and a shorter template are used, though resolution is sacrificed in the case of the shorter template [69, 66].

3.3.1 Mathematical Derivation

The optimal filter requires an assumption of the true pulse shape as well as the noise [56, 57, 69]. We assume that the waveform in any saved data is the sum of the true pulse shape and noise:

$$\mathrm{D}_{(t)} = \mathrm{A} \times \mathrm{S}_{(t)} + \mathrm{N}_{(t)}, \tag{3.26}$$

where $\mathrm{D}_{(t)}$ is the time-domain digitized data waveform, $\mathrm{N}_{(t)}$ is the noise term, $\mathrm{S}_{(t)}$ is our true pulse shape, and A is a scaling factor which can be interpreted as the amplitude of the pulse within $\mathrm{D}_{(t)}$. Our ultimate goal is to find a pulse amplitude that minimizes the difference between our true pulse shape and our data. The measure of this difference can be expressed by the least squares method difference:

$$\chi^2 = \sum \frac{(\mathrm{D}_{(t)} - \mathrm{A} \times \mathrm{S}_{(t)})^2}{|\mathrm{N}_{(t)}|^2}. \tag{3.27}$$

Since the Fourier transform is a linear transform, Equation (3.27) also holds in the frequency domain:

$$\chi^2 = \sum \frac{(\mathrm{D}_{(f)} - \mathrm{A} \times \mathrm{S}_{(f)})^2}{|\mathrm{N}_{(f)}|^2}. \tag{3.28}$$

By differentiating with respect to A and setting the derivative equal to zero, we get:

$$0 = \frac{d\chi^2}{dA} = \sum \frac{2}{|\mathrm{N}_{(f)}|^2}(\mathrm{D}_{(f)} - \mathrm{A} \times \mathrm{S}_{(f)}) \times S^*_{(f)}, \tag{3.29}$$

which simplifies to:

$$\sum \frac{D_{(f)} S^*_{(f)}}{|\mathrm{N}_{(f)}|^2} = \sum \frac{H \times |\mathrm{S}_{(f)}|^2}{|\mathrm{N}_{(f)}|^2}. \tag{3.30}$$

This gives us the equation for the optimal amplitude from which we can extract our optimal filter Φ that can act on the Fourier transform of our digitized waveform $\mathrm{D}_{(t)}$:

$$\Phi = \frac{\sum \frac{S^*_{(f)}}{|\mathrm{N}_{(f)}|^2}}{\sum \frac{|\mathrm{S}_{(f)}|^2}{|\mathrm{N}_{(f)}|^2}}. \tag{3.31}$$

The denominator of Equation (3.31) can be viewed as a normalization term. To construct the optimal filter in practice, we must know both the true pulse shape as well as our noise. The noise on a per-waveform basis cannot be determined using linear filtering and would require an iterative nonlinear analysis where the template is subtracted from the data and the noise term recalculated. However, since the filter is calculated in the frequency domain, the average noise power spectrum can be used for $|\mathrm{N}_{(f)}|^2$.

The true pulse shape template can be calculated by averaging many pulses from an experiment. Care must be taken to ensure that only true signals are accepted into this average as well as to ensure that no "trigger walk" or jitter has occurred as these phenomena can distort the template shape from the true pulse shape. As a point of personal convention, either the template amplitude or the template area is normalized to 1 (depending on circumstance) though this is not strictly necessary.

When generating the pulse template, it is acceptable to either average pulses and take the Fast Fourier Transform (FFT) of the average or to take the FFT of each waveform and take the average of all of the FFTs. When generating the noise template, the FFT of each noise trace must be taken and all the FFTs averaged. If all the noise traces are averaged, this will eliminate all of the noise.

3.3.2 Example (EVE Run 6)

An example power spectrum and template fit built from saved waveform data taken during EVE Run-6. Data was acquired in this run in trigger mode. The output signal was split with one copy being passed through a band-pass amplifier and the other digitized. The band-pass amplifier has zero baseline as the DC component is filtered out. When this signal crosses a threshold in the positive direction, a trigger signal sets the acquisition of the unfiltered signal.

To generate the filter, pulses were selected that had amplitude in the 5–6 MeV range with no

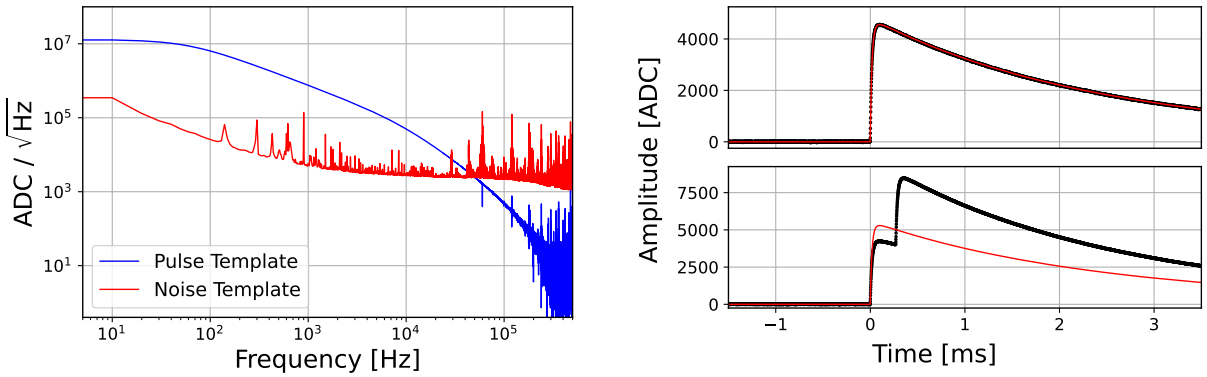

Figure 3.6: *Left*: Power spectrum for the pulse template and noise template used in the analysis of EVE Run-6. *Right*: Template fit to single pulse and pile-up pulse from the EVE Run-6 data set.

pile-up and a flat baseline. These waveforms were averaged together to generate a template. The noise template was generated by saving waveforms with a strobe trigger. Waveforms are selected without any true radiation-induced signal. The power spectrum for the pulse template and the noise template power spectrum used for the optimal filter are depicted in the left plot of Figure 3.6. In effect, the optimal filter for a given scenario is defined by the template and noise power spectra.

One main failure of the optimal filter is dealing with pile-up. Since the filter is applied and calculated in the frequency domain, not the time domain. Another way to think about the optimal filter is that it is a 1-dimensional fit with amplitude being the only free parameter. A third way of thinking about the optimal filter is that it is just a convolution performed in the time domain. Regardless of how one conceptually thinks about the filter, Figure 3.6 depicts the optimal filter output when calculated on a single pulse and when calculated on an instance of pile-up. It should be noted that the optimal filter output is a scalar value, the best-fit amplitude. The *red* fits in Figure 3.6 are this amplitude multiplied by the pulse template. Taking the variance, or some other statistical test of choice, of the fit residual is a good indicator of pile-up or other anomalous artifacts in the data.

3.4 Trapezoidal Shaping

Trapezoidal shaping, or the trapezoidal filter, is commonly implemented for the analysis of signals produced by High Purity Germanium Detectors (HPGe), silicon detectors, and other detection systems with charge-sensitive preamplifiers [55]. Pulse shaping is implemented as it yields considerably better resolution than a simple calculation of the pulse height or area [55]. Trapezoidal shaping has been implemented digitally and on Field Programmable Gate Arrays (FPGAs) since the mid 1990s [53, 54].

The filter transforms an exponential pulse with a fast rise and slow decay into a trapezoidal shape characterized by a "peaking-time" or "shaping-time" and a "flat-top time". The peaking time is typically selected to optimize spectral resolution while the flat-top is set to the order of the pulse rise time to correct for ballistic deficit [55]. Figure 3.8 depicts an example data pulse with Gaussian noise, a short pulse raise-time, and a long decay time (*black*). The trapezoidally shaped signal is shown in *red*. There are two cases, one with correction for the exponential decay (right) and one without (left). This correction for the decay is known as pole-zero correction and is discussed in greater detail below.

Trapezoidal shaping has been implemented on numerous commercial systems such as the Ortec DSPEC and Canberra GENIE systems [70, 71]. Given the filter returns to baseline after a much shorter period than the pulse itself, it is appealing for microcalorimeter applications with high count rates or where accurate measurement of the count rate is required. It should be noted that an exponential cusp-like trapezoidal filter provides better resolution but is more difficult to implement on FPGA hardware [53, 54]).

3.4.1 Iterative Algorithm

The ideal signal output of an HPGe detector is a step function whose raising edge is determined by the charge collection time within the detector crystal [55]. In reality, the signal is passed through a high-pass filter such that the voltage does not exceed the range of the electronics. However, we will first assume a perfect step function.

The trapezoidal shaping algorithm for such a signal is derived by Knoll and Jordanov and is given by [53, 54]:

$$S_{(n)} = S_{(n-1)} + V_{(n)} - 2V_{(n-k)} + V_{(n-2k)} \tag{3.32}$$

Equation (3.32) is implemented via iterative calculation where n is the indexing term and k is an integer value corresponding to the shaping time in sample units. The raw signal input is given by V and the shaped signal by S. Equation (3.32) assumes the step rise-time is short in comparison to the shaping time. If this is not the case, the pulse height will be underestimated by the trapezoidal filter in a phenomenon known as "ballistic deficit" [55]. This deficit is corrected by including a "flat-top" in the trapezoid. The modified algorithm is:

$$S_{(n)} = S_{(n-1)} + V_{(n)} - V_{(n-k)} - V_{(n-k-m)} + V_{(n-2k-m)}, \tag{3.33}$$

where m is the duration of the flat-top in sample units. The output signal from Equations (3.32) and (3.33) will be on a much larger scale than the input signal. To correct this, the output is multiplied by a re-scaling factor of $1/\mathrm{k}$. Application of both filters to a step-function with noise is

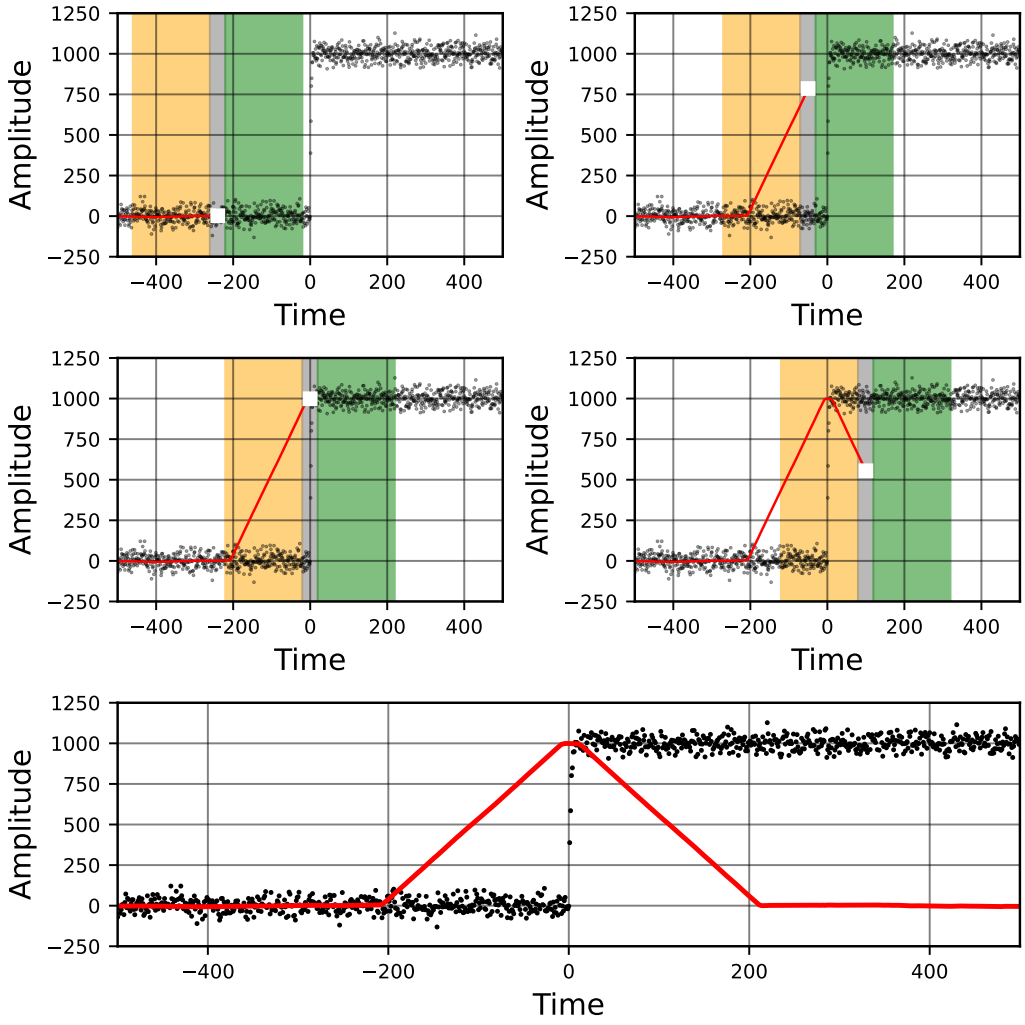

Figure 3.7: The top four panels demonstrate the application of a trapezoidal filter on a step-like pulse input. It is implemented as two offset moving averages similar to that applied in Figure 3.4. In this case, the filtered signal (red line) is computed by taking the difference of the two moving averages (green minus orange). The two averaging windows are offset. This offset creates the flat top seen in the fully filtered signal in the bottom plot.

depicted in Figure 3.7.

3.4.2 Convolution Implementation

Upon closer investigation, Equation (3.32), including the scaling factor of $1/\mathrm{k}$, is simply the difference between two consecutive moving average filters previously described. The two moving average filters can be combined into a single kernel:

$$\mathrm{Ker}_{(i)} = \begin{cases} 1.0/\mathrm{k} & \text{for:} \quad 0 \leq i \leq \mathrm{k}, \\ -1.0/\mathrm{k} & \text{for:} \quad \mathrm{k}+1 \leq i \leq 2\mathrm{k}+1, \end{cases} \tag{3.34}$$

The filtered or "shaped" signal is the convolution of this filter with the raw data. The convolution algorithm was defined previously in Equations (3.10) and (3.11).

The convolution of the kernel defined in Equation (3.34) and a step-function-like signal, in *black*, is depicted in Figure 3.7. The *green* shaded region corresponds to the positive portion of the shaping kernel and the *orange* shaded region corresponds to the negative portion of the shaping kernel. This is mathematically equivalent to taking the difference between the averages within the green and orange regions. Figure 3.7 can just be described as a double version of Figure 3.4. The *red* square corresponds to the filtered output time aligned with the center of the filter. The *blue* trend is the previously calculated filtered values. When the entire kernel is over the baseline, the summed area is equal to zero and hence there is no filtered amplitude. When the *green* integration region overlaps with the signal, the shaped output begins to increase. The maximum amplitude of the trapezoid filter occurs when the positive moving average overlaps completely with the step-up and while the negative moving average overlaps with the baseline just before the step onset.

When a flat-top is needed to be implemented, as in Equation (3.33), this can be achieved with convolution by adding a short "gap" between the two moving average filters. This is now described as:

$$\mathrm{Ker}_{(i)} = \begin{cases} 1.0/\mathrm{k} & \text{for: } 0 \leq i \leq \mathrm{k}, \\ 0.0 & \text{for: } \mathrm{k}+1 \leq i \leq \mathrm{k}+\mathrm{m}, \\ -1.0/\mathrm{k} & \text{for: } \mathrm{k}+\mathrm{m}+1 \leq i \leq 2\mathrm{k}+\mathrm{m}+1, \end{cases} \tag{3.35}$$

The flat-top width is the new parameter m, which is also in sample units. If convolution is performed between the shaping kernel and the step-function pulse, the calculation results in the same shaped trapezoid as calculated by the iterative method defined in Equation (3.32) or (3.33). Convolution will always be implemented in Python via the Numpy function "numpy.convolve(X, Ker, 'same')" where X is the data, "Ker" is the shaping kernel, and 'same' is a programmatic option.

Upon further investigation, it can be noted that Equation (3.37) is simply the derivative operator acting upon a trapezoid function with amplitude and slope k and flat-top m. 1/k is the slope of the rising side, 0 is the slope of the flat-top, and -1/k is the slope of the falling edge. Both convolution and derivative(s) are linear operators and as such obey the Commutative Property. Instead of acting the derivative on the trapezoid, it can be acted on the step function. If the step function had an instantaneous raising edge and no noise, its derivative would be the Dirac delta distribution. Convolution with the Dirac delta distribution is the identity operation within convolution as denoted by Equation (3.8), where "$*$" is the convolution operator. The shaping kernel could therefore be written as a trapezoid:

$$\mathrm{Ker}_{(i)} = \begin{cases} i/\mathrm{k} & \text{for: } 0 \leq i \leq \mathrm{k}, \\ 1 & \text{for: } \mathrm{k}+1 \leq i \leq \mathrm{k}+\mathrm{m}, \\ 1-(i/\mathrm{k}) & \text{for: } \mathrm{k}+\mathrm{m}+1 \leq i \leq 2\mathrm{k}+\mathrm{m}+1, \end{cases} \tag{3.36}$$

Shaping is performed by the convolution operators:

$$F_n = [1.0, -1.0] * \mathrm{Ker} * f_n. \tag{3.37}$$

Here, f_n is our step function input, F_n is the output shaped signal.

3.4.3 Single-Component Pole-Zero

As previously mentioned, the output of a charge-sensitive (integrating) preamplifier is typically passed through a high-pass filter such that it does not step to infinity. This causes our step-function response to become an exponential decay. For microcalorimeters, the decay can be thought of as a temperature high-pass filter as heat flows from the warmed detector into the heat sink.

The application of the trapezoidal filter as previously described will result in an undershoot due to this exponential decay. Such undershoot can be seen in the trapezoidal filtered signal on the left of Figure 3.8. The shaped signal undershoot can be corrected through what is referred to as pole-zero correction [55]. The trapezoid with the application of the pole-zero correction is shown on the right of Figure 3.8.

In effect, pole-zero correction is the application of an inverse high-pass filter in addition to the trapezoidal shaping filter. In practice, the order of operations does not matter as digital filters are linear operators. One point of caution is that as the name implies, an inverse high-pass filter re-introduces DC and low-frequency noise. In a cryogenic detector, the DC component and low-frequency noise are caused by drift in the base temperature of the detector itself. Therefore, for some applications, such as the use of a triggering signal, where baseline shift is not desired and

thus the uncorrected trapezoid is utilized. The inverse high-pass filter can simply be derived from

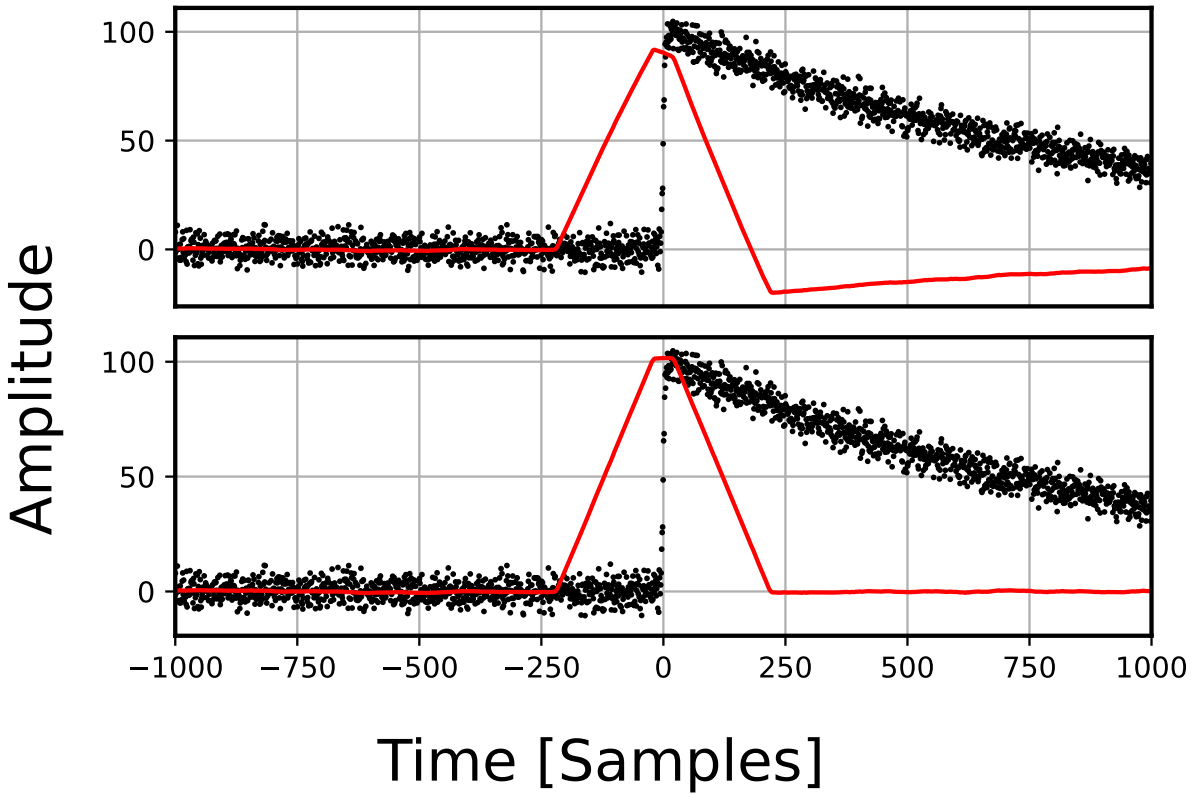

Figure 3.8: Signal with fast rise and exponential decay (*black*) and trapezoidally filtered signal (*red*) without (*top*) and with (*bottom*) pole-zero correction applied. Trapezoid peaking time is 200 samples and flat-top time is 40 samples.

reorienting the high-pass filter equation with the assumption now that y is the input signal and x is the desired output signal. This gives

$$X_{(n)} = X_{(n-1)} + \alpha^{-1} \cdot Y_{(n)} - Y_{(n-1)}. \tag{3.38}$$

Like with the trapezoidal filter itself, the pole-zero correction can be implemented via convolution. The same kernel (3.36) is used but the convolution Equation (3.8) is modified to

$$F_n = [1.0, -1.0 \cdot e^{-1/\tau}] * \mathrm{Ker} * f_n, \tag{3.39}$$

where τ is the time constant of the exponential decay.

3.4.4 Multi-Component Pole-Zero

The thermal model derived in Chapter 2 predicts the system temperature to exponentially decay back down to the base temperature. However, this model assumes the detector system is perfectly thermally isolated from the system except via the gold wire bonds connecting the MMC to the base plate. Realistically, there are multiple paths, with different thermal conductance(s), for heat to flow out of the system.

Examples of other paths for heat to leave the detector system include through the glue connecting the absorber to the sample holder and from the gold of the MMC pixel through the rest of the PCB. If we assume these two paths, in addition to the gold wire bonds between the MMC and the base plate are the three dominant paths for heat to leave the detector, the pulses in practice have a three-component decay:

$$f_{(t)} = A \cdot e^{(-t/\tau_a)} + B \cdot e^{(-t/\tau_b)} + C \cdot e^{(-t/\tau_c)}. \tag{3.40}$$

The decay constants τ_a, τ_b, and τ_c are time constants determined by the conductivity of each path. The amplitudes A, B, and C are the normalization terms for the quantity of heat that flows through each path. Though theoretically all these terms can be calculated from the physical properties of the various materials that comprise the detector mounting, in practice determining them, or if there are additional terms, can only be empirically calculated. From this assumption about pulse shape, we can use the Z-transform (Laplace transform) to define the transfer function that maps a delta function to our pulse shape. We can calculate the inverse transform which takes our pulse shape to a Dirac delta function, which can be mapped to a step function via a running integral filter. The transfer function for an exponentially decaying function with time constant τ is given by:

$$e^{(-t/\tau)} \quad \Rightarrow \quad H_{(z)} = \frac{1}{1 - e^{-1/\tau} \cdot z^{-1}}. \tag{3.41}$$

Because digital filters are linear and the Laplace and Z-transforms are linear, the transfer function that maps Equation (3.40) to a Dirac delta is given by:

$$H_{(z)} = \frac{A}{1 - e^{-1/\tau_a} \cdot z^{-1}} + \frac{B}{1 - e^{-1/\tau_b} \cdot z^{-1}} + \frac{C}{1 - e^{-1/\tau_c} \cdot z^{-1}}. \tag{3.42}$$

Simple algebra to find a common denominator yields the filter coefficients:

$$
\begin{aligned}
a_0 &= 1 \\
a_1 &= (-1.0) * (e^{-1/\tau_a} + e^{-1/\tau_b} + e^{-1/\tau_c}) \\
a_2 &= (e^{-1/\tau_a} e^{-1/\tau_b} + e^{-1/\tau_a} e^{-1/\tau_c} + e^{-1/\tau_b} e^{-1/\tau_c}) \\
a_3 &= (-1.0) * (e^{-1/\tau_a} e^{-1/\tau_b} e^{-1/\tau_c})
\end{aligned}
\tag{3.43}
$$

$$
\begin{aligned}
b_0 &= (A + B + C) \\
b_1 &= -A(e^{-1/\tau_b} + e^{-1/\tau_c}) - B(e^{-1/\tau_a} + e^{-1/\tau_c}) - C(e^{-1/\tau_a} + e^{-1/\tau_b}) \\
b_2 &= A(e^{-1/\tau_b} e^{-1/\tau_c}) + B(e^{-1/\tau_a} e^{-1/\tau_c}) + C(e^{-1/\tau_a} e^{-1/\tau_b})
\end{aligned}
$$

The coefficients in Equation (3.43) define the transform from the delta function to the multi-component exponential decay. The inverse transform is found by simply switching the a and b coefficients. The output of this inverted filter on Equation (3.40) would be a delta function with an amplitude equal to 1. If A, B, and C are divided by the sum $A + B + C$, the output of the inverse filter would be given by $(A + B + C)\delta_{(x-x_0)}$.

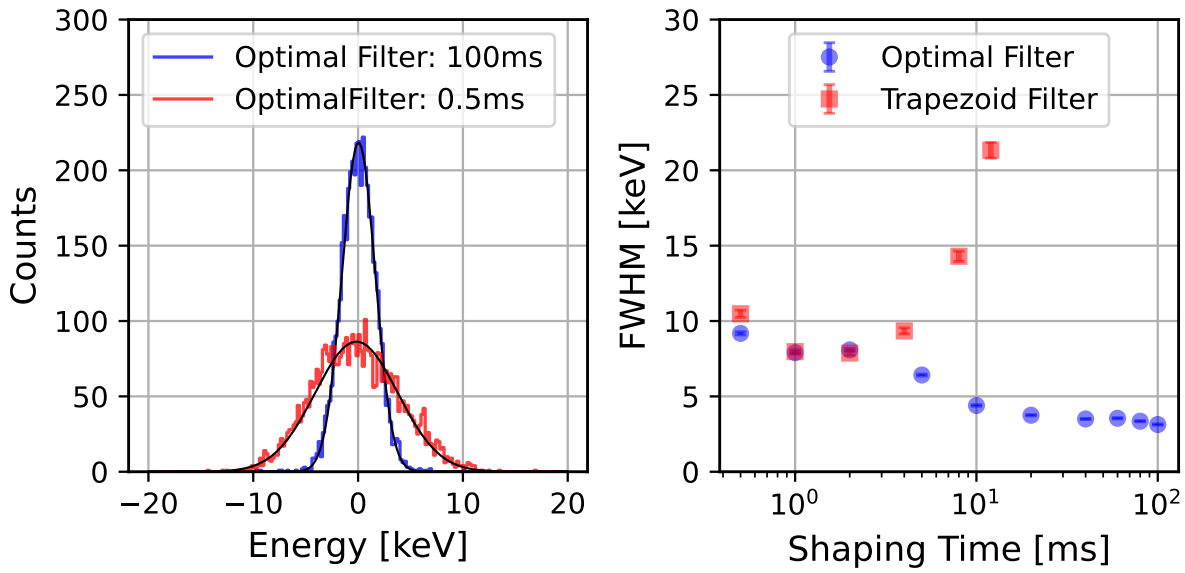

Figure 3.9: *Left*: Baseline resolution of EVE Run-6 for an optimal filter of 100 ms and one of 0.5 ms. Baseline resolution is calculated by the application of the filter to noise traces without signal pulses. *Right*: Comparison of baseline resolution FWHM for trapezoidal and optimal filters of varied widths. To make the filters more comparable, the shaping time of the trapezoidal filter is twice the filter peaking time, which is equivalent to the entire filter width. At short shaping times, the resolution performance of both filters becomes approximately the same.

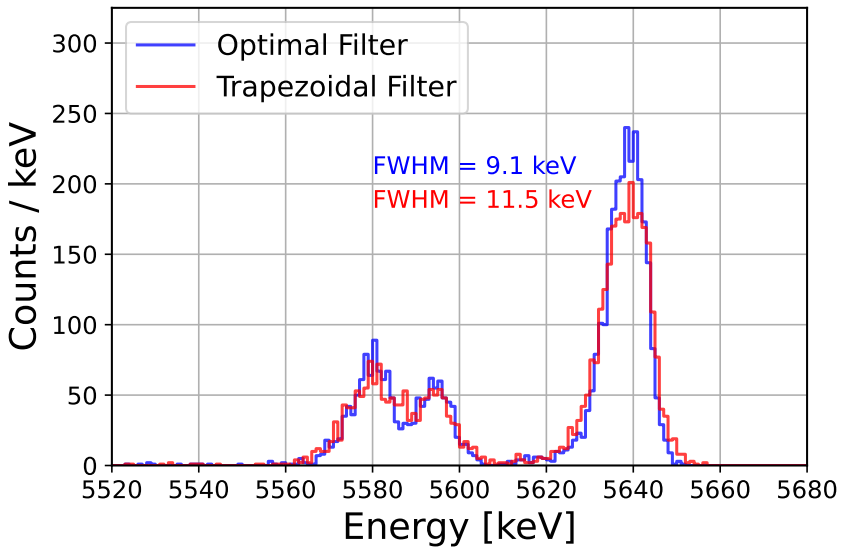

Figure 3.10: Resolution comparison with Optimal filter width 100 ms. Trapezoidal shaping time 1.5 ms.

From here, a trapezoidal filter can be applied by applying a running integral of this output and applying Equation (3.37). Alternatively, since filters obey the associativity property, for example, the running integral and derivative cancel out.

3.4.5 Filter Comparison

The trapezoidal and optimal filters can be compared in terms of baseline resolution and peak resolution as a function of filter width. Baseline resolution is the distortion purely as a function of noise and in the case of decay energy spectroscopy is independent from resolution effects caused by source coupling to the detector. While baseline resolution has less practical effects in terms of system performance, it serves as a demonstration of ideal case performance.

It is first demonstrated that to achieve the best performance, the optimal filter requires long waveform traces. Figure 3.9 on the left shows the distribution of reconstructed amplitudes when an optimal filter of 100 ms and 0.5 ms are performed on blank data traces. The 100 ms optimal filter and noise power spectra are depicted in Figure 3.6. To generate the template for the shorter optimal filter, the noise and pulse templates are truncated to 0.5 ms. In the 100 ms case, the noise FWHM is 3.5 keV while in the 0.5 ms case, it is 9 keV.

For comparison, the baseline noise is measured for both optimal filter and trapezoidal filter at a variety of filter widths or shaping times shown on the right of Figure 3.9. The resolution against shaping time for the trapezoidal filter shows the characteristic parabolic structure described by parallel noise, series noise, and white noise in Knoll [55]. In contrast, the optimal filter resolution

improves in resolution asymptotically with its filter width.

When an energy spectrum from a DES measurement (EVE Run-9), the resolution achieved by the optimal filter and trapezoidal filter are each worse than their optimal. Resolution is measured by the FWHM of the ^{241}Am decay peak at 5637 keV shown in Figure 3.10. The filters were performed with their optimal shaping times, 100 ms and 1.5 ms for the optimal and trapezoidal filters, respectively. The source of this degradation is from imperfect source coupling with the absorber which can manifest from a number of different conditions. The microcalorimetry group at Los Alamos National Laboratory has similarly demonstrated that sample preparation impacts resolution to a great degree [72]. In these cases, there is minimal improvement from choosing the optimal filter over the trapezoidal filter.

Furthermore, the noise performance of the optimal filter and trapezoidal filters are approximately equal at short shaping times. This yields a preference towards the use of trapezoidal filters by the LLNL group as it is computationally simpler and does not require accumulating pulses to produce a template. Modeling and understanding of the response of the trapezoidal filter when processed on MMC data is discussed in the following chapter.

CHAPTER 4

Modeling of Detector Response

4.1 Introduction

4.1.1 Pile-up In Cryogenic Radiation Detectors

Decay Energy Spectroscopy (DES) is the technique of embedding radioactive isotopes within a detector such that the entire decay energy can be measured. This is typically achieved through coupling an absorber to cryogenic thermometers such as metallic magnetic calorimeters (MMCs) or transition edge sensors (TESs). The DES technique is commonly employed in a variety of applications, including actinide nuclear material assay, detection of neutrinoless double beta decay, precise measurement of the beta spectra, measurements of neutrino mass, and others [73, 72, 74, 75, 76, 77, 78].

Pile-up affects all aforementioned DES applications. While pile-up on the tail of previous pulses can be identified and rejected with dead-time correction, identifying pile-up pulses on the rising edge is non-trivial [47]. This non-distinguishable pile-up changes the amplitudes of signals and distorts the energy spectra.

Pile-up effects can be mitigated by reducing the sample activity or increasing the detector speed. However, reducing the sample activity is not always feasible: statistics or practical measurement time can be limiting factors such as fast-turn-around nuclear material assay or the studies of rare nuclear decays. Detector speed can be improved by operating at a higher temperature or through the use of a strong thermal link between the absorber and the sensor. However, these have practical limits: at high temperatures, resolution is degraded or the material assay may require a sufficiently large absorber that thermalization times become the limiting factor. At such a point, it is critical to quantify the spectral and efficiency effects from both distinguishable and indistinguishable pile-up for accurate DES measurement.

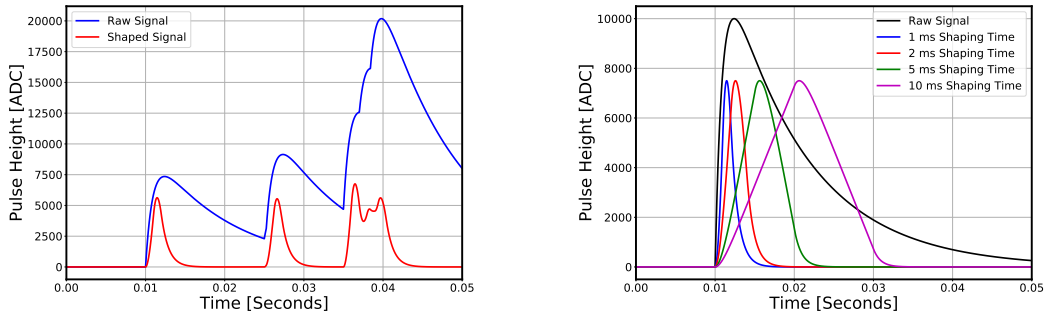

Figure 4.1: *Left*: Simulation of continuously acquired data (*blue*) with six pulses. The raw waveform is filtered with a trapezoidal shaping algorithm using pole-zero correction (*red*). The pulse at 25 ms appears as a single event with the same energy as the preceding event; however, it is actually comprised of two separate pulses with amplitudes 3000 and 4500 ADC offset by 0.25 ms. *Right*: raw detector pulse (*black*) with exponential rise (1 ms) and fall (10 ms) and a variety of trapezoidally shaped signals (*colored*).

4.1.2 Methodology

In this work, we use the Monte-Carlo method to study the systematic effects of pile-up as a function of count rate, pulse shape, and filter time width. We quantify the effects of pile-up on measured energy spectrum and absolute efficiency. We focus on actinide measurements and studies of other alpha decay species, but the results are more generally applicable to other DES and cryogenic experiments.

We simulated template pulses with fast exponential rise and slow exponential decay. The rise times and decay times studied were 0.1, 1, 10 ms, and 10, 100 ms, respectively, to represent various detector speeds. "Rise-time" refers to the exponential time constant of the raw detector pulse's rising edge. Similarly for "decay-time" and the raw pulse's falling time constant. Signal arrival times are generated at various count rates (0.1–10 CPS) using a random number generator. Signal amplitudes were randomly sampled from DES Geant4 simulations [79], and were convolved with a detector response function modeled as a Gaussian with 2 keV FWHM energy resolution.

Our simulated data comprised pulses with exponential rise and decay in a long-time domain trace. We applied various trigger algorithms to investigate trigger losses due to pile-up. For energy extraction, a trapezoidal filter is applied to the entire trace, and then time windows are selected centered around each trigger point. Pulse maximums in each time window were taken as signal amplitudes and energies.

Trapezoidal shaping is employed for its fast timing resolution. The shaped pulses have significantly shorter pulse widths, thus the number of pile-up events can be significantly reduced. We have demonstrated trapezoidal shaping yields similar energy resolution with optimal filters in MMC detectors whose rise time is significantly faster than decay time [55, 68]. The shaping time can be

Isotope	Decay Energy	Half-Life	% by Mass	% by Activity
	[keV]	[years]	[%]	[%]
^{238}Pu	5593.2	87.7	0.05	4.4
^{239}Pu	5244.5	24,110	84.0	26.8
^{240}Pu	5255.8	6561	14.5	17.0
^{241}Pu	20.8	14.4	0.05	26.8
^{241}Am	5637.8	432.6	1.4	25.0

Table 4.1: Isotopic composition of case study sample loosely based upon CRM-137A [80]

easily adjusted and optimized for specific applications. Shorter filters offer faster timing resolution and will reduce the number of pile-up events (Figure 4.1). For this study, we investigate shaping times: 0.1, 1, and 10 ms. Shaping times substantially longer than the pulse rise time worsen the pile-up effects. In our experimental data, filters with shaping times much shorter than the pulse rise time can degrade resolution. Therefore the filter widths are "matched" in time scale to the rise times studied. Pulse decay time was found to negligibly impact pile-up after the application of pole-zero correction.

4.2 Plutonium Case Study

4.2.1 Sample

The plutonium sample was chosen for the relative isotopic ratio and pile-up case study because of its importance in nuclear safeguards [72] and the relative difficulty in making practical measurements of the isotope ratio. The challenge arises from the close Q-Values of Pu-239 and Pu-240 decays as well as the common presence of the Pu-241 isotope [80]. The pile-up of Pu-239 and Pu-241 beta decays causes the Pu-239 decay energy peak to bleed into the Pu-240 peak. This distorts the measured Pu-239/Pu-240 ratio. Our case-study sample comprises Pu-238, Pu-239, Pu-240, Pu-241, and Am-241 and is based upon CRM137 [80]. The composition and activity of each isotope are summarized in Table 4.1.

4.2.2 Efficiency and Ratio Results

Pile-up changes signal amplitudes and reduces the number of counts within the true decay energy peak. We define peak efficiency as the integrated number of counts within the Gaussian fit divided by the known number of simulated events. Both the absolute efficiency and the relative efficiency

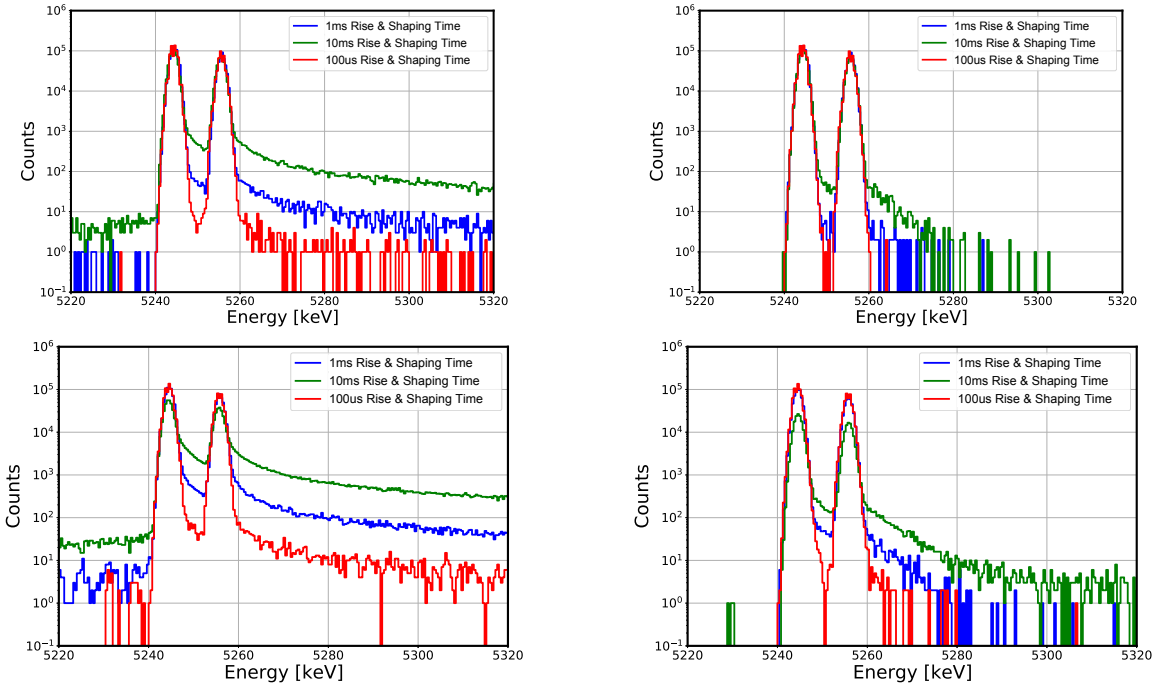

Figure 4.2: Four extracted spectra from the plutonium pile-up simulation. *Top left*: 1 count/s without pile-up rejection. *Top right*: 1 count/s with pile-up rejection. *Bottom left*: 10 counts/s without pile-up rejection. *Bottom right*: 10 counts/s with pile-up rejection.

were calculated in this manner. For the relative efficiency measurement comparing the ^{239}Pu and ^{240}Pu efficiencies, we present the "normalized" ratio: the measured peak ratio divided by the known true ratio.

Two effects contribute to the loss of efficiency. The first is the dead time imposed by the $0.25 \cdot \tau_{\text{rise}}$ to $5 \cdot \tau_{\text{shaping}}$ cut. The second is from indistinguishable pile-up occurring when two pulses' raising edges overlap within $0.25 \cdot \tau_{\text{rise}}$. The two pulses are measured as a signal pulse with approximately combined energy and thus fall outside of the decay energy peak. The efficiency loss due to dead-time rejection is the dominant factor but can be calculated relatively easily given a measurement's average count rate and rejection criteria. The effect of indistinguishable pile-up is an order of magnitude less prevalent but requires a more complex calculation of its effects. The spectral distortion from these two effects can be seen in Figure 4.2 by comparison of the left and right plots. The left spectra demonstrate the spectral distortion from distinguishable and indistinguishable pile-up, whereas the right shows the indistinguishable contribution after pile-up rejection has been performed.

The absolute efficiencies are presented in Figure 4.3 (*Left*) as studied for various average count rates and pulse rise times specifically for the ^{239}Pu decay energy measurement. The inverse of the efficiency value is the correction term to account for losses due to the dead-time cut and for

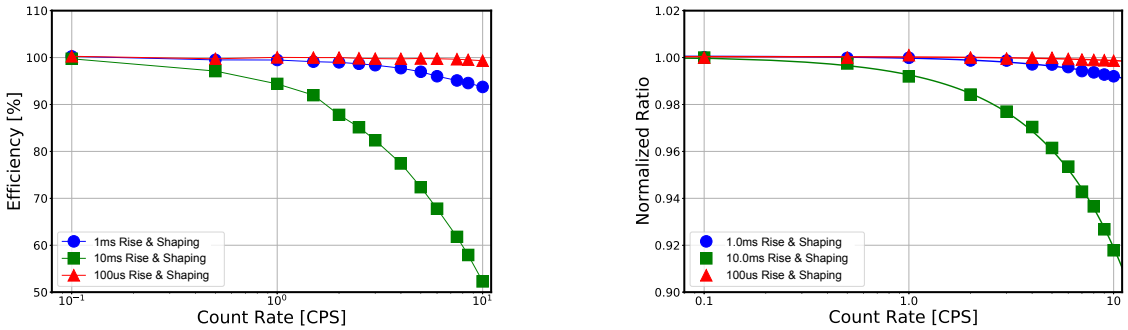

Figure 4.3: *Left*: Absolute efficiency of the simulated Pu-239 peak. Pile-up changes signal amplitudes and reduces the peak efficiency. *Right*: Normalized peak count ratios of the simulated Pu-239 and Pu-240 signals. The changes in peak ratios originate from the indistinguishable pile-up of low energy Pu-241 beta signals on Pu-239 and Pu-240 alpha signals.

indistinguishable pile-up. Further of note, the efficiency factors for the ^{239}Pu and ^{240}Pu isotopes differ resulting in distortion of the normalized ratio. This occurs from the isotope's different count rate and counts from ^{239}Pu bleeding into the ^{240}Pu altering the Gaussian fit. Although subtly for fast (raising) pulses at low count rates, the ratio is greatly distorted in the case of a 10 ms (raising) pulse at more than 1 CPS. This effect can be markedly improved by shortening the shaping time, as discussed in Section 3.3.

4.2.3 High Count Rate Experimental Data and Benchmark

We used experimental DES data obtained with a Sm-147 source and an external Gd-148 source, for benchmarking our simulation of absolute efficiency. The data was taken as part of an experimental campaign to measure the half-lives of the Sm-146 and Sm-147 isotopes [78]. The Gd alpha source dominated the events and produced a total trigger rate of 18 CPS. The rate above 500 keV was measured as 8 CPS; this cut was chosen for closer comparison to the simulation study and because the low energy noise pedestal width was shaping time-dependent. The average pulse shape comprised exponential rise and fall time constants 85 μs (0.1-0.9 rise time was ~250 µs) and 60 ms respectively.

The data was analyzed with trapezoidal filters of width 100 µs to 10 ms, to investigate the shaping time effect. The optimal shaping time was found to be 2.5 ms; however, there is a 20% deficit in the measured count rate relative to the 100 µs shaping analysis. This loss is caused by the increased dead time of the longer algorithm and the merging of multiple pulses into a single-shaped event. With the shaping time analysis, the true activity of a sample can be extrapolated by projecting the trend to a zero-width shaping time and taking that value to be the true activity. This case yields ~6.33 Bq for the Gd-148 alpha peak.

To benchmark the efficiency of the analysis algorithm, the measurement was repeated but with 40,000 pulses with amplitude energy of 5260 keV randomly injected into the data traces at an average count rate of 1 CPS. The injected pulse(s) were given the same exponential time constants as the average pulse shape. The data with simulated events was analyzed via the same methodology as described above and found to be ~100% efficient at a shaping time of 0.1 ms as well as the same 20% efficiency reduction at 2.5 ms shaping time as the true experimental data. This indicates our simulation methodology agrees well with our experimental data.

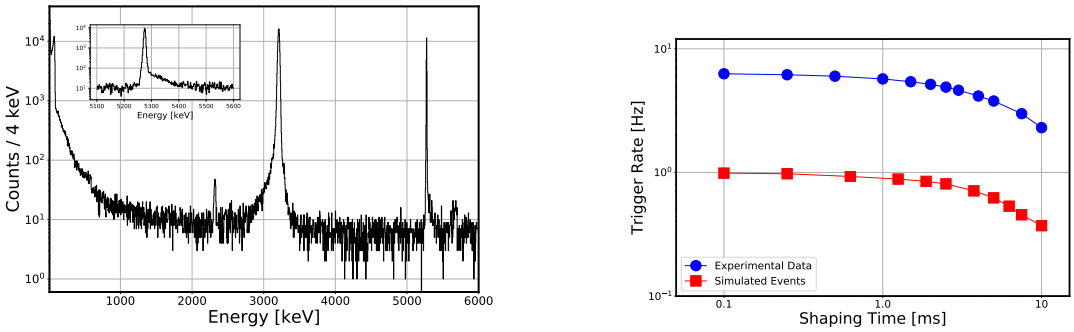

Figure 4.4: *Left*: Energy spectrum of Gd-148 exposed Au-MMC. The primary Gd-148 alpha peak is seen at 3178 keV. The nuclear-recoil peak from the daughter Sm-144 can be seen at low energy with end-point ~90 keV. The injected simulation peak is seen at high energy at 5260 keV. *Insert*: Zoom in on the high-energy peak. *Right*: Count rate plot for the alpha peak, calculated via exponentially modified Gaussian fit, overall count rate, and simulated/injected count rate. The overall count rate only accounts for 500 keV as the noise pedestal is shaping time-dependent.

4.2.4 Programmatic Relevance

Equally important as the absolute activity is relative efficiency, which affects reconstructed spectral features. The practical nuclear assay requires fast turnaround times [81, 82, 72, 83]. This necessitates a detector with many channels, multiplexing, and numerous absorbers prepared with sources. Alternatively, fewer channels can achieve the same statistics with higher count rates at the cost of pile-up. The effect of this pile-up depends on the energy separation of prominent features in the spectrum. This result is further relevant considering reference materials CRM136 and CRM137 contain ~2% Pu-241 by mass [84, 80]. The activity is nearly entirely dominated by low-energy betas, placing emphasis on the need to correct pile-up for plutonium measurements. Our plutonium case study demonstrates the need for such corrective factors and a methodology for their calculation.

4.2.5 ^{146}Sm Relevance

Characterization of pile-up loss is crucial for absolute activity measurements such as half-life measurements of rare isotopes. Accurate characterization of the efficiency loss due to spectral distortion as well as losses due to pile-up rejection cuts is needed in these applications, an example of which is the measurement of the Sm-146 half-life. Sm-146 is of interest for radiometric dating early Solar-System chronology and for evidence of near-Earth supernova [85]. Past half-life measurements disagree by over 30% [78, 24, 20]. Our collaboration is currently working on a new experiment to resolve this tension utilizing the DES technique [78].

The same pile-up simulation was performed for ^{146}Sm alpha source with different count rates and a background model comprised of ^{146}Eu, ^{146}Pm, and ^{146}Gd to quantify their effect on the ^{146}Sm decay peak as shown in Figure 4.5. This modeling was ultimately unnecessary as a result of the highly successful campaign to clean and purify the sample of contaminants before the cryogenic decay counting experiment.

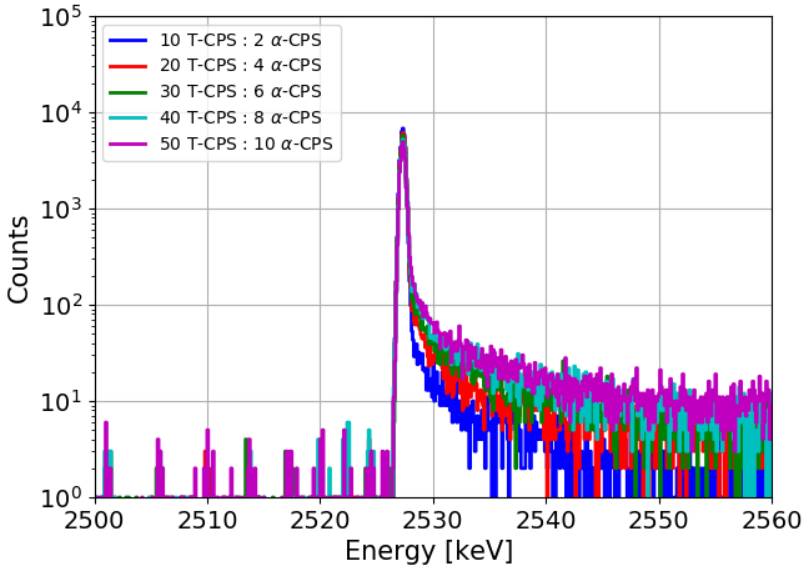

Figure 4.5: Monte-Carlo simulation of pile-up for ^{146}Sm sample.

4.3 MAGNETO-ν Experiment

4.3.1 Experimental Motivation

The MAGNETO-ν Experiment utilizes magnetic microcalorimeters (MMCs) and the decay energy spectroscopy (DES) technique [81, 73, 72, 86]. The idea to conduct neutrino physics experiments

with ^{241}Pu originated during various plutonium and actinide measurements. Despite using low-gain high dynamic range sensors, the ^{241}Pu beta spectrum was distinct and well-defined above the noise. Figure 4.6 depicts a log-log plot from a plutonium measurement (Run 60) where the decay energy peaks are visible at the 5.5 MeV scale and the beta spectrum is simultaneously measured at the 10 keV scale.

The MAGNETO-ν neutrino experiment aims to search for such a sterile neutrino through the performance of a precision study of the ^{241}Pu beta decay spectrum. The scientific goal is to find sterile neutrinos, establish techniques for future iterations and neutrino mass experiments, and complement other neutrino experiments utilizing tritium and other radionuclide sources [87, 88, 89, 90, 91].

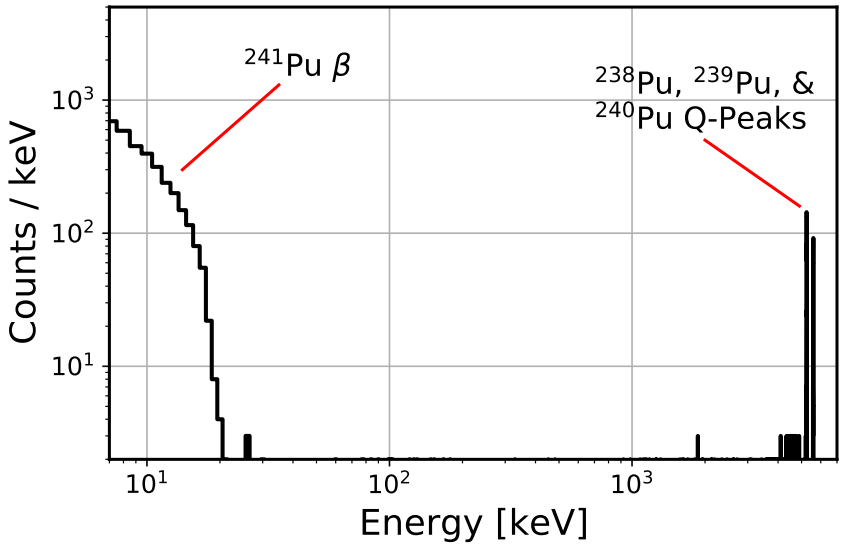

Figure 4.6: Experimentally measured mixed isotopic plutonium spectrum utilizing CRM-137A as a calibration standard. Decay energy peaks from ^{238}Pu, ^{239}Pu, and ^{240}Pu are visible near 5.5 MeV while the ^{241}Pu beta spectrum is visible below 20 keV.

The experimental setup as seen through a microscope lens is depicted in the *right* of Figure 4.7. The MMC sensor was designed and fabricated at the Korea Research Institute of Science and Standards [45, 46]. Signals were amplified and read out by Magnicon XS1 SQUID and preamplifier [52]. The entire experiment was cooled to 20 mK within a BlueFors model LD dilution refrigerator [92].

4.3.2 Spectral Signature

In beta decay, the decay energy is split between the beta particle, recoiling daughter nucleus, and emitted (anti-)neutrino [93]. The maximum beta energy is the difference between the decay energy

and the neutrino rest mass along with the corresponding energy imparted to the daughter nucleus for conservation of momentum [93]. If a heavy sterile neutrino is produced via an alternate decay branch, the maximum beta energy is reduced by the sterile neutrino rest mass. This would produce a beta spectrum with a reduced endpoint which would appear as a "kink" in the total beta spectrum with an excess of events towards lower energy.

Figure 4.7 (*left*) demonstrates the spectral distortion of the ^{241}Pu beta spectrum by a 10 keV sterile neutrino. The *blue* and *red* spectral contributions are from the sub-eV active neutrino and the heavy sterile neutrino respectively. The aforementioned "kink" is visible in the summed spectrum.

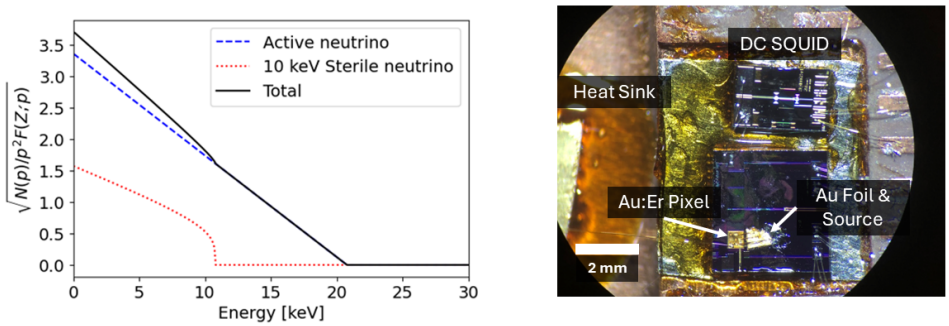

Figure 4.7: *Left*: ^{241}Pu beta spectrum with contribution from a hypothetical 10 keV sterile neutrino. *Right*: First MAGNETO detector used at an early R&D stage of the experiment (Run-99).

4.3.3 Study Motivation

The development of an accurate efficiency response model is crucial for accurate physical interpretation of experimental data. For example, overestimation of the efficiency would lead to insufficient spectral correction which could potentially obscure a true sterile neutrino signal. Alternatively, underestimation of the efficiency would lead to over-correction, potentially producing a false sterile neutrino signal. Misunderstanding of atomic effects and detector response has historically led to retracted claims of a 17 keV sterile neutrino [94, 95].

The primary aim of this study is to quantify spectral distortion as a function of reconstructed event energy. The secondary aim is to correct the spectral distortion caused by triggering below ~2.5 keV, extending MAGNETO-ν's sensitivity to higher mass sterile neutrinos ($\gtrsim$17.5 keV). We define the total efficiency, for a given energy range, as the ratio of events that pass triggering and event selection cuts and the true number of present events. As the underlying true number of events cannot be known, this is achieved via a pulse-template injection method described below.

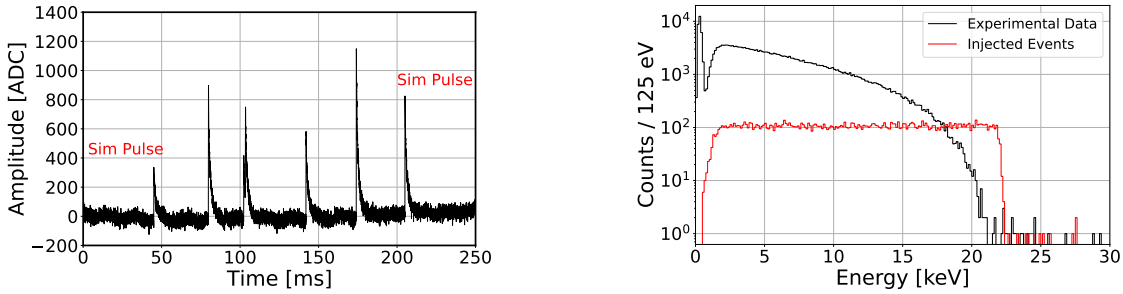

Figure 4.8: *Left*: A 250-ms section of continuously acquired data with two labeled simulated pulses. *Right*: Extracted data spectrum with tagged simulation events plotted in *red*. Un-tagged events in *black* are beta events from ^{241}Pu decay.

4.4 MAGNETO-ν Analysis and Simulation Methodology

4.4.1 Source & Deposition

MAGNETO-ν utilizes a newly purified plutonium standard CRM-137A [80]. The source, dissolved in nitric acid, was deposited on a 5 micron gold foil with a micropipette. The gold foil was placed on top of a heating pad at 90°C allowing the acid to evaporate between successive drops to prevent splattering.

The foil was folded and rolled with a jeweler's mill allowing for the gold to cold weld to itself encapsulating the plutonium [96, 97]. The containment of plutonium was confirmed via null measurement with an alpha detector. Given the null alpha measurement and that the maximum range of a 21 keV beta particle in gold was calculated to be 2 µm [4], while the maximum range of a 5 MeV alpha particle is 10 µm [4], we judge the detection efficiency to be near 100 %. Potential detection efficiency losses can be evaluated by comparison of data to Geant4 [79] simulations with varied distributions of ^{241}Pu throughout the absorber.

The absorber was attached to an insulating G-10 plate with GE-Varnish [98, 99]. The absorber and Au:Er paramagnet were thermally connected with Au wire bonds. A weak thermal link to the base plate is provided through the silicon of the sensor chip. Given the significantly greater thermal conductivity of gold, the majority of heat flows through the sensor and is measured.

4.4.2 Activity & Backgrounds

The total measured (triggered) activity was 32 Bq with the beta activity contributing 23 Bq. External backgrounds have been judged to be negligible via prior assessment of gold foil "blanks". Alpha decays significantly increase the system temperature and necessitate a 15 ms dead-time window imposed after each alpha event. To reduce the dead time and improve temperature stability, future

Isotope	Decay	Decay Energy	Half-Life	Phase 1 Rel. Activity	Phase 2 Rel. Activity
		[keV]	[Years]	[%]	[%]
^{241}Pu [100]	β	20.8	14.4	77.2	99.93
^{238}Pu [102]	α	5593.2	87.7	6.3	1.366E-2
^{239}Pu [5]	α	5244.5	24,110	8.7	3.453E-3
^{240}Pu [103]	α	5255.8	6561	7.7	4.829E-2
^{241}Am [104]	α	5637.8	432.6	9E-3	5.267E-4

Table 4.2: Isotopic composition of MAGNETO-ν plutonium source. The two final columns are activity by percentage with Phase-1 corresponding to CRM-137A and Phase-2 to the enriched source.

iterations of MAGNETO-ν plan to use an enriched ^{241}Pu source. The relative activity contributions of CRM-137A and the enriched source are shown in Table 4.2.

While the primary decay of ^{241}Pu is to ^{241}Am, there is a 0.0025 % branching alpha decay to ^{237}U which then decays via beta emission with a half-life of 6.75 days and contributes to the MAGNETO-ν background [100, 101]. For the current dataset, the ^{237}U contribution to activity is approximately 0.04 Bq.

MAGNETO-ν phase-2 targets a nominal ^{241}Pu activity of 100-200 Bq. If 100 billion ^{241}Pu atoms are loaded (150 Bq), the maximum activity from ^{237}U will be 0.38 Bq 65 days after chemical separation. Given the higher beta endpoint of 518.6 keV and mean beta energy of 68 keV [101], the expected signal-to-background ratio will be greater than 1500:1. At this count rate, with a 50 µs resolving window (discussed below), the pile-up rate would be approximately 3 times greater at 1.2 Bq which we hope to improve with faster sensors.

4.4.3 Data Acquisition & Analysis

Output from the Magnicon preamplifier is filtered through a 100 kHz low-pass filter and then digitized by a National Instruments NI PXIe-5172 digital oscilloscope [105]. Waveforms are saved in 10 second continuous traces digitized at a sampling rate of 1 MHz; samples are then averaged yielding an effective rate of 200 kHz. Beta-decay pulses were found to possess a short rise time of 50 µs and decay time of 1.25 ms.

Waveforms are analyzed offline with two digital trapezoidal filters [53, 54, 68, 6]. A long filter with peaking time 500 µs and flat top 50 µs is used for energy calculation. A short filter with a peaking time 50 µs, matched to the pulse rise time, is used for triggering and timing. Events with amplitudes greater than the triggering threshold, approx. 1.2 keV, are saved.

A 5 ms dead-time cut, corresponding to 4 decay constants, is imposed after each timestamp to eliminate pile-up. However, events within the 50 µs pulse rise time, are indistinguishable from pile-up, where the energies of individual energies are added [6].

Pulse shape cuts were placed around the primary mean-time band, containing ^{241}Pu events centered around a value of 0.75 ms after the trigger. Lastly, the energy scale was determined via a dedicated experiment. The details of the experiment along with the pulse-shape cuts, will be discussed in an upcoming publication.

4.4.4 Pulse Selection

A 10 ms pulse template was generated by selecting pulses that passed two criteria: having energy between 15 and 20 keV, and being at minimum 20 ms apart from any other trigger. The first criterion is chosen to avoid trigger threshold effects, 20 ms being double the length of the template. No other criteria were placed to minimize potential bias. The baseline was subtracted from each pulse, and the median for each time-bin was calculated from all the pulses to eliminate noise. The median technique was chosen over averaging as being more robust against, indistinguishable pile-up, waveforms containing events below the threshold, and anomalous artifacts.

4.4.5 Simulation Data-Set

Two Monte-Carlo generated random timestamps and pulse amplitudes corresponding to energies from 0 to 22 keV. The higher energy bound was chosen such that the simulation would cover the entire ^{241}Pu beta spectrum. At each timestamp, the template pulse multiplied by its Monte-Carlo generated amplitude was added to the digitized data trace according to the method described in Ref. [6]. The new ADC values were rounded to the nearest integer such that they would be in the same format as the original data. The resultant waveforms containing simulation pulses were saved and later processed with the same analysis code used on the original dataset. A total of 25000 simulated pulses were injected with an activity of 1 Bq. A 250-ms period of simulated data containing two injected pulses is shown on the *left* of Figure 4.8.

4.5 MAGNETO-ν Simulation Results

4.5.1 Live Events and Pile-Up

Simulated events were identified in post-processing by comparing all event timestamps with the Monte-Carlo generated list. If an extracted timestamp is within 50 µs of a simulated timestamp, the pulse is labeled as simulated.

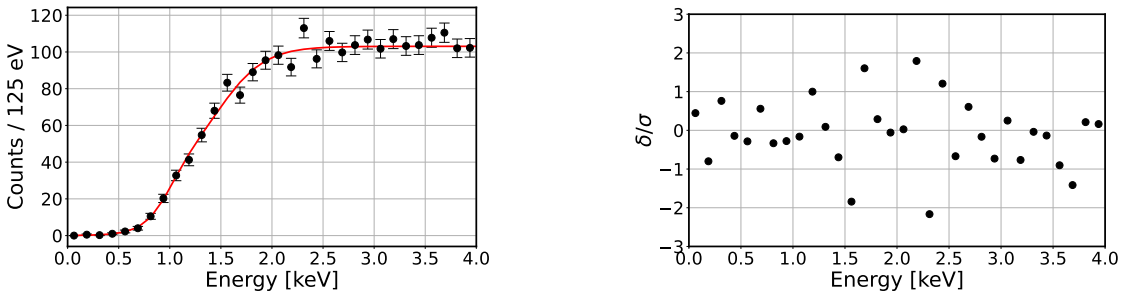

Figure 4.9: *Left*: Efficiency roll-off of simulated events with sigmoidal fit. *Right*: Fit residual.

Of the 25000 injected events, 22749 were identified via the triggering algorithm. 20153 subsequently passed dead-time cuts imposed via proximity to alpha decays or preceding events. The ratio of live to triggered events yields a live time of 88.5 %. Of the live simulated pulses, 19678 (98%) passed the remaining pulse shape cuts. The dead-time and pulse-shape cuts were found to be flat in energy, the energy dependence of the roll-off being due to trigger efficiency.

22 simulated events were tagged as simulation events above the endpoint of the simulated spectrum. By separate Monte-Carlo simulation, it is estimated that with the 50 µs discrimination limit, there would be approximately 50 pile-up events between injected pulses and ^{241}Pu beta decays, half of which would have energies greater than the simulated endpoint. When accounting for alpha dead time, the injection method produces the expected number of pile-up events, the total number of which is significantly smaller than the total number of reconstructed events, ~0.2%

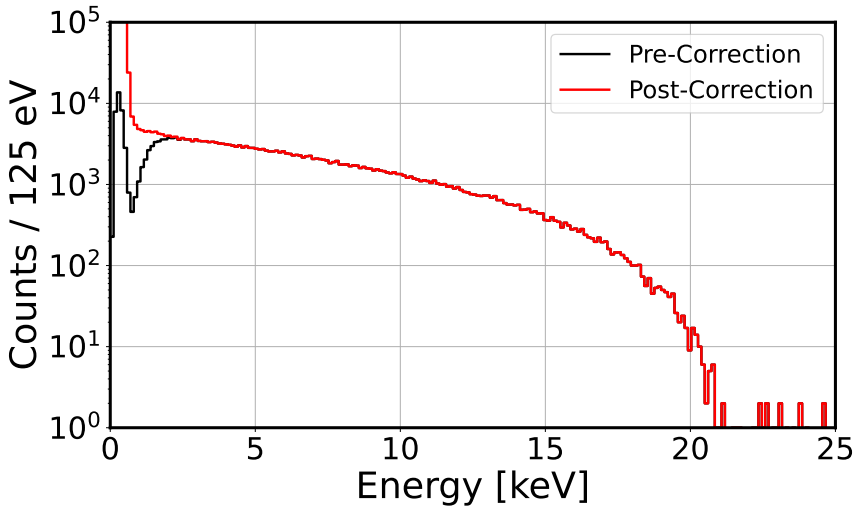

Figure 4.10: Experimentally measured ^{241}Pu beta spectra (*black*) with correction for trigger efficiency (*red*).

4.5.2 Spectral Reconstruction

The efficiency loss model is comprised of two components. The pile-up and pulse-shape cuts were found to be flat with energy; each bin could be simply divided by 0.865 corresponding to the ratio of the number of simulated events that passed cuts to the total number of triggered events. The second component was derived by fitting a sigmoidal curve to the low energy distribution of simulation-injected events. The fit and residual are depicted in Figure 4.9. The difference between the fit curve and flat distribution is the efficiency loss due to triggering. The experimental data is then corrected down to the noise edge at 0.8 keV shown in Figure 4.10.

The resolution of the initial experiment was quite poor. The electronic noise was ascertained to be 380 eV FWHM, which resulted in a high threshold of 1.2 keV and a reduction in efficiency at 2 keV. Work is currently underway to improve resolution. Despite poor resolution, the simulation technique can reconstruct the spectral loss.

4.5.3 Conclusion

We have developed a Monte Carlo simulation technique and created a parallel data set containing simulated pulses injected at random times with a flat energy distribution. The simulated data set was processed using the same triggering and pulse-shape cuts as the true data set. From the comparison of the results extracted from this simulation, efficiency correction terms are derived and applied to the true data set.

The MAGNETO-ν has demonstrated preliminary proof of concept of a sterile neutrino search utilizing MMCs, ^{241}Pu, and the decay energy spectroscopy technique. Further refinements of the experiment are underway, including improvement of energy resolution, more precise calibration of the energy scale, and higher statistics. The Monte Carlo methodology of injecting template pulses is demonstrated as an important tool for reconstructing and understanding the beta spectrum.

CHAPTER 5

First DES Experiments

5.1 ^{241}Am Decay Counting

5.1.1 Introduction

^{241}Am is a commonly used calibration source for its alpha and gamma emissions [104]. It decays to ^{237}Np with a half-life of 432.6(6) years with a decay energy of 5637.82(12) keV. The alpha particle energy associated with the two dominant branches are 5486 keV (85.2%) and 5443 keV (12.8%) [104]. Both branches populate excited states of ^{237}Np which then relaxes via gamma emission or the emission of Auger electrons. shake-off electrons, and/or soft x-rays [44]. The 5486 keV state has a 36% probability of emitting a 60 keV gamma ray and the 5443 keV state has a 0.1% probability of emitting a 43 and then 60 keV gamma rays. This decay scheme is shown on the left of Figure 5.1.

Were the source external to a radiation detector, the various branches could be seen via the alpha particle energy spectrum and relative count intensities. However, in decay energy spectroscopy (DES), when the source is embedded within the detector, the detector is sensitive to the energy deposited via alphas, betas, Auger electrons, shake-off electrons, soft X-rays, and nuclear recoils. Only the 60 keV and 43 keV gamma rays can escape the thermal absorber with non-negligible

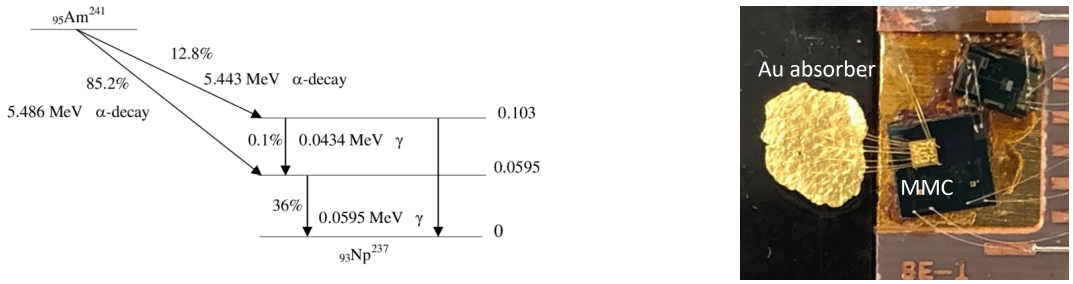

Figure 5.1: *Left*: The primary decay branches of ^{241}Am decay. Diagram is taken from Figure 1 of Reference [106]. *Right*: MMC detector used for ^{241}Am experiments.

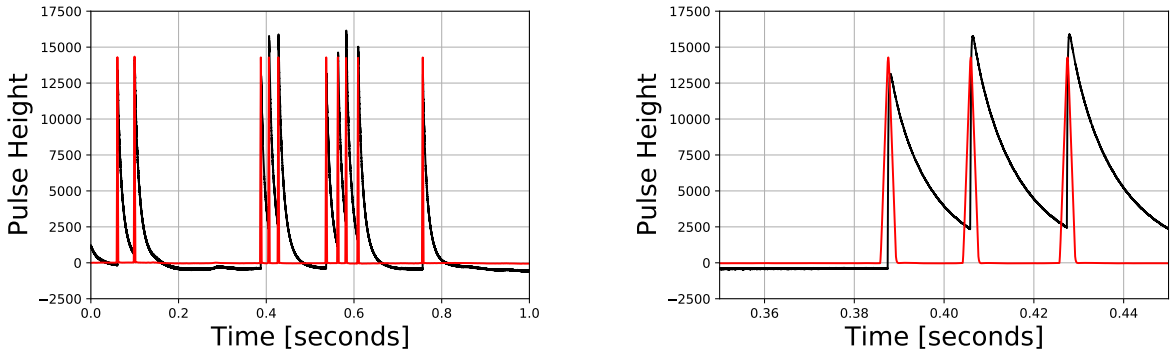

Figure 5.2: Continuously acquired ^{241}Am DES data (black) with digital trapezoidal filtered signal shown in red at two different time scales.

probability. Therefore the expected energy spectrum from an ^{241}Am DES measurement is a primary peak at the decay energy of 5637.82 keV, a secondary peak at 5578.28 keV with approximately one-third the intensity of the primary peak, and a third smaller peak at 5534.88 keV with approximately 0.036% the intensity of the primary peak. The exact intensities of the smaller peaks depend on the thickness of the gold foil used as the absorber as a 60 keV gamma ray has a non-negligible probability of being either photoelectrically absorbed by or Compton scattered off of the gold.

The first decay energy experiments where sources were embedded within thermal absorbers was performed with ^{241}Am. The first experimental setup can be seen on the right of Figure 5.1. Data was acquired in two methods, triggered and continuous. For the triggered data set, the signal was split with one output being fed into a band-pass amplifier and the other being digitized, a threshold crossing of the filtered signal was used for triggering. Continuous data was acquired for comparison as early on it was decided that continuous acquisition would likely be advantageous for the upcoming ^{146}Sm experiment.

5.1.2 Thermal Dependence

As discussed in Chapter 2, the response function of cryogenic detectors depends on the system's heat capacity and thermal conductivity. The magnetization against temperature response can then be observed in the pulse shape of radiation-induced signals at a variety of temperatures. This performance was tested with an ^{241}Am source embedded within a cryogenic detector as one of the early DES experiments. Data was acquired in 50 second traces for a few hours at 20, 60, 80, and 100 mK. A measurement at 40 mK was attempted but from the change in detector response, it appears as though the temperature did not exceed approximately 25–30 mK. This can happen in the Megaman / BlueFors fridge operation if the maximum heater limit is not set sufficiently high enough.

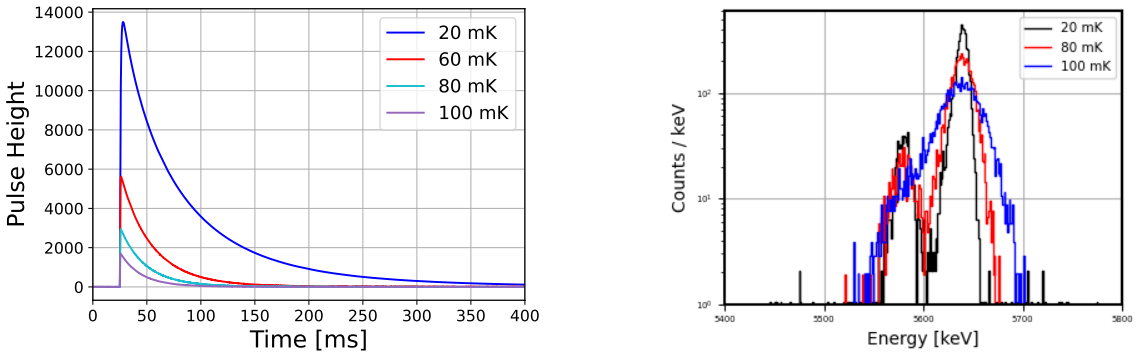

Figure 5.3: *Left*: Pulse shape and amplitude of averaged ^{241}Am waveforms at various temperatures. *Right*: Reconstructed energy spectrum at various temperatures demonstrating how better resolution is achieved at lower temperatures.

Triggered pulse waveforms at each temperature were averaged. Figure 5.3 demonstrates the dependence of pulse height on temperature. This generally confirms the thermal model discussed in Chapter 2. While the pulse height depends on temperature, most noise features are temperature independent below some critical point. For example, SQUID noise is temperature independent once sufficiently cooled to become superconducting. Therefore as the temperature increases from 20 mK to 100 mK, the pulse amplitude shrinks relative to the noise, and hence the overall signal-to-noise ratio deteriorates. Figure 5.3, on the right, demonstrates this behavior. The black, red, and blue spectra are all ^{241}Am DES data but acquired while the detector was at 20 mK, 80 mK, and 100 mK respectively. The spectra are all normalized such that the total counts depicted are the same. At 20 mK, the two peaks can be easily distinguished. At 80 mK the peaks can still be distinguished but are visibly bleeding together while at 100 mK, the peaks are indistinguishable. The lower energy peak could not be differentiated from a low energy tail off of the primary peak.

As discussed in Chapter 4 and Figure 5.2, the pulse rise and decay times also depend on temperature. The rise-time and count rate affect the degree to which pile-up distorts the underlying spectrum. This means in practice, the optimization of various parameters is quite challenging and convoluted.

5.1.3 Pulse Shaping

In Chapter 4 it was generally assumed that the best achievable noise had been reached with the detector. The fundamental noise limit, discussed in Chapter 2, is based on the system heat capacity. Therefore, the choice of shaping time would not significantly affect resolution. In practice, cryogenic experiments struggle to reach their theoretically best resolution, other sources of noise and coupling of sources to detectors degrade resolution. The optimal shaping time for a trapezoidal

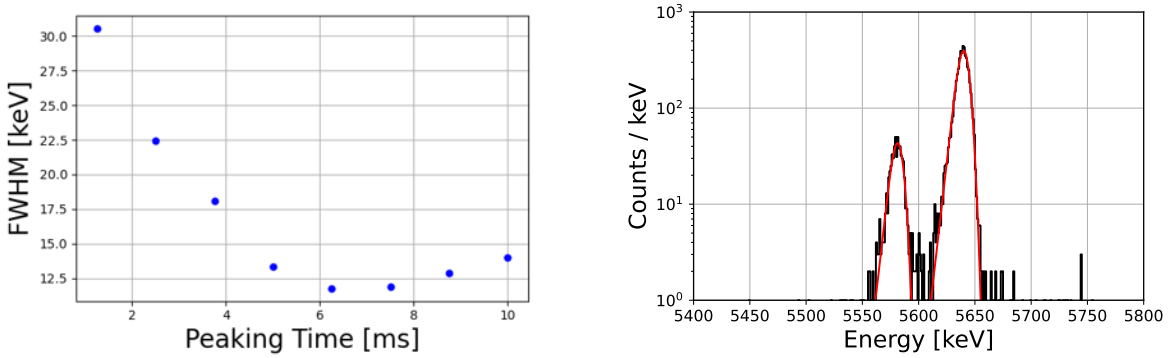

Figure 5.4: *Left*: Energy resolution vs. shaping time. The optimal shaping time was found to be 6.25 ms. *Right*: ^{241}Am decay energy spectrum with primary peak at 5637 keV and second peak 60 keV lower due to gamma escape. Exponentially modified Gaussian fits are drawn in red.

filter (or similar) depends highly on noise. The contrapositive statement is that for a given noise distribution, the resolution depends on shaping time. Figure 5.4 (*left*) demonstrates the dependence of resolution on shaping time. The optimal resolution achieved was 11.5 keV FWHM at a shaping time of 6.25 ms. The resolution exponentially worsens with short shaping times. The resolution deteriorates more slowly when moving to longer shaping times; however, this increases pile-up which may not be desirable in certain circumstances.

In all aforementioned cases, the FWHM is determined by fitting an exponentially modified Gaussian to the full energy decay peak at 5637 keV. Because fits can often confuse the tail and sigma parameters, the FWHM was calculated by finding the index values where the fit reaches half of its maximum.

5.1.4 Peak Ratios

The relative ratio of counts in each peak was determined in two manners. The first is by fitting both peaks with exponentially modified Gaussian functions and comparison of the area parameter and the second is by finding the middle position and integrating each peak independently. The fits shown on the right of Figure 5.4 returned nominal count values of 5132.53 ± 71.65 and 562.07 ± 23.75 for the larger and smaller peaks respectively. This equates to a ratio of 11% ± 0.5% of events being in the smaller of the two peaks. Numerically integrating each of the peaks yields a similar result of 11.5% ± 0.5%. This demonstrates that the 60 keV gamma ray must be absorbed a significant fraction of the time. This makes sense as though it may be only 25–50 µm of gold between the source and the surface, it can be up to a few millimeters in the plane of the gold foil. This demonstrates the challenge of simulating decay energy spectroscopy experiments as the absorber is almost always irregularly shaped and its geometry is difficult to capture in a simulation

model.

5.2 ^{147}Sm Decay Energy Measurement

5.2.1 Motivation

Naturally occurring Sm comprises two long-lived radioactive isotopes, ^{147}Sm and ^{148}Sm. ^{147}Sm with half-life $1.06 \cdot 10^{11}$ years comprises 14.99% of the isotopic abundance of Sm [29]. ^{148}Sm with half-life $7 \cdot 10^{15}$ years comprises 11.24% [107]. The remaining naturally occurring isotopes, ^{144}Sm, ^{149}Sm, ^{150}Sm, ^{152}Sm, and ^{154}Sm are all observed to be stable [108]. To demonstrate the viability of the ^{146}Sm experiment, several DES measurements were performed on ^{147}Sm. ^{147}Sm is a good representation for ^{146}Sm as they are chemically identical, their decay energies differ by only 200 keV [29, 109], and the half-life of the former is known to $\sim$ 1 % uncertainty [29]. In addition to proof of concept tests, these experiments would be used to develop and validate analysis techniques for the later ^{146}Sm experiment.

An enriched ^{147}Sm sample purchased from Oak Ridge National Laboratory's National Isotope Development Center [110]. The ^{147}Sm was dissolved in HCL acid and a quantity with estimated activity of $\sim$ 15 mBq was separated. The solution was then deposited via the use of a micropipette by LLNL chemist and project collaborator Dr. Kelly Kmak. After the acid evaporated, the gold foil was folded over itself approximately 10 times and struck with a ball-tipped hammer. Mechanically kneading the sample was demonstrated by Los Alamos National Laboratory to improve resolution by breaking down source crystals and preventing self-absorption [72]. Figure 5.5 on the left depicts the solution containing ^{147}Sm deposited onto the gold foil inside of a gel pack for transport. The right depicts source preparation via repeated folding and hammering. Another primary purpose of the ^{147}Sm experiment was to test source processing to ensure the best possible results for the later ^{146}Sm measurement.

5.2.2 Calibration Experiment

The first ^{147}Sm calibration experiment comprised the kneaded gold foil thermally coupled to the MMC sensor and an external ^{148}Gd alpha source. The aim of this measurement was twofold, to demonstrate sensitivity to sources with activity of $\mathcal{O}$(mBq) and to demonstrate full measurement of the ^{147}Sm decay energy. Several potential factors could lead to partial energy collection such as poor thermal coupling of the various gold layers, poor thermal coupling of the source to the gold, large source crystals acting as heat sinks, quenching of nuclear recoils, alpha particle escape, or the escape of x-rays, Auger electrons, and shake off electrons. Any one of these factors would prevent

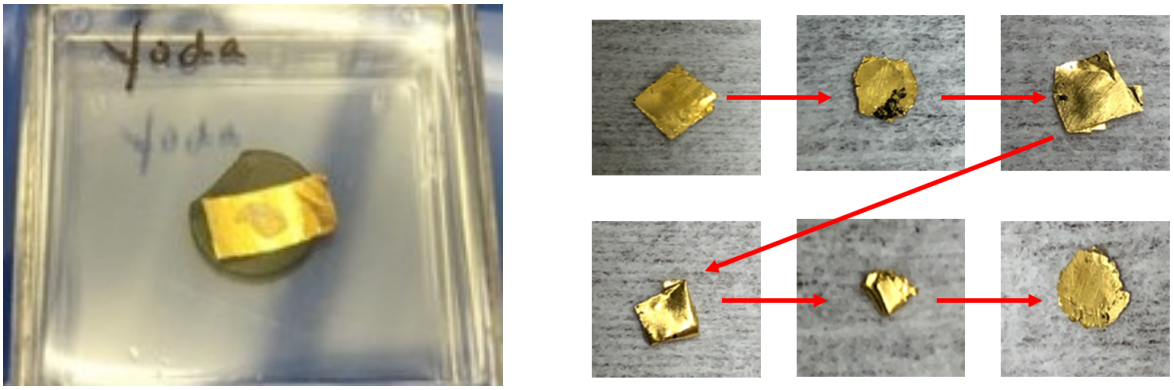

Figure 5.5: *Left*: ^{147}Sm sample deposited on gold foil absorber. A small ring of residue can be seen in the center of the foil. Minimization of residue proved critical for optimal decay counting results. *Right*: The process of folding a gold foil over itself to encapsulate the source. At the time of the early ^{147}Sm measurements, after folding, the foil, placed between two aluminum shims, was hit with a ballpoint hammer. The indentation from the hammer can be seen in the last picture on the lower right.

measurement of the full decay energy as well as degrade energy resolution.

The experiment aimed at establishing optimal run conditions in terms of gain, energy calibration, dynamic range, and base temperature as well as verifying that samarium signals can be observed. For this experiment, the enriched ^{147}Sm source within the gold absorber was exposed to a ^{148}Gd alpha-source with an alpha energy of 3182.69 keV. The Gd source dominated the count rate > 10 CPS for events with energies above 500 keV. The ^{147}Sm decay energy peak can be seen above the alpha-induced background near the expected energy of 2311 keV in the left plot of Figure 5.6.

5.2.3 Results

A more precise energy scale was determined by fitting the ^{148}Gd alpha peak with an exponentially modified Gaussian distribution. The mean was then set to an energy value of 3182.69 keV. No other alpha energy is emitted by ^{148}Gd [111]. The gain of MMCs is approximately linear but is actually quadratic [112, 3, 113]. Given the closeness in proximity of the ^{147}Sm decay to the ^{148}Gd α-peak, only a single point calibration was used. The ^{147}Sm peak was fit with an exponentially modified Gaussian, the peak of which was found to be 2309.5 keV with a fit uncertainty of 0.5 keV. The analyzed energy spectrum with major features labeled can be seen in Figure 5.6 along with the fit to the ^{147}Sm decay peak.

An additional uncertainty of 0.5 keV was added to account for both the uncertainty in the ^{148}Gd peak fit as well as the uncertainty in gain. The latter was assessed by finding the energy of the ^{144}Sm nuclear recoil peak and taking the difference between this value and its kinematically predicted value. A scale correction factor was derived by dividing the distance (in keV) between ^{147}Sm peak

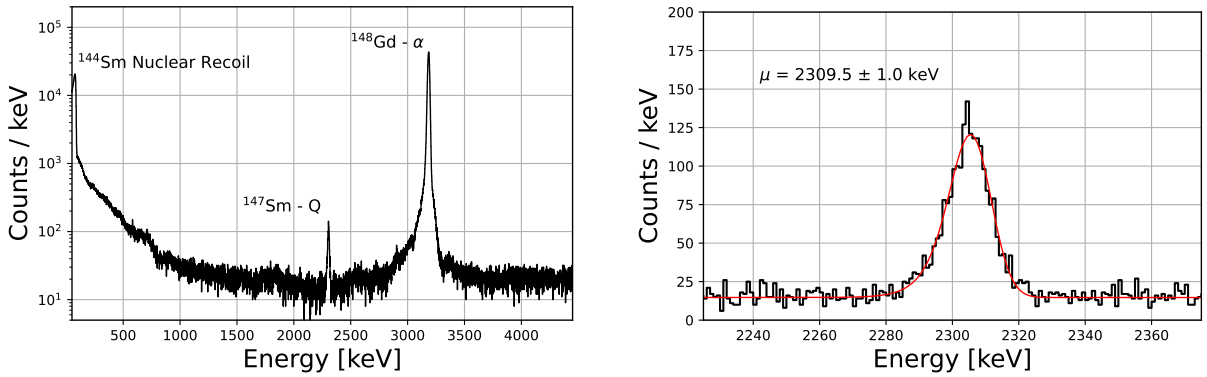

Figure 5.6: *Left*: ^{148}Gd alpha spectrum with ^{147}Sm decay peak seen at 2311 keV. *Right*: Zoom-in on the ^{147}Sm decay peak with exponentially modified Gaussian fit drawn in red.

and the ^{148}Gd peak by the distance between the ^{144}Sm and the ^{148}Gd peak. ^{144}Sm is the daughter of ^{148}Gd [111]. The nuclear recoil observed in the spectrum originates from the case when the alpha particle is emitted in the opposite direction of the detector and the recoiling nucleus hits the detector.

The uncertainty total uncertainty of 1 keV is not meant to be taken as a precise quantification of the uncertainty but as an order of magnitude estimator. Within this margin, the measured energy does agree well with the literature value of 2311.0(5) keV [29]. While neither sufficient analysis nor statistics were acquired for a publication-grade result, the experiment provided confidence in the feasibility of the ^{146}Sm measurement. A decay counting experiment with the ^{148}Gd source was removed to perform a decay counting measurement on the ^{147}Sm sample to measure its half-life and compare it to previous measurements. This experiment and the results are described in the remainder of this chapter.

5.3 ^{147}Sm Decay Counting

5.3.1 Preface

This section describes in detail the analysis methodology developed on ^{147}Sm absolute decay counting experiments, Megaman data runs 52 and 54 between which approximately two weeks of data was acquired.

The purpose is twofold. First, the aim was to develop a data analysis framework on the ^{147}Sm decay counting such that it would be effectively finalized before the ^{146}Sm decay counting to eliminate potential bias injected in the stage of analysis. Specific shaping times, parameter cuts, etc. are of course tailored as necessary but the following framework is the same as the ^{146}Sm

analysis. The second aim is to describe the lower-level stages of analysis here such that Chapter 6 can focus more on statistical analysis.

The topics covered are the following: pulse triggering, pulse shaping and resolution, thermal drift correction, calculation of pulse shape parameters, calculation of live-time / dead-time, and template injection for efficiency estimation. Techniques similar to those described in this section were utilized for previous experiments including the ^{241}Am and ^{148}Gd measurements discussed earlier in this chapter but were not fully developed nor optimized for absolute activity measurements.

5.3.2 Pulse Triggering

Data traces were acquired continuously in segments 50 seconds long at a digitizer sampling rate of 200 kHz. Samples are averaged together in groups of 5 yielding an effective sampling rate of 40 kHz. This averaging is performed to reduce digitizer noise. The signal output from the Magnicon preamplifier [52] is passed through a Stanford Research Systems SR560 amplifier with a 100 kHz low-pass filter applied. The output of the SR560 was fed into the input of the used National Instruments NI PXIe-5172 digitizer [105]. Waveforms were acquired in this digital manner as it greatly simplifies the decay counting analysis. Were a trigger applied, its efficiency, dead time, and data-transfer rate would all have to be studied as a function of the count rate. A triggering algorithm is then applied to identify events for analysis.

A short trapezoidal filter whose shaping time is set to the same time scale as the pulse rise time is used to reduce noise and increase the sensitivity of the trigger algorithm. The trigger logic applied to this fast-shaped signal is a simple threshold crossing requirement that triggers if the following two conditions are met: $S_i \geq T$ and $S_{i-1} < T$. Here, S is the fast trapezoid filtered signal, T is the threshold value, and i is an indexing term. The short filter shaping time was set to 15 samples, 0.375 ms, approximately double the fit to the exponential rise time constant of 8 samples (0.200 ms). The threshold was set to an ADC level corresponding to approximately 5 keV.

As mentioned in Section 3.4, pole-zero correction is not always desired as it reintroduces low-frequency noise. In microcalorimeters, this includes slow temperature fluctuations that affect the sensor's heat capacity and, therefore, its gain. As the DC offset is a measure of the detector's temperature it is less than ideal for this value to change drastically when setting a threshol -crossing trigger. As discussed in Chapter 3, the trapezoidal filter without pole-zero correction is the difference of two moving average filters. Equivalently, the area of the shaping kernel is zero. For either of these reasons, the filter acts as a high-pass filter and eliminates any DC offset. Therefore, this filter is used for triggering. The trapezoid peaking time is set to be approximately the same length as the pulse rise time. A longer filter could improve triggering efficiency to low-energy pulses, but this would come at the sacrifice of timing performance. A trigger-filtered signal (green) is shown

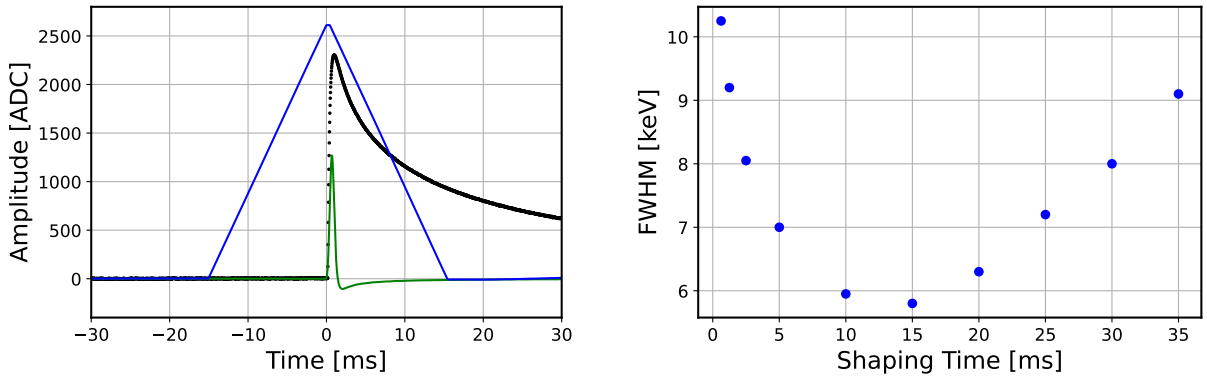

Figure 5.7: *Left*: Typical 60 ms acquisition window containing raw data (black), the short-shaped signal (*green*), and the long-shaped signal (*blue*). The short signal is used for triggering when it passes a set threshold value. The longer-shaped signal is used for energy determination. *Right*: Resolution of the ^{147}Sm decay peak assessed at various shaping times. The noise minimum is found near 15 ms and hence this shaping time is chosen.

along the raw pulse (black) for a typical ^{147}Sm event in the left plot of Figure 5.7. The inclusion of pole-zero correction, which can be thought of as an inverse high-pass filter, can re-introduce a DC component depending on implementation.

5.3.3 Shaping & Resolution

An initial data analysis was performed by running the trigger filter over the data. The ^{147}Sm and ^{241}Am peaks could be identified at the correct energy ratio via the distribution of trigger signal amplitudes. A pulse template was generated by selecting ^{147}Sm waveforms separated in time from any other trigger event by at least 500 ms. The pulses were then averaged with their baselines subtracted. The average pulse shape was found to be well modeled by a single-component rising edge and a three-component exponential decay. The multi-component pole-zero correction described in Section 3.4 was applied with a trapezoidal filter.

Trapezoidal filters of varied peaking times were run over a subset of the data, Run 54-11, to assess the best shaping time. As discussed in Section 3.4, pole-zero correction re-introduces a DC offset component. The shaped baseline was estimated by averaging the shaped signal immediately before and after the trapezoid. Averaging the preceding and subsequent baselines was found to improve resolution when the DC level varied significantly. To reduce complexity, the width of the time windows was set equal to the shaping time. The flat-top time was chosen to be 20 samples long (0.5 ms), based on the pulse rise time. Parameters can be infinitely tuned, but it was decided to be "good enough" to optimize the filter shaping time. The dependence of resolution on shaping time for this measurement is shown in Figure 5.7 in the right plot. A shaping time of 15 ms was

selected for the full analysis.

5.3.4 Event Acquisition Window

Every instance of a threshold crossing by the fast trapezoid results in a "capture" of an acquisition window from which various parameters are extracted. The window is centered on the position at which the fast filter crosses the threshold the width of which is set to four times the shaping time, plus the flat-top time, plus five percent extra for a buffer. By personal preference, I shift the trapezoidally-shaped signal such that the middle of the flat-top is aligned in time with the trigger time-stamp. The amplitude is then taken as an average of the flat top centered around that position. Other calculated parameters include the prior and post-shaped baseline, the raw pulse amplitude, trigger signal amplitude, and pulse shape parameters discussed below. A typical event acquisition window with raw signal, trigger signal (short trapezoidally filtered), and energy (long trapezoidally filtered) signal is shown in Figure 5.7. The window is centered on the point where the trigger signal (green) crosses the threshold, it is from this reference point that the mean time is calculated within the window. The filtered signal baseline is calculated by averaging the first and last 15 ms. While the Y-axis is in units of ADC, the gain is set such that it is approximately equal to energy units of keV.

5.3.5 Live / Dead Time

Accurate parameters cannot be extracted from every pulse acquisition window. The most obvious example is a trigger too close in time to the start or end of the full continuous acquired trace. Two "end-zones" are defined at the beginning and end of each 50 second (10 second) trace, the width of each being slightly longer than the width of the acquisition window. Pile-up is the second main reason by which inaccurate parameters may be extracted from an acquisition window. How pile-up affects the energy spectrum is discussed in greater detail in Chapter 4. Pile-up is treated in a paralyzable manner. In higher count rate experiments, events on the tail of preceding events are downshifted in gain due to the system being at an elevated temperature. This can degrade resolution, the degree to which depends on the heat capacity of the system. In MAGNETO-ν, beta events on alpha decay tails are all cut from analysis for this reason.

Lastly, 50-second (later 10-second) waveforms with large instabilities are eliminated from the analysis and count neither toward the live nor dead time. No events from these waveforms were counted at any stage of the analysis. Such instabilities were caused by rapid temperature fluctuations or instances of SQUID unlocking and re-locking. These periods were identified by a significantly higher than the average number of triggers per file. Figure 5.8 depicts such unlocking and re-locking at two time positions, during Run 54-11. The disturbance times are highlighted in red where excess

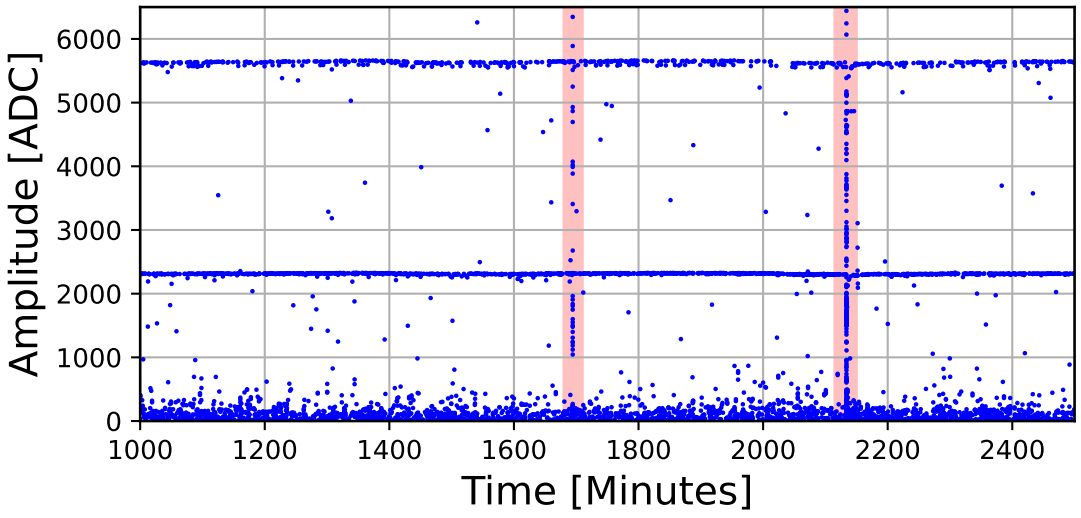

Figure 5.8: Plot of event energy against the timestamp for Run 54-11. The red bands highlight periods of detector instabilities with greatly increased count rates. Waveforms with instabilities such as this are eliminated from further analysis.

counts can be seen. The highlighting is emphasized in width for demonstrative purposes; typically, only 2–3 50 second traces are cut as a result.

The total acquisition time for each sub-run of the measurement is shown in the second column of Table 5.1. The third and fourth columns show the live time in seconds and the fraction of the total time. A very high live-time faction was achieved, above 99% as a result of the use of the trapezoidal filter. The optimal filter would require that no pile-up occurs until after the pulse decay to baseline. From projecting the decay trend of the pulse in Figure 5.7, a dead-time buffer of more than 100 ms per pulse would be required leading to significantly higher dead-time.

5.3.6 Drift Correction

The heat capacity of gold varies with temperature affecting detector gain. Instabilities in the temperature can be caused by imperfections in the PID control, the slow release of heat from various components with low conductivity, changes in the operational parameters of the dilution unit or compressor, global changes in temperature or pressure, or any number of other potential factors. The temperature change is adiabatic and can be visualized by plotting event timestamp against energy as depicted in Figure 5.8 and Figure 5.9. In the former, the individual peaks, ^{147}Sm and ^{241}Am can be identified by eye.

A gain correction factor is derived by fitting to the trend of a selected calibration peak. The ideal peak to select is one with high activity and high energy. Higher activity samples the gain

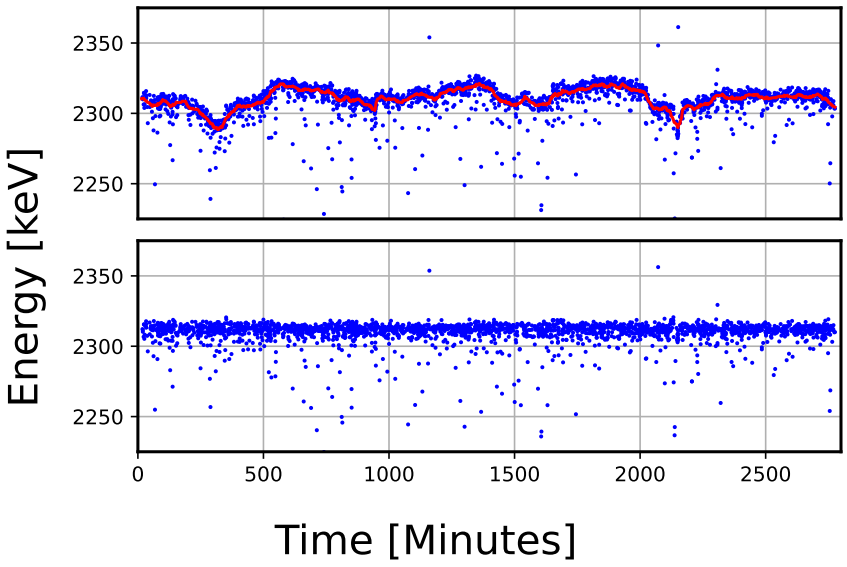

Figure 5.9: Drift correction for Run 54-11. The top plot shows the uncorrected energy vs. timestamp data with the fit trend in red. The lower shows the result of the correction. Small imperfections can be found in the drift correction, for example, at approximately 1700 minutes. This makes modeling the spectrum difficult and hence why integration is preferred overfitting for determination of activity.

distribution finer in time. Projecting the correction downwards in energy has less possibility to introduce systematic effects than projecting upwards in energy. The ^{147}Sm peak was chosen due to its significantly greater activity in comparison to the ^{241}Am.

An initial upper and lower energy bound is placed around the ^{147}Sm decay peak and a median filter is run over all the events within this band. This produces an initial trend line. The initial trend line is then used to create a second set of bounds that follow the trend of the gain drift. Events between this second set of bounds are selected and a Savitzky-Golay filter is run over these events. The Savizky-Golay filter is chosen over a median filter as the latter tends to cause an artificial "spike" in the energy spectrum of the drift-corrected data. Choosing a filter width is not an "exact science"; too short a filter will over-correct while too long a filter will not capture features of the data. A good check is the resolution of different peaks than the one used for the correction as over or under correction will distort features at different energies. The drift correction process is depicted in Figure 5.9

5.3.7 Pulse Shape Parameters & Distribution

The rise-time and fall-time of the detector signals contain physically relevant information. The rise-time is the time scale by which heat flows into the MMC pixel and the fall-time is the time scale

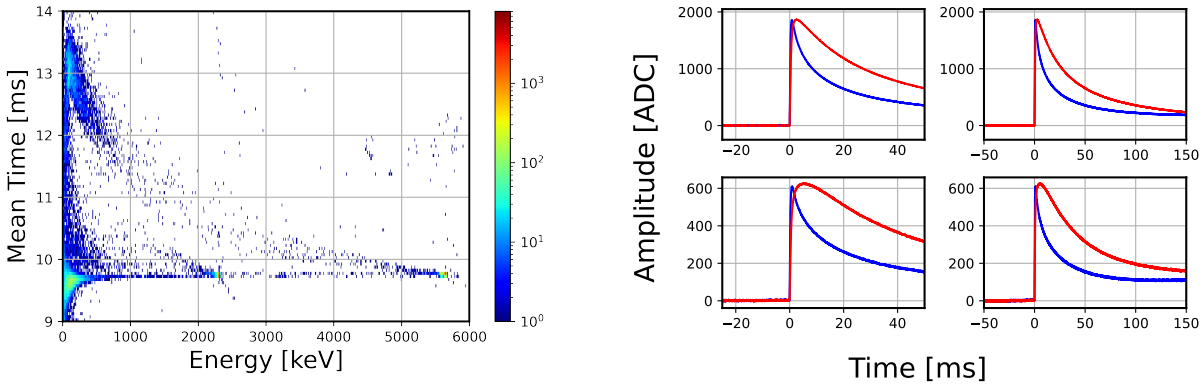

Figure 5.10: *Left*: Mean-time distribution from runs 52 and 54. The primary decay peaks of ^{147}Sm and ^{241}Am can be seen at a mean-time value of 9.8 ms. Slow tails coming off the main peaks can be seen with mean times up to 14 ms. *Right*: 9.8 ms events are shown in blue and slower mean-time events are shown in *red*. The *upper* two plots show the same fast and slow events at different time scales. Similarly, the *bottom* two plots show the same two events at different time scales. Note the upper events have an amplitude of 2000 ADC while the lower events have an amplitude of 600 ADC. The lower amplitude slow event has a longer rise time than the larger amplitude event while the main trend events have the same rise time and pulse shape.

by which heat leaves the pixel. The time scale for heat originating within the absorber and flowing through the pixel is characteristic. From this basis, pulse-shape cuts can be used to eliminate other sources of heat that produce signals within the detector. Additionally, pulse shape cutting can be used to identify and eliminate pile-up and other artifacts such as SQUID resets.

Three sets of parameters were explored and ultimately found to be highly degenerate with one another. The first is the amplitude-weighted "mean-time". This is simply taking a weighted average of the timestamps in the acquisition window weighted by the ADC value. The trigger timestamp is subtracted such that the weighted mean is relative to the trigger position. The parameter is sensitive to rise-time, pile-up, unstable baseline, or any other distortion of the characteristic event time profile within the acquisition window.

The second parameter is the ratio of shaping times, i.e. the ratio of amplitude of the short trapezoidal filter used for triggering to the amplitude of the long trapezoidal filter once the baseline is subtracted. This method has been utilized for noise and pile-up rejection for other detector types such as HPGe dark matter experiments [114].

For the third parameter, the pulse within the acquisition window is fit with a simple four parameter pulse model. The parameters are initial onset position, amplitude, rise time, and decay time. The specific parameter being used is rise time. Even though the rise-time cut was not used, the fit onset position was found to be less sensitive to trigger walk than the threshold crossing of the short trapezoid.

5.3.8 Event Populations

The mean time distribution, shown on the left of Figure 5.10, is prominently defined by a band at 9.8 ms with ^{241}Am and ^{147}Sm peaks at 5.6 and 2.3 MeV respectively. Then a gradually increasing count rate along 9.8 ms towards low energy. At low energies, the band shifts towards earlier mean times due to the trigger walk of low-energy events. This band defines the main event population of decays that occur within the absorber. From the ^{148}Gd calibration experiment, it is known the ^{147}Sm is distributed within the absorber as full decay energy is measured. Energy would escape and be deposited on the surface.

A broad tail can be seen coming off the ^{241}Am peak sweeping to lower energies at slower mean times. These so-called "slow"-events are an anomalous source which are clearly from the ^{241}Am but full energy is not deposited. They are predominantly characterized by a continuously slowing rise time for lower energy pulses. This can be seen on the right of Figure 5.10. The two upper plots are of approx. 1.8 MeV fast (blue) and slow (red) events. The left plot is a more narrow time window than the left. The lower two plots show the same but for approximately 600 keV fast and slow pulses. The 1.8 MeV and 600 keV fast pulses show the same time profile while the 600 keV slow pulse has a slower rise time than the 1.8 MeV slow pulse.

At a given pulse amplitude, the slow event has a greater area. This is indicative of a greater energy than what is measured by the trapezoidal filter. The total energy is proportional to the pulse area, not the pulse height. Energy can be extracted from pulse height if the pulse shape is consistent between events. Since the slow events are clearly not the same pulse shape, their energy is clearly greater than what is calculated by the trapezoidal filter. Pulse area was calculated in a separate analysis, where only events far separated from others were selected. However, the pulse integral calculation of energy only increased the energy of slow events by less than 50%. This can be seen in Figure 5.10 as for a given pulse height the area of the red curve is no more than 50% greater than the area of the blue curve. This leads to the hypothesis of alpha escape and heating of the base plate when this occurs only a fraction of the heat deposited in the base plate flows back to the absorber, the remaining heat flows out of the system. Were the heat trapped within crystals, eventually the heat would be released and the area would sum up to the full decay energy peak. This hypothesis was later confirmed by measurements discussed in Chapter 7. Discussion of efforts to prevent this from occurring during the ^{146}Sm counting experiment.

The complication to the decay counting of ^{147}Sm is that a smaller similar tail can be seen coming off of the ^{147}Sm peak. It appears as though this tail has substantially fewer counts than the ^{241}Am tail despite the ^{147}Sm possessing double the activity of the ^{241}Am. This is consistent with our hypothesis given that the ^{241}Am was added at a later date after some folding and pressing of the gold foil had occurred. However, it cannot be clearly determined which events are from the ^{241}Am and which are from the ^{147}Sm. Estimation of the ^{147}Sm slow tail activity is discussed in the

following section.

5.3.9 Template Injection

Trigger and pulse selection efficiency were determined via a methodology derived from the Monte-Carlo discussed in Chapter 4. The pulse template used for calculating the pole-zero correction shape was injected into the continuously acquired data traces at random timestamps generated by Monte Carlo. The pulse was kept mono-energetic given the gain drift is small as a percentage of pulse amplitude. Figure 5.11 demonstrates the pulse injection process, a time-stamp is selected and an array with the template pulse initiating at the appropriate index is generated. This array is then added to the data array, array values are rounded to the nearest integer, and the data file is saved.

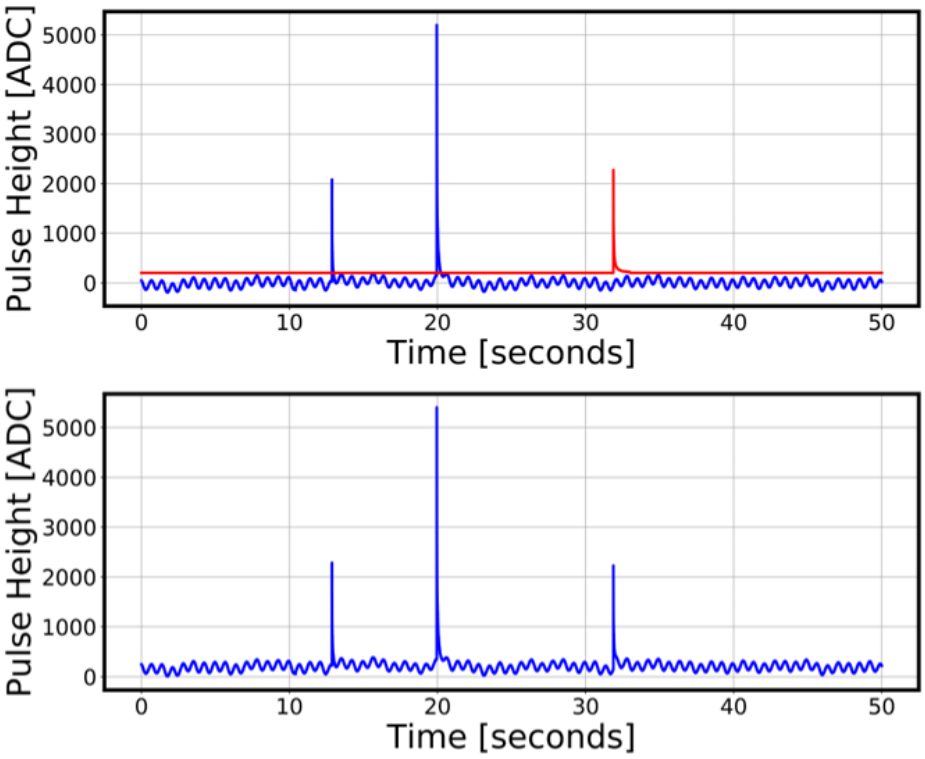

Figure 5.11: *Top*: A 50 second continuous data trace in blue with a template pulse at a randomly selected time-stamp offset above the trace. *Bottom*: Addition of the saved data and simulated pulse. This saved data was re-analyzed with the same pulse processing for efficiency measurements.

The large caveat to this methodology is that the template injection technique only accounts for pulse-shape distortion caused by pile-up or electronic instabilities. It cannot account for changes in pulse shape as a result of source coupling or other thermalization effects.

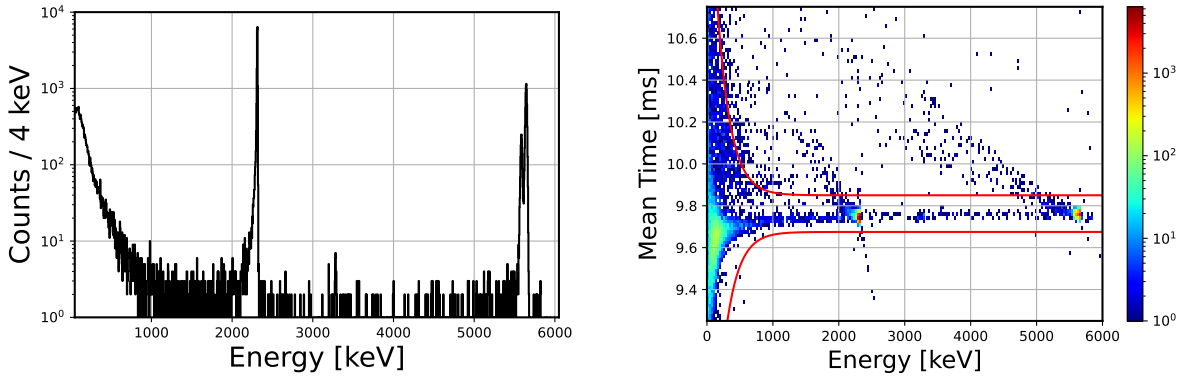

Figure 5.12: *Left*: Measured energy spectrum of live events before application of pulse shape cuts. *Right*: Zoomed in mean-time distribution with event selection cut bounds drawn on top in red.

5.4 ^{147}Sm Decay Counting Results

5.4.1 Data Summary

Approximately two weeks of data were acquired over two cool-down cycles. As mentioned previously, in addition to the observed ^{147}Sm and ^{241}Am decay energy peaks, a slow tail was seen originating from each of the clusters. The tail originating from the ^{241}Am appears significantly stronger than the one from the ^{147}Sm whereas the ^{147}Sm decay peak contains more events than the ^{241}Am peaks as seen on the left plot of Figure 5.12. The ^{241}Am was added later by mistake and the gold foil was heated with a torch indicating that it's possible the ^{241}Am had significant amounts deposited on or near the surface of the gold. However, without precision radiography, it is impossible to determine this for certain.

The first analysis focused solely on the primary event trend. A tight cut was placed around the primary mean-time band at 9.75 ms. The width of this band was determined via the reconstructed mean times of simulation injected events. The cut bands can be seen on the right of Figure 5.12. Both tails can be seen coming off of the decay energy peaks while the tail from the ^{147}Sm seems to "peter-out" at approximately 1000 keV. The events seen at low energies below 500 keV and with mean times in the range of 10–11 ms were observed to be noise events caused by the periodic noise observed in Figure 5.11. Normally these events could be removed with a more precisely placed cut, but this is complicated by the presence of the slow events.

A region of interest (ROI) was defined around the ^{147}Sm decay peak from 2000 to 2400 keV. The total number of counts within this ROI was integrated and tallied at each step of the analysis and is recorded in Table 5.1. The column labeled "Total" is the total counts before any cuts, "Live" are the live events after the dead-time cut described in Section 5.3 was applied, and "Accepted" is the number of counts that pass the pulse-shape cuts, *i.e.*, the events within the red band on the right

Run ID	Exposure [s]	Live-Time [s]	Live [%]	Total [#]	Live [#]	Accepted [#]	BKG [#]	Analysis [#]
52-0	85100	84477.28	99.27	1245	1234	1218	3	1215
54-0	83700	83061.07	99.24	1151	1146	1140	1	1139
54-1	51350	50962.76	99.25	711	708	705	1	704
54-2	97300	96566.56	99.25	1344	1334	1330	3	1327
54-3	54000	53595.71	99.25	731	721	715	0	715
54-4	77900	77413.40	99.38	1050	1040	1034	4	1030
54-5	52000	51659.02	99.34	742	736	733	0	733
54-6	53400	53062.25	99.37	761	759	757	0	757
54-7	176350	175236.12	99.37	2498	2483	2470	8	2462
54-8	71750	71311.94	99.39	1022	1015	1011	1	1010
54-9	65750	65337.50	99.37	905	900	897	3	894
54-10	67300	66876.52	99.37	938	931	928	1	927
54-11	164200	163135.55	99.35	2275	2258	2242	11	2231
54-12	130800	129970.52	99.37	1847	1837	1828	2	1826
All	1230900	1222666.20	99.33	17220	17102	17008	38	16970

Table 5.1: Summary of data run times and counts integrated in the ROI from 2000 to 2400 keV. Background counts are estimated by integrating 1800 to 2000 keV and 2400 to 2600 keV and interpolating within the ROI. These background counts are subtracted from the Accepted counts giving the Analysis counts.

plot of Figure 5.12.

The number of background events within the ROI is estimated by integrating and then averaging the number of counts from 1800–2000 keV and from 2400–2600 keV. This method is equivalent to taking a linear interpolation between the two regions. The number of background estimated events is listed in the column labeled "BKG" of Table 5.1. The final column "Analysis" are the background events subtracted from the "Accepted" events.

5.4.2 Peak Fits

Fits were performed on the ^{147}Sm peak to perform two assessments. The first is within the accepted pulse data to determine whether a "fast" tail extending from the peak to lower energies exists within the acceptance band. These events would not be accounted for in the integration technique. The second set of fits was performed on the total live data as a means of estimating the counts in the slow tail.

The first test, assessed on the accepted events, comprised a comparison of fitting three functional forms. The peak would be modeled in all cases by two exponentially modified Gaussians. The background model varied between an exponential decay, a step extending to low energies, and a

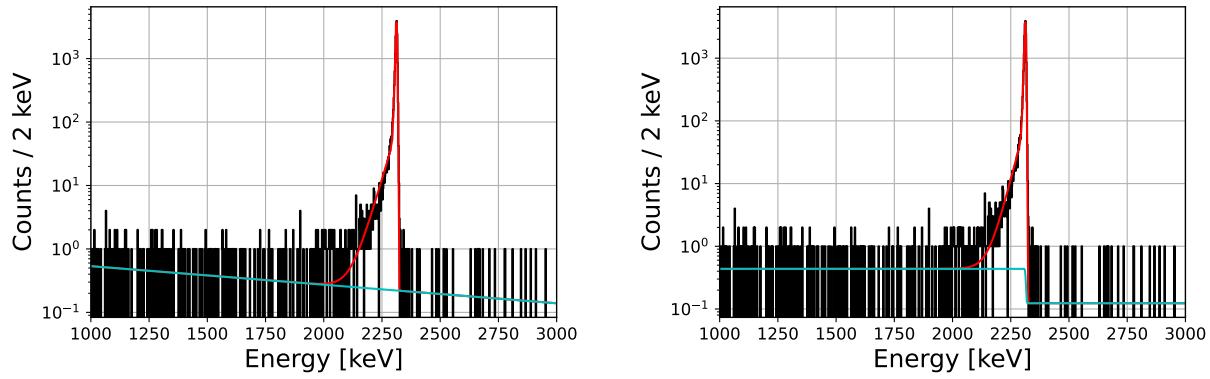

Figure 5.13: *Left*: Fit on ^{147}Sm decay peak with exponential only background model drawn in cyan. *Right*: Fit with step function background model. Both data sets (*black*) are the accepted spectra (events that pass pulse-shape cuts). As discussed in the text, the exponential model is preferred.

combined model. Fits were performed utilizing the Iminuit fitting package [115] in a range from 1000 to 3000 keV.

The best fits from the exponential decay background model and the low energy tail model are shown in Figure 5.13 on the left and right respectively. In each case, the total fit is drawn in red and the exponential / step is drawn in cyan. The preferred fit is evaluated by calculating the log-likelihood. The exponential model was found to be a better fit than the step with an (arbitrary) value of -108053.08 compared to -107781.15 for the step and -107782.54 for the combined model. The number of background counts between 2000 and 2400 keV predicted by the exponential model is 47 ± 10 compared to 38 found by the integration / linear interpolation technique. It would later be decided to use the number of counts determined through linear interpolation and assign 100% uncertainty to account for the possibility that all of these events were ^{147}Sm decays or the case the background was significantly underestimated.

The previous fits were performed on the data which passed the pulse-shape cut. To attempt to estimate the activity contribution from the slow tail, the aforementioned exponentially modified Gaussian (EMG) with exponential background and low energy step fit was performed on the data without the application of pulse-shape cuts. The flat step, projected from the fit peak centroid of 2311 keV down to zero possessed an area of 630.79 counts. One large assumption of this was that the slow events from ^{147}Sm would be approximately flat in energy. This is clearly not the case with the slow tail coming off of the ^{241}Am events; however, assessing the functional shape is difficult in practice. It was originally planned that measurement of the source mass via thermal ionization mass spectrometry (TIMS) would provide insight into the true quantity of slow tail events. The event counts assessed via integration, fitting on the accepted counts that passed pulse shape selection cuts, and fitting on the live counts before the pulse shape cut are summarized in Table 5.2.

Method	EMG-1 [#]	EMG-2 [#]	Peak-Total [#]	Tail [#]	Total [#]
Integration	15770	1192	16962	N/A	16962
Accepted Fit	15550	1345	16895	N/A	16895
Live Fit	15300	1531	16831	631	17462

Table 5.2: Summary of counts assessed in the various means. For the integration row, EMG-1 corresponds to integrating the peak from 2300 to 2400 keV while EMG-2 corresponds to integrating from 2000 to 2300 keV. For the other two rows, EMG-1 and 2 correspond to the count total in each component of the fit.

5.4.3 Activity & Half-Life

The exponentially modified Gaussian functional model is only an approximation of the peak shape. For example, it does not account for slight imperfections in the drift correction or other potential distortions. Therefore the ^{147}Sm activity was determined by adding the counts assessed via integration with the flat tail estimation given by the aforementioned fit, *i.e.*, the final row, the fifth column of Table 5.2. Because of the large uncertainty in the slow counts, 100% error would be assigned to them. This accounts for the possibility of drastic under-counting as well as over-counting. This gives a count total of 17601 ± 761. Dividing this number by the live-time yields an activity of 14.40 ± 0.62 mBq.

The half-life is then assessed by dividing the number of ^{147}Sm atoms within the sample by this activity. The original plan was to dissolve the gold foil and chemically extract the Sm which would then be assessed by LLNL radio-chemists via TIMS. The radio-chemistry group later expressed concerns that processing an enriched ^{147}Sm sample could contaminate their lab "throwing off" the isotopic standard which would complicate both the upcoming ^{146}Sm measurement as well as other dating experiments the group was conducting. It was then decided to send the sample to a collaborator at the Australian National University who would perform the TIMS measurement. Unfortunately, the collaborator was never heard from again. Perhaps he followed the example of a former Australian prime minister.

5.4.4 Discussion on Source Preparation

The experiments with ^{147}Sm can be described as partially a success and partially a failure. Valuable lessons were learned in the context of both analysis and experimental setup. Though no half-life information was extracted from these measurements, they demonstrate the viability of precision decay energy spectroscopy measurements. These measurements also demonstrate the importance of sample preparation and the mitigation of radioactive contaminants for accurate results. For the

^{146}Sm measurement, it was decided that thicker and larger gold foils would be used, and the source would be deposited more slowly and in HCL instead of nitric acid. Given the shorter half-life of ^{146}Sm, less material would be deposited. And great care would be taken in the folding and processing of the gold foil containing the sample.

CHAPTER 6

^{146}Sm Half-Life Measurement

6.1 Introduction

6.1.1 Experimental Outline

The experimental plan devised was to produce an ultra-pure ^{146}Sm source and precisely determine its mass, *i.e.*, the number of atoms, and then perform an absolute decay counting experiment utilizing the techniques described in the preceding chapters. As the half-life of ^{146}Sm is long, it is not enough to be found naturally in any substantial quantities [9]. The source would be produced at the TRIUMF accelerator and chemically purified by radio-chemists at Lawrence Livermore National Laboratory. Mass spectrometry would be performed on the sample, the sample would then undergo cryogenic decay counting, and then would be separated from the gold foil and its mass remeasured.

This work was a collaborative effort. My contributions focused on the decay counting aspect of the experiment. Many others contributed without which this experiment would not have been possible. The accelerator experiment was devised by Aaron Gallant and Nicholas Scielzo (both LLNL). TRIUMF scientists Anna Kwiatkowski and Peter Kunz ran the spallation, ion implantation, and measurement of beam quality. Chemical separations, purification, mass spectrometry, and source deposition were performed by LLNL scientists Quinn Shollenberger, Kelly Kmak, John Despotopulos, and Lars Borg. Sensors were designed and fabricated at the Institute for Basic Science in South Korea and provided by Yong-Hamb Kim and Dong Kwon. LLNL scientist Donnie Lee provided simulation work regarding the energy deposited by contaminant sources. Inwook Kim assisted with the decay counting analysis. Guidance and mentorship were provided by Igor Jovanovic, Stephan Friedrich, Stephen Boyd, and Owen Drury. The overarching project was envisioned, managed, and overseen by Dr. Geon-Bo Kim.

6.1.2 Experimental Challenges

Several challenges complicate cryogenic absolute decay counting as a viable half-life measurement technique. Only nanogram-scale quantities of isotopes such as ^{146}Sm can be reasonably produced [78]. Such quantities of material are most precisely determined using isotope dilution mass spectrometry on an aliquot of the sample dissolved in solution [116]. For a half-life measurement, a continuous record of the number of atoms deposited for counting must be maintained.

To address this, we have developed a technique whereby the ^{146}Sm is dissolved within a solution. A volumetric fraction of the solution was then taken for atomic counting via thermal ionization mass spectrometry (TIMS). The remaining solution was then used for the decay counting. Post counting, the absorber was re-dissolved, and the ^{146}Sm was chemically extracted for a post-assessment via TIMS.

The second challenge is to ensure that every decay from the sample is counted. To accomplish this, the source must be fully encapsulated within and well thermally coupled to the absorber. If portions of the source material are not well thermally coupled, the heat propagation will be nonuniform, resulting in degraded resolution and possibly "missed" decays.

Kneading of the absorber improves coupling to the source which improves detector resolution, examples of this can be found in References [117, 72, 81, 73]. However, over-compressing the sample risks both loss of source material as well as positioning the source too close to the surface of the absorber where alpha-escape can occur. To address this trade-off, two decay counting experiments were performed, one with minimal kneading of the absorber, Experiment 1, and a second counting with more kneading and compression of the absorber (Experiment 2). We address other possible signatures of heat loss through pulse shape analysis. The data is heavily scrutinized for periods of instability or insensitivity.

6.2 ^{146}Sm Sample

6.2.1 Production & Purification

The ^{146}Sm sample was produced at the Isotope Separator and Accelerator facility at the TRIUMF laboratory in Vancouver, Canada [118]. Mass-146 isobars (^{146}Sm, ^{146}Gd, and ^{146}Eu) were produced via spallation of 480-MeV protons on a tantalum foil and then implanted in a 3-μm thick aluminum foil. The foil was stored for ~6 months to allow the ^{146}Gd ($T_{1/2}$=48.27 days) and ^{146}Eu ($T_{1/2}$=4.61 days) to decay to ^{146}Sm. Approximately 10^{14} atoms of ^{146}Sm were estimated to be produced by this procedure. Further discussion of the ion beam and implantation can be found in Ref. [78].

The beam profile assessed by TRIUMF utilizing time-of-flight mass spectrometry can be seen on

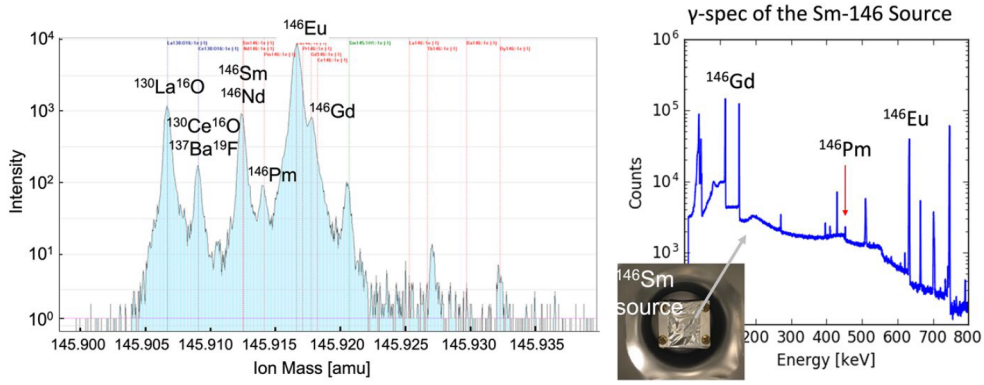

Figure 6.1: *Left*: Time of flight mass spectroscopy assessed by TRIUMF during ion implantation. *Right*: Initial gamma ray spectroscopy assessment performed by counting lab at LLNL.

the left of Figure 6.1. Various contaminants are labeled and their relative concentrations assessed. The sample embedded in the foil was initially assessed via gamma-ray spectroscopy at LLNL to quantify the absolute quantity of contaminants within the sample.

The aluminum foil was dissolved in hydrochloric acid (HCL), and contaminants were removed via a two-step ion-exchange chromatography procedure with AG50W-X8 resin followed by LN resin. The cleaning procedure was repeated, and the source was assessed via gamma-ray spectroscopy at each step. Further details regarding this procedure for extraction and purification of the ^{146}Sm are provided in Ref. [116]. The success of the ion exchange resin chromatography procedure is demonstrated in Table 6.1. The initial assessment was performed after ^{146}Sm built up in the sample. After the chemical procedures, practically no activity from ^{146}Gd, ^{146}Eu, and ^{146}Pm remained.

6.2.2 ^{146}Sm Impurity

^{145}Sm was the only contaminant observed during the DES measurement. Several lower energy peaks were observed, the highest energy of which being at ~120 keV. ^{145}Sm decays via electron capture and populates a 492.6 keV excited state of ^{145m}Pm which decays immediately to the ground state or via a 431.4-keV and then 61.2-keV gamma rays [119]. The resultant decay energy spectrum is the convolution of the ^{145}Sm X rays and Auger electrons with the 61.2-keV gamma ray. The spectrum was identified via comparison to Geant4 simulation [79]. From the simulation, we estimated that ~1–2 $\cdot 10^7$ atoms of ^{145}Sm existed within the sample at the time of measurement, yielding a total activity less than 1 Bq. The activity from the ^{145}Pm daughter is much lower given its longer half-life [120].

Isotope	Initial	After 1st Chemistry	After 2nd Chemistry
	06/10/2021	11/04/2021	11/22/2021
	[Bq]	[Bq]	[Bq]
^{146}Gd	$1.474(3) \cdot 10^{5}$	$< 6 \cdot 10^{-4}$	$< 2 \cdot 10^{-4}$
^{146}Eu	$1.6255(11) \cdot 10^{5}$	$1.108(9) \cdot 10^{2}$	$1.3(5) \cdot 10^{-1}$
^{146}Pm	$2.188(17) \cdot 10^{3}$	$4.92(19) \cdot 10^{0}$	$< 2 \cdot 10^{-4}$
	# of Atoms	# of Atoms	# of Atoms
^{146}Gd	$8.87(17) \cdot 10^{11}$	$< 4 \cdot 10^{3}$	$< 1 \cdot 10^{3}$
^{146}Eu	$9.34(7) \cdot 10^{11}$	$6.36(5) \cdot 10^{7}$	$8(3) \cdot 10^{4}$
^{146}Pm	$5.5(4) \cdot 10^{11}$	$1.24(5) \cdot 10^{9}$	$< 5 \cdot 10^{4}$

Table 6.1: Quantification of ^{146}Gd, ^{146}Eu, and ^{146}Pm isotopes throughout before and after the ion exchange chromatography.

6.2.3 Detector Integration

A 5% aliquot was taken from the HCL solution for an initial precision atom counting via thermal ionization mass spectrometry (TIMS). A second and third aliquot of 3% and 1% aliquot were then taken to verify the results. The measured quantities of ^{146}Sm were consistent between the three TIMS experiments. The quantitative results are discussed at the end of Section 6.4.

The remaining solution was deposited on a small gold foil utilizing a micropipette. The ~3 mm × 6 mm × 25 µm foil was pressed to a glass tray, which was heated using a hot plate. Time was allowed for the acid to evaporate between subsequent drops. The source deposition was performed by LLNL Chemist Dr. Kelly Kmak.

The gold foil was weighed before and after source deposition with no change in mass measured 43 mg. Additionally, no residue or precipitate was visible on the surface of the gold foil. This provided encouragement that the ^{146}Sm would be in good contact with the gold and not within the bulk of a crystal that may have formed on the surface.

The foil was then folded several times over itself to fully encapsulate the ^{146}Sm and ensure good thermal coupling between the source and the foil.

For the first experiment, the gold foil was pressed only by the force of hands and the use of a hammer. The foil was folded within a fiber-free cloth and placed between two aluminum plates for the application of the hammer.

In the second, the foils were rolled with a jeweler's mill to knead them similarly as described in Ref. [117, 73]. Similarly to the first level of sample preparation, the sample was placed between two steel shims to not be in direct contact with the roller itself. Both experimental configurations

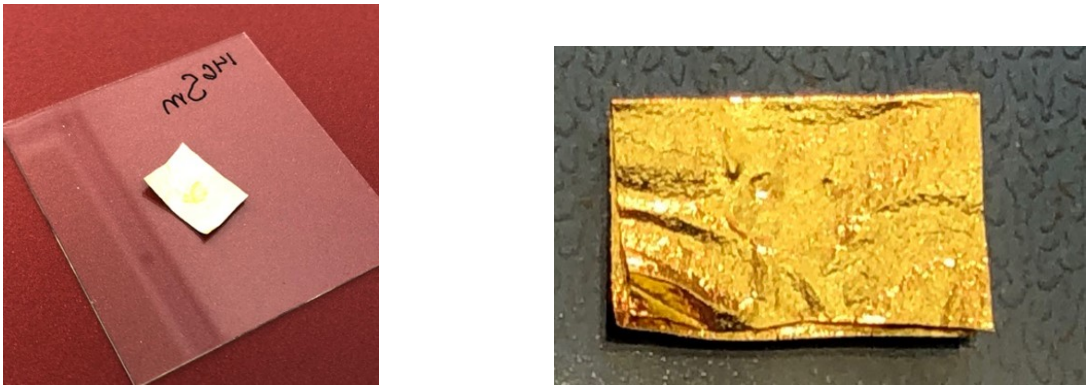

Figure 6.2: *Left*: Gold foil with ^{146}Sm deposited. The discoloration in the center is a reflection off of not yet evaporated acid. After the procedure no, residue was visible on the surface. *Right*: Foil containing ^{146}Sm folded over once and pressed by hand. The foil was folded twice more and struck with a hammer (when placed between shims). The foil after folding and hammering is seen on the *top left* of Figure 6.3.

of the absorber can be seen in Figure 6.3.

Comparison of the two decay counting experiments allows for assessment of the source integration within the absorber. Were the count rate in Experiment 2 greater than in Experiment 1, it would suggest the source is not well integrated within the gold. Were the count rate to decrease, low-energy tailing or other signs of partial energy deposition would be observed, and it would suggest the source had been pressed too close to the surface of the gold allowing for alpha escape. The rolled and unrolled foils containing ^{146}Sm corresponding to each experiment are shown on the left of Figure 6.3.

6.2.4 Experimental Runs

Data was acquired over a two-month period divided into pre-rolled and post-rolled experiments labeled Experiment 1 (Run-64) and Experiment 2 (Run-65), with several sub-runs each. The MMC utilized for this experiment was designed and fabricated at the Institute for Basic Sciences (IBS) in South Korea [121]. The sensor utilized contained two paramagnet pixels, one of which is thermally connected to the gold foil absorber. The difference between the two pixels is taken to eliminate the effect of temperature fluctuations of the heat sink. A 100 mA current was applied to the MMC magnetization loop. A large bias was selected to help amplify sensitivity given the large heat capacity of the gold foil used.

A two-stage SQUID amplification scheme was utilized with a Magnicon XS SQUID [52] hooked directly to the MMC device as shown in Figure 6.3. The feedback line of the input SQUID was coupled to the input coil of a second Magnicon SQUID mounted to the 4 K plate [52]. The

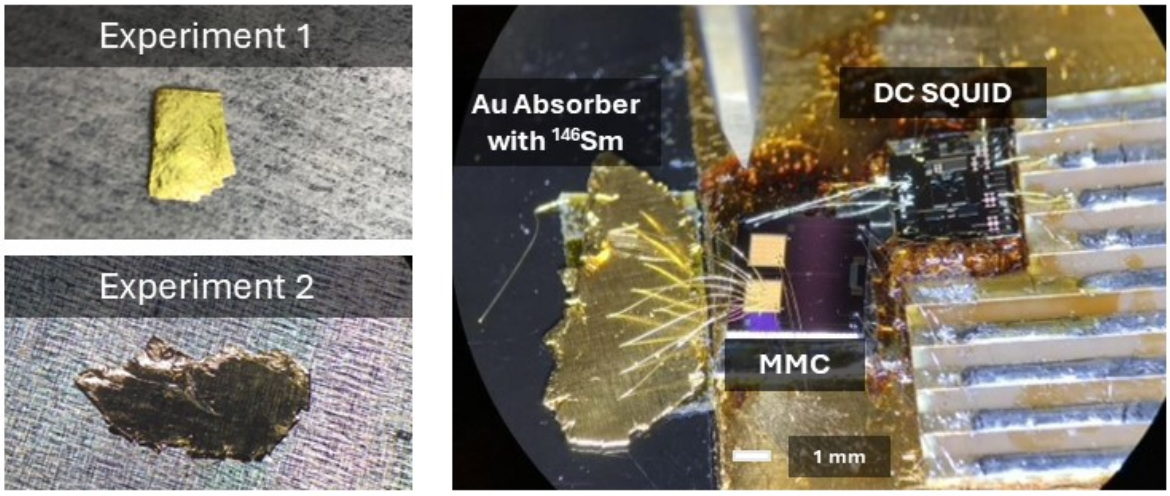

Figure 6.3: *Left*: ^{146}Sm sample contained in the Au absorber as configured for Experiment-1 with minimal source preparation and for Experiment-2 after being pressed with the rolling mill. *Right*: The detector assembly as configured for Experiment-2 viewed through a microscope objective.

assembly mounted to the mixing chamber was cooled to ~7 mK using the BlueFors LD dilution refrigerator [92].

6.3 Data Analysis

6.3.1 Data Acquisition

Detector output waveforms were collected in continuously acquired 10 second traces utilizing a National Instruments NI PXIe-5172 digitizer [105]. Such a 10 second digitized trace is depicted in Figure 6.4 (*Top*). The digitizer sampled at an initial rate of 200 kHz but samples were averaged together in groupings of 5 yielding an effective sampling rate of 40 kHz. This method of averaging is performed by the group at LLNL when using the NI system to help eliminate ADC noise from the digitizer itself which is high-frequency in nature.

A 10 millisecond window containing a randomly selected ^{146}Sm event is shown in the (*Bottom*) of Figure 6.4 in *black* with the calculated triggering and energy trapezoids in *green* and *blue* respectively [55].

The trapezoidal filter was chosen over the more commonly implemented (for cryogenic detectors) optimal filter due to its superior time resolution at the expense of energy resolution [6, 66, 68]. Sufficiently good resolutions were achieved with trapezoid peaking times of 20 ms and 2.5 ms,

whereas the optimal filter width would be several hundred ms, on the order of the pulse decay time. The trapezoidal filter response was extensively studied with particular emphasis on pile-up and spectral reconstruction [6].

Each instance of the fast-filtered signal crossing the threshold triggers the capture of an analysis window as depicted in Figure 6.4. The pulse amplitude was then determined by taking an average over the slow-trapezoid flat-top. Other physically meaningful parameters including baseline, time-stamp, rise time, and amplitude-weighted mean time were calculated. Periods of SQUID and detector instability were found to be characterized by abnormally high trigger rates and events with nonphysical energies. These periods were flagged and discarded from the analysis.

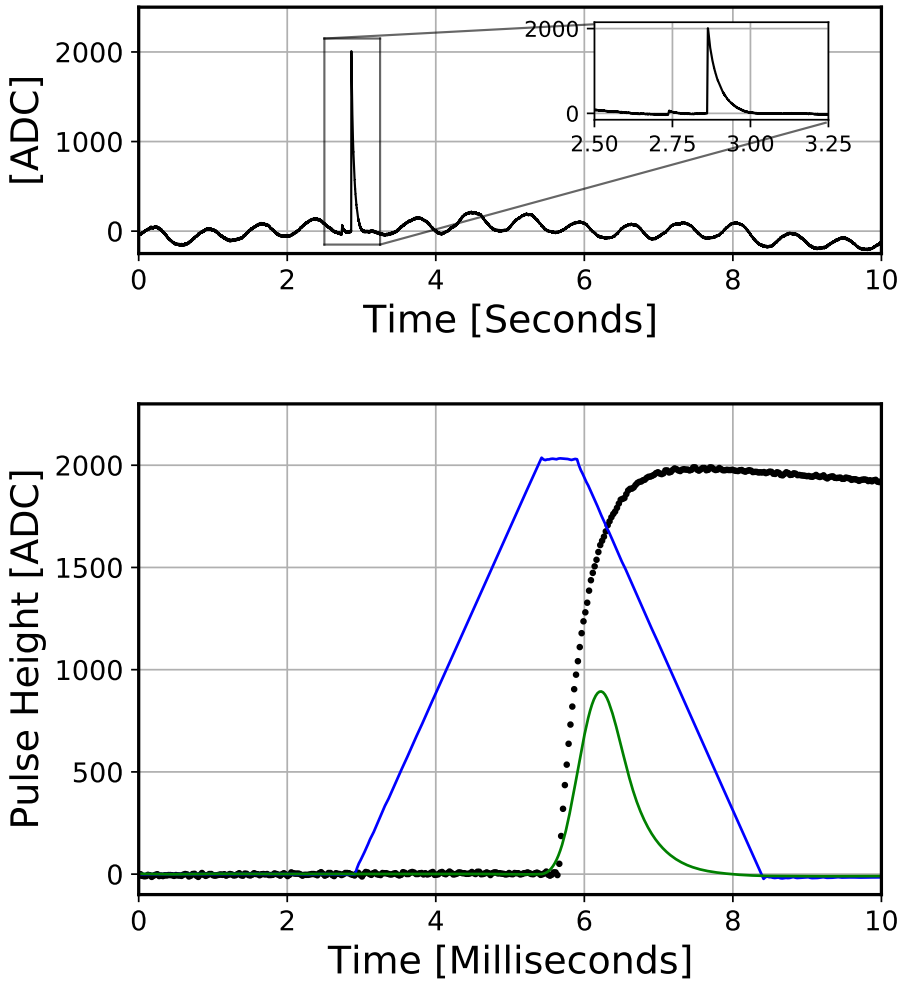

Figure 6.4: *Top*: Typical 10-second waveform taken with continuous data acquisition containing ^{146}Sm decay and lower energy event. *Bottom*: Analysis window of a raw trace (*black*), fast filtered trigger signal (*green*), and slow filtered signal (*blue*)

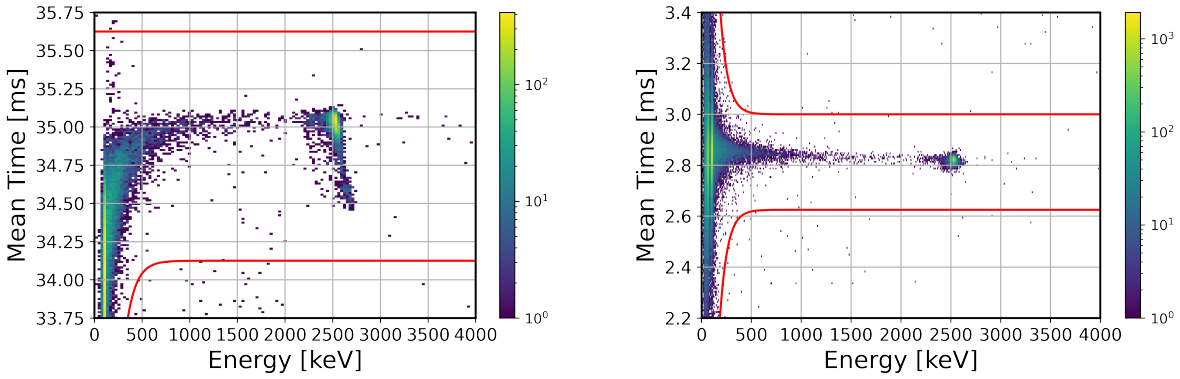

Figure 6.5: Mean time plots for Experiment 1, Run-64, (*left*) and Experiment 2, Run-65, (*right*) with acceptance curves drawn in *red*. Features are discussed in the text.

6.3.2 Dead-Time

Events are flagged as "dead" for one of two reasons: either the trigger is too close to the "edge" of each 10-second acquisition, or is within a buffer period close in time to the preceding trigger. This buffer period is set to give adequate time for the trapezoid filter to return to baseline and then for a new filtered baseline to be calculated [6]. These buffer periods are added in a paralyzable manner described in Ref. [55] and are summed with the edge buffers to calculate the total dead time. Flagged "dead" events are accounted for in the "total" event count column of Table 6.2 but are cut from the "live" event count column.

The total experimental live-time fraction was 97.6% broken down as 96.3 % and 98.3 % for Experiments 1 and 2, respectively. The larger dead time in Experiment 1 is a result of requiring longer shaping times due to longer pulse rise times and greater high-frequency noise compared to Experiment 2. This dead-time analysis cannot account for indistinguishable pile-up where the rising edges of two pulses overlap. However, such pile-up has been well characterized, and a correction factor was determined as a function of pulse rise time and filter length [6].

6.3.3 Event Selection

Radiation decays within the absorber bulk are differentiated from those of external origin by a characteristic rise time. Events not originating in the absorber follow different time profiles and are cut. The most commonly observed "anomalous" events were pulses characterized by either fast rising and falling edges or being negative polarity pulses. These were identified as radiation interactions with the pixel attached to the Au foil and the unattached pixel, respectively.

The amplitude-weighted mean time was chosen as the cut parameter as it was found to be sensitive to both the pulse rise and fall times while also being more sensitive to pulse polarity and

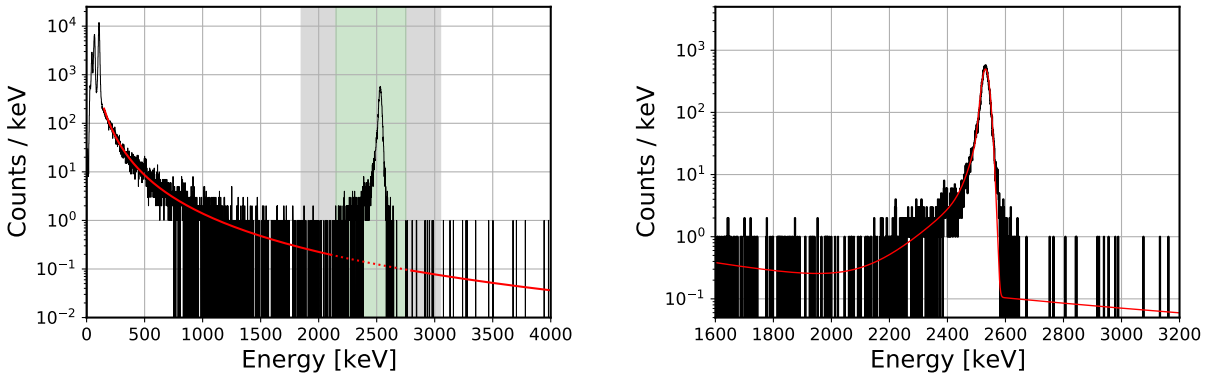

Figure 6.6: *Left*: Measured energy spectrum with power-law background fit (*red*), count integration ROI (shaded *green*) and linear interpolation regions (shaded *grey*). *Right*: wo-component exponentially modified Gaussian fit to ^{146}Sm peak with power-law background model.

pile-up of small signals, the latter not always being evident in the rise time.

The mean time distributions for Experiments 1 and 2 are depicted in Figure 6.5 with acceptance curves. The Experiment 1 distribution is broader and contains a tail of faster events caused by the relatively poor thermal coupling of the hand-pressed absorber. We hypothesize that population of fast events are decays which occur in a region of the absorber physically closer to the wire bond connection to the MMC. When the foil was further compressed for Experiment 2, the pulse rise times narrowed and shifted earlier. The time offset between Experiment 1 and Experiment 2 was due to faster rise times and shorter shaping times of the latter.

6.3.4 Peak Counts & Background Estimation

An energy range of interest (ROI) was defined around the peak from 2150 keV to 2750 keV, where notable excess above the background was observed, depicted as the green-shaded region of Figure 6.6.

At each stage of the analysis, the counts within the ROI are integrated. Table 6.2 summarizes the number of counts at three important analysis stages: the total number of counts without any cuts ("Total"), the number of counts after the dead-time cut is applied ("Live"), and the number of counts after both dead-time and pulse-shape cuts are applied ("Accepted"). Only a small fraction of events are cut.

The measured background is well-described by a falling power law distribution, which appropriately models the amplitude distribution in many physical systems [122]. The spectrum in the 200–2000 keV region appended to the 2800–4000 keV region was fit with a power law function; an excellent spectral match is observed in the *left* plot of Figure 6.6.

The higher energy background counts are estimated via two methodologies. The first method

Run ID	Exposure [s]	Live-Time [s]	Live [%]	Total [#]	Live [#]	Accepted [#]	Background [#]	Analysis [#]
64-1	60080	57811.5	96.2	1118	1076	1064	3.75	1062.05
64-2	324130	312198.6	96.3	6605	6428	6386	19.5	6377.34
64-3	80800	77869.7	96.4	1765	1710	1694	6.0	1690.87
65-1	308430	303152.8	98.3	6197	6095	6057	12.75	6054.54
65-2	11200	10924.6	97.5	192	188	187	0.0	187.32
65-3	239600	235439.7	98.3	4887	4804	4789	8.25	4788.89
65-4	283700	278801.7	98.3	5733	5629	5614	15.75	5607.78
All	1307940	1276198.6	97.6	26497	25930	25791	66.0	25768.81

Table 6.2: Summary of experimental data. The count values refer to the number of events within the analysis ROI at corresponding stages of the analysis. The final analysis column is the total number of counts after background subtraction and efficiency correction.

takes the number of counts in the peak ROI of the power-law background fit. For the second method, the counts per keV are calculated in the energy range just above and below the peak ROI. The background estimation regions can be seen as the gray-shaded areas to the left and right of the green-shaded ROI in the *left* plot of Figure 6.6. From this, the number of counts per keV in the peak integration region is estimated via linear interpolation, from which a total number of background events in the ROI was calculated.

For consistency with the peak count determination, the method of integration and linear interpolation is used for the background measurement, while the fit value is used for consistency check. The uncertainty contribution from the background estimation is the total number of counts subtracted from the background. This accounts for the possibility that all events within the energy ROI originate from ^{146}Sm decays as well as the possibility of vast underestimation of the background.

6.3.5 Spectral Analysis

Various fits were performed to the ^{146}Sm peak to assess the possibility of an unaccounted low-energy "tail" with the same pulse shape as the peak events. The decay energy peak was fit with a Gaussian and two exponentially modified Gaussian peaks with shared mean and resolution parameters. Three fits were performed with varied additional spectral features: a step function extending from the peak mean to low energies, a power-law background, and both a step function as well as a power-law background. The iminuit [115] fitting routine was used in the energy range of 1500–3000 keV. Activity contributions for the background and tail are reported in Table 6.3.

In the case of the low-energy tail, the fit was projected down to 0 keV and yielded a contributing activity of 0.169 mBq. This value is a large overestimation since it considers background events as

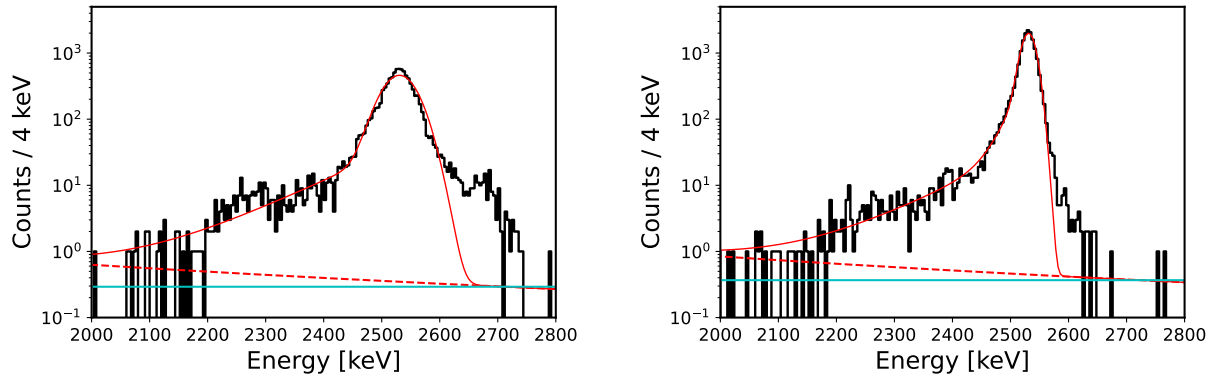

Figure 6.7: ^{146}Sm decay energy peaks for both Run-64 and Run-65, *left* and *right* respectively. The linear interpolation background estimation is plotted in blue while the power law background is shown as the dashed red line. The difference in the two different background estimation methods is smaller than the background estimated via linear interpolation and is therefore accounted for within the background uncertainty.

part of the tail fit.

In the fit where both a low-energy tail and a decaying background model were included, the fitting algorithm set the tail amplitude to zero and picked the same power-law parameters for the power-law-only fit. Additionally, the greater log-likelihood prefers the case with no tail component as seen in Table 6.3.

The fit estimate of the number of background events under the decay energy peak is slightly higher than that calculated by linear interpolation. This is likely due to the exponentially modified Gaussian fits being an imperfect functional form for the true peak shape. It can be concluded from the spectral analysis that a negligible number of ^{146}Sm events lie below 2150 keV and, therefore, integration of the peak is an accurate measure of the number of decay events.

The peak fit with power-law decaying background is shown in the *right* of Figure 6.6. Each component of the fit is shown below in Figure 6.8. The primary Gaussian component is printed in *green*, with the two exponentially modified Gaussians in *magenta* and *cyan*. The power-law background is in *orange* and the summed fit is in *red*. The summed fit in Figure 6.8 is the same as depicted in Figure 6.6.

6.4 Monte-Carlo & Uncertainty Terms

6.4.1 Monte-Carlo Template Injection

The major contributions to the activity uncertainty include statistics, background estimation, trigger efficiency, pulse-selection efficiency, dead time, and spectral analysis. To assess these uncertainties,

Fit Func.	Fit (-) Log Like.	Tail Activity	Fit BKG.	Lin. Interp. BKG
	[Arb.]	[mBq]	[mBq]	[mBq]
Tail	-72976.154	0.169	0.064	0.052
Decay	-73004.394	0.0	0.086	0.052
Decay & Tail	-73004.394	7.5E-5	0.086	0.052

Table 6.3: Activity estimation of possible tail contribution via fits with and without a flat low energy tail and with and without background model.

a simulated dataset was prepared by adding pulses to the true data trace utilizing the Monte-Carlo methodology developed in Ref. [6]. A template was generated by averaging events within the energy ROI and the pulse-shape acceptance band. Template pulses were added to the continuously acquired traces at random timestamps. To ensure the data with simulated events is representative of the true dataset, pulses were injected at a significantly lower count rate than the measured ^{146}Sm count rate. To generate sufficient statistics, the simulation was re-run with different random seed initialization of the Monte-Carlo generator.

6.4.2 Triggering & Pulse-Selection Uncertainties

The trigger efficiency was determined as the ratio of triggered simulated events and the known number of injected events. The pulse selection efficiency was similarly determined as the fraction of simulated events that passed the pulse-shape cuts and were found within the analysis ROI after accounting for both the trigger efficiency and dead-time cuts. The pulse-selection efficiency, combining both trigger and cut efficiencies was found to be 99.83%. The injected simulated events that did not trigger or did not pass the pulse-shape cuts were caused by indistinguishable pile-ups with another radiation-induced event or a period of SQUID instability. The 0.2% correction factor was applied to the accepted counts after subtracting for background events. The uncertainty was taken as 0.1%, half of the correction factor.

One caveat of this analysis is that the simulation did not capture the observed distribution of rise times seen in the data. The spread in the rise-time distribution is caused by both noise as well as positional dependence of the source within the absorber. The simulated events only showed the rise-time distribution caused by noise. Large acceptance bands in the mean-time space account for the distribution of rise times caused by position dependence within the absorber. To conservatively estimate the possibility of ^{146}Sm events with a different pulse shape, all events within the energy ROI but outside of the pulse-shape cut were summed and added to the total pulse-selection uncertainty.

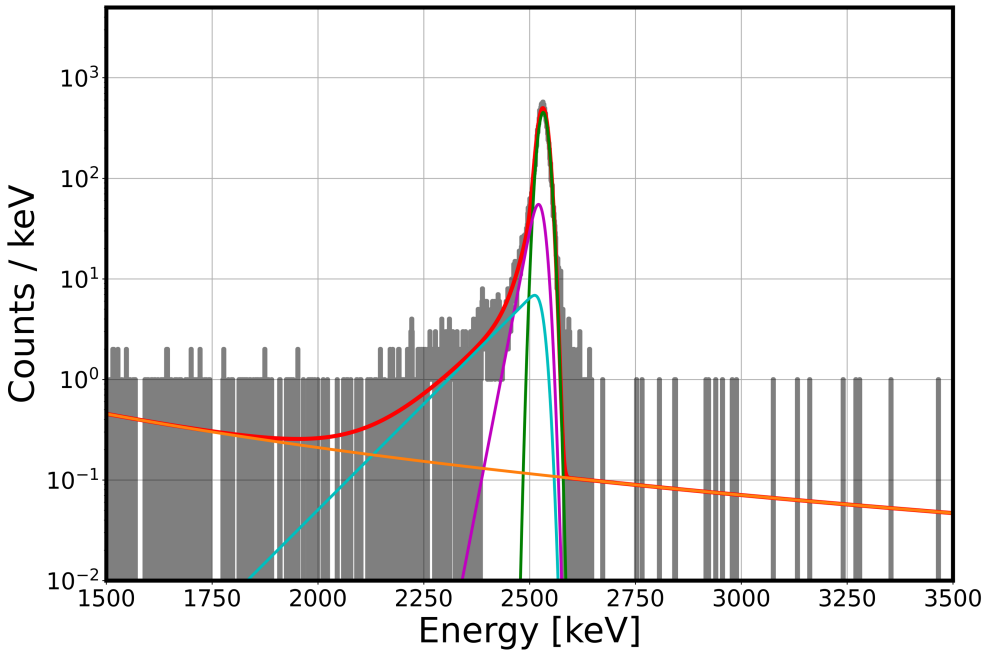

Figure 6.8: Fit to the Run-65 ^{146}Sm peak with spectral components plotted in different colors.

6.4.3 Live-Time Uncertainty

The Monte-Carlo simulation inherently has a higher count rate than the true data as it includes all the events of the analysis data sets as well as the injected simulation events. The dead time in the Monte Carlo analysis is assessed in two ways: the same as in the primary ^{146}Sm analysis and by taking the ratio of the number of live to total simulated events. The difference between these two methods of calculating dead time was 0.2 %. This value is taken as the uncertainty of the dead time.

6.4.4 Activity & Total Uncertainty

The contributions to the uncertainty are listed as an uncertainty budget in Table 6.4. The total uncertainty, from addition in quadrature, is less than 1% with statistical uncertainty being the term. The activity of the ^{146}Sm sample is calculated by taking the total number of accepted counts in the integrated ROI and subtracting the number of calculated background events (columns 7 and 8 of Table 6.2 respectively) and then applying the efficiency correction. This value is then divided by the live time (column 3 of Table 6.2). The activities and uncertainties from each sub-run are listed in Table 6.5. The total activity is calculated by an inverse error weighted average of all the sub-runs and is reported as 20.161 ± 0.138 mBq.

Run	Statistical Uncertainty [%]	Background Uncertainty [%]	Event-Selection Uncertainty [%]	Dead-Time Uncertainty [%]	Total Uncertainty [%]
64-1	3.07	0.36	1.13	0.20	3.29
64-2	1.25	0.30	0.66	0.20	1.46
64-3	2.43	0.35	0.94	0.20	2.64
65-1	1.28	0.21	0.63	0.20	1.46
65-2	7.31	0.00	0.54	0.20	7.34
65-3	1.44	0.18	0.31	0.20	1.50
All	0.62	0.115	0.171	0.20	0.68

Table 6.4: Uncertainty budget breakdown in percent from major sources. The *total uncertainty* is calculated by adding each contribution in quadrature. The final activity and uncertainty are calculated by an error-weighted average from each of the runs.

$$\textbf{Activity} = \frac{1}{0.9983}\frac{(\text{Acpt.} - \text{Bkg.})}{\text{Live-Time}} \tag{6.1}$$

The activities determined from Experiment 1 and 2 are 20.327 ± 0.242 mBq and 20.083 ± 0.167 mBq, respectively. The difference divided by the quadrature summed uncertainty is $\delta/\sigma = 0.244/0.294 = 0.830$, less than one standard deviation. This good consistency supports the hypothesis of good thermal integration of the sample and absorber, indicating that signal loss due to poor thermal integration is negligible.

$$\frac{\delta}{\sigma} = \frac{|20.327 - 20.083|}{\sqrt{0.242^2 + 0.167^2}} = 0.830 \tag{6.2}$$

The activities determined from Experiment 1 and 2 are 20.327 ± 0.242 mBq and 20.083 ± 0.167 mBq, respectively. The difference divided by the quadrature summed uncertainty, defined in Equation (6.2) is less than one standard deviation with a value of $\delta/\sigma = 0.830$. This good consistency supports the hypothesis of good thermal integration of the sample and absorber, indicating that signal loss due to poor thermal integration is negligible.

6.5 Statistical Analysis

6.5.1 Poisson & Event Spacing Analysis

A further statistical analysis of the timing distribution of events was performed. The accepted event multiplicity per 10-second acquired waveform is shown on the left of Figure 6.9. The event

	64-1	64-2	64-3	65-1	65-2	65-3	65-4	All
Activity	18.371	20.427	21.714	19.972	17.147	20.340	20.114	20.161
Uncertainty	0.605	0.298	0.573	0.291	1.258	0.305	0.282	0.138

Table 6.5: Activities for each experiment are calculated by dividing the *Analysis* column by the *Live-Time* column, both from Table 6.2. The *total uncertainty* is calculated by adding each contribution in quadrature from Table 6.4. The final activity and uncertainty are calculated by an error-weighted average from each of the runs. All values are expressed in mBq

multiplicity was found to follow a Poisson Distribution with extreme precision, as expected by counting statistics for a constant event rate. The extracted count rate from the Poisson fit was found to be 20.125 ± 0.124 mBq as compared to 20.161 ± 0.138 mBq from the spectral analysis. The difference between the Poisson analysis and the integration activity analysis, 0.17%, is smaller than the systematic uncertainty 0.29%. The difference is therefore well constrained within the methodological uncertainty.

The distribution of the time difference between consecutive ^{146}Sm decays is expected to be exponential. The time distribution of all events within the ROI that passed event cuts was fit with an exponential model depicted on the right of Figure 6.9. If the detector were periodically malfunctioning or insensitive, a population with large time differences beyond the exponential tail would be expected. Four high time-difference events are observed that could plausibly be described either by the exponential model or be considered outliers. However, if we consider these four events outliers caused by detector insensitivity, they limit the total summed duration of these periods by ~2000 seconds or 0.15% of the experiment duration. This value is less than the 0.2% uncertainty assigned to dead time and, therefore, the possibility of insensitivity at this scale is accounted for.

The activity extracted from the exponential fit time constant is compared to the activity from peak integration and the Poisson distribution of events and compared in Table 6.6. The time difference method contains a large systematic uncertainty of 0.25 mBq which does not affect the Poisson nor integration activity calculations. The difference between the time difference activity and the Poisson and integration activity is well within the methodological uncertainty.

6.5.2 Event Inspection

Multiple levels of data consistency checks were performed to ensure the accuracy of results and to demonstrate the absence of any unaccounted large systematic uncertainty. Every event that passed event selection cuts within the ROI was visually inspected. Every cut event with energy greater than 500 keV was similarly inspected.

The visualized inspected pulses from Experiments 1–2 and 2–4 are plotted in Figure 6.10 *upper*

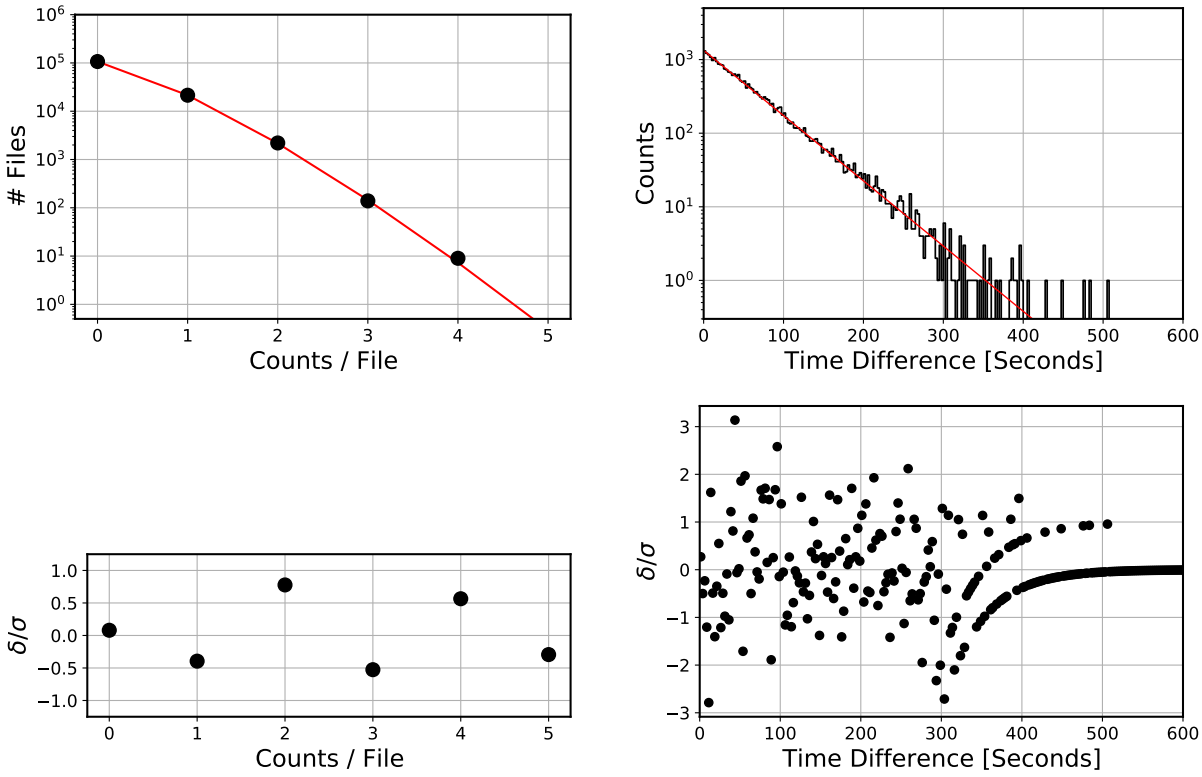

Figure 6.9: *Left*: The distribution of the number of ROI events within each 10 second data file from all data runs in Run 64 and 65. The red curve is the best fit Poisson distribution with two free parameters, rate and total number of counts. The residual of the fit is shown below. *Right*: Distribution of time space of all events within the ROI. This is calculated as the time to the preceding event. The histogram is from all data runs in Run 64 and 65 with the best fit in red and fit residual below.

Experiment	Integration [mBq]	Poisson [mBq]	Time-Difference [mBq]
Exp. 1-1	18.4 (6)	18.4 (5)	18.5 (6)
Exp. 1-2	20.4 (3)	20.2 (2)	20.1 (2)
Exp. 1-3	21.7 (6)	21.1 (5)	21.1 (5)
Exp. 2-1	20.0 (3)	20.0 (3)	19.0 (2)
Exp. 2-2	17.1 (1.3)	16.7 (1.3)	17.5 (1.6)
Exp. 2-3	20.3 (3)	20.3 (3)	20.3 (3)
Exp. 2-4	20.1 (3)	20.1 (3)	20.1 (3)
Combined	20.161 (138)	20.125 (124)	20.092 (278)

Table 6.6: Activities extracted from the Poisson and time-difference distributions compared to integrated activities. The combined value for the integration is computed by an inverse error weighted average while the combined values for the Poisson and time-difference methods are extracted from the fits to the entire Experiment-1 and 2 data sets, *i.e.*, the *red* fit lines in Figure 6.9.

and *lower* respectively. These comprise approximately half the experimental data. The inspection concludes no anomalous population of events is present in the counting analysis.

As a demonstration, the saved windows for each accepted pulse from Experiments 1–2 and Experiments 2–4 are plotted in Figure 6.10 *upper* and *lower* respectively. These 12,000 displayed pulses comprise 46.5 % of the total number of accepted events. This inspection, along with inspection of the other data runs concluded no anomalous population of events is present in the counting analysis.

The longer average rise-time and greater high-frequency noise in the pre-rolled experiment can be observed by comparison of the two plots in Figure 6.10. The small population of fast-rise events in the *upper* plot of Figure 6.10 corresponds to the short tail observed in the *upper* mean time plot of Figure 6.5. By rolling the sample, better thermal conduction within the absorber was achieved which both eliminated the fast-rise population and increased the average rise time. Similarly, 10-ms snapshots of all events rejected by the dead time and by pulse-selection cuts were visually inspected. No anomalous nor unexpected number of radiation-induced pulses were observed.

6.5.3 ^{145}Sm Event Rate

The previously discussed time-difference analysis rules out periods of detector insensitivity longer than ~10 minutes. The presence of ^{145}Sm with approximately twenty times the activity of ^{146}Sm allows for the identification of detector-insensitive periods on shorter time scales. The distribution of ^{145}Sm decays with energy depositions within the highest energy peak was plotted and no periods

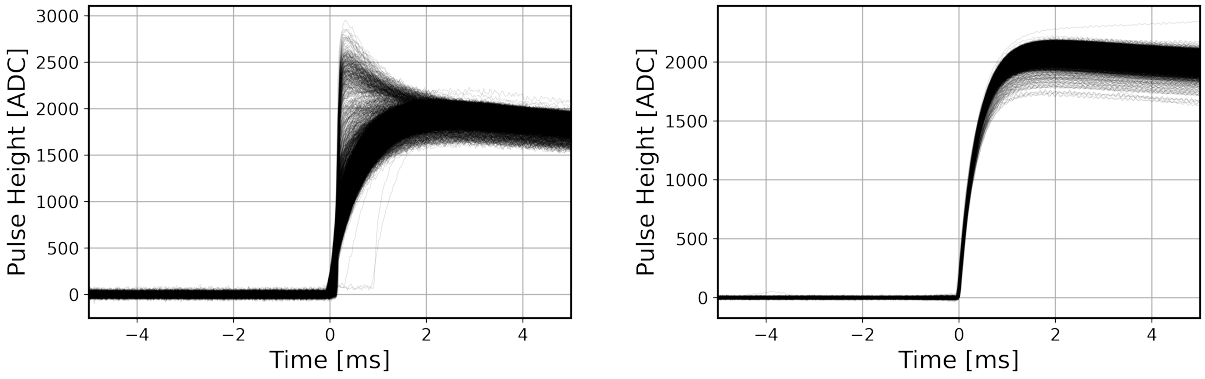

Figure 6.10: *Left*: All accepted pulses from Experiments 1-2. *Right*: All accepted pulses from Experiments 2-4. The total number of pulses shown in 12000 is approximately 46% of the total number of ^{146}Sm events.

with abnormally low rates were observed. This increases the confidence that the periods of detector insensitivity were entirely accounted for. The activities for the highest energy peak were calculated for each experimental run with half-life corrections applied and plotted in the *top* plot of Figure 6.11. The consistency of the ^{145}Sm activity with the average trend suggests that the fluctuations of the ^{146}Sm mean activity are statistical in nature and are not caused by some underlying systematic detector or analysis effect.

6.5.4 Independent Analyzers

The ^{146}Sm half-life affects the Sm-Nd chronometer's accuracy, which can impact the astrophysical interpretation of early solar-system formation [23, 25, 26, 27]. To ensure no systematic bias affected these results, several layers of blinding were implemented. First, all activity numbers were blinded from the chemistry and mass spectrometry collaborators. Secondly, three individuals performed independent activity analysis without communication or shared insight. Activity numbers were not unblinded from the three analyzers until each had completed their independent analysis. Similarly, activity and sample mass results were not shared between the decay counting team and the mass spectroscopy team until the completion of the experimental campaign. Figure 6.11 shows the activity of each data run performed by independent analyzers. Note: data runs 1–2, 2–1, 2–3, and 2–4 comprise ~90% of the experimental live time.

The spread of values around the mean and the χ^2 was assessed for Analyzer 1's results. The value is calculated as the difference between the mean activity value and each individual activity squared divided by the uncertainty of each measurement squared and is 4.84 with 6 degrees of freedom. This is near the 60^{th} percentile, therefore the spread of the activities measured is viewed as not statistically significant. The χ^2-per degree of freedom is equal to 0.81.

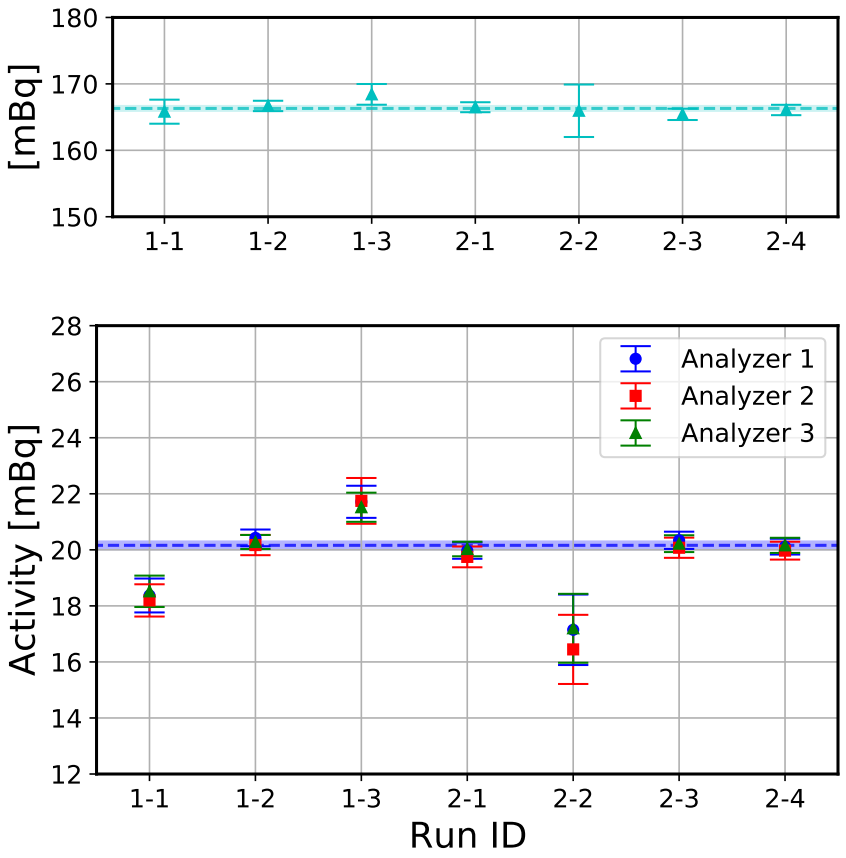

Figure 6.11: *Top*: Measured activity of the highest energy ^{145}Sm peak at ~ 120 keV *cyan*. A correction is applied to account for the relatively short half-life of 340 days. *Bottom*: Measured activity of ^{146}Sm decay peak with data points in *blue* and lines correspond to activity values in Table 6.5. *Red* and *green* data points correspond to the two independent analyzers. For context, I was analyzer 1, Inwook Kim analyzer 2, and Geon-Bo Kim analyzer 3.

6.5.5 Half-Life Result

The final activity was calculated via an error-weighted average of all the sub-runs from both experiments. The finalized activity value was 20.161 mBq with an uncertainty of 0.138 mBq. The final counts and activity values can be found in Table 6.7. The activity values can also be found in Table 6.6 where they are compared against values calculated via statistical measures.

After the finalization of this activity number and the agreement between analyzers established, the atom counting results were unblinded. From the half-life equation, re-stated in Equation (6.3), the half-life can be calculated where N is the number of atoms and A is the sample activity.

$$T_{1/2} = \log(2)\frac{N}{A} \tag{6.3}$$

Run	Counts [#]	Corrected [#]	Live-Time [s]	Activity [mBq]	Uncertainty [mBq]
64-1	1060.25	1062.05	57811.5	18.371	0.605
64-2	6366.50	6377.34	312198.6	20.427	0.298
64-3	1688.00	1690.87	77869.7	21.714	0.573
64-All	9114.75	9130.26	447879.8	20.327	0.242
65-1	6044.25	6054.54	303152.8	19.972	0.291
65-2	187.00	187.32	10924.6	17.147	1.258
65-3	4780.75	4788.89	235439.7	20.340	0.305
65-4	5599.25	5607.78	278801.7	20.114	0.282
65-All	16611.25	16638.53	828318.8	20.083	0.167
All	25725	25768.81	1276198.6	20.161	0.138

Table 6.7: Final activity values. The first column (Counts) are the background subtracted counts, *i.e.*, the difference between the Accepted and Background columns of Table 6.2. The second column (Corrected) shows the efficiency corrected values from the first column. The live-time is restated for completeness and the final two columns are the activity and corresponding uncertainty. The final value of 20.161 ± 0.138 mBq is the finalized activity value.

The prior mass spectrometry yielded a result of $7.877 \cdot 10^{13}$ atoms with an uncertainty of 0.32%. The second post-counting measurement yielded a result of $7.585 \cdot 10^{13}$ with an uncertainty of 0.79%. Of the two notes, the larger uncertainty on the second measurement is due to a smaller aliquot taken from the sample. In the prior measurement, a 5% aliquot and 1% aliquot were taken. In the post, only a 1% aliquot was used for the measurement.

More importantly, the second measurement is 3.7% lower than the first measurement. During the post-counting chemistry, a small quantity of solution containing ^{146}Sm was not transferred between steps erroneously. It was later confirmed by separate measurement ^{146}Sm was present within the un-transferred sample. However, it was not possible to determine the quantity of ^{146}Sm.

Since it is known ^{146}Sm was lost but in a manner independent of the decay counting experiment, the collaboration decided the original number of $7.877 \cdot 10^{13}$ atoms would be used for the half-life calculation. An asymmetric error bar would be added with 3.7% corresponding to two sigma. This determination of two sigma comes from confidence that the transfer error is the cause of the discrepancy though we cannot be absolutely certain. The error bar from this mistake is only applicable in the direction of shorter half-lives, given that a lower number of atoms in Equation (6.3) reduces the calculated half-life value. Therefore the final results of the experiment are a half-life of 85.82 million years. The one-sigma confidence range is 84.10 to 86.46 million years. Equivalently in percentages −2.0% to +0.75%. Note: the Gregorian calendar length of 365.2425 days is used

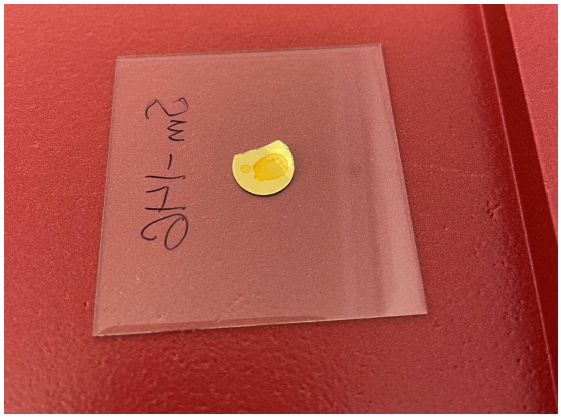

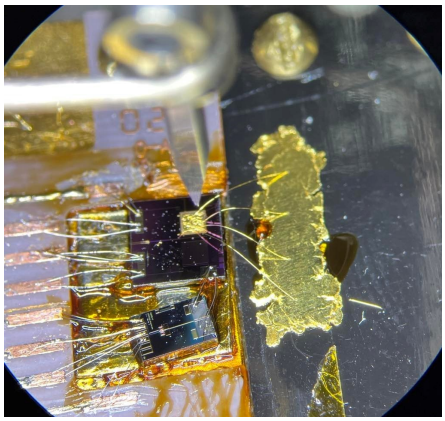

Figure 6.12: *Left*: Au foil with ^{146}Sm solution deposited on the surface. Residue can be seen as an oval shape with a red discoloration. *Right*: Experimental setup with self-made detector.

for the calculation.

6.6 Run 79

6.6.1 Second Experimental Campaign

As a result of the disagreement between the results of the half-life measurement and the prior measurements by Kinoshita and by Meissner, a second experiment was undertaken to verify the results of the first experiment. The ^{146}Sm had been chemically separated from the original gold foil and was available in solution form. The second mass spectrometry measurement was performed after the end of the prior experimental campaign; the results from it would be used as the initial source quantity measurement.

Challenges arose as a result of the chemical separation of the ^{146}Sm from the gold foil the solution contained numerous chemical impurities. In contrast to the original solution, this was opaque and cloudy. Best efforts were made by Dr. Quinn Shollenberger to purify the solution. Deposition of the solution onto the new gold foil was performed in the same manner as the previous experiment by Dr. Kelly Kmak. In contrast to the first deposition, visible precipitates were observed on the foil as seen in the left picture of Figure 6.12.

The presence of extra residue has complicated source preparation on several occasions for both myself and Dr. Geon-Bo Kim. Best efforts were made but a loss of source material occurred. It was decided to continue with the decay counting experiment although the prior mass spectrometry results would no longer be valid.

6.6.2 Experimental Setup

The IBS MMC and Magnicon XS SQUID detector setup were in use for other experiments and thus a new detector recently assembled by myself over the summer of 2022 would be utilized. The detector comprised an MMC fabricated and produced at the Korea Research Institute of Science and Standards [45, 46]. A Star Cryoelectronics Model 2250-V1 SQUID was utilized for the first stage of amplification. The same second-stage amplifier attached to the upper 4 K stage of Megaman was used. The detector dubbed "Alex's Detector" is shown in Figure 6.12.

The decay counting was performed and acquired in the same manner described in Chapter 5 as well as throughout this chapter. As a summary, the traces were digitized in 10 second continuous acquisition sampled at 400 kHz and then averaged down to 40 kHz. Other than the MMC and input SQUID itself, the remaining hardware was the same as used in Runs 64 and 65. The MMC was biased with 100 mA of current.

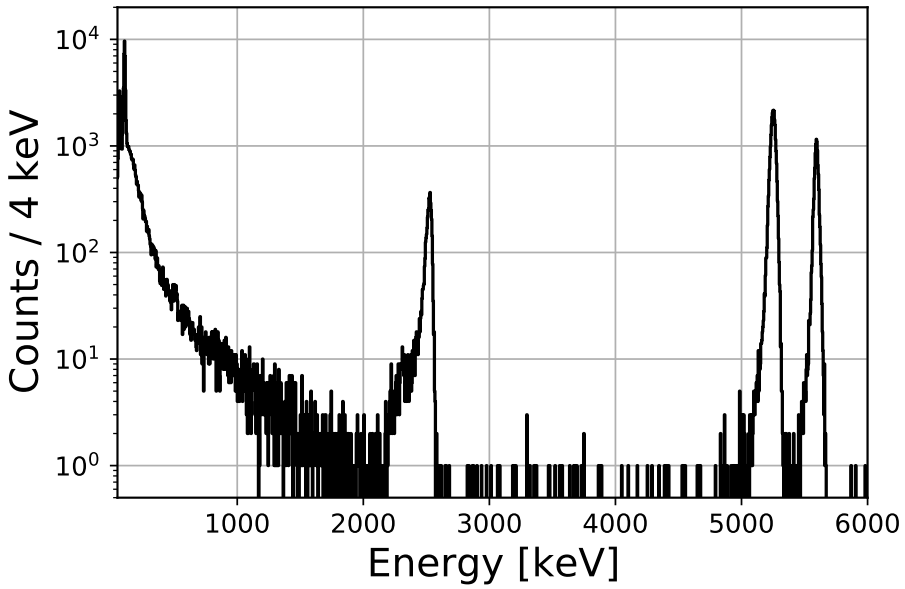

Figure 6.13: Measured energy spectrum from Run-79 decay counting experiment prior to the application of pulse shape cuts

6.6.3 Decay Counting

The data acquisition occurred over a two-week period in November of 2022. From initial observation via an oscilloscope the alpha decay rate was estimated to be approximately 0.035–0.040 CPS. Upon initial analysis of the data, a plutonium contamination was found. Given the significantly shorter half-life of plutonium isotopes compared to ^{146}Sm, the activity would be explained by order

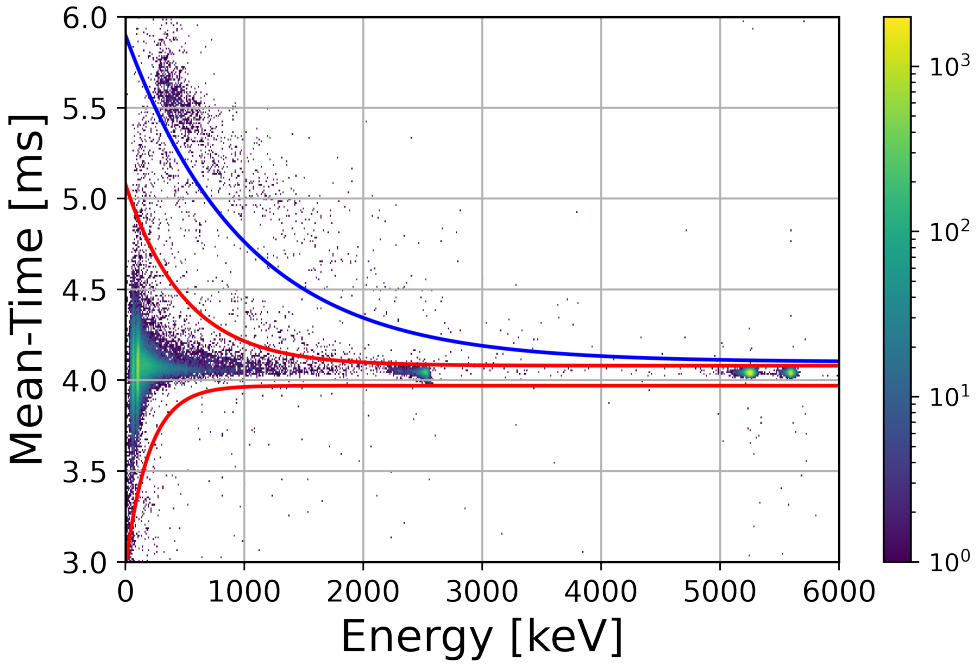

Figure 6.14: Mean-time distribution with tight cuts drawn in *red* and the separation cut drawn in *blue*.

10 pg of plutonium. It is hypothesized that the plutonium was added by human error by the use of contaminated steel shims during the rolling process. Given the count rate of plutonium decays was still of order mBq, it did not dominate the ^{146}Sm decay counts nor cause a significant excess pile-up.

Similarly to the ^{147}Sm decay counting experiment discussed in Chapter 5, a slow-event tail was observed coming off both the ^{146}Sm peak and the plutonium peaks. It was decided that the analysis would be split into two parts. A fast event pulse selection cut would be applied, the events selected from which would be counted and treated in the same manner as the earlier experiment discussed in Sections 6.3 and 6.4 of this chapter.

6.6.4 Event Selection

The slow event tails can be seen coming off the main decay energy peaks in Figure 6.14. The primary decay energy trend with ^{146}Sm and plutonium peaks are seen at a mean-time value of 4.1 ms, relative to the trigger position. The slow contributions continue to a delayed mean-time of 5.5 ms.

Cuts are drawn in red on top of the mean-time trend in Figure 6.14. The lower curve to shorter mean times below the primary trend eliminates sensor hits while two slower curves are cut. One tight

and one broad. The tight curve and lower curve are placed based of the reconstructed distribution of mean times from simulation-injected events. The upper cut drawn in blue is placed to roughly divide the tail seen originating from the ^{146}Sm from the tail originating from the plutonium.

The analysis was handled in two steps. The fast events within the primary mean-time band were analyzed in the same manner as described for Runs 64 and 65. The slow event tails are assessed by two means. One based on the drawn mean-time cuts and one where the total number of slow events is integrated and proportioned based on the ratio of relative activities from ^{146}Sm and plutonium full energy decay peaks.

6.6.5 Peak Counts & Background estimation

The total time and live time as well as the counts at each stage of analysis are recorded in Table 6.8. The live time fraction is a high 98.78%. This is a higher fraction than the first experiment as the reduction in total activity from less ^{145}Sm was greater than the activity introduced by the plutonium contamination. The peak counts were calculated by integrating from 2100 to 2600 keV. Column "Total", "Live", and "Accepted" of Table 6.8 have the same meaning as those in Table 6.2. The full energy spectrum is shown in Figure 6.13. The ^{146}Sm decay peak can be seen at 2.5 MeV and the plutonium peaks at approximately 5250 and 5600 keV.

Run ID	**Exposure**	**Live Time**	**Live**	**Total**	**Live**	**Accepted**	**Background**
	[s]	[s]	[%]	[#]	[#]	[#]	[#]
S2	151990	150055.30	98.73	711	698	653	8
S3	3910	3859.27	98.70	19	19	18	0
S4	93640	92458.48	98.74	485	478	457	5
S5	72430	71513.24	98.73	304	298	285	5
S6	255750	252964.82	98.91	773	760	709	14
S7	166270	164176.36	98.74	788	784	750	6
S8	14410	14228.61	98.74	74	73	72	0
S9	64980	64165.56	98.75	297	290	284	6
S10	74530	73588.87	98.74	355	350	323	8
S11	90960	89812.76	98.74	399	393	375	4
S12	84080	83016.49	98.74	418	414	388	9
All	1072950	1059839.78	98.78	4623	4557	4314	65

Table 6.8: Summary of data runs from Run-79.

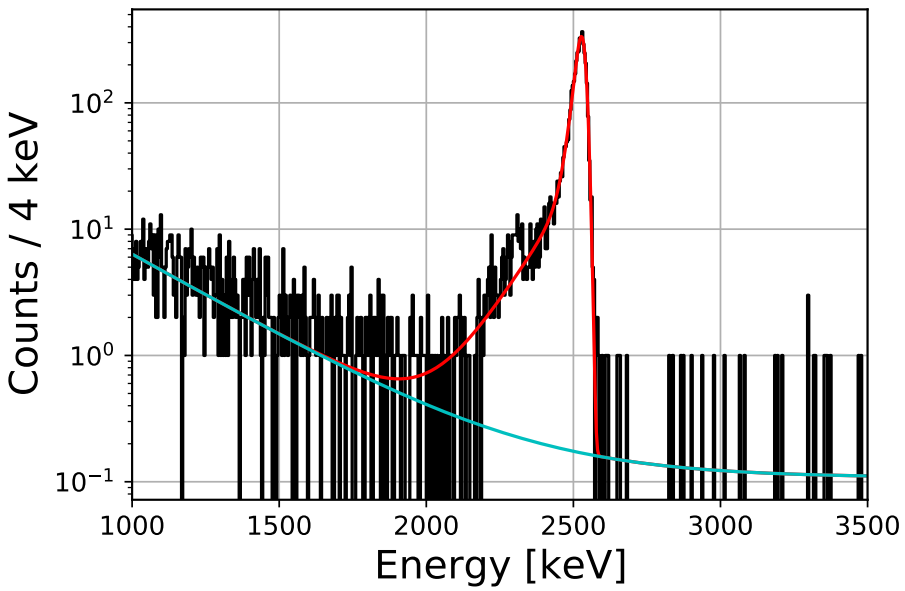

Figure 6.15: Fit to ^{146}Sm decay peak with the functional form of two exponentially modified Gaussians with their means and standard deviation terms fixed on top of an exponentially decaying background. The background component alone is drawn in *cyan*.

6.6.6 Spectral Analysis

Just as in the prior decay counting experiment, fits were used to verify no tail component extended down to low energies within the accepted pulse distributions. The accepted energy spectra were fit with a double exponentially modified Gaussian functional form with one of three background models: exponential decay, low energy step extending from the decay peak to low energies, and a combined model. An exponential model was chosen as it best fits the background above 500 keV.

Similarly to the fits performed in the prior experiment(s), the likelihood minimization algorithm preferred an exponential background to the step model. In the case of the combined model, the best-fit amplitude for a step was always within small error regardless of the fit lower energy bound. The arbitrary log-likelihood values were -17663.77 for the exponential model, -17139.84 for the step model, and -17663.77 for the combined model. The best-fit model predicted a background of 45 counts with an uncertainty of 22 counts under the decay energy peak. This is consistent with the assigned background of 65 counts with the conservative estimate of 100% uncertainty. The fit peak area value was 4337.58 with an uncertainty of 217 counts. This is also consistent with the background subtracted peak area calculated by integration of 4249 counts. The peak and fit are shown in Figure 6.15. From this combined analysis, we conclude that the number of counts extending below the peak is negligible and is accounted for in the conservative estimation of the background uncertainty.

6.6.7 Slow Tail Contribution

The primary complication posed by the plutonium contamination was distinguishing the tail contribution rate from the plutonium and the contribution rate from the ^{146}Sm. Two distinct tails can be observed, one originating from the plutonium at 5 MeV and another from the ^{146}Sm decay peak at 2.5 MeV. The relative contributions were assessed in two manners. The first, by drawing pulse shape contours within the energy mean-time phase space, and the second by integrating the total number of slow counts and assigning them based on the ratio of the number of counts in the plutonium peaks to those in the ^{147}Sm decay peak.

The lower curve, the same as the upper cut applied for event selection, is the *green* line in Figure 6.14. The upper curve, the *red*, line in Figure 6.14 was used as a separation boundary between the slow ^{146}Sm and slow plutonium events.

The total number of counts integrated between the *green* and *red* curves from 50 to 2600 keV were associated as being ^{146}Sm events. The counts between the *red* curve and below an upper bound of 8 ms and from 50 to 5650 keV were associated with plutonium. The lower bound of 50 keV is justified and discussed later in Chapter 7 as slow events were found to be alpha particles escaping the foil and interacting with the G-10 base plate. In this case, by kinematics, the nuclear recoil must be contained within the foil so the heat from it is measured. A total of 631 counts were integrated in the ^{146}Sm assigned region while 1825 were integrated in the plutonium region.

The second method involved integrating all counts between the event selection cut (*green* curve) and 8 ms from 50 to 2600 keV. The fraction of these events would be assigned by the ratio of total counts within the ^{146}Sm decay peak by the total counts within the plutonium decay peaks. The total number of slow counts integrated was 2456. These were then "split" by the ratio of 4314, the accepted number of ^{146}Sm counts to 34694 plutonium counts. By this method, 305.40 of the slow events are associated with ^{146}Sm decays.

After discussion, method two was selected to ascertain the counts to be reported in the activity as it is less dependent on the specific choice of cuts. The two-sigma uncertainty contribution from the slow counts was chosen to be 100 % the number of slow ^{146}Sm events. One sigma is therefore 50%. Two sigma is chosen as it is more commonly used in the reporting of numbers within the geochemistry community according to Dr. Quinn Shollenberger.

This was chosen based on two scenarios. Scenario A: only plutonium is actually near the surface of the foil and the ^{146}Sm is fully contained within the bulk of the absorber medium. In this case, all slow events are caused by plutonium and not samarium. Scenario B: the plutonium and ^{146}Sm have the same underlying distribution and thus contribute to a ratio set by the ratio of their full energy decay peaks. However, our understanding is that these slow events occur when the alpha escapes downwards into the base plate which then re-heats the absorber. It is then probable that up to the same number of events are being ejected from the top of the foil while depositing only a

fraction of their energy. The maximum number of events this could be would be the same number as counted. These scenarios set the lower and upper uncertainty bound from the slow events at 100% the number of slow counts (attributed to ^{146}Sm). Given that the likely contamination vector was from the use of contaminated steel shims when rolling the foil, the true scenario is likely somewhere between A and B.

A scenario exists in which a larger relative fraction of the the ^{146}Sm is near the absorber surface than the plutonium requires more assumptions such as the solution itself being contaminated and some chemical preference of the plutonium to more strongly incorporate itself with a gold medium. Therefore it is deemed highly unlikely in comparison to the other two scenarios.

6.6.8 Activity and Half-Life

In contrast to runs 64 and 65 where various physical changes were made and experiments performed on different cool-down cycles, run 79 was one long continuous acquisition. The sub-runs are only differentiated by saving data into new folders such that existing folders can be transferred and backed up. For this reason, the activity and half-life will be calculated with all the counts divided by the total live-time with subsequent efficiency correction thereafter applied.

For the peak itself, 65 background counts are subtracted from 4314 counts giving 4249 signal counts. Efficiency correction is then applied to yield a total of 4322.48 analysis counts. Dividing by the live-time the (peak only) activity is 4.078 mBq. Statistical uncertainty is 1.52%, live-time uncertainty is 0.2%, and background uncertainty is 1.51%. The combined uncertainty is then 2.15%. Because the events outside the acceptance cut are included with those in the slow event counts, their uncertainty contribution is also contained within the uncertainty contribution from the slow counts.

The slow counts contribute an additional 0.3 mBq to the total activity but contribute 6.17% to the uncertainty. This is calculated by $310.68/(310.68 + 4322.48)$. This is viewed as an overly conservative estimate. If we halve the uncertainty, this gives 3.353% and the combined total uncertainty is then 3.984%. The total activity and uncertainty then being 4.371 mBq ± 0.174 mBq.

After counting, the gold foil was again dissolved and the samarium was chemically extracted. Because a large amount of sample was lost and this was likely to be the final measurement, a larger 10% aliquot was taken from the solution. The TIMS result yielded $1.698 \cdot 10^{13}$ atoms in the sample at the time of counting (the 10% aliquot being accounted for). The half-life from the peak alone is 91.46 million years while the inclusion of the tail yields 85.32 million years.

	Half-Live [Ma]	Uncertainty [Ma]	Uncertainty [%]
Run-79 Peak Only	91.458	1.968	2.152
Run-79	85.316	3.40	3.984
Run-64	85.117	1.01	1.187
Run-65	86.151	0.69	0.801

Table 6.9: Half-life values from the three independent decay counting experiments. The half-life from Run-79 peak only serves as a strong upper bound to the half-life which cannot be longer than 91.5 ± 2 million years.

CHAPTER 7

Assay of ^{239}Pu Samples

7.1 CRM-126A Measurements

7.1.1 Motivation

Additional verification campaigns were undertaken to support the 86 million-year half-life result. Two further attempts were made to measure the ^{147}Sm half-life via decay counting of natural samarium. Solutions containing 1 mg and 100 µg of natural samarium were deposited onto gold foils but folding and kneading the absorber failed both by my own attempts as well as Dr. Geon-Bo Kim's attempts. It was decided that a plutonium standard would be used, due to the smaller mass requirements for a comparable activity as well as experience performing decay counting experiments on plutonium. The CRM-126 plutonium standard was chosen as being readily available, its mass dominated by the ^{239}Pu isotope, and minimal activity contribution from ^{241}Pu [123, 124].

Dr. Quinn Shollenberger would take an aliquot of known volume from a well-characterized stock solution of CRM-126A, Dr. Kelly Kmak would deposit the source, and it would be decay counted in a similar manner to the preceding experiments. Three samples would be prepared and deposited onto 25µm thick gold foils. Sample 1 was prepared by myself, Sample 2 was prepared by myself and Dr. Nathan Hines, and Sample 3 was prepared by Geon-Bo.

Plutonium is one of the most regulated and dangerous substances created by mankind. Very few facilities aside from LLNL, LLNL, or ORNL have access to such and in high enrichment levels of ^{239}Pu. It was quite a lot of fun to measure (see Table 7.4).

7.1.2 Source Composition

The source volume was chosen such that a precise mass of ^{239}Pu, around 20 pg, would be known to Quinn. The aim of the decay counting experiment(s) was to reproduce this mass value. Due to the large foil, resolution was not expected to be sufficient to resolve the ^{239}Pu and ^{240}Pu peak

Isotope	Mass [AMU]	Half-Live [years]	Uncertainty [years]	Atom Percentage [%]	Uncertainty [%]
^{238}Pu	238.0496	87.7	0.3	0.012229	0.000028
^{239}Pu	239.0522	24110	30	93.9110	0.0015
^{240}Pu	240.0538	6564	11	5.8923	0.0015
^{241}Pu	241.0568	14.290	0.006	0.148272	0.000072
^{242}Pu	242.0587	373300	1200	0.036123	0.000024

Table 7.1: CRM-126A Isotopic Standard. Evaluated on July 30th 2003 [123]

separations. The activity of the combined (^{239}Pu and ^{240}Pu) peak would be measured and then the ^{239}Pu quantity extracted via the relative isotopic composition of the source expressed in Table 7.1.

$$\frac{A^{240}}{A^{239}} = \frac{T_{1/2}^{239}}{T_{1/2}^{240}} R \tag{7.1}$$

The atomic ratio of ^{240}Pu to ^{239}Pu is reported as 0.062744 ± 0.000016 as assessed on July 30th 2003 [123, 124]. If this original ratio value is denoted as R and the respective half-lives as $T_{1/2}$, then the original activity ratio is given by Equation (7.1). The new ratio R' at some time $\triangle T$ past the characterization date is given by Equation (7.2).

$$R' = R \frac{0.5^{\triangle T / T_{1/2}^{240}}}{0.5^{\triangle T / T_{1/2}^{239}}} \tag{7.2}$$

The samples were measured on and around late October to early November of 2023. The time difference $\triangle T$ is 20.25 years. At the time of the decay counting experiments R' equaled a value of 0.0626464. This value is the atom fraction ratio which needs to be converted to the activity ratio which can be done by rearranging Equation (7.1):

$$A^{240} = \frac{T_{1/2}^{239}}{T_{1/2}^{240}} R' \cdot A^{239}. \tag{7.3}$$

If the summed ^{239}Pu and ^{240}Pu activities equal the value "X", then the conversion factor can be obtained from

$$A^{239} \left(1 + \frac{T_{1/2}^{239}}{T_{1/2}^{240}} R' \right) = X \tag{7.4}$$

$$A^{239} = X \cdot \left(1 + \frac{T_{1/2}^{239}}{T_{1/2}^{240}} R' \right)^{-1} = X / 1.23010444. \tag{7.5}$$

Uncertainty in the original contributions of ^{239}Pu and ^{240}Pu as well as their half-lives contribute to the overall uncertainty in the theoretically calculated ratio. Both the atomic and activity ratios as reported in Reference [123] and calculated for the time of the experiment in 2023 ($\triangle T$ = 20.25 years), are listed in Table 7.2. The summed ^{239}Pu + ^{240}Pu activities will be divided by 1.23010444 to extract the ^{239}Pu activity and quantity of atoms / mass. An uncertainty of 0.21% will be carried with the ratio for inclusion in the calculation of the sample mass. This value is calculated by adding in quadrature the uncertainty in the ^{239}Pu and ^{240}Pu half-lives, the 0.0255 % uncertainty of the original atomic ratio, and an additional time uncertainty factor of 3 months. This additional time uncertainty accounts for both possible small fluctuations in the reported dates as well as an additional nuisance uncertainty.

	Atomic Ratio	Activity Ratio
2003	0.062744	0.230463
2023	0.062646	0.230104

Table 7.2: 3-month additional time uncertainty 0.002%. Uncertainty of the ratio calculation 0.21%

An additional ratio can be extracted from the data which is the ratio of ^{239}Pu + ^{240}Pu to ^{238}Pu + ^{241}Am. The ^{241}Am is the daughter of ^{241}Pu which then decays via a 432.6 year half-life. While the resolution of measurements was sufficient to separate the primary ^{241}Am decay peak from the ^{238}Pu decay peak, the exact escape probability of the 60 keV gamma ray from ^{241}Am is difficult to know in practice for a given absorber geometry. Therefore the ratio is calculated as the ratio of the two activities summed.

$$A' = A \cdot 0.5^{\triangle T / T_{1/2}} \tag{7.6}$$

The current activities for ^{238}Pu, ^{239}Pu, and ^{240}Pu are all calculated via Equation (7.6) where A is the atomic abundance ratio multiplied by the corresponding half-life with values provided in Table 7.1. The activity of ^{241}Am is calculated using the transient equilibrium equation. The transient equilibrium for the relative quantity of ^{241}Am in the sample at a given time $\triangle T$ after July 30th, 2003 and is described by:

$$N_{Am} = \frac{\lambda_{Pu} N^0_{Pu}}{\lambda_{Am} - \lambda_{Pu}} \left(e^{-\lambda_{Pu} \cdot \triangle T} - e^{-\lambda_{Am} \cdot \triangle T} \right). \tag{7.7}$$

. The superscripts Pu and Am refer to ^{241}Pu and ^{241}Am respectively. λ is the decay constant related to the half-life as $\lambda = \ln(2)/T_{1/2}$. A general assumption is made regarding the branching of ^{241}Pu

decaying to ^{237}U to be negligible; uncertainty is accounted for later.

Calculating the ratio at the time of the conducted experiments yields a relative fractional value of 0.06889510274608451. Or the ^{238}Pu + ^{241}Am summed activity is 6.89% the summed activity of ^{239}Pu + ^{240}Pu. The half-life and atomic contribution uncertainties come from the final column (Total) of Table 7.3. An additional uncertainty factor of 0.37% is added in quadrature with these values corresponding to a three-month time-uncertainty as well as to account for other uncertainty terms such as the small branching of ^{241}Pu to ^{237}U. The assigned uncertainty of the ratio is 0.61%, or the value being 6.89 ± 0.04%.

	^{238}Pu [%]	^{239}Pu [%]	^{240}Pu [%]	^{241}Pu [%]	^{241}Am [%]	Total [%]
Half-Life	0.34	0.12	0.17	0.04	0.13	0.42
Composition	0.23	0.0016	0.0255	0.0486	0.00	0.23

Table 7.3: Half-Life Total: 0.42, Composition 5.50, 3 months = 0.37%

7.1.3 Comments on CRM-126A

Table 7.4 compares the relative plutonium atomic composition of CRM-126A to that of various grades of plutonium as reported by [125]. As demonstrated in Table 7.4, the composition appears nearly identical to that of weapons-grade plutonium.

Grade	^{238}Pu [%]	^{239}Pu [%]	^{240}Pu [%]	^{241}Pu [%]	^{242}Pu [%]
CRM-126A	0.012229	93.110	5.8923	0.148272	0.036123
Super	-	98.0	2.0	-	-
Weapons	0.012	93.8	5.8	0.035	0.022
Reactor	1.3	60.3	24.3	9.1	5.0
MOX	1.9	40.4	32.1	17.8	7.8
FBR	-	96.0	4.0	-	-

Table 7.4: Isotopic composition of CRM-126A compared to graded plutonium as reported by [125].

7.1.4 Experimental Results

A total of seven experiments were performed with each of the samples being measured at least twice and with at least 10000 counts within the ^{239}Pu–^{240}Pu peak. The resolution was never great enough to separate these peaks. In some runs the ^{238}Pu and ^{241}Am decay peaks can be separated.

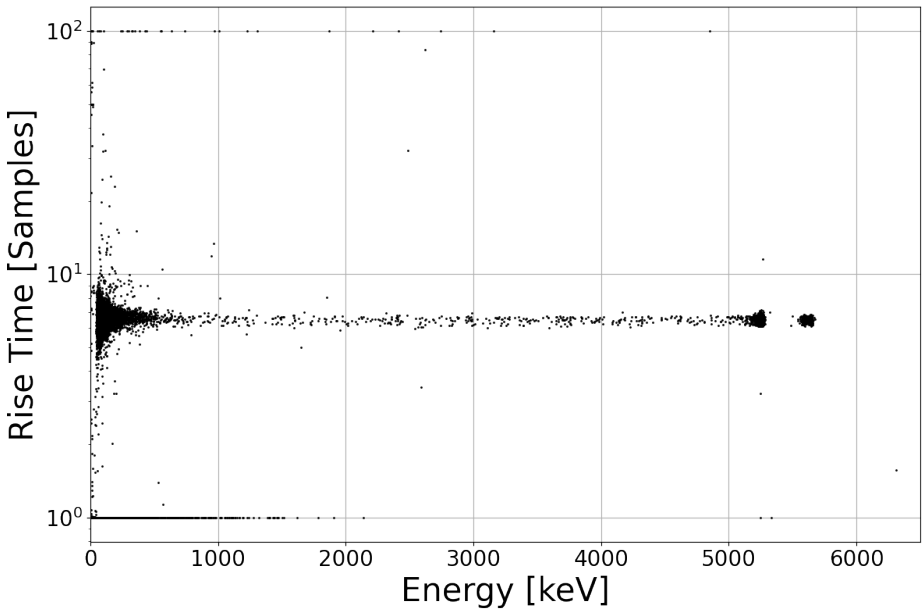

Figure 7.1: Rise-time distribution for data taken from Sample 3. The "fast" tail can be seen extending from the decay peaks towards low energy. The population at the bottom of the y-scale are fast-rise fast-decay sensor hit events.

The areas in the double peaks are assessed via integration. The primary peak is integrated from 4800 keV to 5400 keV and the second from 5400 keV to 5800 keV. A low-energy tail can be observed from the peaks with low activity. This tail was comprised of normal and not slow events. The descriptor "fast" corresponds to the normal rise time of events as depicted in Figure 7.1 and is not faster than the normal distribution.

The tail activity was assessed by integrating from 2000 keV to 4800 keV over which the tail is flat and then projecting down to zero. The relative tail activity was not constant between samples indicating it was related to sample preparation. The tail was not able to be assessed in runs 105 and 115 due to anomalous events discussed later in this chapter. The energy spectrum around the decay peaks are shown in Figure 7.2 and Figure 7.3 for each of the seven data runs.

The example of the tail for Sample 3 is evident in the rise-time distribution as shown in Figure 7.1. The events clearly originate from plutonium decays but preserve pule shape. A better understanding of these events is crucial for being able to use MMCs for nuclear forensics and other national security programs.

The energy spectra from 4800 to 5800 keV for each experiment of the seven conducted experiments are shown in Figure 7.2 and Figure 7.3. Resolution varied but was generally improved in the latter three measurements compared to the earlier four. The live times and counts for each experiment is summarized in Table 7.5.

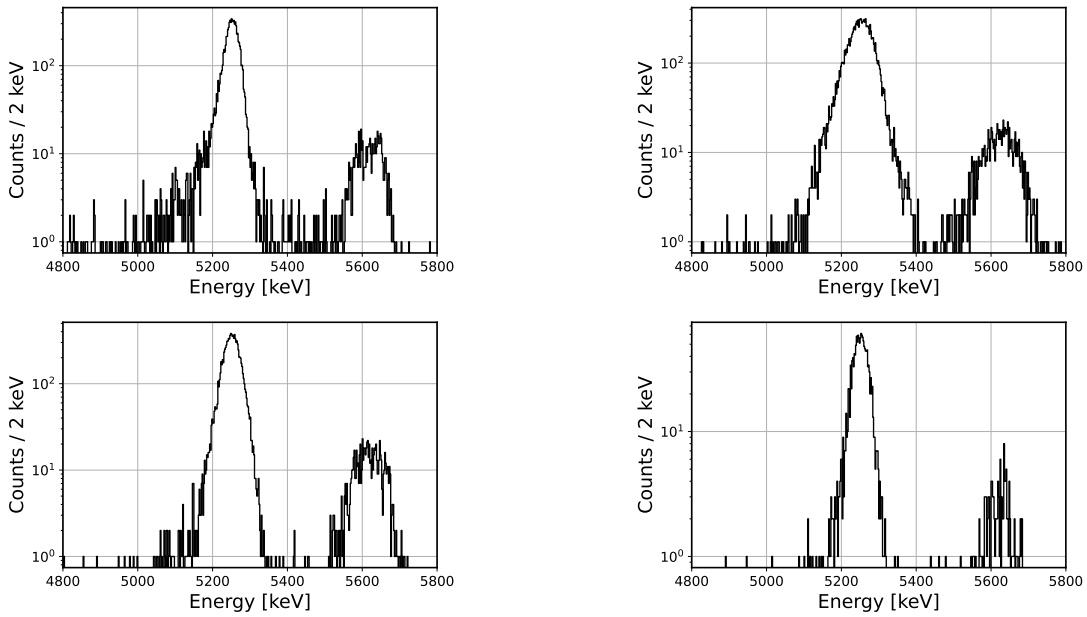

Figure 7.2: Decay energy spectra.*Top Left*: Run-105. *Top Right*: Run-107. *Bottom Left*: Run-113. *Bottom Right*: Run-115.

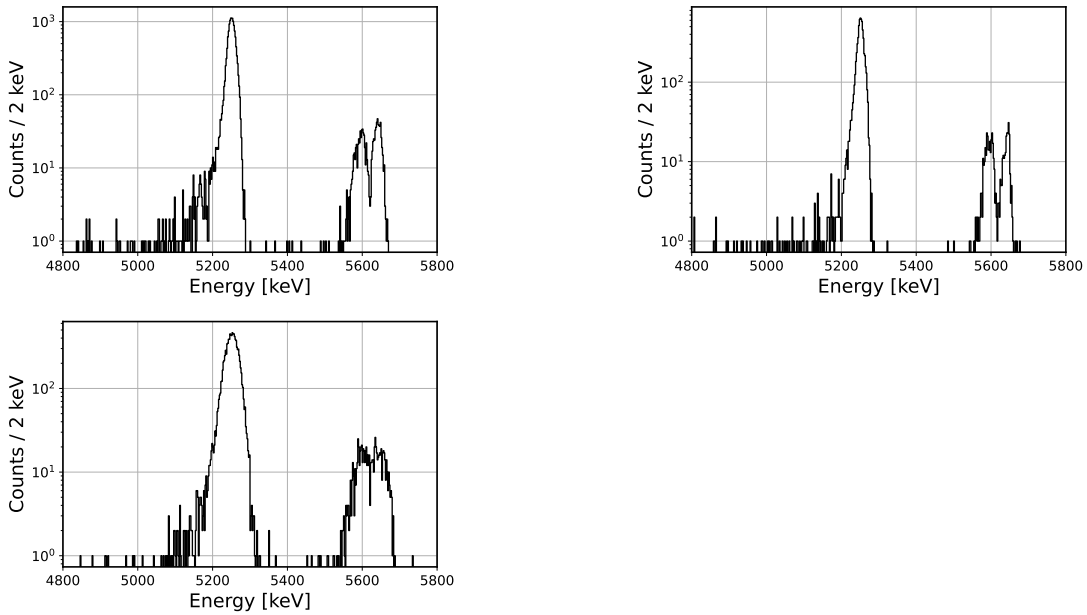

Figure 7.3: Decay energy spectra. *Top Left*: Run-105. *Top Right*: Run-107. *Bottom Left*: Run-113. *Bottom Right*: Run-115.

Run	Sample	Live Time [s]	^{239}Pu + ^{240}Pu [#]	^{238}Pu + ^{241}Am [#]	2000-4800 keV [#]	Tail [#]
105	2	163253.72	7642	582	-	-
107	3	244364.77	12549	958	95	162.9
113	1	191064.24	10032	801	26	44.6
115	1	75199.85	3847	296	-	-
118	1	249325.13	13456	1005	39	66.9
119	3	129606.42	6465	500	73	125.1
121	2	222928.31	9926	799	50	85.7

Table 7.5: Summary of experimental data runs with CRM-126A sample acquired utilizing "Alex's Detector".

7.1.5 Mass Results

The ^{239}Pu activity was separated from the total peak activity via Equation (7.5). The activities of the summed ^{239}Pu + ^{240}Pu peak are given in Table 7.6. The mass values are calculated via the relationship $T_{1/2} = \log(2)N/A$. The uncertainty is calculated in the same manner as with the ^{146}Sm activity and is dominated by statistics. Very few events ~20 were cut by the pulse shape cut and background subtraction across the entire set of experiments with the exception of Run-105 in which contamination was observed. Table 7.6 contains data from all data in Table 7.1.

Sample	Activity [mBq]	Activity [mBq]	Mass [pg]	Uncertainty [pg]
1	53.02	43.10	18.78	0.11
2	45.49	36.98	16.11	0.12
3	50.96	41.43	18.05	0.13

Table 7.6: Mass and activity results.

As previously mentioned, while no slow tail originating from the plutonium decay peaks was observed, "fast" tails with the characteristic rise-time were observed. This tail, as depicted in Figure 7.1, clearly originates from the plutonium sample and should therefore be counted. Table 7.7 includes the tail activity and sums with the activity in Table 7.6. The entire tail contribution is added as uncertainty since its calculation is based on the assumption it continues to be flat down to low energies. The tail could not be estimated in Run-105 and Run-115 due to external contamination of the runs. The mass of sample-2 decreases when the tail is included as only Run-121 is used which has a lower peak activity.

Given the spectral evidence, it seems most reasonable to include the tail as well as the peak. The "known" source mass was assessed by Dr. Quinn Shollenberger. The values and uncertainties

Sample	Peak Activity [mBq]	Tail Activity [mBq]	Summed Activity [mBq]	^{239}Pu Activity [mBq]	Mass [pg]	Uncertainty [pg]
1	53.33	0.25	53.59	43.57	18.98	0.14
2	44.53	0.39	44.91	36.51	15.91	0.18
3	50.84	0.77	51.61	41.96	18.23	0.31

Table 7.7: Activity and mass results by sample with tail consideration

reported by her are given in Table 7.8. If just samples 1 and 3 are considered, there appears to be a 1% deficit from the known quantity (2% if only the peak is considered). Both values are approximately 1 σ lower. If this asymmetric value is considered to apply to the ^{146}Sm data runs, it would hardly affect when added in quadrature with the 3% lower error from sample loss in the post mass measurement. Sample 2 is significantly lower than measured by Dr. Shollenberger. The only plausible explanation is that a mistake was made in either the deposition of the source onto the gold foil or the enclosure of the gold foil.

Sample	Mass [pg]	Uncertainty [pg]	Mass [pg]	Uncertainty [pg]	Difference [pg]	Difference [%]	Difference [σ]
1	18.98	0.14	19.2	0.1	-0.22	-1.15	-1.3
2	15.91	0.18	17.9	0.1	-1.91	-10.67	-9.3
3	18.23	0.31	18.4	0.1	-0.17	-0.92	-0.5

Table 7.8: Summary of ^{239}Pu Mass results with tail compared against mass values provided by Dr. Quinn Shollenberger.

7.1.6 Anomalous Pulse Shapes

As previously mentioned, slow pulses were observed in Run-105. However, in this experiment, the energy of the slow pulse tail did not go up to 5000 keV but appeared to stop at 4700 keV as shown in the upper plots of Figure 7.4. With this exception, the pulses appeared the same as those previously described in Chapter 5. This difference however gives the strong impression that the slow events originated from some external source as their full decay energy was never deposited. The hypothesis is that they were caused by external contamination on the base plate. A decay occurring on the base plate would locally heat the gold foil. Due to the insulating nature of the G-10 [98, 99] the absorber sat upon heat would flow back up into the gold foil and exit the system through this pathway.

The hypothesis was tested through measurements with the same and different base plates. Figure 7.4 shows the experimental data spectrum from Run-105 and Run-121. The former used the

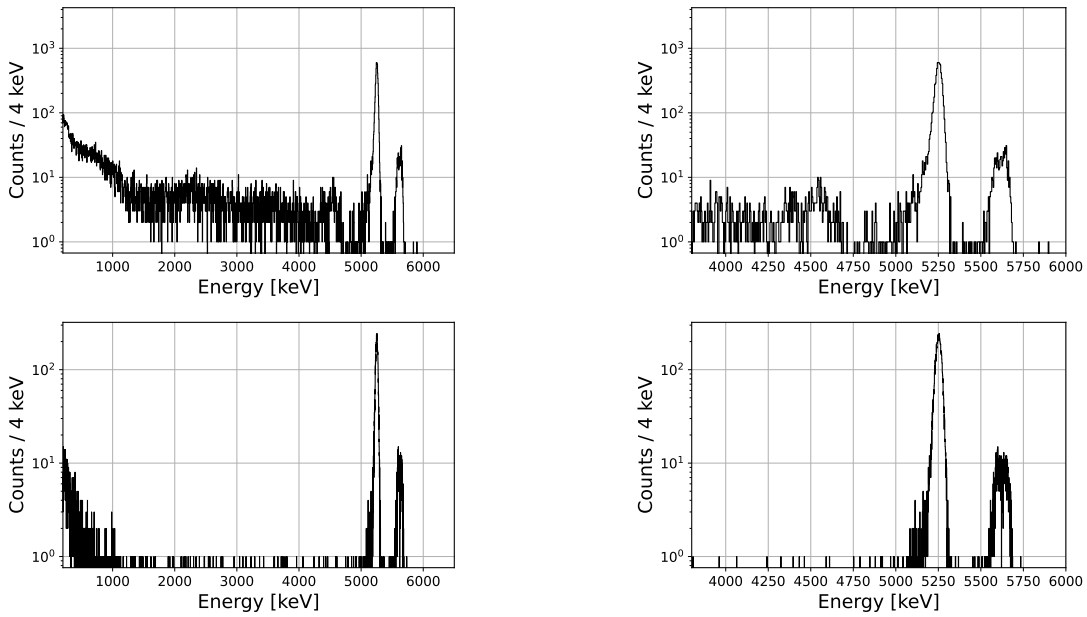

Figure 7.4: Energy spectra from Run-105 (*top*) and Run-121 (*bottom*) with contaminated base plate sample and clean sample respectively. Both are shown in different ranges from which the slow event population can be seen in the case of Run-105.

original base plate while the latter used a newly opened aluminum base plate. In the latter measurement, slow events completely disappeared from the spectrum. While this does not definitively prove the hypothesis, strong evidence is given to the assertion that slow events are those that interact with the base plate from which heat re-flows up into the absorber. This further supports the hypothesis that material was lost in the preparation of sample 2 which should not be used as a point of comparison for the ^{146}Sm program.

7.2 Nuclear Forensics

7.2.1 Mixed Actinide Sample

Applications of DES beyond fundamental science are of high interest, particularly those that can contribute to national security. One potential application is in the assay of mixed actinide samples for nuclear forensics. Mixed actinide samples pose challenges to mass spectrometry-based assay techniques. For example, the near identical masses of ^{241}Pu and ^{241}Am result in signal overlap by when assay is performed via TIMS. ^{238}Pu and ^{238}U similarly overlap though they can be separated via alpha spectroscopy. Other measurements such as the separation of ^{239}Pu and ^{240}Pu is extremely challenging via alpha spectroscopy.

Typically, these issues are resolved via chemical separation of the various actinides [124].

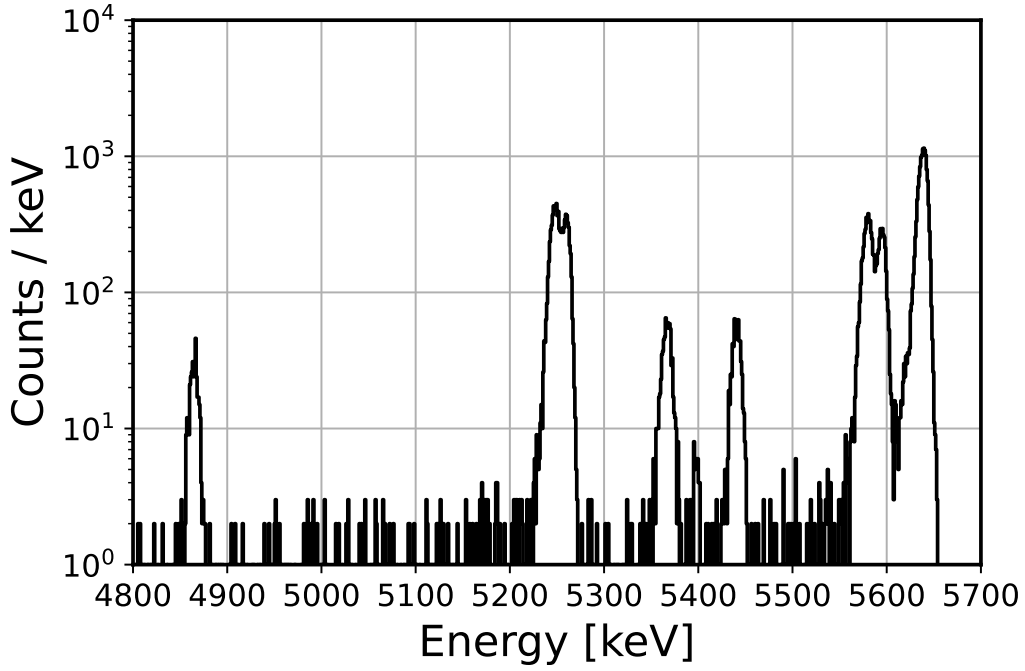

Figure 7.5: Experimentally measured decay energy spectrum of actinide sample Eve Run-6.

Though the chemical procedure can introduce additional uncertainties as noted in [124]. DES can provide assay of nuclear materials and simultaneously measure ^{241}Pu, ^{241}Am, ^{238}Pu,^{238}U, ^{239}Pu, and ^{240}Pu without performance of any actinide chemistry.

The first sample was provided by the LLNL RRR group for use in a proof of concept test. The sample was embedded within a gold foil absorber, coupled to an MMC device, and cooled to a temperature of 40 mK utilizing EVE. This measurement was one of the first performed once EVE was recommissioned.

Due to the necessity of high resolution to separate ^{239}Pu and ^{240}Pu decay peaks, waveforms were saved in 50 ms traces for analysis via optimal filtering. The optimal filter utilized for this experiment is described in Chapter 3. Pile-up pulses and other artifacts were rejected utilizing a cut on mean time and the variance of the template subtracted residual.

The measured energy spectrum is shown in Figure 7.5. The observed peak structures from lower to higher energies are: ^{234}U decay peak at 4860 keV, the double ^{239}Pu–^{240}Pu peak at 5244 and 5255 keV, the ^{234}Am decay peak and two gamma escape peaks from 5350 to 5450 keV. Regarding the four peaks at highest energy, one peak is ^{238}Pu at 5593 keV and the other three are from ^{241}Am, the decay peak at 5637 keV, a small gamma escape peak at 5620 keV and a larger gamma escape peak at 5577 keV. The ^{238}Pu and ^{241}Am can be more readily distinguished in Figure 7.8.

7.2.2 Peak Shape

The evaluation metric of the DES method is the accuracy of reconstruction of the atomic ratio of ^{239}Pu to ^{240}Pu. This has been chosen both as the metric for the analysis presented within this section as well as the metric to be evaluated in the future.

This choice of metric is somewhat arbitrary. The reasons to choose the ^{239}Pu to ^{240}Pu ratio is that it is the most difficult actinide feature to resolve with DES [72, 82, 117] and that weapons-grade plutonium requires a high purity of ^{239}Pu as ^{240}Pu can cause a weapon to pre-detonate [126, 125]. Weapons-grade plutonium requires less than 7% ^{240}Pu [125].

$$\frac{A}{2\tau_1} e^{(\frac{1}{2\tau_1})(2\mu - 2x + \sigma^2/\tau_1)} \cdot \textbf{erfc}\left(\frac{\mu - x + \sigma^2/\tau_1}{\sqrt{2}\sigma}\right) + \frac{A \cdot R}{2} e^{(x-\mu)/\tau_2} \cdot \textbf{erfc}\left(\frac{x-\mu}{\sqrt{2}\sigma}\right) \tag{7.8}$$

The ^{239}Pu to ^{240}Pu activity ratio is assessed via spectral fitting. The functional form chosen is an exponentially modified Gaussian with a second lower energy tail. The functional form is given in Equation (7.8) where **erfc** is the complementary error function. The first term accounts for the peak with area A, centroid μ, spread σ, and time-constant τ_1. The second accounts for the small continuum extending to lower energies from each peak. This low energy tail, with time-constant τ_2 is assumed to be some fraction R of the peak amplitude where R is assumed to be the same for each peak.

The only free parameters for a given peak are its area A and its centroid μ. The shape parameters are all shared between the peaks. This allows maximum information to be used in assessing the underlying true peak shape.

7.2.3 MCMC Fitting

The fits were originally performed utilizing the python Iminuit package [115]. However, the way in which pre-built fitting routines handle uncertainty is a bit of a "black-box". To address this, in 2010, Goodman and Weare mathematically developed an affine-invariant ensemble sampler which enabled fitting routines to be developed upon Monte-Carlo Markov Chains (MCMC) [127]. Readily accessible Python packages have been written based upon MCMC fitting and have been implemented in spectral fitting for radiation detection applications [128, 129, 130, 131]. The growing popularity can be seen by the reference records of [127, 128].

Following a derivation learned at UChicago, and summarized in [131], if the underlying distribution of counts within a given energy bin follows a Poisson distribution, then the probability of there being N counts in bin i is given by Equation (7.9).

$$P(N_i|\mu_i) = \frac{(\mu_i)^N e^{-\mu_i}}{N_i!} \tag{7.9}$$

µis the theoretically predicted number of counts based upon some functional form, and our fit model is based upon some set of parameters $\vec{\pi}$. If f is the function we want to fit to our data then µcan be expressed as Equation (7.10). Again, the subscript i indicates the evaluation of this function at bin number i.

$$\mu_i = f(\vec{\pi})|_i \tag{7.10}$$

The log-likelihood for a Poisson model can be readily found online at sources such as [132]. Expressed in the variables described above yields

$$\ln(\vec{N}|\vec{\pi}) = \sum N_i \ln(\mu_i) - \sum \mu_i - \sum \ln N_i!. \tag{7.11}$$

MCMC fitting can then be summarized in a relatively simple manner. Assuming our functional form is well defined over our set of parameters over the range of the data (to be fit) a number of "walkers" are initialized over that parameter space. By personal assumption, given that the parameter range can be set somewhat near the true underlying parameters, *i.e.*, good guesses for the amplitude, mean, and standard deviation of a peak can be made, I think it is best to initialize the walker locations uniformly in some neighborhood around this point in parameter space. Each walker will take a small "step" in the parameter space and calculate the likelihood, shown in Equation (7.11), and compare it to the likelihood at the previous position. The walker will then choose the more likely position and then repeat. In ideal circumstances, all of the walkers will converge around a single point in parameter space, this point is taken as the set of best-fit parameters. Taking the mean walker value as the nominal value and some statistical measure of its spread (variance) mathematically account for the underlying Poisson statistics via Equation (7.9) [127].

This algorithm was used to fit the functional form described in Equation (7.8) to the mixed actinide dataset. In this case, our parameter vector is given by

$$\vec{\pi} = (A_k, \mu_k, \sigma, \tau_1, R, \tau_2). \tag{7.12}$$

Parameters A_k and μ_k are the area and mean terms for the k-th isotope decay peak/gamma escape peak. Parameters σ, τ_1, R, and τ_2 are the shape parameters shared between all peaks. The paths taken by the walkers associated with A_{239}, μ_{239}, A_{240}, μ_{240} are shown in Figure 7.6. These paths are shown as the ^{239}Pu–^{240}Pu ratio is as previously discussed, our evaluation metric. The initialized flat distribution begins to consolidate after 10 steps. After 1000 steps the walkers converge to their final positions.

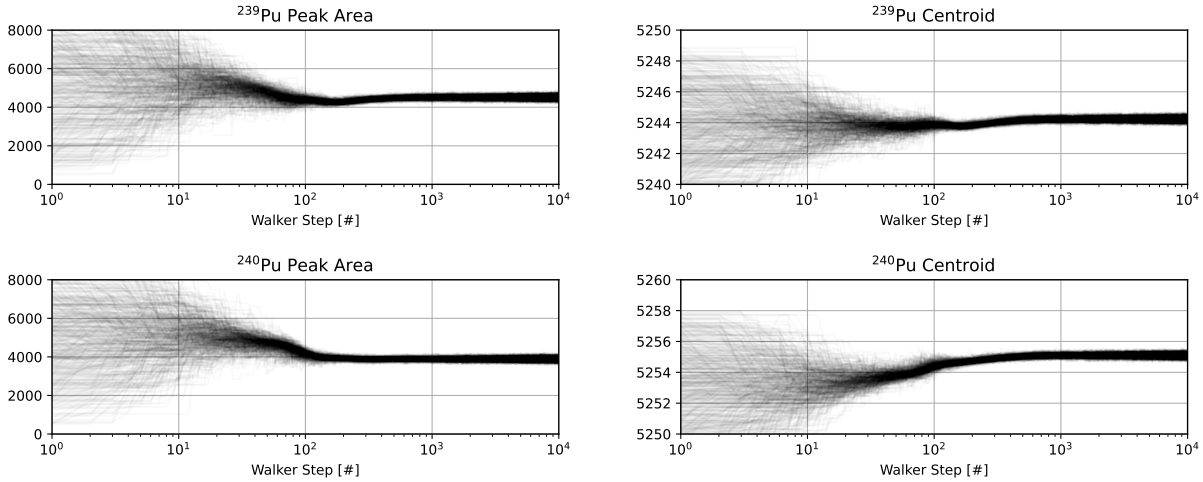

Figure 7.6: MCMC walker paths for fitting of the ^{239}Pu and ^{240}Pu peaks of EVE Run-6.

Isotope	^{239}Pu	^{240}Pu	^{243}Am	^{243}Am	^{243}Am	^{241}Am	^{238}Pu	^{241}Am	^{241}Am
Iminuit	4495.93	3849.94	695.99	29.98	620.95	4012.44	3212.34	190.74	12810.99
Uncertainty	78.65	75.68	27.93	6.93	25.12	66.76	61.41	24.11	115.35
MCMC	4510.58	3893.70	718.57	42.72	643.96	4024.11	3229.77	180.55	12874.43
Uncertainty	83.67	75.35	26.31	7.90	28.51	71.17	67.27	20.57	116.99

Table 7.9: Best fit area and centroid parameters with uncertainties for Eve Run-6 as evaluated by Iminuit and MCMC fitting routines.

7.2.4 Results

The best-fit parameters found by the MCMC algorithm are taken by projecting the final position of every walker in Figure 7.6 against the y-axis. This is shown for the ^{239}Pu and ^{240}Pu cases in Figure 7.7. The nominal values could be assessed by fitting Gaussian function(s) to the walker distribution(s). However, given that their shape is visually symmetric and regular, best-fit values are calculated by taking a simple arithmetic mean of the walker distribution while the uncertainty is taken as the square root of the variance of the walker distribution. In terms of count areas, the nominal number of ^{239}Pu decays is 4510.58 ± 83.67 and the nominal number of ^{240}Pu decays is 3893.70 ± 75.35.

Comparison between the best-fit parameters found by the Iminuit fitting routine and the MCMC fitting routine for each peak area and centroid recorded in Table 7.9 and for the peak shape parameters in Table 7.10. The nominal parameter value and uncertainty for the MCMC fit are computed in the same manner as described above in the case for ^{239}Pu and ^{240}Pu. i.e. calculating the means and variances for the distributions in Figure 7.7 but corresponding to the appropriate isotope peak. The resultant energy spectrum both as a total spectrum and individually is shown in Figure 7.8. In the left plot, the long tail component of the fits can be seen. (Reiterating) this is fit by only two parameters: a ratio parameter and a "time-constant". The ratio of long-tail amplitude (area) to peak amplitude (area) is assumed to be the same for each peak.

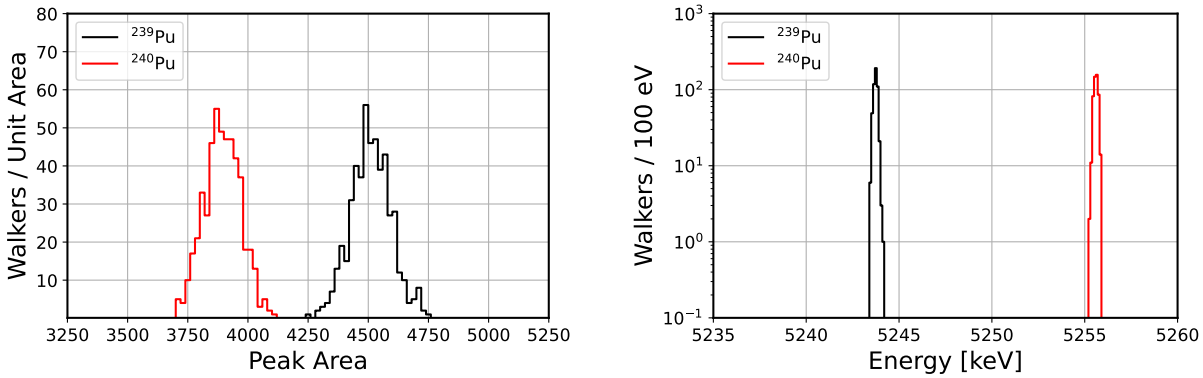

Figure 7.7: *Left*: Final-step walker position distribution of areas. *Right*: Final-step walker position distribution for centroids. Both correspond to the walker paths shown in Figure 7.6.

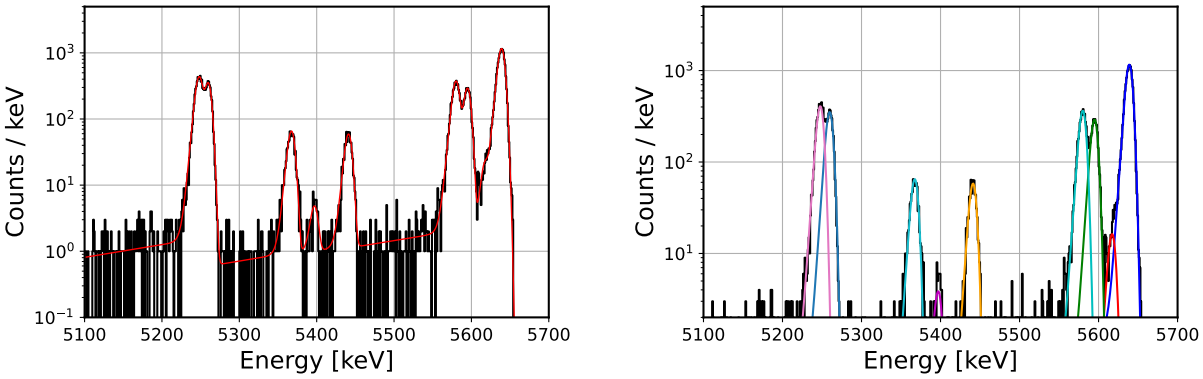

Figure 7.8: Spectral fit and components to Eve-Run-6 mixed actinide sample run.

	σ [keV]	τ_1 [keV]	R [x 10,000]	τ_2 [keV]
Iminuit	3.50	3.23	0.69	280.60
Uncertainty	0.04	0.07	0.18	94.68
MCMC	3.50	3.37	1.22	227.03
Uncertainty	0.04	0.08	0.22	51.95

Table 7.10: Best fit shape parameters with uncertainties for Eve Run-6 as evaluated by Iminuit and MCMC fitting routines.

Generally, the values converge to similar values, and in every case, Iminuit and MCMC values are within uncertainty bounds of one another. By this metric alone, it cannot be determined which fitting routine is more accurate. However, the MCMC method is preferred since the uncertainty is taken from the (square root of the) variance of the walker final positions. The convergence of the MCMC routine can be visually represented as depicted in Figure 7.6

As previously mentioned the best-fit areas for the ^{239}Pu and ^{240}Pu peaks are 4510.5813 and 3893.6956 with 1.855% and 1.935% uncertainty respectively. The activity ratio is then 1.158 with an uncertainty of 2.681%. Converting to atomic ratio composition, using Equation (7.1), gives a 239–240 ratio of 4.4846 with an uncertainty of 2.689% which includes the half-life uncertainty as reported by [123]. The possible uncertainty in the ^{239}Pu half-life is not discussed here. A large assumption built into this analysis is that any systematic effect within the measurement affects every isotope equally. If this is found to be the case, one possible approach more generally speaking would be to add a tracer isotope unrelated to nuclear forensics (e.g. ^{226}Ra or ^{210}Po) by which isotopes can be compared.

7.2.5 High β Contaminated Sample

In a realistic post-detonation scenario, or a scenario similar to the Boeing Michigan Aeronautical Research Center (BOMARC) missile explosion where fission did occur [133], a sample will be heavily contaminated with fission products. Many fission products are beta decay or electron capture decay isotopes that are short-lived, with half-lives typically of order months to years [134]. As a result, the activity from even a small quantity of contamination can vastly dominate the activities of ^{239}Pu and ^{240}Pu. It is unclear what fraction of fission products can be removed chemically before a sample is deposited for decay counting. Even the removal of a high percentage, greater than 99% may still contain a high activity fraction of fission products.

To test MMC performance under high levels of fission fragment contamination, a more realistic scenario was tested in which ^{95}Zr was added to a mixed actinide sample. ^{95}Zr is a short half-life (64 day) beta emitter with a decay energy of 1123.6(18) keV and dominant beta end points at 366.9 keV (54.5%) and 399.4 keV (44.3%) [135]. A quantity of ^{95}Zr was added to achieve a beta-to-alpha activity ratio of 1000:1. Two samples were prepared one with a nominal activity of 500 Bq and one with a nominal activity of 1000 Bq measured

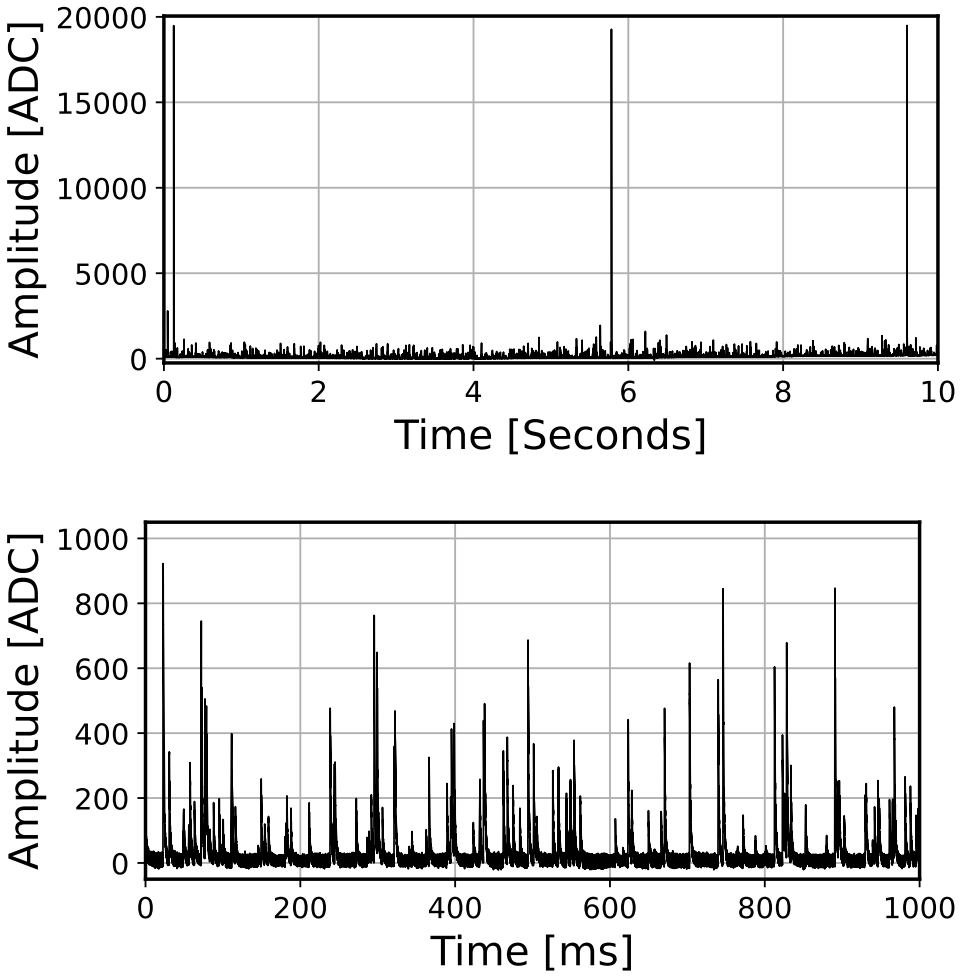

Figure 7.9: *Top*: Ten-second acquisition from Run-107 containing three alpha pulses seen at near time stamps 0.5 s, 5.75 s, and 9.5 s. Many beta events can be seen as fluctuations in the baseline. *Bottom*: Zoomed in 1 second window containing around 500 beta pulses.

in Run-107 and Run-114 respectively. This high level of beta-to-alpha is demonstrated in a 10 second and 1 second saved waveform traces shown in Figure 7.9

The total broad-range energy spectrum is shown in Figure 7.10 where the activity is evidently dominated by the decays of ^{95}Zr. A single lower energy peak can be observed on top of the beta continuum 235 keV. This line is from the internal transition decay of ^{95m}Nb. 1.13% of ^{95}Zr decays populate the excited state of ^{95}Nb which decays with a 3.6 day half-life via internal conversion [135]. The full energy is released in a single step in 24.8 % of decays [135].

The alpha spectrum was fit with the same fitting functional from, Equation (7.8), as the data of Eve Run-6. The resolution, in this case, is slightly worse and the ^{239}Pu–^{240}Pu peaks cannot be distinguished by eye, as seen in Figure 7.11. As with Eve Run-6, the spectrum was fit with both Iminuit and MCMC fitting algorithms.

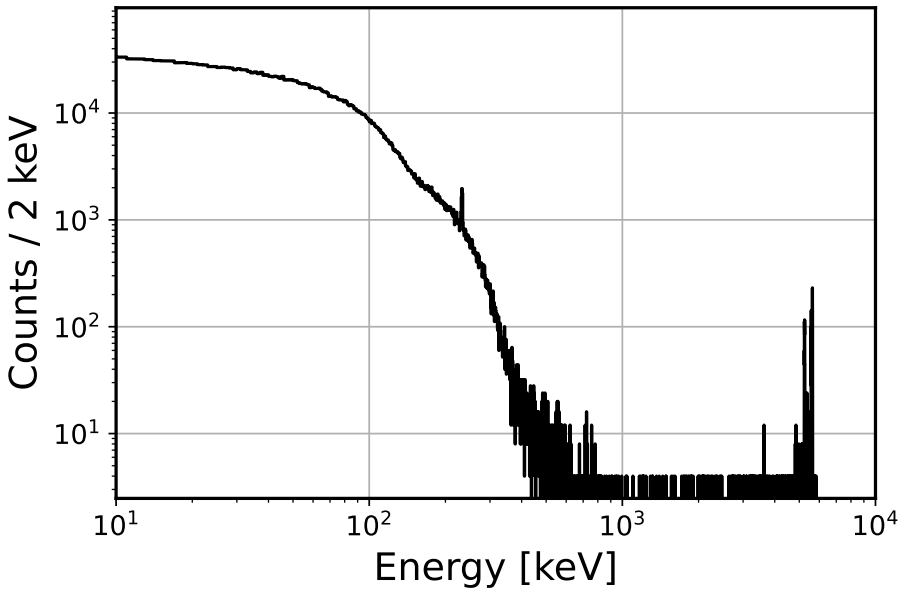

Figure 7.10: Experimentally measured decay energy spectrum from Run-107. Beta spectrum from ^{95}Zr clearly dominates the total activity. The peak observed at 235 keV is from the internal transition decay of the daughter ^{95m}Nb.

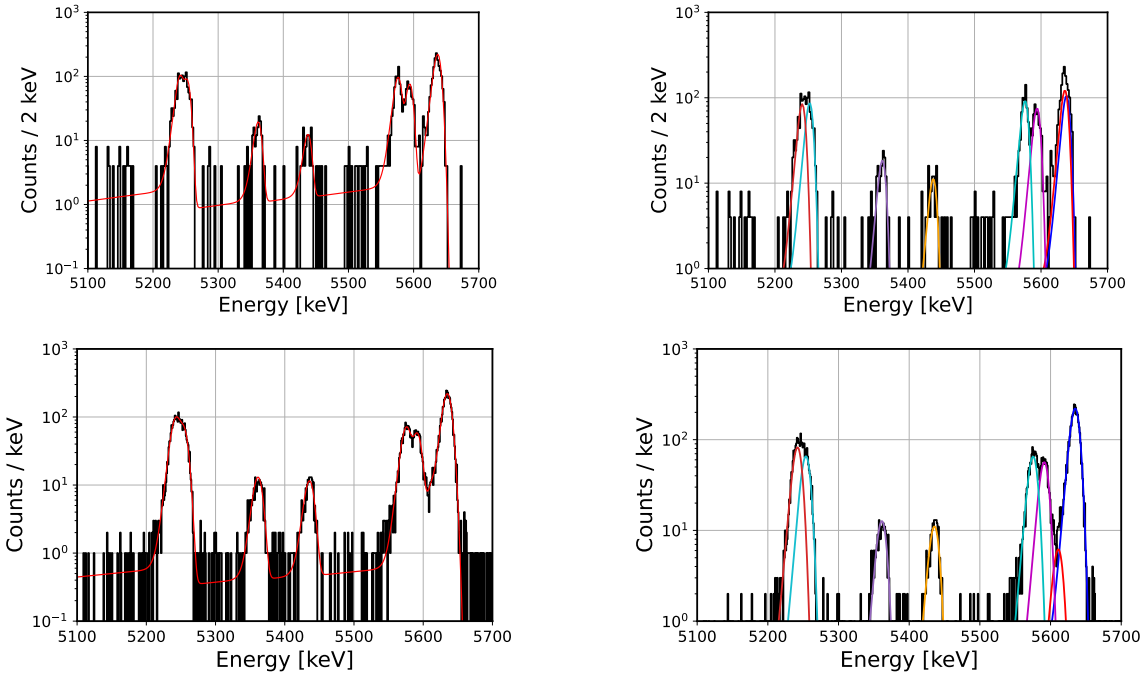

Figure 7.11: Spectral fits (left) and component fits (right) to high beta contamination sample data. The top two plots correspond to Run-107 while the bottom two correspond to Run-114.

CHAPTER 8

Measurement of Ionization Produced by 254 eV_{nr} Nuclear Recoils in Germanium

8.1 Introduction

8.1.1 Dark Matter and Neutrino Detection with High Purity Germanium

Direct detection of dark matter is among the highest priorities in experimental cosmology and particle physics [136, 137, 138]. Measurement of dark matter requires detectors with sensitivity to low energy nuclear recoils $\lesssim$ keV_{nr} as well as a good understanding of the quenching factor, the fraction of nuclear recoil kinetic energy released as ionization and/or scintillation [31]. The necessity for accurate modeling of such nuclear recoils has increased with the recent 2017 measurement of Coherent Elastic Neutrino Nucleus Scattering (CEνNS). It has been shown that the choice of quenching factor model greatly affects the degree to which experimental data agrees (or disagrees) with Standard Model predictions [139].

The application of high-purity germanium (HPGe) detectors for dark matter searches and other rare-event physics experiments have increased in popularity [140]. This trend is in part due to the commercial availability of multi-kilogram HPGe detectors with suitably low noise and low backgrounds [38, 35, 141].

Numerous collaborations have or plan to deploy HPGe detectors for experiments aimed at detecting dark matter or neutrinos via CEνNS [32, 34, 36, 142, 143, 35, 38, 39, 144, 145]. The CDEX collaboration is investigating the dark matter sensitivity of a 50 kg array of HPGe detectors [37]. Given these advancements, a dark matter search or CEνNS experiment with 100 kg of detection material could be considered in the near future.

8.1.2 Low Energy Quenching Factor

A detailed understanding of detector response to low-energy nuclear recoils is a prerequisite for experiments aimed at measuring neutrinos via CEvNS or discovering dark matter [138, 31]. For a given detection material, the percentage of nuclear recoil energy which produces electron-hole pairs is defined as the Quenching Factor [31], the micro-physics of which is described by the Lindhard interpolation of the Bethe-

Bloch stopping equation [146]. In many detector materials, including HPGe, the quenching factor is not well understood below $\sim$ 10 keV_{nr} [31, 147, 148, 149, 150, 151, 152, 153, 32, 154, 155, 156, 131, 157, 158].

A recent multi-pronged study performed by the University of Chicago (UChicago) extensively studied the HPGe detector response to low-energy nuclear recoils and reported a significantly enhanced quenching factor, greater than what is predicted by Lindhard Model in the sub-keV_{nr} regime [157, 146]. Of particular note is the measurement of the ionization produced by mono-energetic 254 eV_{nr} ^{73}Ge nuclei. The UChicago study performed the same experiment as originally conducted by Jones and Kraner (Brookhaven) but reported a 44% greater ionization yield[1] [157, 151, 150].

To address this discrepancy between the prior measurements, as well as to better understand the nuclear structure of germanium, we have re-performed the measurement with an improved experimental setup utilizing multiple detectors, modern digital electronics, and saving raw detector outputs. Our results corroborate the UChicago study [157] in disagreement with the earlier Jones and Kraner experiment [151].

8.1.3 Level Structure of ^{73m}Ge

In our experiment, 254 eV nuclear recoils are produced by the capture of a thermal neutron on a ^{72}Ge nucleus, comprising 27.4% of natural Ge, populating a 6785.2 keV excited state of ^{73m}Ge [159, 150, 151]. The decay path of interest is depicted in the right plot of Figure 8.1, where the majority of nuclear excitation is radiated via emission of a 5852.2 keV or a 5868.8 keV gamma ray and feed into the 915.2 keV or the 931.5 keV level, respectively. Only the 915.2 keV and 931.5 keV levels feed into the subsequent 68.75 keV state, which then decays to the ground state of ^{73}Ge [159, 150, 151, 160].

The de-excitation of ^{73m}Ge results in nuclear recoils by conservation of momentum. Emission of the 5852.2 keV and 5868.8 keV gamma rays produces 253.5 eV_{nr} and 252.1 eV_{nr} nuclear recoil energies, respectively. The other gamma rays emitted contribute negligibly, $\lesssim$ 1%, to the total nuclear recoil energy. Jones and Kraner calculated intensity-weighted average recoil energy of 254.1 eV_{nr} with a spread of 1.5 eV_{nr}[2] [151].

All the gamma rays released in de-excitation of ^{73m}Ge, save the lowest energy 68.75 keV gamma, have a high probability of escaping a small 2 cm^3 HPGe crystal: 1.6 cm (diameter) x 1 cm (height) [3] without interaction; the attenuation lengths in germanium are all longer than a centimeter. Attenuation lengths are calculated from the XCOM (NIST) database [161] and are listed in Table 8.2.

Simulations in MCNPX [162] framework were used to model a uniform gamma-ray source emitted from a 1.6 cm (diameter) $\times$ 1.0 cm (height) cylindrical germanium crystal. The escape fraction is given in Table 8.1 which we defined as the fraction of gamma rays for a given emission line that do not interact with the crystal, either photoelectrically or by Compton scattering. The combined probability that none of the gamma rays preceding the 68.75 keV level interact with the crystal is 30.35%, and the probability of a 68.75 keV gamma

[1] The value of 44 % is calculated using gamma-ray energy of 68.753 keV and values of 68.811 and 68.793 keV for the gamma ray plus ionization produced by the nuclear recoil.

[2] The calculation is based upon calculating the fast stopping of the ^{73}Ge nucleus compared to the lifetimes of the nuclear states.

[3] Crystal geometry of the Ortec GLP-16195/10P4 detector used in our experiment.

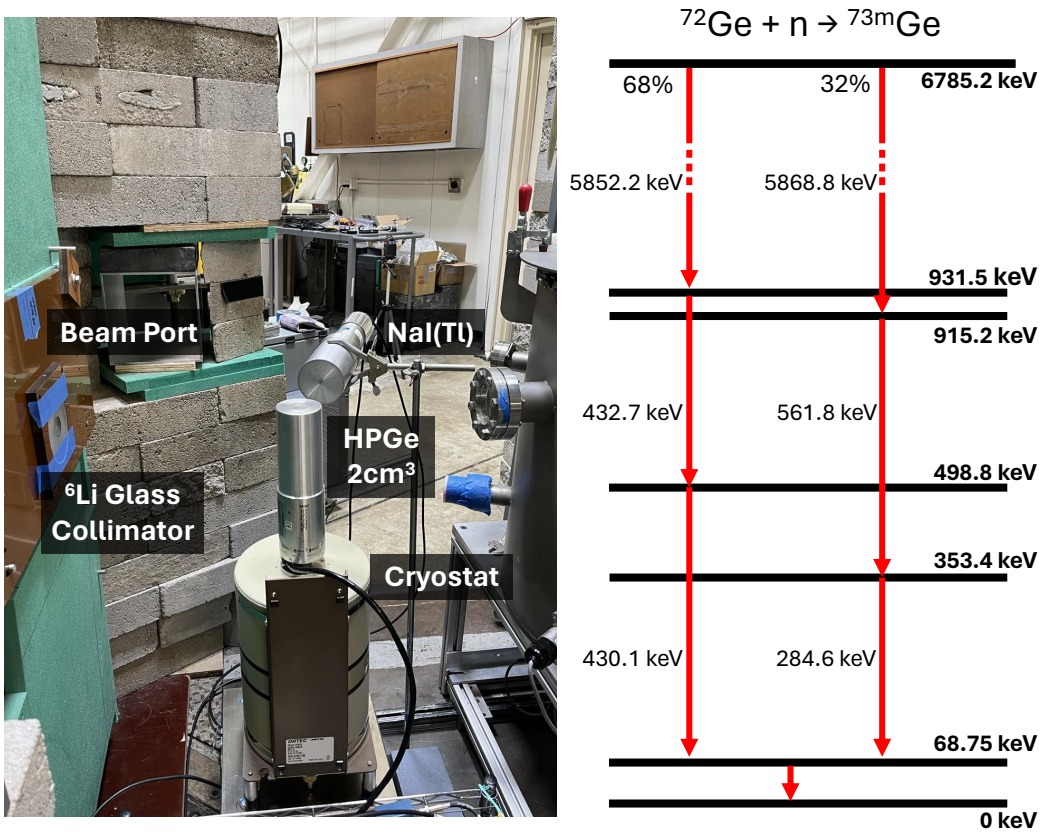

Figure 8.1: *Left*: Ortec GLP HPGe detector in OSU thermal neutron beam-line. Calibration sources were placed on top of the beryllium window for in situ calibration. The NaI(Tl) gamma tagging detector can be seen a few inches behind the HPGe detector. *Right*: De-excitation path of ^{73m}Ge which feed the 68.75 keV level.

E_γ [keV]	E_{nr} [eV_{nr}]	Attenuation [mm]	Escape Fraction [%]
5868.8	253.5	60.4	91.3
5852.2	252.1	60.3	91.3
561.8	2.3	24.3	80.7
432.7	1.4	21.1	78.4
430.1	1.4	20.0	78.3
284.6	0.6	15.9	73.5
68.75	0.0	1.3	15.2

Table 8.1: Emitted gamma rays from de-excitation of ^{73m}Ge which decay to ground via the 68.75 keV state. Attenuation lengths are calculated from the XCOM NIST database [161]. The escape fraction is calculated as the percentage of gamma rays that do not interact with the crystal and is calculated via Monte-Carlo simulation assuming a uniform source over the 2 cm^3 GLP crystal.

ray being photo-electrically absorbed within the crystal volume is 84.82%. The signal from the 68.75 keV gamma ray summed nuclear recoil is detected with an efficiency of 25.5%.

8.1.4 Prior Results

To the best of our knowledge, Refs. [151] and [157] are the only two prior measurements of combined energy deposition by the 68.75 keV gamma ray and the nuclear recoil. The ionization yield from 254.1 eV_{nr} nuclear recoils can be calculated by subtracting the gamma-ray energy from the total measured energy. We adopt a gamma-ray value of 68.753 ± 0.004 keV computed via the uncertainty-weighted arithmetic mean of the aforementioned measurements [150, 151, 163, 157, 164]

With this gamma-ray energy, the Brookhaven measurement yielded an electron equivalent nuclear recoil ionization energy of 39 eV_{ee} corresponding to a quenching factor of 15.5%. Subtracting the same gamma-ray energy from the UChicago result yields an ionization energy of 58 eV_{ee} corresponding to a quenching factor of 23%. In their work, the UChicago study adopts a gamma ray energy of 68.734 keV which when subtracted from their measured gamma plus recoil energy yields a quenching factor of 30% [157]. The energy of the gamma-ray alone significantly impacts the ionization yield, as demonstrated in Table 8.2.

Regardless of the accepted value of the gamma ray, 68.734 keV or 68.753 keV, the UChicago result is significantly greater than the ionization predicted by Lindhard theory [146]. This discrepancy motivates additional study as such an enhancement in the quenching factor would significantly improve the sensitivity of HPGe detectors to dark matter or CEνNS.

8.1.5 Digital Electronics

Jones and Kraner's result is consistent with the predicted ionization yield from Lindhard model [151, 146] while the UChicago result is in tension [157]. To address the discrepancy, we re-perform the UChicago

Study	γ + Recoil [keV]	γ [keV]	Ionization [eV_{ee}]	Quenching [%]
Brookhaven	68.793	68.753	39 ± 5	15.4 ± 2.1
UChicago	68.811	68.734	77 ± 20	30.3 ± 7.9
Brookhaven	68.793	68.753	39 ± 5	15.5 ± 2.1
UChicago	68.811	68.753	58 ± 4	22.7 ± 17
Lindhard	-	-	36.2	14.3

Table 8.2: Ionization yields and quenching factors are presented both as reported in [151, 157] and using a gamma ray energy of 68.753 keV. The Lindhard model prediction is based on a free parameter of $\kappa = 0.157$ as theoretically predicted for Germanium [146].

experiment to measure the 68.75 keV de-excitation gamma-ray summed with the nuclear recoil signal.

Both Refs. [151] and [157] utilized traditional analog shaping amplifiers and multichannel analyzers whereby only shaped pulse amplitude was saved as a data histogram [151, 157]. We measure time-coincident gamma-ray events in both an HPGe and an external NaI(Tl) detector and save raw waveforms from both detectors. We measure the lifetime of the gamma-cascade as well as perform a novel multi-shaping analysis from which we reject the hypothesis posed by Collar, Kavner, and Lewis [157] as to the difference between their result and that of Jones and Kraner [151].

8.2 Experimental Methodology

8.2.1 OSU Reactor Laboratory

The experiment was deployed at the OSU Reactor Laboratory [165]. The reactor was operated at an estimated thermal neutron flux of $1 - 2 \cdot 10^6$ cm^{-2} s^{-1}. The OSU reactor was chosen for the high thermal thermal purity of the neutron beam. The thermal neutron facility has been well characterized; only 3.76 neutrons in every 1000 emitted have energy above 0.4 eV [166]. Thermal neutron purity is critical as any momentum imparted by inelastic scattering will result in an erroneously high measurement of the quenching factor. The OSU facility is the same used by the UChicago study [157].

8.2.2 Detectors and Data Acquisition

The experimental apparatus comprised two radiation detectors: the HPGe detector, which acted as the neutron beam target, and a large external scintillation detector to tag the emitted 5.8 MeV gamma ray. The HPGe detector utilized was an Ortec GLP-16195/10P4 detector within a poptop style mounted on a multi-orientation portable cryostat [167, 168]. The HPGe crystal volume was 2 cm^3, comparable in volume to the detector used by the UChicago studies [157]. Additionally, the outward-facing ion implanted layer of the GLP detector is only 0.3 µm thick and attenuates external X rays and gamma rays to a negligible

level [168, 157, 169]. The GLP detector series is commonly used for measurement and spectroscopy of X rays and γ rays with energies between 1 and 200 keV [169], an ideal match to the energy of interest in this experiment.

The detector was placed in the reactor thermal neutron beam-line as depicted in Figure 8.1. A ^{6}Li glass disc with a 1 inch diameter hole was used to collimate the beam and reduce activation backgrounds. A null measurement was performed by placing a different ^{6}Li disc with no hole, which completely blocked the beam port. A large 3 in diameter 5 in long NaI(Tl) scintillation detector was employed for coincident gamma tagging and can be seen behind the GLP detector in Figure 8.1.

Both detector outputs were digitized at a rate of 100 MHz by a CAEN DT5780 module [170]. High voltage bias and preamplifier power to the GLP detector were provided by the same DT5780 unit. High voltage for the NaI(Tl) detector was provided by a separate CAEN DT5533E high voltage module [171].

8.2.3 Calibration

The energy scale was established using the 59.5409 keV gamma ray from ^{241}Am and the Pb Kα_1 and Kα_2 X rays, 74.9694 keV and 72.8042 keV, respectively. A ^{57}Co source and lead foil were used to produce the X rays. The calibration sources were placed on top of a copper shim just above the beryllium window of the detector. The sources were present throughout the experiment to perform *in-situ* calibration and monitor for gain drift. No such drift was observed during the experimental runs, but the calibration changed by $\sim$1% from day to day as a result of the detector being unbiased and re-biased over multiple days of measurements.

The relative timing between the GLP and NaI(Tl) detectors was calibrated at the start, middle, and end of each day of the experiment. The energy scale in the NaI(Tl) detector was established with a ^{60}Co gamma-ray source during the same periods. Continuous calibration was not performed with the NaI(Tl) detector as the source would cause an increased rate of spurious coincidences. The mid-day calibrations delineated the experiment into seven approximately equal-sized data sets. The runs were analyzed separately and the results averaged.

8.2.4 Data Analysis

Raw preamplifier output waveforms were saved in 80 µs long traces. This allowed the same data to be processed and analyzed with multiple algorithms. Pulse amplitude was determined using three digital pulse shaping algorithms: the optimal filter [57, 56, 66, 69], the trapezoidal shaping filter, and a digitally synthesized CR-RC^{8} Gaussian shaping filter. The energy of the gamma ray plus nuclear recoil was extracted from the optimally filtered data while the use of multiple shaping filters facilitated quantification of the effect of analysis methodology on the result and comparison to prior studies.

Gaussian shaping filters are commonly implemented by analog shaping amplifiers [172, 173]. A Canberra (Mirion) 2022 NIM spectroscopy amplifier with a shaping time constant of 8 µs was used in the UChicago study [157]. The specific amplifier used by Jones and Kraner [151] is not reported though the peaking time

of 4 µs is stated [4] [151]. As both prior studies utilized multichannel analyzers, the maximum value of the Gaussian-shaped signal within the saved trace window is taken as the pulse energy [5] The waveforms were processed with multiple shaping time constants as to test the previous hypothesis that the choice of shaping time is the cause of the difference between their result and Jones and Kraner's result [157, 151].

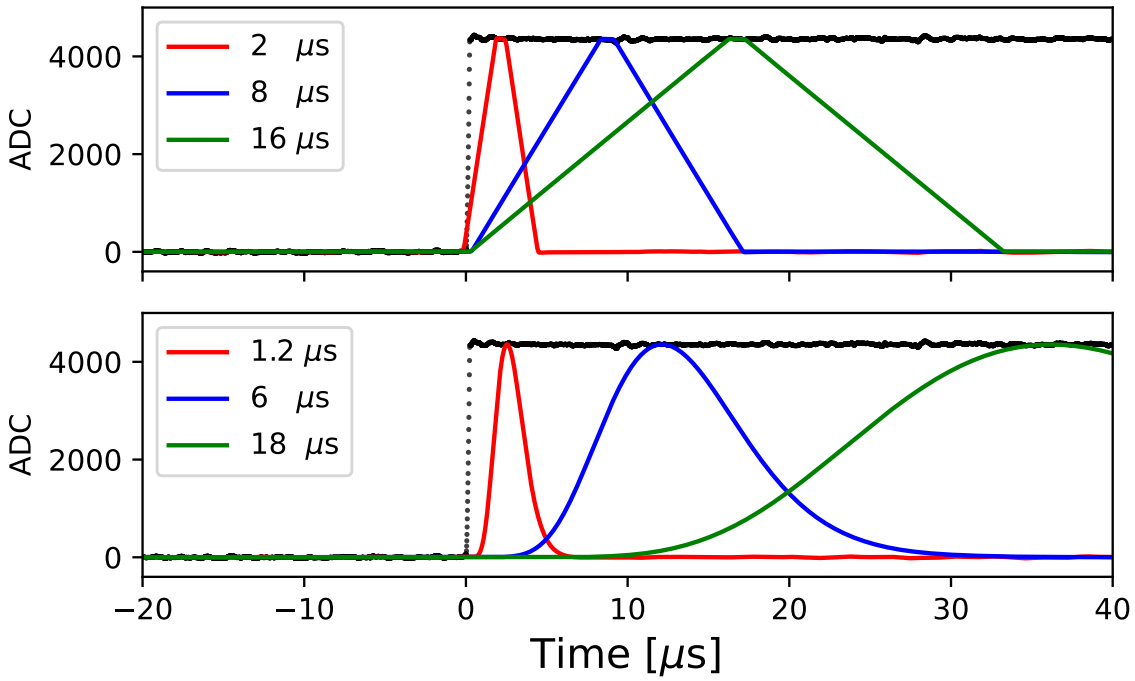

Figure 8.2: Multiple shaping time Trapezoidal and Gaussian (CR-RC^8) filters (*colored*) applied to the same digitized waveform from the HPGe detector (*black*).

The trapezoidal filter was also implemented as it is typically the filter of choice for HPGe signal analysis [172, 174, 175]. The filter is well characterized and has been digitally implemented since the mid 1990's [53, 54, 172, 174]. Three trapezoids with different peaking times, 2, 8, and 16 µs, were chosen to similarly test the effect of shaping time. An 800 ns flat-top time was chosen to be sufficiently longer than the detector ~100 ns (10–90%) rise time such that ballistic deficit is minimized [172]. The amplitude of the trapezoidally shaped signal was determined by sampling the middle of the flat top. The sample position was chosen by adding the associated peaking time and half the flat-top time to the pulse onset position. Sampling the flat-top is more robust to noise fluctuations than taking the shaped signal maximum.

Minimal cuts were applied to the dataset in an attempt to not bias the result. Events were cut from the analysis based on a saturation cut and a pile-up cut. The effects of the pulse cuts within the energy range of interest are shown in Figure 8.4. The pile-up cut minimally affects the region around the 68.752 keV gamma

[4]The peaking time of a Gaussian filter is typically 2–2.5 times longer than the shaping time constant [173, 172]

[5]Jones and Kraner do not directly state use of a multi-channel analyzer but it can be inferred as the x-axis units on their spectra are labeled in units of channel number.

ray. The region from 55 keV to 66 keV is greatly affected due to the 66.725 keV state, which decays by emission of 53.4 keV and 13.3 keV gamma rays, the latter with a half-life of 2.91 µs [176, 177, 178]. The energy spectrum with and without the pile-up cut applied is shown in Figure 8.4. This exponential feature is observed in the UChicago study [157]as well as other neutron irradiation experiments [179] but is not observed in Jones and Kraner's measurement [151].

8.3 Results

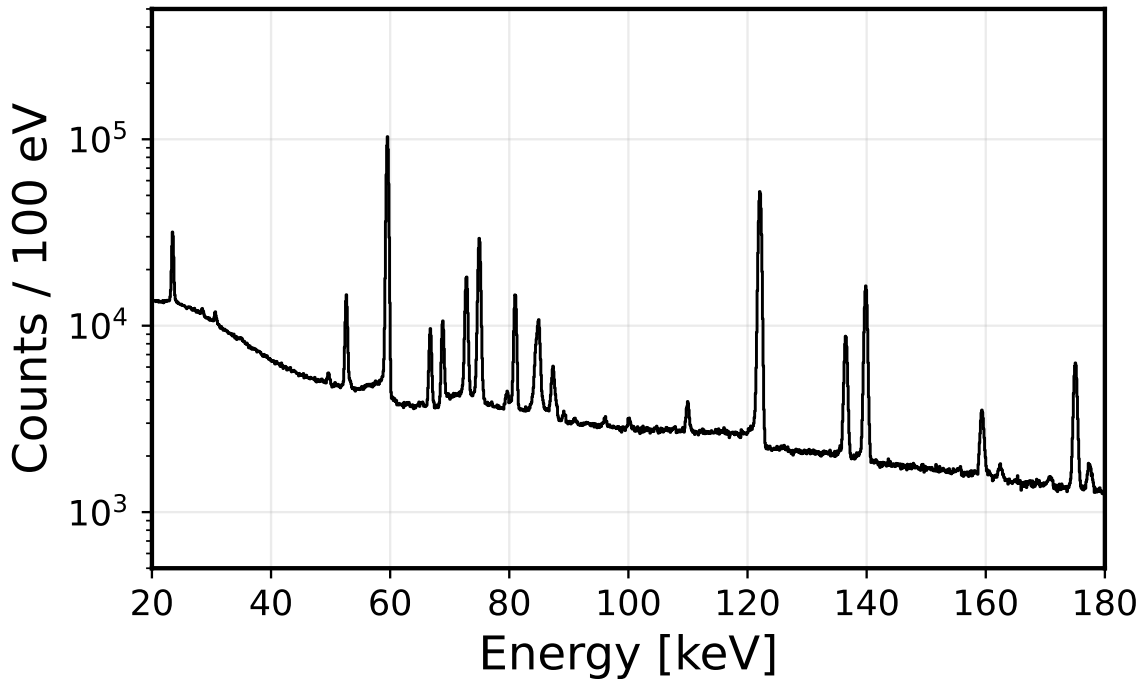

Figure 8.3: Acquired energy spectrum for all data sets (1–7) form 20 keV to 180 keV with the analysis region from ~55 keV to ~80 keV.

8.3.1 Energy Spectrum

The best resolution was achieved with the optimally filtered data set. We use this data set for our primary analysis while the trapezoidally filtered and Gaussian shaped data sets were used for assessing the systematic contribution from the choice of pulse processing methodology.

In each of the data runs, the ^{241}Am gamma peak and the Pb kα_1 and kα_2 X-ray peaks were fit with Gaussian functional forms with small correction functions based on [180]. The peak centroids were fit with a linear calibration function. These three peaks were chosen to provide the most accurate energy scale where

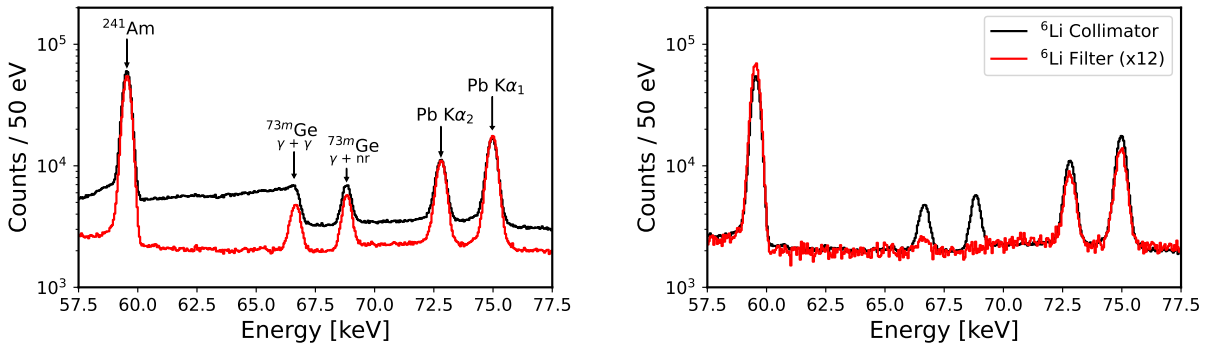

Figure 8.4: *Left*: Experimental energy spectrum within energy range of interest with calibration and ^{72}Ge (n,γ) peaks labeled as acquired in black and after pile-up cuts in red. *Right:* Overlay of the null run with ^{6}Li disk filter.

the total energy deposition from a 68.75 keV gamma ray and nuclear recoil. The entire energy spectrum is shown Figure 8.3. The calibration peaks can be seen bounding the gamma plus recoil peak in Figure 8.4.

The robustness of the energy scale was tested by performing an additional calibration using the 122 keV and 136 keV gamma-ray peaks. The change in scale was negligible compared to other uncertainties. The combined energy spectrum from 50 keV to 80 keV is shown in Figure 8.4 before (black) and after (red) pile-up cuts.

The only feature strongly affected by the cuts is the aforementioned decay of the 66.7 keV state which is not associated with the decay path of interest but is seen just to the left of the gamma plus recoil peak in Figure 8.4. The 66.7 keV peak was fit with an exponentially modified Gaussian functional form, the extracted energy from which was 66.720 ± 0.011 keV, which closely agrees with the literature reported value of 66.725 ± 0.009 keV [164].

Thermal neutrons emitted from the beam port were verified to be the source of the signal. This was achieved by replacing the ^{6}Li glass collimator with a solid ^{6}Li glass glass disk for one three-hour data run. During this null measurement, the 68.75 keV gamma plus nuclear recoil peak was not observed. Other peaks associated with neutron reactions on germanium observed during the data runs similarly were not seen or were seen at a significantly reduced rate during the null measurement as shown on the right of Figure 8.4.

8.3.2 Recoil Ionization + Gamma Energy

The peak attributed to the combined energy deposition of a 68.75 keV gamma ray and nuclear recoil is fit with a Gaussian with a step to high energy with the functional form described by Equation (8.1).

$$f(x,\vec{\pi}) = \frac{A}{\sqrt{2\pi}\sigma} e^{-(x-\mu)^2/(2\sigma^2)} + \frac{B}{2} \cdot \mathbf{erfc}\left[\frac{\mu - x}{\sqrt{2}\sigma}\right] \tag{8.1}$$

Parameters A and B are the area of the Gaussian and the amplitude of the step, respectively; μ and σ are the mean position and resolution. The step position and smearing of the rising edge are fixed to the same

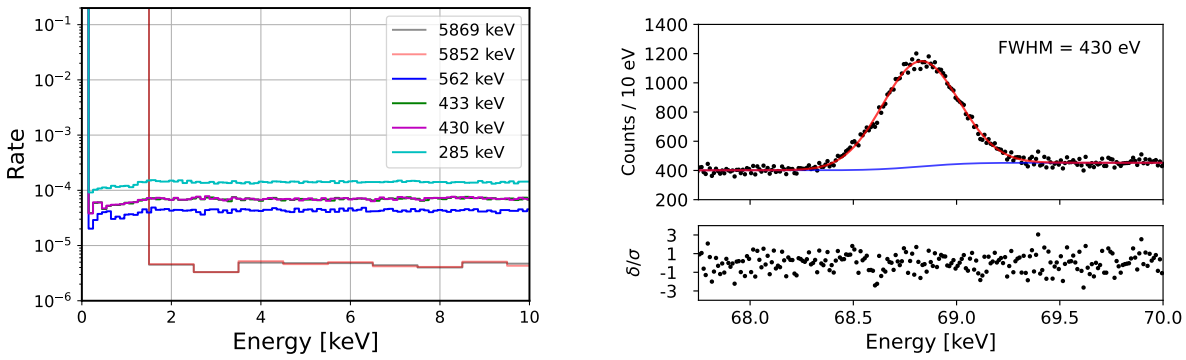

Figure 8.5: *Left*: MCNP spectrum Compton Spectrum with rates normalized to per 68.75 keV gamma decay. *Right:* Fit and residual to peak associated with the 68.75 keV gamma ray and nuclear recoil signal for all data sets (1–7).

centroid and resolution as the peak as justified in [181, 180]. Fit to the Optimal filtered data spectrum peak with this functional form and the fit residual are shown in Figure 8.5.

We hypothesize the step structure to be formed when one of the gamma rays emitted prior to the 68.75 keV gamma ray and within the same gamma cascade Compton scatters within the crystal volume. Energy is summed from the 68.75 keV gamma ray, nuclear recoil, and the Compton electron. This pushes the deposited energy higher and outside of the primary peak. To test this hypothesis, the Compton spectra from each of the preceding gamma rays in the energy region of 0–2 keV was simulated in the MCNP framework [162] which are shown on the left plot of Figure 8.5. After accounting for the branching ratios and detection efficiency, the simulated ratio of the Compton spectrum amplitude in the total gamma plus recoil peak area was calculated to be 0.125% whereas the ratio of best fit A and B parameters yields 0.16 ± 0.01 %. This functional form was found to fit the combined total data set well with a reduced Chi-Squared value of 211.43/(225 - 5) = 0.961.

Each data set was fit with the functional form. The mean value, uncertainty of the mean, and calibration uncertainties are reported in Table 8.3. The fit values were averaged using an inverse error-squared weighted arithmetic mean. The energy of the gamma ray plus ionization from the 254 eV_{nr} nuclear recoil as 68.816 ± 0.002 keV_{ee}. Subtracting the gamma energy of 68.7532 keV yields an ionization of 62.7 ± 4.7 eV_{ee}, corresponding to a quenching factor value of 24.7 ± 1.8%.

8.3.3 Lifetime of Nuclear States

Jones and Kraner state the lifetime of the 68.75 keV state to be 700 ns, and the preceding states in the de-excitation cascade have sub-nanosecond lifetimes [151]. We define the *effective lifetime* of the 68.75 keV state as the sum of its lifetime and the lifetimes of the preceding 353 and 915 keV states (or 499 and 932 keV states depending on the de-excitation path). This determines the delay between the nuclear recoil and the 68.753 keV gamma-ray signal within the HPGe detector. The UChicago study stipulates this 700 ns lifetime paired with the difference in time constants utilized in their shaping amplifiers to be the root cause in the difference between their and the earlier result [157].

Run	E_γ + E_{nr} [keV]	Fit [eV]	Slope [eV]	Intercept [eV]	Total [eV]
Run-1	68.8190	6.6	2.4	2.4	7.4
Run-2	68.8486	10.8	4.5	5.1	12.7
Run-3	68.8205	5.5	3.1	3.3	7.1
Run-4	68.8206	4.2	2.5	3.0	5.8
Run-5	68.8269	3.8	2.4	2.4	5.1
Run-6	68.7998	4.5	2.8	3.9	6.6
Run-7	68.8032	4.2	1.4	2.0	4.9
Combined	68.8159	1.8	0.9	1.1	2.4

Table 8.3: Mean parameter of Gaussian fit to the 68.75 keV gamma plus recoil peak and uncertainty parameters.

The effective lifetime is measured by finding time-coincident pairs of events between the GLP and NaI(Tl) detectors. Energy gating is enforced such that only coincident pairs where between 68.4 and 69.3 keV of energy was deposited within the Germanium detector and more than 4 MeV was deposited within the NaI(TL).

A strong time-correlated signal was observed for the energy-gated events as shown in Figure 8.6. 373 coincident pairs were found between -100 and 200 ns. We define two background populations, spurious and accidental coincident events. Spurious events are defined as randomly time coincident events within the HPGe and NaI(Tl) detectors which are from unrelated sources. This flat background is estimated to be 6 pairs per 100 ns. We define the "accidental" background as true coincident interactions between the two detectors, such as Compton scattering from external gamma rays which are not associated with the 68.75 keV state of ^{73}Ge.

The accidental coincidence rate was estimated by applying a similar energy gate around the 122 keV ^{57}Co peak; 36 accidental coincident pairs were found after scaling for the peak area. Therefore, of the 373 time-tagged events, 319 are a result of the ^{72}Ge (n,γ) reaction, a signal-to-background of ~7:1.

$$f(x,\vec{\pi}) = \frac{A \cdot e^{-(x-\mu)/\tau}}{2} \cdot \mathbf{erfc}\left[\frac{\mu - x}{\sqrt{2}\sigma}\right] \tag{8.2}$$

The 100 MHz digitizer was selected with the expectation of a 700 ns state lifetime and therefore was sub-optimal to precisely measure the lifetimes shorter than a few 10s of ns. However, it can be concluded that the lifetime is significantly shorter than 700 ns. The nuclear lifetime was evaluated by fitting the functional form defined in Equation (8.2) to the time difference distribution of coincident pairs. The nominal fit values found a full-width half-maximum of 24 ns with a tail time constant of 22 ns. After de-convolution of the inherent detector response, determined from the ^{22}Na calibration data, the effective lifetime was found to be 17.2 ± 7.6 ns. This effective lifetime is ~100 times shorter than the shaping time constant utilized by Jones and Kraner and would therefore have a negligible effect on their result. The shaping time argument is therefore insufficient to explain the difference between the UChicago result and Brookhaven result.

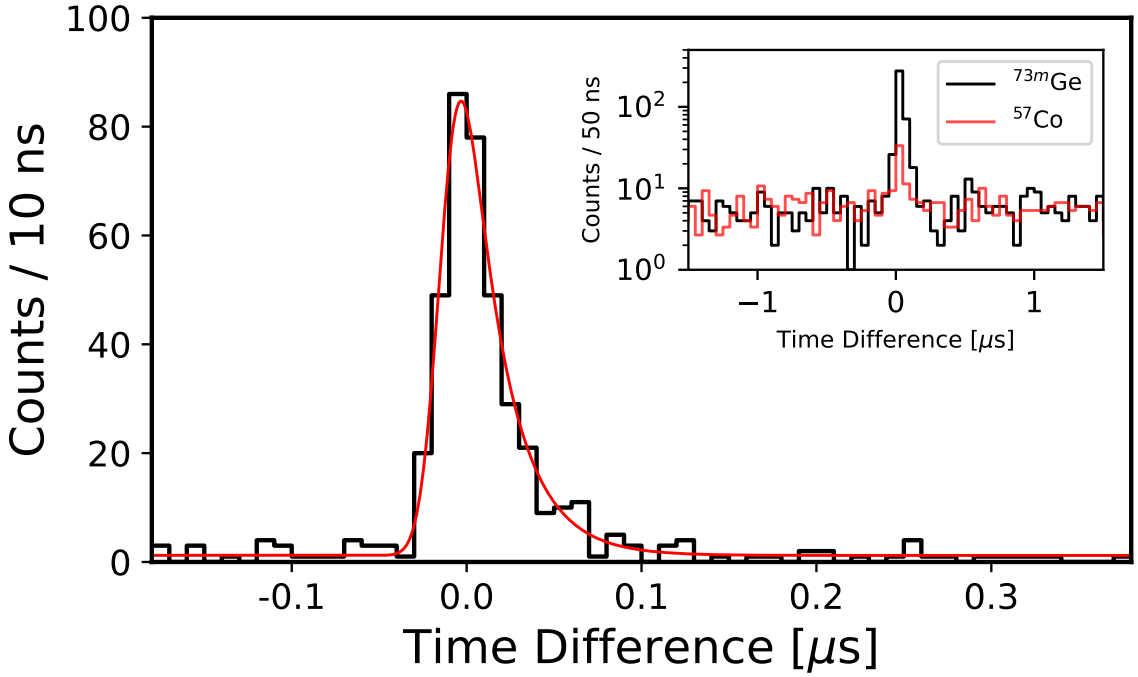

Figure 8.6: Time difference distribution between GLP and NaI(Tl) detectors after application of energy gating cuts to select events within the 68.75 keV gamma plus recoil peak and greater than 4 MeV energy deposition within the NaI(Tl). *Insert*: Time difference for both the aforementioned gamma plus recoil peak as well as the 122 keV ^{57}Co gamma peak to access the level of spurious and accidental coincident events.

8.3.4 Energy of Time Coincident Events

The energy of the gamma plus recoil signal can be assessed directly from the saved time-tagged waveforms independent from the fictional form fit to the peak. The amplitude of the time-coincident waveforms is averaged and found to be 68.814 keV with a standard mean error of 7 eV. The total uncertainty This uncertainty is added in quadrature with the calibration slope and intercept uncertainty of 0.9 eV and 1.1 eV respectively the values of which are the combined uncertainties in Table 8.3.

Additional uncertainty arises from the 18 spurious coincident events. The contribution of which was estimated by running a Monte-Carlo by which the energy of 18 randomly selected waveforms was changed to a new value sampled from a flat energy distribution and then the mean was re-calculated. This was found to alter the average by 3 eV. A Gaussian distribution was also sampled but found to change the mean by less than 1 eV. The more conservative case value of 3 eV was selected to represent this uncertainty. The 36 accidental coincident events by contrast are not expected to alter the average of the waveform population. The requirement of a minimum of 4 MeV being deposited within the NaI(Tl) detector necessitates that any accidental coincident event originate from a high-energy gamma-ray interaction. Therefore, the energy deposited within the HPGe crystal from the Compton interaction will be flat with energy.

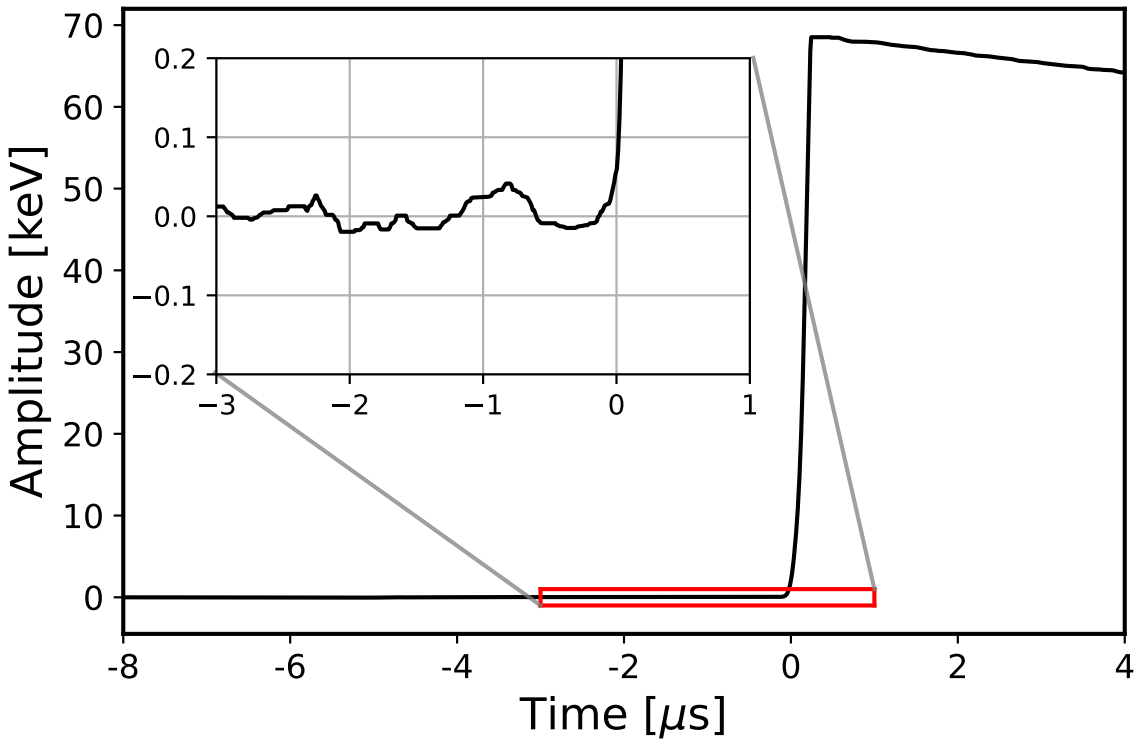

Figure 8.7: Average waveform from time tagged events with zoom-in on baseline. The pulse amplitude has been scaled to approximately be in units of keV. The enhanced view has a dynamic range from -200 eV to 200 eV. Even with limited statistics, a 60 eV signal could be seen were it sufficiently separated in time before the 68.75 keV gamma ray onset.

From this analysis we attest the energy of events known to be comprised of both the 68.75 keV gamma ray and the 254 eV nuclear recoil signal to be within the energy range of 68.814 ± 0.008 keV_{ee}. This value is in agreement with 68.816 ± 0.002 keV_{ee} found by spectral fitting and supports it's adoption as our reported value.

When the 700 ns lifetime was hypothesized, it was hoped that the ionization from the nuclear recoil signal could be extracted and separated from the 68.75 keV gamma signal by aligning waveforms in time and averaging them to eliminate the noise. Since the lifetime of state is shorter than both the detector rise time as well as the sampling rate of the digitizer, this is not possible.

8.3.5 Multi-Shaping Analysis

To further study the hypothesis of the impact of shaping time impacts the reconstructed energy of the gamma plus recoil peak, trapezoidal and Gaussian shaping filters varying the shaping time-constants. The data was analyzed with three trapezoidal shaping times, 2, 8, and 16 μ s, and four Gaussian shaping times, 2, 6, 12, and 18 μ s. This analysis is enabled by saving raw preamplifier outputs from the detector(s) and a digital signal processing-based analysis.

For both the trapezoidal as well as the Gaussian shaping filters of all time constants, the reconstructed energy of the 68.75 keV gamma-ray plus nuclear recoil signal did not significantly vary. The uncertainty terms are larger due to poorer resolution of both the calibration lines as well as the gamma plus recoil peak itself.

The results of the multi-shaping analysis are shown in Figure 8.8 with our accepted value from the optimal filter in black, trapezoidally filtered in blue, and Gaussian filtered in red. The results are compared against those from Ref. [157] and Ref. [151]. The multi-shaping analysis does not account (find a better word) for statistical nor other systematic effects but demonstrates that analysis methodology, choice of shaping filter, and shaping time-constant are not capable of explaining the difference between the more recent studies (this work and Ref. [157]) and the earlier Brookhaven study [151]. This is further consistent with our measured lifetime of the nuclear states which decay on a time scale more ~three orders of magnitude faster than the shaping time constants utilized in this study as well as in Refs. [151, 157].

8.3.6 Position Dependence

One potential systematic effect discussed in neither of the two previous studies is the possibility of a calibration offset caused by the difference in the average location of ^{72}Ge(n,γ) events compared to the calibration sources. The combined 68.75 keV gamma and nuclear recoil signals are produced uniformly in the HPGe crystal whereas the ^{241}Am gamma rays and Pb X rays predominantly interact near its top surface. We demonstrate no evidence for such position dependence through measurement of the decay of ^{71}Ge produced in the crystal by neutron activation.

Neutron irradiation resulted in HPGe detector activation by production of radioactive ^{71}Ge, which decays via electron capture and emits 10.367 keV X rays corresponding to the K-edge of the daughter

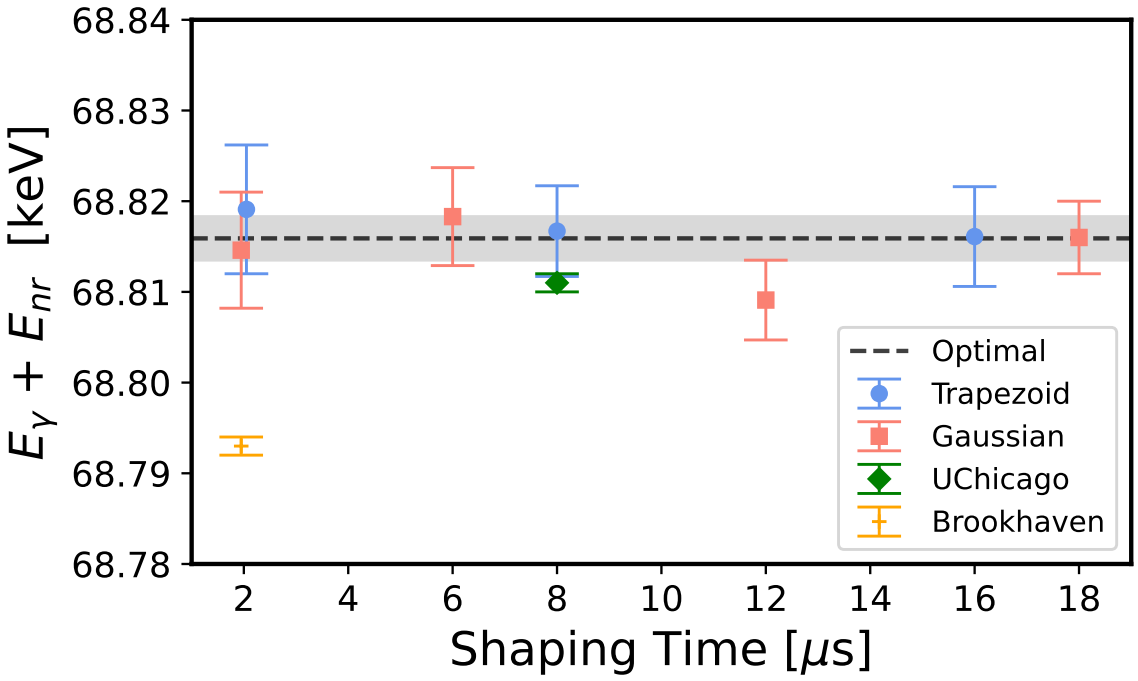

Figure 8.8: Energy of the gamma ray plus nuclear recoil signal evaluated by Optimal filter (*black*), Trapezoidal filter (*red*), and Gaussian filter (*blue*) compared against the results from Ref. [151] and [157].

^{71}Ga [182, 183, 184]. Similarly to the combined energy deposition by the ^{73m}Ge gamma ray and nuclear recoil, the ^{71}Ge decays are uniformly distributed throughout the depth of the HPGe crystal. Following the neutron irradiation, we measured the 10.37 keV X rays, utilizing the 14.4 keV gamma ray, and 6.4 and 7.1 keV Fe X rays from ^{57}Co for calibration. The ^{71}Ge peak and calibration peaks analyzed with the same optimal filter analysis are shown in Figure 8.9. The ^{71}Ge was fit with a Gaussian and a linear background term. The peak centroid was found to be 10.370 keV with a combined (fit and calibration) uncertainty of 4.4 eV. This value is within the uncertainty of both the accepted literature value of the ^{71}Ga k-edge and the other measurements of ^{71}Ge decay [182, 183, 184, 33, 185]. Were there a calibration offset between events near the surface and in the bulk of the crystal, the effect would be even more evident for the less penetrating 10.37 keV than for the 68.75 keV gamma rays. From this analysis, we conclude that no significant systematic offset exists due to the event position dependence.

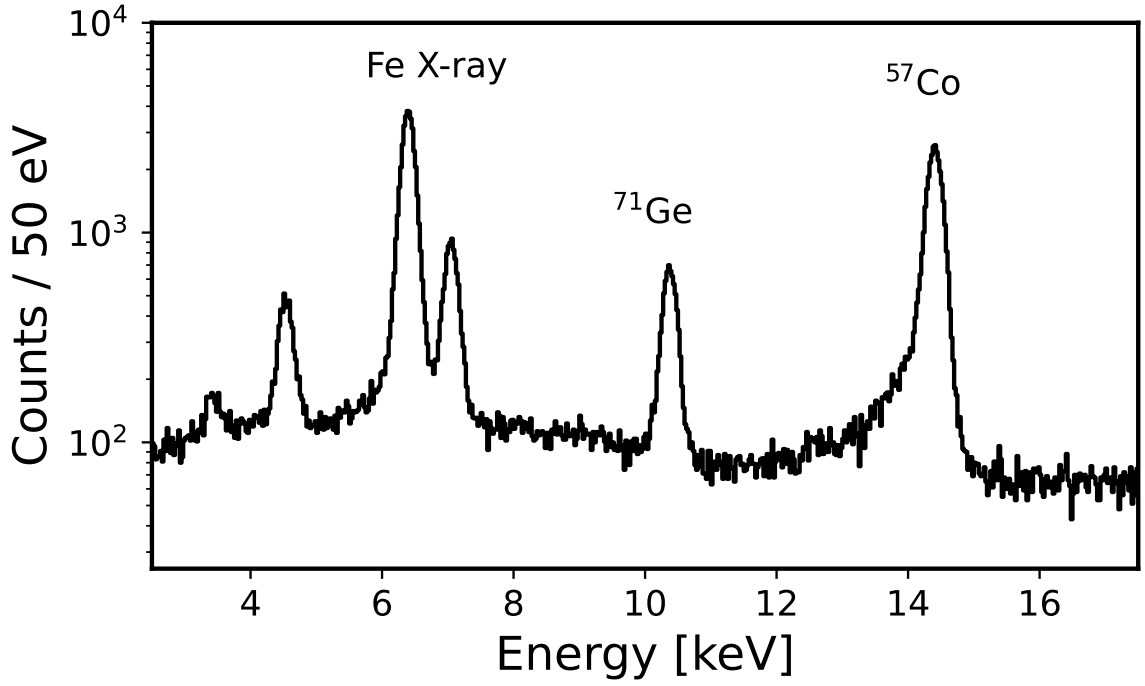

Figure 8.9: Low-energy spectrum following neutron irradiation. The ^{71}Ge 10.37 keV peak is between the Fe X-ray peaks and the 14.4 keV gamma-ray peak, both from the ^{57}Co calibration source.

8.4 Quenching Factor

8.4.1 Gamma Ray Energy

The quenching factor is determined by subtracting the nuclear state energy from the combined gamma plus recoil energy. The energy of the state has been measured several times from which we compute our average value of 68.753 keV [151, 157, 160]. It is possible that some yet unknown systematic affected these past results but this would not explain the discrepancy between the Brookhaven result and the more recent results. For this reason, as well as good agreement in the measurement of the 66.725 keV state, we maintain our adopted 68.753 keV until future measurement demonstrates otherwise.

8.4.2 Enhanced Quenching & Toy Model

Our result, in agreement with the 2021 UChicago result, indicates an enhancement in the quenching factor of Germanium over the theoretical prediction by Lindhard [146]. Furthermore, in the keV $_{nr}$ regime, nearly all the experimental quenching data is above what is predicted by Lindard, as demonstrated in Figure 8.10. The CDMS experiment measures a lower quenching factor but the experiment is conducted at millikelvin temperatures and thus different microphysics occur, though I personally am convinced their

points are systematically low for experimental measurement/analysis reasons. A recent study by the CONUS collaboration in the nuclear recoil range of 1–10 keV_{nr} found a best fit Lindhard parameter of $\kappa = 0.162 \pm 0.004$ [158].

A toy model has been developed by which the ionization produced by a nuclear recoil is predicted by the Lindhard model plus a fixed number of electrons. The theoretical prediction curves for the Lindhard model $\kappa = 0.157$, Lindhard plus 6 electrons, and Lindhard plus 12 electrons are drawn in Figure 8.10. This is not a rigidly motivated model but demonstrates the addition of a few extra electrons dramatically enhances the quenching factor below 1–2 keV_{nr} while converging back to Lindhard above. Further work is being undertaken by Professor Fei Gao who is a topical expert in radiation damage by heavy ions.

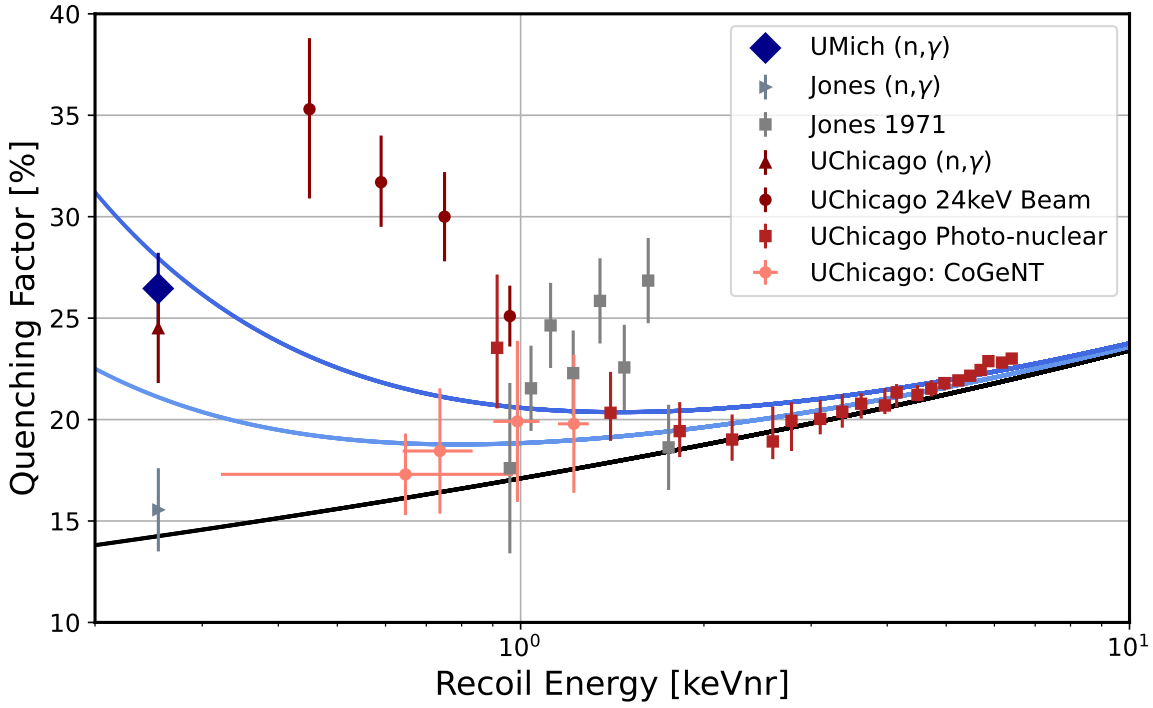

Figure 8.10: Quenching factor data by measurements performed by Jones and Kraner, UChicago, and UMichigan. Lindhard model with free parameter $\kappa = 0.157$ is drawn in black with the blue curves being the motivated toy model.

CHAPTER 9

Conclusion

9.1 Summary of Results

To the best of knowledge of our team, this work represents the first half-life experiment of a long-lived isotope utilizing cryogenic detectors. The scientific interpretation of the 86 million year half-life value of ^{146}Sm is outside of my scientific expertise. However, according to Dr. Lars Borg at LLNL, this "fixes more than it breaks". The implication can be more quantitatively assessed in context that a second group performed a ^{146}Sm half-life measurement (with more traditional detector technology) and is expected to publish a result of ~90 million years. Therefore in the time of my PhD, the spread in the measured half-life value has shrunk from 67–103 million years to 86-90 million years. Ironically, if one took the average of the Kinoshita and Meissner values it would give a half-life of 85 million years while an error-weighted average would give 91 million years.

More broadly speaking the techniques to perform precision half-life measurements utilizing cryogenic microcalorimeters have been developed in addition to various means of accessing the uncertainty. A digital signal processing toolkit has been developed in addition to numerous statistical analyses. Source preparation has been studied and repeatability demonstrated. Further work is required on the latter given that in the CRM-126 case study, only 2 of the 3 measurements yielded close results. The broader success of these experimental campaigns demonstrates growing use cases for cryogenic detectors as a tool for nuclear physics measurement.

9.2 Future MMC Work

Improved understanding of source preparation and the micro-physics / chemistry of how the source embeds itself within a thermal absorber is of high relevance to the continued development of microcalorimetry for nuclear physics applications. Extreme levels of care were taken in preparation of the ^{146}Sm source and its deposition for the half-life experiment. Such levels of care are not always practical for nuclear safeguards or nuclear forensics systems. However, as demonstrated by the CRM-126 case study, only 2 of the 3 samples attained consistent results. It is not known where or how the sample-2 was affected or altered. A systematic

study of source preparation, handling, deposition, and integration within the absorber would provide valuable insight for the development of higher technical readiness level systems.

9.3 Future Germanium Work

9.3.1 Gamma Ray Measurement

The quenching factor of germanium at 254 eV_{nr} is calculated from the difference between the measured gamma ray plus recoil energy with the energy of the gamma ray alone. The gamma ray energy has been measured by several different groups by different means [151, 157, 160]. However, given the implications of the result, a new measurement is motivated.

The challenge with the measurement of the gamma ray alone is that high-purity germanium detectors are the instrument of choice for gamma-ray spectroscopy in this energy region. However, the HPGe detector would be sensitive to the recoil and thus cannot be used to measure the gamma ray alone. The efficiency of silicon detectors diminishes significantly and thus something like a CdTe detector or CZT detector would be the optimal choice.

The experimental setup described in Chapter 8 should be recreated but replacing the HPGe detector with a CdTe detector and the germanium with an inert piece of the metal. Statistics can be enhanced by using an enriched ^{72}Ge sample. An example of such a viable CdTe detector available is shown in Figure 9.1.

Figure 9.1: Amptek CdTe detector system designed for gamma ray measurements from 3 keV to ~150 keV. The detector preamplifier output is available and can be digitized by a CAEN digitizer or similar.

9.3.2 Higher Statistics Measurement

A higher fidelity measurement of the quenching factor can be performed by improving the statistics in the previous measurement. This can be achieved by adding additional gamma-ray detectors in an array. This also allows directional reconstruction of the recoiling nucleus which would allow testing of radiation damage models based on the recoil's direction relative to the crystal lattice. Since we have demonstrated a very short lifetime of the nuclear state(s) a faster digitizer such as the CAEN model 5725 or 5730 would allow for improved timing.

The previous measurement suffered high dead time due to the significant quantity of traces being saved. This can be improved by implementing a forced coincident cut on board. This is not ideal as it eliminates the *in-situ* energy calibration but this can be overcome using multiple digitizers. For example, one output from the HPGe detector is digitized by the 5780 for energy calibration and the other is digitized by the 5725 / 5730 with forced timing coincidence with gamma-ray detectors.

Other tests of the model could be varying bias to test charge collection/trapping and other radiation damage effects. Further work would be the use of this data and model to produce a simulation of neutrino and dark matter signals within HPGe within the new quenching paradigm.

BIBLIOGRAPHY

[1] A. Fleischmann, C. Enss, and G.M. Seidel. *Metallic Magnetic Calorimeters*, pages 151–216. Springer Berlin Heidelberg, 2005.

[2] S. Kempf, A. Fleischmann, L. Gastaldo, and C. Enss. Physics and applications of metallic magnetic calorimeters. *Journal of Low Temperature Physics*, 193(3-4):365–379, 2018.

[3] A. Fleischmann, T. Daniyarov, H. Rotzinger, M. Linck, C. Enss, and G.M. Seidel. Magnetic calorimeters for high resolution x-ray spectroscopy. *Rev Sci Instrum*, 74:3947–3954, 2003.

[4] M.J. Berger, J.S. Coursey, M.A. Zucker, and J. Chang. Estar pstar and astar: Computer programs for calculating stopping-power and range tables for electrons, protons, and helium ions (version 1.2.3). http://physics.nist.gov/Star.

[5] E. Browne and J.K. Tuli. *Nuclear Data Sheets*, 122, 2014. https://www.nndc.bnl.gov/nudat3/.

[6] A.R.L. Kavner and *et. al.* Study of pile-up effects in decay energy spectroscopy. *Journal of Low Temperature Physics*, 209:1070–1078, 2022.

[7] S Pommé. The uncertainty of the half-life. *Metrologia*, 52(3), 2015.

[8] S Pommé. Fundamental uncertainty equations for nuclear dating applied to the ^{140}ba-^{140}la and ^{227}th-^{223}ra chronometers. *Journal of Environmental Radioactivity*, 162-163:358–370, 2016.

[9] N.K. Kuzmenko. Current status of the recommended half-lives for the radionuclides used as the standards of photon emitters. *Applied Radiation and Isotopes*, 180, 2022.

[10] S. Heinitz, I. Kajan, and D. Schumann. How accurate are half-life data of long-lived radionuclides? *Radiochimica Acta*, 110:589–608, 2022.

[11] K.D. McKeegan and A.M. Davis. *Early Solar System Chronology*. Pergamon, Oxford, 2007.

[12] L.K. Fifield and U. Morgenstern. Silicon-32 as a tool for dating the recent past. *Quaternary Geochronology*, 4(5):400–405, 2009.

[13] M. Veicht, I. Mihalcea, D. Cvjetinovic, and D. Schumann. Radiochemical separation and purification of non-carrier-added silicon-32. *Radiochimica Acta*, 109(10):735–741, 2021.

[14] S. Pommé, S.M. Jerome, and C. Venchiarutti. Uncertainty propagation in nuclear forensics. *Applied Radiation and Isotopes*, 89:58–64, 2014.

[15] M.A. Kellett. Assessment of actinide decay data evaluations: findings of an iaea coordinated research project. *Applied Radiation and Isotopes*, 70(9):1919–1923, 2006.

[16] A.L. Nichols. Nuclear decay data: observations and reflections. *Applied Radiation and Isotopes*, 64(10):1384–1391, 2006.

[17] A.L. Nichols. Two determinations of the ge-68 half-life. *Applied Radiation and Isotopes*, 134:416–420, 2018.

[18] S Pommé. Typical uncertainties in alpha-particle spectrometry. *Applied Radiation and Isotopes*, 52:146, 2015.

[19] W. Westmeier. Detection probabilities using surface barrier detectors for alpha-decay-chain members. *Nuclear Instruments and Methods*, 163(2):593–595, 1979.

[20] F. Meissner, W.D. Schmidt-Otto, and L. Ziegeler. Half-life and α-ray energy of ^{146}sm. *Zeitschrift für Physik A Atomic Nuclei*, 327-2:171–174, 1987.

[21] A. Carles and A. Malonda. Liquid scintillation high resolution spectral analysis. *CIEMAT1208*, 41, 2010. Reference number: 41084085.

[22] W.J. McDowell. Alpha counting and spectrometry using liquid scintillation methods. 1986. https://www.osti.gov/biblio/6035149.

[23] N.E. Marks, L.E. Borg, I.D. Hutcheon, B. Jacobsen, and R.N. Clayton. Samarium-neodymium chronology and rubidium-strontium systematics of an allende calcium-aluminum-rich inclusion with implications for ^{146}sm half-life. *Earth and Planetary Science Letters*, 405:15–24, 2014.

[24] N. Kinoshita, M. Paul, Y. Kashiv, P. Collon, C. M. Deibel, B. DiGiovine, J. P. Greene, D. J. Henderson, C. L. Jiang, S. T. Marley, T. Nakanishi, R. C. Pardo, K. E. Rehm, D. Robertson, R. Scott, C. Schmitt, X. D. Tang, R. Vondrasek, and A. Yokoyama. Shorter ^{146}sm half-life measured and implications for ^{146}sm-^{142}nd chronology in the solar system. *Science*, 335(6076):1614–1617, 2012. Redacted on 3/31/2023.

[25] T.S. Kruijer and et al. The early differentiation of mars inferred from hf–w chronometry. *Earth and Planetary Science Letters*, 474:345–354, 2017.

[26] L.E. Borg and *et. al.* Accretion timescale and impact history of mars deduced from the isotopic systematics of martian meteorites. *Geochimica et Cosmochimica Acta*, 175:150–167, 2016.

[27] L.E. Borg and *et. al.* Chronological evidence that the moon is either young or did not have a global magma ocean. *Nature*, 477:70–72, 2011.

[28] M.E. Sanborn, R.W. Carlson, and M. Wadhwa. ^{147,146}sm–^{143,142}nd, ^{176}lu–^{176}hf, and ^{87}rb–^{87}sr systematics in the angrites: Implications for chronology and processes on the angrite parent body. *Geochimica et Cosmochimica Acta*, 171:80–99, 2015.

[29] E. Browne and J. K. Tuli, 2012. https://www.nndc.bnl.gov/nudat3.

[30] https://www.nasa.gov/image-article/planetary-smash-up/.

[31] J. Xu, P. Barbeau, and Z. Hong. Detection and calibration of low-energy nuclear recoils for dark matter and neutrino scattering experiments. *Annual Review of Nuclear and Particle Science*, 73(1):95–121, 2023.

[32] P.S. Barbeau, J.I. Collar, and O. Tench. Large-mass ultralow noise germanium detectors: performance and applications in neutrino and astroparticle physics. *Journal of Cosmology and Astroparticle Physics*, 2007(09), sep 2007.

[33] C.E. Aalseth and *et. al.* Results from a search for light-mass dark matter with a p-type point contact germanium detector. *Phys. Rev. Lett.*, 106, 2011.

[34] C.E. Aalseth, P.S. Barbeau, J. Colaresi, J.I. Collar, J. Diaz Leon, J.E. Fast, N.E. Fields, T.W. Hossbach, A. Knecht, M.S. Kos, M.G. Marino, H.S. Miley, M.L. Miller, J.L. Orrell, and K.M. Yocum. Cogent: A search for low-mass dark matter using p-type point contact germanium detectors. *Phys. Rev. D*, 88, 2013.

[35] H. Bonet and et al. Large-size sub-kev sensitive germanium detectors for the conus experiment. *The European Physical Journal C*, 81, 2021.

[36] R.M. Bonicalzi, J.I. Collar, J. Colaresi, J.E. Fast, N.E. Fields, E.S. Fuller, M. Hai, T.W. Hossbach, M.S. Kos, J.L. Orrell, C.T. Overman, D.J. Reid, B.A. VanDevender, C. Wiseman, and K.M. Yocum. The c-4 dark matter experiment. *Nuclear Instruments and Methods in Physics Research Section A: Accelerators, Spectrometers, Detectors and Associated Equipment*, 712:27–33, 2013.

[37] X. P. Geng and *et. al.* Projected sensitivity of the cdex-50 experiment, 2023.

[38] J. Colaresi, J.I. Collar, T.W. Hossbach, A.R.L. Kavner, C.M. Lewis, A.E. Robinson, and M.K. Yocum. First results from a search for coherent elastic neutrino-nucleus scattering at a reactor site. *Phys. Rev. D*, 104, 2021.

[39] J. Colaresi, J.I. Collar, T.W. Hossbach, C.M. Lewis, and K.M. Yocum. Measurement of coherent elastic neutrino-nucleus scattering from reactor antineutrinos. *Phys. Rev. Lett.*, 129, 2022.

[40] F. Simon. Application of low temperature calorimetry to radioactive measurements. *Nature*, 135, 1935.

[41] S.H. Moseley, J.C. Mather, and D. McCammon. Thermal detectors as x-ray spectrometers. *Journal of Applied Physics*, 56(5):1257–1262, 09 1984.

[42] E. Fiorini and T.O. Niinikoski. Low-temperature calorimetry for rare decays. *Nuclear Instruments and Methods in Physics Research*, 224(1):83–88, 1984.

[43] M.W. Goodman and E. Witten. Detectability of certain dark-matter candidates. *Phys. Rev. D*, 31:3059–3063, Jun 1985.

[44] Y.S. Jang and *et. al. Journal of Low Temperature Physics*, 167(5):967–972, 2012.

[45] W.S. Yoon and et al. Development of a high resolution alpha spectrometer using a magnetic calorimeter. *NIM. A.*, 784:143–146, 2015.

[46] W.S. Yoon, G.B. Kim, H.J. Lee, J.Y. Lee, J.H. Lee, Y.S. Jang, S.J. Lee, M.K. Lee, and Y.H. Kim. Fabrication of metallic magnetic calorimeter for radionuclide analysis. *Journal of Low Temperature Physics*, 176(5-6):644 – 649, 2014.

[47] G.B. Kim. *A $0\nu\beta\beta$ search using large scintillating crystal with metallic magnetic calorimeter.* PhD thesis, Seoul National University, 2016.

[48] D. McCammon. *Semiconductor Thermistors*, pages 36–62. Springer Berlin Heidelberg, 2005.

[49] C.R. Bates. *Development of Metallic Magnetic Calorimeters for Nuclear Safeguards Applications*. PhD thesis, University of California, Berkeley, 2015.

[50] K. Irwin and G. Hilton. *Transition-edge Sensors*, pages 63–150. Springer Berlin Heidelberg, 2005.

[51] T. Van Duzer and C.W. Turner. *Principles of superconductive devices and circuits*. Edward Arnold, 1981.

[52] Magnicon. Magnicon single stage current sensorsr. http://www.magnicon.com/squid-sensors/single-stage-current-sensors.

[53] Valentin T. Jordanov, Glenn F. Knoll, Alan C. Huber, and John A. Pantazis. Digital techniques for real-time pulse shaping in radiation measurements. *Nuclear Instruments and Methods in Physics Research Section A: Accelerators, Spectrometers, Detectors and Associated Equipment*, 353(1):261–264, 1994.

[54] V.T. Jordanov and G.F. Knoll. Digital synthesis of pulse shapes in real time for high resolution radiation spectroscopy. *Nuclear Instruments and Methods in Physics Research Section A: Accelerators, Spectrometers, Detectors and Associated Equipment*, 345(2):337–345, 1994.

[55] Glenn F. Knoll. *Radiation Detection and Measurement*. John Wiley and Sons, 2010.

[56] Steven W. Smith. *The Scientist and Engineer's Guide to Digital Signal Processing*. California Technical Publishing, 1997. http://www.dspguide.com/.

[57] W.H. Press, S.A. Teukolsky, W.T. Vetterling, and B.P. Flannery. *Numerical Recipes in C*. Cambridge University Press, Cambridge, USA, second edition, 1992.

[58] E. Gatti, M. Sampietro, and P.F. Manfredi. Optimum filters for detector charge measurements in presence of 1f noise. *Nuclear Instruments and Methods in Physics Research Section A: Accelerators, Spectrometers, Detectors and Associated Equipment*, 287(3):513–520, 1990.

[59] F.S Goulding. Semiconductor detectors for nuclear spectrometry, i. *Nuclear Instruments and Methods*, 43(1):1–54, 1966. Proceedings of the Tenth Summer Meeting of Nuclear Physicists.

[60] Compass multiparametric daq software for physics applications. https://www.caen.it/products/compass/ Users Manual 5960 Rev. 21.

[61] J.O. Smith. Musics and by courtesy electrical engineering.

[62] Table of laplace and z transforms. http://lpsa.swarthmore.edu/LaplaceZTable/LaplaceZFuncTable.html.

[63] Ronald W. Schafer. What is a savitzky-golay filter? [lecture notes]. *IEEE Signal Processing Magazine*, 28(4):111–117, 2011.

[64] Scipy signal. https://docs.scipy.org/doc/scipy/reference/signal.html.

[65] Arrow Electronics. Rc circuit basics - low and high pass filtering and formulas.

[66] Y.N. Yuryev, Y.S. Jang, S.K. Kim, K.B. Lee, M.K. Lee, S.J. Lee, W.S. Yoon, and Y.H. Kim. Signal processing in cryogenic particle detection. *Nuclear Instruments and Methods*, 635(1):82–85, 2021.

[67] S. Friedrich. Safeguards measurements with ultra-high resolution magnetic microcalorimeter radiation detectors. *Comprehensive Technology Readiness Assessment*, 2020.

[68] C.R. Bates and *et. al.* Reproducibility and calibration of mmc-based high-resolution gamma detectors. *Appl. Phys. Lett.*, 109(2), 2016.

[69] Goddard Space Flight Center Astrophysics Science Division. Xrs-2 pulse height analysis - details.

[70] Ortec Amptek. Dspec pro digital gamma-ray spectrometer hardware user's manual, 2014. https://www.ortec-online.com/products/electronics/multichannel-analyzers-mca/workstation/dspec-pro.

[71] Canberra Mirion. Genie 2000, 2015. https://www.mirion.com/products/genie-2000-gamma-analysis-software.

[72] A.S. Hoover, E.M. Bond, M.P. Croce, T.G. Holesinger, G.J. Kunde, M.W. Rabin, L.E. Wolfsberg, D.A. Bennett, J.P. Hays-Wehle, D.R. Schmidt, D. Swetz, and J.N. Ullom. Measurement of the 240pu/239pu mass ratio using a transition-edge-sensor microcalorimeter for total decay energy spectroscopy. *Analytical Chemistry*, 87(7):3996 – 4000, 2015.

[73] K.E. Koehler. Low temperature microcalorimeters for decay energy spectroscopy. *Applied Sciences*, 11:40–44, 2021.

[74] P.C.-O Ranitzsch, D. Arnold, J. Beyer, L. Bockhorn, J.J Bonaparte, and et al. Metrommc: Electron-capture spectrometry with cryogenic calorimeters for science and technology. *Journal of Low Temperature Physics*, 199:441–450, 2020.

[75] M. Rodrigues, M. Laarraj, M. Loidl, X.F. Navick, and R. Mariam. Development of total decay energy spectrometry of alpha-emitting radionuclides using metallic magnetic calorimeters. *Journal of Low Temperature Physics*, 193:1263 – 1268, 2018.

[76] H. Rotzinger, M. Linck, A. Burck, M. Rodrigues, M. Loidl, E. Leblanc, L. Fleischmann, A. Fleischmann, and C. Enss. Beta spectrometry with magnetic calorimeters. *Journal of Low Temperature Physics*, 151:1087–1093, 2008.

[77] C. Hassel and et al. Recent results for the echo experiment. *Journal of Low Temperature Physics*, 184, 2016.

[78] G.B. Kim, L.E. Borg, S.T.P. Boyd, R.H. Cantor, J.D. Despotopulos, O.B. Drury, S. Friedrich, A. Gallant, N.R. Hines, A. Jacobs, I. Jovanovic, K.N. Kmak, A.R.L. Kavner, Y.H. Kim, P. Kunz, A.A. Kwiatkowski, D.H. Kwon, D. Lee, T. Murböck, N.D. Scielzo, Q.R. Shollenberger, C.K.I. Sio, K.J. Thomas, T. Wooddy, and C. Walls. Absolute decay counting of ^{146}sm and ^{147}sm for early solar system chronology. *Journal of Low Temperature Physics*, 209:824–831, 2022.

[79] S. Agostinelli and *et. al.* Geant4—a simulation toolkit. *Nuclear Instruments and Methods in Physics Research Section A: Accelerators, Spectrometers, Detectors and Associated Equipment*, 506(3):250–303, 2003.

[80] T. Parsons-Davis and *et. al.* Progress on plutonium certified reference material 946 – 948 recertification, 2021. https://www.osti.gov/servlets/purl/1818406.

[81] K.E. Koehler and *et. al.* Q spectroscopy with superconducting sensor microcalorimeters. *IEEE Transactions on Nuclear Science*, 60(2):624 – 629, 2013.

[82] M.P. Croce, A.S. Hoover, M.W. Rabin, E.M Bond, L.E. Wolfsberg, D.R. Schmidt, and J.N. Ullom. Quantitative analysis of plutonium content in particles collected from a certified reference material by total nuclear reaction energy (q value) spectroscopy. *Journal of Low Temperature Physics*, 184:938 – 943, 2016.

[83] P. Guss, M.W. Rabin, M.P. Croce, N.J. Hoteling, D. Schwellenbach, C. Kruschwitz, V. Mocko, and S. Mukhopadhyay. High–resolution photon spectroscopy with a microwavemultiplexed 4-pixel transition edge sensor array. 2017.

[84] NBL Program Office. Certificate of analysis certified reference material c136 plutonium isotopic standard. https://www.energy.gov/nnsa/articles/nbl-program-office-certificate-analysis-certified-reference-material-c136-10mg.

[85] B.D. Fields, A.L. Melott, J. Ellis, A.F. Ertel, B.J. Fry, B.S. Lieberman, Z. Liu, J.A. Miller, and B.C. Thomas. Supernova triggers for end-devonian extinctions. *Proceedings of the National Academy of Sciences*, 117(35), 2020.

[86] S.T.P. Boyd and *et. al. IEEE Transactions on Applied Superconductivity*, 33:1–5, 2023.

[87] A.N. Kevork and H.G. Escudero. Visible in the laboratory and invisible in cosmology: decaying sterile neutrinos, 2023.

[88] K.G. Leach and S. Friedrich. The beest experiment: Searching for beyond standard model neutrinos using ^{7}be decay in stjs. *Journal of Low Temperature Physics*, 209:796–803, 2022.

[89] M. Aker and *et. al.* 10.1038/s41567-021-01463-1. *Nature Physics*, 18:160–166, 2022.

[90] A. Nucciotti and *et. al.* Status of the holmes experiment to directly measure the neutrino mass. *Journal of Low Temperature Physics*, 193:1137–1145, 2018.

[91] M.G. Betti and *et. al.* Neutrino physics with the ptolemy project: active neutrino properties and the light sterile case. *Journal of Cosmology and Astroparticle Physics*, 2019(07):047, 2019.

[92] Bluefors. Bluefors products ld diltion refrigerator. https://bluefors.com/products/ld-dilution-refrigerator/.

[93] A. Algora, J.L. Tain, B. Rubio, M. Fallot, and W. Gelletly. Beta-decay studies for applied and basic nuclear physics. *The European Physical Journal A*, 57(3), 2021.

[94] J.J. Simpson and A. Hime. Evidence of the 17-kev neutrino in the β spectrum of ^{35}S. *Phys. Rev. D*, 39:1825–1836, 1989.

[95] D.R.O. Morrison. The rise and fall of the 17-kev neutrino. *Nature*, 366:29–32, 1993.

[96] M. Loidl, E. Leblanc, M. Rodrigues, T. Branger, D. Lacour, J. Bouchard, and B. Censier. Validation study of a new technique for absolute activity measurement with 4pi solid angle metallic magnetic calorimeters. *Applied Radiation and Isotopes*, 66(6):872–876, 2008.

[97] M. Loidl, M. Rodrigues, B. Censier, S. Kowalski, X. Mougeot, P. Cassette, T. Branger, and D. Lacour. First measurement of the beta spectrum of 241pu with a cryogenic detector. *Applied Radiation and Isotopes*, 68(7-8):1454 – 1458, 2010.

[98] Meyer-Tool. Common cryogenic materials: G-10 and g-11. https://www.mtm-inc.com/common-cryogenic-materials-g-10-and-g-11-fiberglass.html.

[99] CMR-Rirect. Ge varnish. https://www.cmr-direct.com/en/ge-varnish.

[100] M.S. Basunia and C.D. Nesaraja. *Nuclear Data Sheets*, 107, 2006. https://www.nndc.bnl.gov/nudat3/.

[101] M.S. Basunia. *Nuclear Data Sheets*, 107, 2006. https://www.nndc.bnl.gov/nudat3/.

[102] E. Browne and J. K. Tuli. *Nuclear Data Sheets*, 108, 2007. https://www.nndc.bnl.gov/nudat3/.

[103] S. Zhu. *Nuclear Data Sheets*, 182, 2014. https://www.nndc.bnl.gov/nudat3/.

[104] M.S. Basunia. *Nuclear Data Sheets*, 107, 2006. https://www.nndc.bnl.gov/nudat3/.

[105] National-Instruments. Systems and hardware. https://www.ni.com/en-us/shop.html.

[106] D Malain and P Kanchana. Evaluation of radiation safety for ionization chamber smoke detectors containing am-241. 1285(1), 2019.

[107] A.A. Sonzogni, 2001. https://www.nndc.bnl.gov/nudat3.

[108] National nuclear data center.

[109] T.D. Johnson, D. Symochko, M. Fadil, and J.K. Tuli. *Nuclear Data Sheets*, 112, 2011. https://www.nndc.bnl.gov/nudat3.

[110] Oak Ridge National Laboratory. National isotope development center. https://www.isotopes.gov/.

[111] J. Tuli. *Nuclear Data Sheets*, 84. https://www.nndc.bnl.gov/nudat3/.

[112] A. Fleischmann, L. Gastaldo, S. Kempf, A. Kirsch, A. Pabinger, C. Pies, J.P. Porst, P. Ranitzsch, S. Schäfer, V.F. Seggern, and *et. al. Metallic magnetic calorimeters*, volume 1185. 2009.

[113] A. Fleischmann, T. Daniyarov, M. Linck, H. Rotzinger, S. Hunklinger, C. Enss, and G. M. Seidel. Metallic magnetic microcalorimeters: Energy dispersive x-ray detectors with high spectral resolving power. *Phonons2004*, 1:2824–2827, 2004.

[114] C.E. Aalseth, P.S. Barbeau, J. Colaresi, J.I. Collar, J.D. Leon, J.E. Fast, N.E. Fields, T.W. Hossbach, A. Knecht, M.S. Kos, M.G. Marino, H.S. Miley, M.L. Miller, J.L. Orrell, and K.M. Yocum. Cogent: A search for low-mass dark matter using -type point contact germanium detectors. *Phys. Rev. D*, 88:012002, 2013.

[115] PyPi. iminuit 2.17.0. https://pypi.org/project/iminuit/.

[116] Q.R. Shollenberger and *et. al.* Chemical separation of ^{146}sm for half-life determination. *Journal of Radioanalytical and Nuclear Chemistry*, 331:4963–4969, 2022.

[117] M.P. Croce and *et. al.* Quantitative analysis of plutonium content in particles collected from a certified reference material by total nuclear reaction energy (q value) spectroscopy. *Journal of Low Temperature Physics*, 184:938–943, 2016.

[118] J. Dilling, R. Krucken, and L. Merminga. *ISAC and ARIEL: The TRIUMF Radioactive Beam Facilities and the Scientific Program*. Springer, 2014.

[119] E. Browne and J. K. Tuli, 2009. https://www.nndc.bnl.gov/nudat3.

[120] N. Nica. *Nuclear Data Sheets*, 187, 2023. https://www.nndc.bnl.gov/nudat3.

[121] S.G. Kim and *et. al.* Low temperature property study of mmcs used for neutrinoless double beta decay. *IEEE Transactions on Applied Superconductivity*, 31:1–5, 2021.

[122] M. Newman. Power laws, pareto distributions and zipf's law. *Contemporary Physics*, 46(5):323–351, 2005.

[123] New Brunswick Laboratory. Nbl certified reference materials catalog. https://www.nrc.gov/docs/ML0512/ML051220501.pdf.

[124] F.E. Stanley, K.J. Mathew, B.L. Byerly, R. Keller, K.J. Spencer, and M.R. Thomas. ursuing standards strategies in nuclear forensics: investigating extraction of progeny uranium in crm-126a as a quality control material in pu–u chronometry. *Journal of Radioanalytical and Nuclear Chemistry*, 311:1819–1824, 2017.

[125] J.M. Carson, F.V. Hippel, and E. LYMAN. Explosive properties of reactor-grade plutonium. *Science and Global Security*, 17(2-3):170–185, 2009.

[126] W. Seifritz. Remarks on the plutonium-240 induced pre-ignition problem in a nuclear device. *Nuclear Technology*, 54(3):431–431, 1981.

[127] Jonathan Goodman and Jonathan Weare. Ensemble samplers with affine invariance. *Communications in Applied Mathematics and Computational Science*, 5(1), 2010.

[128] Daniel Foreman-Mackey, David W. Hogg, Dustin Lang, and Jonathan Goodman. emcee: The mcmc hammer. *Publications of the Astronomical Society of the Pacific*, 125(925):306, feb 2013.

[129] D. Foreman-Mackey, D.W. Hogg, D. Lang, and J. Goodman. The mcmc hammer. *Publications of the Astronomical Society of the Pacific*, 125(925), 2013.

[130] https://emcee.readthedocs.io/en/stable/.

[131] B.J. Scholz, A.E. Chavarria, J.I. Collar, P. Privitera, and A.E. Robinson. Measurement of the low-energy quenching factor in germanium using an ^{88}Y/Be photoneutron source. *Phys. Rev. D*, 94, 2016.

[132] https://www.statlect.com/fundamentals-of-statistics/Poisson-distribution-maximum-likelihood.

[133] R.C. Gostic. *Characterization of plutonium particles originating from the BOMARC accident -1960*. PhD thesis, UNLV, 2010.

[134] F. Bloch and H. Staub. Fission spectrum. 8 1943.

[135] S.K. Basu, G. Mukherjee, and A.A. Sonzogni. *Nuclear Data Sheets*, 111(2555), 2010. https://www.nndc.bnl.gov/nudat3.

[136] R. Kolb, H. Weerts, N. Toro, R. Van de Water, R. Essig, D. McKinsey, K. Zurek, A. Chou, P. Graham, J. Estrada, J. Incandela, and T. Tait. Basic research needs for dark-matter small projects new initiatives: Report of the department of energy's high energy physics workshop on dark matter. 2018.

[137] J.L. Feng. The wimp paradigm: Theme and variations. *SciPost Phys. Lect. Notes*, 2023.

[138] R. Essig and et al. Snowmass2021 cosmic frontier: The landscape of low-threshold dark matter direct detection in the next decade.

[139] J.I. Collar, A.R.L. Kavner, and C.M. Lewis. Response of csi[na] to nuclear recoils: Impact on coherent elastic neutrino-nucleus scattering. *Phys. Rev. D*, 100:033003, 2019.

[140] N. Fourches, M. Zielińska, and G. Charles. *High Purity Germanium: From Gamma-Ray Detection to Dark Matter Subterranean Detectors*, chapter 5. IntechOpen, 2019.

[141] P.R. Scovell, E. Meehan, S.M. Paling, M. Thiesse, X. Liu, C. Ghag, M. Ginsz, P. Quirin, and D. Ralet. Ultra-low background germanium assay at the boulby underground laboratory. *Journal of Instrumentation*, 19(01), 2024.

[142] D Akimov and *et. al.* Coherent experiment: current status. *Journal of Physics: Conference Series*, 798(1), 2017.

[143] Kate Scholberg. Coherent elastic neutrino-nucleus scattering. *Journal of Physics: Conference Series*, 1468(1):012126, 2020.

[144] Z.Y. Zhang and *et. al.* Constraints on sub-gev dark matter–electron scattering from the cdex-10 experiment. *Phys. Rev. Lett.*, 129, 2022.

[145] L. Singh and *et. al.* Constraints on millicharged particles with low-threshold germanium detectors at kuo-sheng reactor neutrino laboratory. *Phys. Rev. D*, 99, 2019.

[146] J. Lindhard, V. Nielsen, M. Scharff, and P.V. Thomsen. Integral equations governing radiation effects. (notes on atomic collisions, iii). *Kgl. Danske Videnskab. Selskab. Mat. Fys. Medd.*, 33, 1963. https://www.osti.gov/biblio/4701226.

[147] C. Chasman, K.W. Jones, and R.A. Ristinen. Measurement of the energy loss of germanium atoms to electrons in germanium at energies below 100 kev. *Phys. Rev. Lett.*, 15:245–248, Aug 1965.

[148] C. Chasman, K.W. Jones, R.A. Ristinen, and J.T. Sample. Measurement of the energy loss of germanium atoms to electrons in germanium at energies below 100 kev. ii. *Physical Review*, 154(2):239 – 244, 1967.

[149] C. Chasman, K.W. Jones, H.W. Kraner, and W. Brandt. Band-gap effects in the stopping of ge^{72*} atoms in germanium. *Phys. Rev. Lett.*, 21:1430–1433, Nov 1968.

[150] K.W. Jones, H.W., and Kraner. Stopping of 1- to 1.8-kev ^{73}Ge atoms in germanium. *Phys. Rev. C*, 4:125–129, 1971.

[151] K.W. Jones, H.W., and Kraner. Energy lost to ionization by 254-ev ^{73}Ge atoms stopping in ge. *Phys. Rev. A*, 11:1347–1353, 1975.

[152] Y. Messous and *et. al.* Calibration of a ge crystal with nuclear recoils for the development of a dark matter detector. *Astroparticle Physics*, 3(4):361–366, 1995.

[153] E. Simon and *et. al.* Sicane: a detector array for the measurement of nuclear recoil quenching factors using a monoenergetic neutron beam. *Nuclear Instruments and Methods in Physics Research Section A: Accelerators, Spectrometers, Detectors and Associated Equipment*, 507(3):643–656, 2003.

[154] A. Benoit and *et. al.* Measurement of the response of heat-and-ionization germanium detectors to nuclear recoils. *Nuclear Instruments and Methods in Physics Research Section A: Accelerators, Spectrometers, Detectors and Associated Equipment*, 577(3):558–568, 2007.

[155] A. Ahmed and *et. al.* Results from a low-energy analysis of the cdms ii germanium data. *Phys. Rev. Lett.*, 106:131302, Mar 2011.

[156] A.K. Soma and *et. al.* Characterization and performance of germanium detectors with sub-kev sensitivities for neutrino and dark matter experiments. *Nuclear Instruments and Methods in Physics Research Section A: Accelerators, Spectrometers, Detectors and Associated Equipment*, 836:67–82, 2016.

[157] J.I. Collar, A.R.L. Kavner, and C.M. Lewis. Germanium response to sub-kev nuclear recoils: A multipronged experimental characterization. *Phys. Rev. D*, 103, 2021.

[158] A. Bonhomme, H. Bonet, C. Buck, J. Hakenmüller, G. Heusser, T. Hugle, M. Linder, W. Maneschg, R. Nolte, T. Rink, E. Pirovano, and H. Strecker. Direct measurement of the ionization quenching factor of nuclear recoils in germanium in the kev energy range. *The European Physical Journal C*, 82, 2022.

[159] M.A. Islam, T.J. Kennett, and W.V. Prestwich. Radiative strength functions of germanium from thermal neutron capture. *Phys. Rev. C*, 43:1086–1098, Mar 1991.

[160] Iaea nuclear data services. https://www-nds.iaea.org/relnsd/vcharthtml/VChartHTML.html.

[161] M.J. Berger, J.H. Hubbell, S.M. Seltzer, J. Chang, J.S. Coursey, R. Sukumar, D.S. Zucker, and K. Olsen. Xcom: Photon cross sections database. NIST Standard Reference Database 8 (XGAM).

[162] L.S. Waters, G.W. McKinney, J.W. Durkee, M.L. Fensin, J.S. Hendricks, M.R. James, R.C. Johns, and D.B. Pelowitz. The mcnpx monte carlo radiation transport code. *AIP Conference Proceedings*, 896:81–90, 2007.

[163] Coulomb excitation of 73ge and quasiparticle-phonon coupling theories. *Nuclear Physics A*, 192(2):312–328, 1972.

[164] B. Singh and J. Chen. Adopted levels and gammas for 73ge. *Nucl. Data Sheets*, 158(1), 2019. https://www.nndc.bnl.gov/nudat3/.

[165] https://reactor.osu.edu/.

[166] D. Turkoglu, J. Burke, R. Lewandowski, and L.R. Cao. Characterization of a new external neutron beam facility at the ohio state university. *Journal of Radioanalytical and Nuclear Chemistry*, 291, 2012.

[167] https://www.ortec-online.com/products/radiation-detectors/high-purity-germanium-hpge-radiation-detectors.

[168] https://www.ortec-online.com/-/media/ametekortec/brochures/g/glp.pdf.

[169] F. Cannizzaro, G. Greco, M. Raneli, M.C. Spitale, and E. Tomarchio. A low-level spectrometer with a planar low-energy hpge: shielding arrangement tests and system performance for 210pb determination in air filter samples. *Applied Radiation and Isotopes*, 55(1):129–133, 2001.

[170] https://www.caen.it/products/dt5780.

[171] https://www.caen.it/products/dt5533e.

[172] Glen Knoll. *Radiation Detection and Measurement (4th ed.)*. John Wiley, 2010.

[173] Ortec. Introduction to amplifiers.

[174] Ieee standard test procedures for germanium gamma-ray detectors. *IEEE Std 325-1996*, 1997.

[175] R.M. Keyser and T.R. Twomey. Optimization of pulse processing parameters for hpge gamma-ray spectroscopy systems used in extreme count rate conditions and wide count rate ranges. *Journal of Radioanalytical and Nuclear Chemistry*, 296:503–508, 2013. https://api.semanticscholar.org/CorpusID:95036177.

[176] G. Czjzek, J.L.C. Ford, J.C. Love, F.E. Obenshain, and H.H.F. Wegener. Coulomb-recoil-implantation mössbauer experiments with ^{73}Ge. *Phys. Rev.*, 174:331–345, 1968.

[177] L. Pfeiffer, R.S. Raghavan, C.P. Lichtenwalner, and A.G. Cullis. Mössbauer effect of the 13.3-kev transition in ^{73}Ge. *Phys. Rev. B*, 12:4793–4804, 1975.

[178] R.S. Raghavan and L. Pfeiffer. Observation of the high-resolution mössbauer resonance in ^{73}Ge. *Phys. Rev. Lett.*, 32:512–514, 1974.

[179] R. Weishaupt and D. Rabenstein. *Zeitschrift für Physik A Hadrons and nuclei*, 251, 1972.

[180] L.C. Longoria, A.H. Naboulsi, P.W. Gray, and T.D. MacMahon. Analytical peak fitting for gamma-ray spectrum analysis with ge detectors. *Nuclear Instruments and Methods in Physics Research Section A: Accelerators, Spectrometers, Detectors and Associated Equipment*, 299(1):308–312, 1990.

[181] Gary W. Phillips and Keith W. Marlow. Automatic analysis of gamma-ray spectra from germanium detectors. *Nuclear Instruments and Methods*, 137(3):525–536, 1976.

[182] A. Thompson and *et. al.* X-ray data booklet. https://cxro.lbl.gov/x-ray-data-booklet.

[183] J.A. Bearden and A.F. Burr. Reevaluation of x-ray atomic energy levels. *Reviews of Modern Physics*, 39(1), 1967.

[184] J.C. Fuggle and N. Martensson. Core-level binding energies in metals. *Journal of Electron Spectroscopy and Related Phenomena*, 21(3):275–281, 1980.

[185] K. Ke-Jun and *et. al.* Cdex-1 1 kg point-contact germanium detector for low mass dark matter searches. *Chinese Physics C*, 37(12), 2013.